

UNIVERSITÀ DEGLI STUDI DI TRIESTE

XXXVIII CICLO DEL DOTTORATO DI RICERCA IN FISICA

Disorder and interaction effects in topological insulators

Settore scientifico-disciplinare: PHYS/04

DOTTORANDA

Roberta Favata

COORDINATORE

Prof. Angelo Bassi

SUPERVISORI DI TESI

Prof. Federico Becca

Antimo Marrazzo

ANNO ACCADEMICO 2024/2025

Contents

Introduction **5**

List of Publications **9**

1 An introduction to topological insulators **10**
1.1 The band theory of solids 12
1.1.1 Bloch wavefunctions 14
1.1.2 Wannier functions 17
1.2 Topological band theory 19
1.2.1 Berry phase and Chern number 20
1.2.2 Berryology of the Brillouin zone 23
1.3 Chern insulators 26
1.3.1 The Haldane model 27
1.4 Time-reversal protected topological insulators 30
1.4.1 The Kane–Mele model 32
1.4.2 The Bernevig–Hughes–Zhang model 34
1.5 Topology beyond the non-interacting crystalline limit 37

2 Topological invariants in disordered systems **39**
2.1 Single-point topological invariants in supercell framework 40
2.1.1 Single-point Chern number 42
2.1.2 Single-point spin Chern number 44
2.2 Local topological markers 46
2.2.1 Local Chern and $\mathbb{Z}_2$ markers in finite systems 47
2.2.2 Local Chern and $\mathbb{Z}_2$ markers in periodic systems 49

3 Fluctuations and correlations of local topological order parameters in disordered two-dimensional topological insulators 52
3.1 Fluctuations and correlation function of local Chern marker 54
3.1.1 Disorder-driven transition from QAHI to trivial insulator 54
3.1.2 Topological Anderson insulator transitions 57
3.1.3 Vacancy-driven transition 58
3.2 Fluctuations and correlations in quantum spin Hall insulators 59
3.3 Critical exponents from topological correlation functions 61

4 Towards realistic topological materials: monolayer jacutingaite with defects 64
4.1 First-principles electronic structure calculations 65
4.1.1 Density-functional theory 66
4.1.2 Wannier interpolation and *ab initio* tight-binding models 69
4.1.3 Bands unfolding 73
4.2 Hg vacancies in a monolayer of jacutingaite 75
4.2.1 *Ab initio* characterization of a single Hg vacancy 77
4.2.2 Vacancy effects within effective tight-binding models 80

5 Variational Monte Carlo approach for correlated topological systems 82
5.1 Hamiltonian models for interacting electronic systems 83
5.1.1 The multi-orbital Hubbard-Kanamori Hamiltonian 85
5.1.2 The single-band Hubbard model 87
5.2 The Jastrow factor 90
5.3 Ground-state probes of electronic and topological properties 91
5.3.1 Feynman construction for charge and spin excitations 92
5.3.2 Topological invariants for interacting systems 93
5.3.2.1 Berry phase for correlated systems 95
5.3.2.2 Many-body marker for correlated $\mathbb{Z}_2$ topological insulators . . . 97
5.4 Variational Monte Carlo framework 98
5.4.1 Variational principle 99
5.4.2 The Metropolis algorithm 101
5.4.3 The Jastrow-Slater wavefunction 102
5.4.4 The Stochastic Reconfiguration optimization method 103

6 Interaction-induced phases in the Bernevig-Hughes-Zhang model 107
6.1 The interacting one-dimensional BHZ model 108
6.1.1 The symmetries of the model 110

6.1.2 The non-interacting and the "atomic" limit . . . 111
6.1.3 The variational wavefunction . . . 114
6.1.4 Numerical results . . . 115
6.1.4.1 The case with $V = 0$ . . . 115
6.1.4.2 The case with $V > 0$ . . . 122
6.2 The interacting two-dimensional BHZ model . . . 124
6.2.1 The symmetries of the non-interacting model . . . 126
6.2.2 Strong-coupling limit . . . 127
6.2.3 The variational wavefunction . . . 130
6.2.4 Numerical results . . . 131
6.2.4.1 The case with $U' = 0$ and the antiferromagnetic phase . . . 132
6.2.4.2 The case with $U' = U$ and the excitonic insulator . . . 135

Conclusions and Outlook **139**

Acknowledgements **142**

Appendix A Time-reversal symmetry **143**
A.1 Time-reversal invariant Hamiltonians . . . 144
A.2 Time-reversal in crystalline systems . . . 145
A.3 Consequences for Berry curvature and Chern number . . . 146

Appendix B Covariant derivative **148**

Appendix C Fast-update algorithm **152**
C.1 Fast computation of the Slater determinant . . . 153
C.2 Fast computation of the Jastrow factor . . . 156

Bibliography **159**

Introduction

Physical matter is organized in an extraordinary variety of phases, and the classification of these phases of matter, together with the understanding of the transitions between them, is one of the central themes of condensed matter physics. For much of the 20th century, this problem was successfully addressed within the Landau theory of phase transitions, that provided an effective description in which the complexity of the system at the microscopic level is replaced by a simplified expression of the free energy function written in terms of *order parameters*. Within this framework, continuous phase transitions are understood as processes driven by spontaneous symmetry breaking, whereby the system selects a ground-state configuration that does not share the full symmetry of the underlying Hamiltonian. The order parameter distinguishes different phases by acquiring a finite value in the symmetry-broken phase and vanishing in the symmetric one. In Landau's original mean-field formulation [1], the order parameter is assumed to be spatially uniform. A major step toward a more accurate description of phase transitions came with the development of Landau-Ginzburg theory [2], where the order parameter is promoted to a field depending on position, and the free energy becomes a functional. This extension makes it possible to account for spatial fluctuations of the local order parameter around the average value m, which play a crucial role near the phase transition. In particular, it provides access to key concepts such as correlation functions, critical behavior, and the role of dimensionality. This approach is extraordinarily powerful and successfully describes a huge variety of phenomena, from boiling water to the loss of magnetization in ferromagnets at high temperature, to superconductivity. Different phase transitions correspond to different broken symmetries and order parameters, but the concept of universality unifies different phenomena in terms of their critical behavior.

Despite its remarkable success, the Landau paradigm relies on the assumption that phases can be distinguished by local order parameters and symmetry considerations. This picture was challenged by the discovery of new quantum phases that do not fit into such a scheme. A paradigmatic example is the integer quantum Hall effect (IQHE), observed in two-dimensional electron systems subjected to strong perpendicular magnetic fields. This phenomenon exhibits

a Hall conductance that is quantized with extraordinary precision and remains robust against perturbations, yet it cannot be associated with any conventional symmetry breaking or local order parameter. Its origin lies instead in the global properties of the quantum state.

These developments led to a broader classification of phases of matter based on *topology*. Within this perspective, two insulating states of matter share the same symmetries and display indistinguishable local properties, while still belonging to distinct topological phases. Their difference is detected by topological invariants, which are global quantities that remain unchanged under continuous deformations, provided that the bulk gap does not close and the relevant symmetries are preserved. Although this characterization is rooted in abstract geometrical ideas, its consequences are directly observable, and a topologically non-trivial insulator is characterized by conducting states at its boundary that are robust against perturbations.

Topological features of materials are commonly established at the non-interacting level in the band-theory framework, where the ground state is represented as a Slater determinant of single-particle Bloch orbitals and the calculation of topological invariants is crucially based on tracking the evolution of occupied states throughout the Brillouin zone.

However, the band-theory paradigm becomes inadequate when its basic assumptions need to be relaxed. This occurs, for instance, in the presence of disorder, which breaks translational symmetry and invalidates the usual notion of Brillouin zone, or in strongly interacting systems, where the single-particle description itself fails, and the topology must be characterized at the many-body level. At the same time, the interplay between band topology, disorder, and electronic correlations is expected to give rise to a rich and unconventional phenomenology. Disorder, which is inevitably present in real materials, does not immediately destroy topological phases, and on the contrary, in some cases, it can even induce a topological character in systems that would be trivial in the clean limit, suggesting possible routes toward defect-engineered topological devices. Strong interactions, on the other hand, may compete with topology giving rise to exotic correlated regimes with no direct counterpart in single-particle band theory.

For these reasons, understanding topology beyond the clean and non-interacting limit is essential for bridging the gap between the formal classification of topological phases and the properties of realistic quantum materials.

Outline

This thesis investigates the effects of non-perturbative disorder and strong correlations in topological insulators, combining methodological developments with numerical applications, with the common goal of extending topological concepts and diagnostics beyond the crystalline and non-interacting framework.

The thesis develops along two main directions. The first part is devoted to disordered topological systems. From a methodological point of view, we introduce and discuss tools for detecting topological phases when translational symmetry is absent, including single-point invariants in the supercell framework and local topological markers. We examine these methods in tight-binding models, with the aim of clarifying their role in disorder-driven topological phase transitions. From an applicative perspective, these techniques are employed to study realistic materials in the presence of atomic defects, using effective Wannier Hamiltonians derived from first-principles calculations.

The second part focuses on the effect of strong electron–electron interactions in topological insulators. This problem is addressed within the variational Monte Carlo framework, which provides a flexible and scalable way to incorporate correlation effects beyond a single-particle description. We use a Jastrow–Slater variational wavefunction, whose structure is physically transparent and allows us to control possible symmetry-breaking tendencies in an interpretable way. The topological properties of interacting systems are characterized using many-body markers inspired by the modern theory of polarization and which are applied here in a novel way to large system sizes, in both one- and two-dimensional systems.

The thesis is organized as follows:

- In Chapter 1, we introduce topological insulators within the non-interacting band-theory framework. We present the formal tools needed to define and compute topological invariants, and discuss paradigmatic lattice models realizing topological phases. In particular, we introduce the Haldane model [3] for Chern insulators, and the Kane–Mele [4, 5] and Bernevig–Hughes–Zhang [6] models for quantum spin Hall insulators, which will be used throughout the thesis.

- In Chapter 2, we develop the theoretical framework used to detect topology in disordered systems. We discuss the supercell approach and present single-point formulas for topological invariants [7, 8], considering both Chern insulators and quantum spin Hall insulators. For these two classes of systems, we also review local topological markers [9–11], which are applicable to finite and periodic geometries and provide a real-space and spatially resolved description of topology.

- In Chapter 3, we apply the tools introduced in the previous chapter to the study of disorder-driven topological phase transitions in paradigmatic tight-binding models. A central result is the demonstration that local topological markers can behave as genuine local order parameters for topological phases in disordered systems, displaying the characteristic

signatures of critical behavior across a disorder-driven transition. The numerical results supporting this analysis are based on Ref. [12].

- In Chapter 4, we turn to realistic topological materials by focusing on a monolayer of jacutingaite (Pt_2HgSe_3), a promising candidate for realizing a quantum spin Hall insulating (QSHI) phase [13]. After introducing first-principles methods, we analyze the response of this material to Hg vacancies by combining fully *ab initio* calculations with Wannier-based effective Hamiltonians. We then use some of the methods introduced in the previous chapters to assess the robustness of the QSHI phase against vacancy disorder and to estimate the critical vacancy concentration at which the topological phase is eventually lost.

- In Chapter 5 we introduce the theoretical tools for investigating correlated topological systems. We present the Hamiltonian description of interacting systems with multi-orbital degrees of freedom, together with ground-state probes for distinguishing insulating phases and characterizing their topological properties in the presence of interactions. We then outline the Variational Monte Carlo framework for studying correlated topological systems through a Jastrow-Slater wavefunction.

- In Chapter 6 we present our variational Monte Carlo study of the Bernevig–Hughes–Zhang model with strong electron-electron correlations, using a multi-orbital Jastrow-Slater wavefunction, both in one and two dimensions. The one-dimensional results, largely based on Ref. [14], reveal a very rich phase diagram in which electronic correlations do not simply renormalize the non-interacting picture but give rise to new emergent phases, including an insulating phase with signatures of gapless spin excitations, at the transition between the topological and trivial phases. We then extend the method to the two-dimensional case, where long-range ordered phases, such as antiferromagnetism, can stabilize. In this setting, we also report the emergence of an excitonic insulating phase, further highlighting the richness of correlation-driven topological phenomena in higher-dimensional systems.

List of Publications

The results presented in this thesis are mainly adapted from the following publications:

- ◇ R. Favata, and A. Marrazzo, *Single-point spin Chern number in a supercell framework*, Electron. Struct. **5** 014005 (2023)
- ◇ R. Favata, D. Piccioni, A. Parola, and F. Becca, *Interaction-induced phases in the half-filled Bernevig-Hughes-Zhang model in one dimension*, Phys. Rev. B **111**, 155105 (2025)
- ◇ R. Favata, N. Baù, and A. Marrazzo, *Fluctuations and correlations of local topological order parameters in disordered two-dimensional topological insulators*, Phys. Rev. Lett. **135**, 026603 (2025)

Additional original results are also presented in this Thesis. They are unpublished and are expected to form the basis of forthcoming manuscripts currently in preparation.

Chapter 1

An introduction to topological insulators

Many problems in condensed matter physics can be successfully described within approximations that, at first sight, may appear quite drastic. This is the case of *band theory*, which has long been one of the most effective frameworks for understanding the electronic properties of solids. Although real materials consist of interacting electrons and nuclei, in many cases the dominant effects of these interactions can be incorporated into an effective potential V_{eff}. Within this approximation, the many-body problem is reduced to the motion of independent electrons in a mean-field environment.

When this effective potential has the periodicity of the crystal lattice, Bloch's theorem applies. The ground-state wavefunction of the system can be written in terms of single-particle states that are labeled by a crystal momentum $\mathbf{k}$ defined in the Brillouin zone. The corresponding energy eigenvalues $\varepsilon_{n\mathbf{k}}$ form the electronic band structure of the material. In the conventional picture, the structure and filling of these bands determine the electronic character of a solid, providing the natural language for distinguishing metals, semimetals, and band insulators.

The discovery of topological insulators originated from a deeper reconsideration of this framework. Its central insight is that a classification based only on energy eigenvalues does not exhaust the information contained in band theory. Indeed, the Bloch wavefunctions themselves carry additional geometrical information. Although the overall phase of a Bloch state is arbitrary, the way in which the phase of occupied states evolves across the entire Brillouin zone can have physical consequences.

From this perspective, an insulating phase is not characterized solely by the presence of an energy gap. Two insulators may have the same symmetries and similar band structures, while still being impossible to continuously deform into one another and, therefore, being distinguishable.

Their classification is encoded in the global structure of the occupied Bloch states over the Brillouin zone and can be quantified by suitable quantities, typically integer numbers, that remain unchanged under smooth deformations of the Hamiltonian, as long as the bulk gap remains open and the relevant symmetries are preserved. Examples of these quantities, known as *topological invariants*, include the Chern number and, in time-reversal-invariant systems, the $\mathbb{Z}_2$ invariant.

Topological insulators are insulating phases distinguished precisely by non-vanishing values of the topological invariants. In the bulk, they display a finite energy gap, as ordinary band insulators do. At their boundaries, however, they host conducting states that are protected by the topology of the bulk electronic structure. This relation between the non-trivial topology of the ground-state wavefunction, encoded in topological invariants, and the appearance of edge states is known as the bulk–boundary correspondence.

For non-interacting systems, topological properties can therefore be naturally formulated within band theory. They are diagnosed by topological invariants constructed from the occupied Bloch states and, equivalently, by the presence of robust boundary modes crossing the bulk gap. A change in the topological invariant necessarily involves the closing and reopening of the bulk gap, unless the protecting symmetry is broken. Such topological phase transitions are not generally described in terms of spontaneous symmetry breaking or local order parameters, and therefore lie outside the traditional Landau paradigm.

The aim of this chapter is to introduce the band-theory framework for topological insulators and the formal tools needed to define and compute topological invariants. Building on this foundation, we discuss lattice models that realize topological phases in the absence of external magnetic fields, starting from the Haldane model for the quantum anomalous Hall effect. We then turn to time-reversal-invariant systems, introducing quantum spin Hall insulators and their realizations in the Kane–Mele and Bernevig–Hughes–Zhang models.

This introductory chapter provides the starting point for the main themes of the thesis: the investigation of topological phases of matter in regimes where the standard band-theory paradigm fails, namely in the presence of disorder, which breaks lattice translational symmetry, and in the presence of strong electronic correlations, which invalidate the independent-electron approximation on which conventional band theory is based.

1.1 The band theory of solids

The variety and complexity of problems studied in condensed matter physics can generally be traced back to the solution of the many-body Hamiltonian

$$\begin{aligned} H_{tot} &= T_e + T_n + V_{ee} + V_{nn} + V_{en} \\ &= -\sum_i^{N_e} \frac{\mathbf{p}_i^2}{2m_e} - \sum_I^N \frac{\mathbf{P}_I^2}{2M_I} + \frac{1}{2}\sum_{i\neq j} \frac{e^2}{|\mathbf{r}_i - \mathbf{r}_j|} + \frac{1}{2}\sum_{I\neq J} \frac{Z_I Z_J e^2}{|\mathbf{R}_I - \mathbf{R}_J|} - \sum_{i,I} \frac{Z_I e^2}{|\mathbf{r}_i - \mathbf{R}_I|} \end{aligned} \tag{1.1}$$

which describes a system of N_e electrons with mass m_e and charge e and N nuclei with mass M_I and charge Z_I. The first two terms T_e and T_n correspond to the kinetic energy of electrons and ions, respectively, while the remaining terms are the electron-electron V_{ee}, nucleus-nucleus V_{nn} and electron-nucleus V_{en} Coulomb interactions. The main challenge in condensed matter is to simplify the Hamiltonian through approximations, according to the aspect that one wants to investigate, without missing the description of the main physical properties. The starting point is the many-body Schrödinger equation

$$H_{\text{tot}}\, \Xi\big(\{\mathbf{R}_I, \sigma_I\}, \{\mathbf{r}_i, \sigma_i\}\big) = E_{\text{tot}}\, \Xi\big(\{\mathbf{R}_I, \sigma_I\}, \{\mathbf{r}_i, \sigma_i\}\big), \tag{1.2}$$

where the total wavefunction Ξ depends on the nuclear $\{\mathbf{R}_I, \sigma_I\}$ and the electronic $\{\mathbf{r}_i, \sigma_i\}$ degrees of freedom, including position and spin.

A first key simplification is provided by the *Born-Oppenheimer approximation*, which exploits the large mass difference between electrons and nuclei to separate the total problem into an electronic problem for fixed nuclei and a nuclear problem under an effective potential generated by electrons. This translates into an *Ansatz* for the total wavefunction which is written as the product

$$\Xi(\{\mathbf{R}_I, \sigma_I\}, \{\mathbf{q}_i\}) = \Phi(\{\mathbf{R}_I, \sigma_I\})\ \Psi_{\mathbf{R}}(\{\mathbf{r}_i, \sigma_i\}) \tag{1.3}$$

where $\Phi(\{\mathbf{R}_I, \sigma_I\})$ is the nuclear wavefunction and $\Psi_{\mathbf{R}}(\{\mathbf{r}_i, \sigma_i\})$ is the electronic wavefunction that depends on the set of nuclear coordinates $\mathbf{R} \equiv \{\mathbf{R}_I\}$. As a result, the electronic problem can be isolated as

$$\mathcal{H}_{el}(\mathbf{R})\ \Psi_{\mathbf{R}}(\{\mathbf{r}_i, \sigma_i\}) = E_{el}(\mathbf{R})\ \Psi_{\mathbf{R}}(\{\mathbf{r}_i, \sigma_i\}), \tag{1.4}$$

where the electronic Hamiltonian is defined as

$$\mathcal{H}_{el}(\mathbf{R}) = T_e + V_{ee} + V_{nn}(\mathbf{R}) + V_{en}(\mathbf{R}). \tag{1.5}$$

where $V_{nn}(\mathbf{R})$ and $V_{en}(\mathbf{R})$ are the previously defined Coulomb interactions computed at a given configuration $\mathbf{R}$ of the nuclei. Then, in the *frozen nuclei approximation*, i.e., by treating the nuclear positions as fixed, the nucleus-nucleus interaction reduces to a constant term, while the

electron-nucleus contribution becomes a one-body operator that describes one electron moving in the field of fixed positive charges. In this approximation, the explicit dependence on $\mathbf{R}$ can be dropped, and the electronic Hamiltonian takes the form

$$\mathcal{H}_{el} = \sum_{i}^{N_e} \left[\frac{\mathbf{p}_i^2}{2m_e} + V_{\text{ext}}(\mathbf{r}_i) \right] + \frac{1}{2} \sum_{i \neq j} U(\mathbf{r}_i - \mathbf{r}_j), \tag{1.6}$$

where $V_{\text{ext}}(\mathbf{r}_i)$ is the external potential generated by the fixed nuclei and felt by the ith electron, and we define $U(\mathbf{r}_i - \mathbf{r}_j) = \frac{e^2}{|\mathbf{r}_i - \mathbf{r}_j|}$.

The final approximation, which is crucial in the band theory of solids, is to consider *non-interacting electrons*. In this framework, the electron-electron interaction $U(\mathbf{r}_i - \mathbf{r}_j)$ is incorporated, for example through a mean-field theory, in an effective potential $V_{\text{eff}}(\mathbf{r})$ describing the average effects on a single electron, due to the other electrons and the nuclei. The many-body problem in Eq. (1.2) is then replaced by a set of N_e independent single-particle equations

$$\mathcal{H}\, \psi_\alpha(\mathbf{r}, \sigma) = \varepsilon_\alpha\, \psi_\alpha(\mathbf{r}, \sigma), \tag{1.7}$$

with the single-particle Hamiltonian given by

$$\mathcal{H} = \frac{\mathbf{p}^2}{2m_e} + V_{eff}(\mathbf{r}). \tag{1.8}$$

We note that in this equation the spin degree of freedom is absent. If the Hamiltonian describes spin$-1/2$ electrons but is spin-independent, as in Eq. (1.8), the single-particle wavefunction $\psi_\alpha(\mathbf{r}, \sigma)$ factorizes into an orbital part $\psi_\alpha(\mathbf{r})$ and a spin state, and each orbital level ε_α is simply twofold spin degenerate. The two spin sectors are therefore equivalent and decoupled, and in the following, to keep the notation lighter and focus on the orbital structure of the single-particle wavefunctions, we omit the spin index whenever it does not play an active role. When needed, for spin-independent Hamiltonian, the spin label can be restored by writing the states as $\psi_{\alpha\sigma}(\mathbf{r})$, with $\sigma = \uparrow, \downarrow$. In general, however, the electronic wavefunction is a spinor

$$\psi_\alpha(\mathbf{r}, \sigma) = \begin{pmatrix} \psi_{\alpha\uparrow}(\mathbf{r}) \\ \psi_{\alpha\downarrow}(\mathbf{r}) \end{pmatrix}. \tag{1.9}$$

This spinor structure becomes essential in the presence of spin-orbit coupling, a relativistic effects originating from the motion of electrons in the electric field generated by the nuclei. The spin-orbit coupling introduces an additional term that couples momentum, orbital motion and spin degrees of freedom. In an effective single-particle description, it can be written as

$$V_{\text{SOC}}(\mathbf{r}, \sigma) = \frac{\hbar}{4m_e^2 c^2} \boldsymbol{\sigma} \cdot \nabla V_{\text{eff}}(\mathbf{r}) \times \mathbf{p} \tag{1.10}$$

where $\boldsymbol{\sigma}$ is the vector of Pauli matrices.

The electronic Hamiltonian should then be written schematically as

$$\mathcal{H} = \frac{\mathbf{p}^2}{2m_e} + V_{\text{eff}}(\mathbf{r}) + V_{\text{SOC}}(\mathbf{r}, \sigma), \tag{1.11}$$

where $V_{\text{SOC}}(\mathbf{r}, \sigma)$ acts non-trivially in spin space. Spin-orbit coupling can lift spin degeneracies, mix spin components and, as we will see, plays a central role in the topological insulators.

Once the single-particle orbitals $\psi_\alpha(\mathbf{r}, \sigma)$ have been obtained from the Schrödinger equation for the electronic Hamiltonian, then in general the many-body wavefunction of N_e non-interacting electrons can be written as the Slater determinant

$$\Psi(\{\mathbf{r}_i, \sigma_i\}) = \frac{1}{\sqrt{N_e!}} \sum_P \xi_P \prod_{i=1}^{N_e} \psi_{P\{\alpha_i\}}(\mathbf{r}_i, \sigma_i), \tag{1.12}$$

where P runs over all permutations of the occupied orbitals α_i, for $i = 1, \dots N_e$, and ξ_P is the sign of the permutation.

In what follows, we specialize to the case in which $V_{\text{eff}}(\mathbf{r})$ describes electrons in a crystalline solid. In such systems, the N nuclei occupy periodic positions in space, forming a Bravais lattice ($\mathcal{B}$). The resulting effective potential is therefore periodic

$$V_{\text{eff}}(\mathbf{r} + \mathbf{R}) = V_{\text{eff}}(\mathbf{r}), \qquad \forall\, \mathbf{R} \in \mathcal{B}. \tag{1.13}$$

1.1.1 Bloch wavefunctions

For a periodic potential, Bloch's theorem can be applied to the single-particle problem in Eq. (1.7). Namely, the Schrödinger equation can be written as

$$\mathcal{H}\, \psi_{n\mathbf{k}}(\mathbf{r}) = \varepsilon_{n\mathbf{k}}\, \psi_{n\mathbf{k}}(\mathbf{r}) \tag{1.14}$$

and admits solutions of the Bloch form

$$\psi_{n\mathbf{k}}(\mathbf{r}) = e^{i\mathbf{k}\cdot\mathbf{r}} u_{n\mathbf{k}}(\mathbf{r}), \tag{1.15}$$

where, consistent with the notation introduced above, the spin index is temporarily omitted for simplicity. Here, n is the band index, $\mathbf{k}$ is the crystal momentum, and $u_{n\mathbf{k}}(\mathbf{r})$ has the periodicity of the Bravais lattice

$$u_{n\mathbf{k}}(\mathbf{r} + \mathbf{R}) = u_{n\mathbf{k}}(\mathbf{r}), \qquad \forall\, \mathbf{R} \in \mathcal{B}. \tag{1.16}$$

The wavevector $\mathbf{k}$ is the quantum number associated with discrete translations in the lattice and is defined in the reciprocal space. Since momenta differing by a reciprocal lattice vector are equivalent, any wavevector $\mathbf{k}'$ can be written as

$$\mathbf{k}' = \mathbf{k} + \mathbf{G}, \tag{1.17}$$

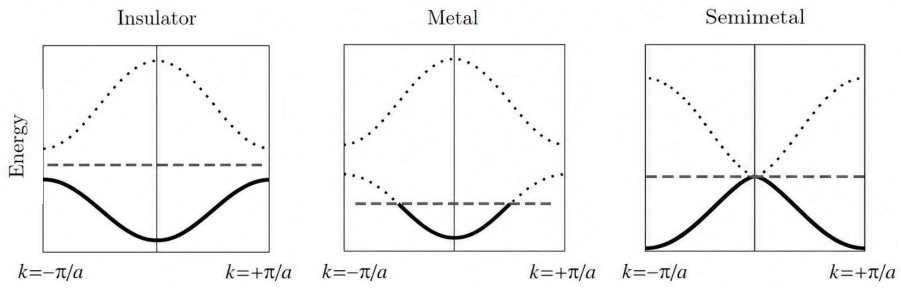


Figure 1.1: Schematic electronic band structures of a one-dimensional system. Occupied states are shown by solid lines, while empty states are dotted. The horizontal dashed line indicates the Fermi energy ε_F. In an insulator, ε_F lies inside a finite energy gap separating the fully occupied valence band from the empty conduction band. In a metal, ε_F crosses one or more bands, giving rise to partially occupied bands. In a semimetal, the gap between valence and conduction bands vanishes at isolated points in momentum space.

where $\mathbf{G}$ is any point of the reciprocal lattice and satisfies

$$e^{i\mathbf{G}\cdot\mathbf{R}} = 1, \qquad \forall\, \mathbf{R} \in \mathcal{B}, \tag{1.18}$$

while $\mathbf{k}$ can be chosen to lie in the first Brillouin zone (BZ). As a consequence, the BZ can be regarded as a closed manifold, whose boundaries are periodic images of each other.

The many-body ground state $\Psi(\{\mathbf{r}_i\})$ of N_e non-interacting electrons in a periodic potential is then obtained as the Slater determinant of single-particle Bloch states $\psi_{n\mathbf{k}}(\mathbf{r})$ which are occupied in order of increasing energy $\varepsilon_{n\mathbf{k}}$ and consistently with the Pauli exclusion principle. The allowed values of $\mathbf{k}$ are determined by the boundary conditions imposed on the many-body wavefunction. A standard choice is given by Born–von Karman boundary conditions, which require the many-body wavefunction to be invariant when any particle coordinate $\mathbf{r}_i$ is translated by the size of a finite cluster

$$\Psi(\ldots, \mathbf{r}_i + N_j\mathbf{a}_j, \ldots) = \Psi(\ldots, \mathbf{r}_i, \ldots). \tag{1.19}$$

where $\mathbf{a}_j$ is a primitive lattice vector of the Bravais lattice and N_j is the number of lattice points along the jth direction, so that $N = \prod_{j=1}^{d} N_j$ is the total number of sites of the d-dimensional cluster. These boundary conditions lead to the discretization of the allowed values of $\mathbf{k}$ in the reciprocal space, with which is associated a volume

$$\Delta v_{\mathbf{k}} = \frac{(2\pi)^d}{N V_{cell}} \tag{1.20}$$

where V_{cell} is the volume of the unit cell of the Bravais lattice. In the thermodynamic limit of an infinite number of lattice sites $N \to \infty$, this discretization vanishes and $\mathbf{k}$ can be treated as a continuous variable in the BZ.

The information encoded in the eigenvalues $\varepsilon_{n\mathbf{k}}$, which satisfy $\varepsilon_{n\mathbf{k}+\mathbf{G}} = \varepsilon_{n\mathbf{k}}$, is usually referred to as the electronic band structure, whose emergence is a direct consequence of the periodic potential generated by the ionic lattice. As schematically shown in Figure 1.1, the highest occupied energy defines the Fermi level ε_F, and the electronic occupation of the bands below the Fermi level (the valence bands) determines the conduction properties of the system. Partially filled valence bands result in metallic behavior, while completely filled bands separated by an energy gap from the unoccupied ones (the conduction bands) lead to band insulators. If the valence and conduction bands touch at isolated points or along lines in momentum space, the system is instead classified as a semimetal. A particularly important example is a Dirac semimetal, in which the valence and conduction bands touch at isolated points, known as Dirac points, around which the energy dispersion is linear. Within this framework, transitions between metallic and insulating phases can occur through modifications of the electronic population, for instance via chemical doping or the application of external fields.

The Bloch solution $\psi_{n\mathbf{k}}(\mathbf{r})$ in Eq. (1.15) can equivalently be written as

$$\psi_{n\mathbf{k}}(\mathbf{r}+\mathbf{R}) = e^{i\mathbf{k}\cdot\mathbf{R}}\psi_{n\mathbf{k}}(\mathbf{r}). \tag{1.21}$$

This equation expresses the transformation property of a Bloch wavefunction under lattice translation and highlights that $\psi_{n\mathbf{k}}(\mathbf{r})$ generally does not have the periodicity of the Bravais lattice. Instead, under a translation by $\mathbf{R}$, it acquires a phase factor fixed by the crystal momentum $\mathbf{k}$.

A further subtlety arises in reciprocal space, where the Bloch wavefunctions at momenta $\mathbf{k}$ and $\mathbf{k}+\mathbf{G}$ must describe the same physical state, since momenta differing by a reciprocal lattice vector $\mathbf{G}$ correspond to the same crystal momentum. However, in general, they do not need to be identical. Because of the gauge freedom of quantum states, a Bloch wavefunction can be multiplied by a momentum-dependent phase without changing any physical observable

$$\psi_{n\mathbf{k}}(\mathbf{r}) \longrightarrow e^{i\varphi_n(\mathbf{k})}\psi_{n\mathbf{k}}(\mathbf{r}). \tag{1.22}$$

Therefore, the relation between $\psi_{n\mathbf{k}}(\mathbf{r})$ and $\psi_{n,\mathbf{k}+\mathbf{G}}(\mathbf{r})$ depends on the gauge choice. The convention in which the Bloch wavefunctions are required to be periodic in reciprocal space is known as *periodic gauge*

$$\psi_{n,\mathbf{k}+\mathbf{G}}(\mathbf{r}) = \psi_{n\mathbf{k}}(\mathbf{r}). \tag{1.23}$$

Using the Bloch form in Eq. (1.15) we have

$$\psi_{n,\mathbf{k}+\mathbf{G}}(\mathbf{r}) = e^{i(\mathbf{k}+\mathbf{G})\cdot\mathbf{r}}u_{n,\mathbf{k}+\mathbf{G}}(\mathbf{r}), \tag{1.24}$$

and one finds that condition in Eq. (1.23) is equivalent to requiring

$$u_{n,\mathbf{k}+\mathbf{G}}(\mathbf{r}) = e^{-i\mathbf{G}\cdot\mathbf{r}}u_{n\mathbf{k}}(\mathbf{r}). \tag{1.25}$$

The periodic gauge in Eq. (1.23) is useful because it makes explicit the identification of opposite boundaries of the Brillouin zone. This issue becomes essential in the theory of topological phases. A smooth gauge for the Bloch states can generally be chosen locally in the Brillouin zone, but it may not be possible to keep it both smooth and periodic over the entire BZ. As is discussed in the following, this obstruction is a property of the occupied-band subspace which encodes its topology.

1.1.2 Wannier functions

The Bloch representation provides the standard description of electrons in a translationally invariant crystalline system. However, for many purposes, and in particular the construction of lattice Hamiltonians, it is useful to work with a basis localized in real space. Such a basis is provided by the Wannier functions, which are obtained by Fourier transforming the Bloch states. For an isolated band n, the Wannier function associated with the unit cell $\mathbf{R}$ is defined as

$$w_{n\mathbf{R}}(\mathbf{r}) = \frac{V_{\text{cell}}}{(2\pi)^d}\int_{\text{BZ}} d\mathbf{k}\, e^{-i\mathbf{k}\cdot\mathbf{R}}\,\psi_{n\mathbf{k}}(\mathbf{r}) \quad \overset{FT}{\Longleftrightarrow} \quad \psi_{n\mathbf{k}}(\mathbf{r}) = \sum_{\mathbf{R}} e^{i\mathbf{k}\cdot\mathbf{R}} w_{n\mathbf{R}}(\mathbf{r}) \tag{1.26}$$

where V_{cell} is the volume of the unit cell, and we have used the thermodynamic-limit convention in which $\mathbf{k}$ is treated as a continuous variable.

The Wannier functions form an orthonormal set and span the same Hilbert space as the Bloch functions from which they are constructed. However, they are not uniquely defined, since we can perform a gauge transformation on the Bloch states, as in Eq. (1.22), without changing physical observables. Different gauge choices therefore produce different Wannier functions spanning the same Hilbert space, but with different shapes and localization properties.

The degree of localization of the Wannier orbitals is controlled by the regularity of the Bloch states as functions of momentum: the smoother the Bloch functions are over the Brillouin zone, the more localized the corresponding Wannier functions are in real space. In particular, if a smooth and periodic gauge can be chosen over the whole BZ, the Wannier functions can be made exponentially localized around their centers [15]. In practical calculations, this gauge freedom is exploited to construct Wannier functions that are as localized as possible. This leads to the so-called maximally localized Wannier functions (MLWFs), obtained by minimizing the quadratic spread functional [16]

$$\Omega = \sum_n \Omega_n, \qquad \Omega_n = \langle w_{n\mathbf{0}}|r^2|w_{n\mathbf{0}}\rangle - \langle w_{n\mathbf{0}}|\mathbf{r}|w_{n\mathbf{0}}\rangle^2. \tag{1.27}$$

Note that, since Wannier functions in different unit cells are related by translations

$$w_{n\mathbf{R}}(\mathbf{r}) = w_{n\mathbf{0}}(\mathbf{r}-\mathbf{R}), \tag{1.28}$$

it is sufficient to consider the Wannier function in the reference unit cell $\mathbf{R} = \mathbf{0}$.

Wannier functions provide the natural language for constructing tight-binding models. In the Wannier basis, one introduces fermionic creation and annihilation operators $\hat{c}^\dagger_{\mathbf{R}n\sigma}$ and $\hat{c}_{\mathbf{R}n\sigma}$, which respectively create and annihilate an electron with spin σ in the nth Wannier orbital localized in the unit cell $\mathbf{R}$. These operators satisfy the canonical anticommutation relations

$$\{\hat{c}_{\mathbf{R}n\sigma}, \hat{c}^\dagger_{\mathbf{R}'m\sigma'}\} = \delta_{\mathbf{R}\mathbf{R}'}\delta_{nm}\delta_{\sigma\sigma'} \tag{1.29}$$

and

$$\{\hat{c}_{\mathbf{R}n\sigma}, \hat{c}_{\mathbf{R}'m\sigma'}\} = \{\hat{c}^\dagger_{\mathbf{R}n\sigma}, \hat{c}^\dagger_{\mathbf{R}'m\sigma'}\} = 0. \tag{1.30}$$

Projecting the single-particle Hamiltonian $\hat{\mathcal{H}}$ onto the Wannier basis gives the second-quantized Hamiltonian

$$\hat{H} = \sum_{\mathbf{R},\mathbf{R}'} \sum_{n,m,\sigma} t^{nm}_{\mathbf{R}\mathbf{R}'} \hat{c}^\dagger_{\mathbf{R}n\sigma} \hat{c}_{\mathbf{R}'m\sigma}, \tag{1.31}$$

where

$$t^{nm}_{\mathbf{R}\mathbf{R}'} = \langle w_{n\mathbf{R}} | \hat{\mathcal{H}} | w_{m\mathbf{R}'} \rangle \tag{1.32}$$

are the matrix elements of the Hamiltonian in the Wannier basis. These coefficients contain both on-site contributions, for $\mathbf{R} = \mathbf{R}'$, and hopping processes between different unit cells. For a translationally invariant system, they depend only on the relative displacement, namely

$$t^{nm}_{\mathbf{R}\mathbf{R}'} = t^{nm}_{\mathbf{0},\mathbf{R}'-\mathbf{R}}. \tag{1.33}$$

If the Wannier functions are well localized, these matrix elements decay rapidly with $|\mathbf{R}' - \mathbf{R}|$. This is the reason why MLWFs are especially useful in practice: they allow one to construct accurate tight-binding models with a finite number of real-space hopping amplitudes.

Introducing momentum-space operators

$$\hat{c}_{\mathbf{k}n\sigma} = \frac{1}{\sqrt{N}} \sum_{\mathbf{R}} e^{-i\mathbf{k}\cdot\mathbf{R}} \hat{c}_{\mathbf{R}n\sigma}, \tag{1.34}$$

the tight-binding Hamiltonian can be written as

$$\hat{H} = \sum_{\mathbf{k},\sigma} \sum_{n,m} H_{nm}(\mathbf{k}) \hat{c}^\dagger_{\mathbf{k}n\sigma} \hat{c}_{\mathbf{k}m\sigma}, \tag{1.35}$$

where

$$H_{nm}(\mathbf{k}) = \sum_{\mathbf{R}} e^{i\mathbf{k}\cdot\mathbf{R}} t^{nm}_{\mathbf{0}\mathbf{R}} \tag{1.36}$$

are the matrix elements of the Bloch Hamiltonian $\hat{H}(\mathbf{k})$ obtained by Fourier transforming the real-space hopping amplitudes.

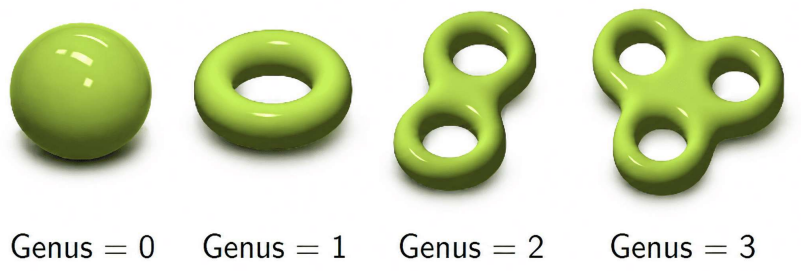


Figure 1.2: Examples of two-dimensional closed surfaces with different genus g. The integer number distinguishes geometric objects that are topologically different, since they cannot be adiabatically deformed into another without "creating" a hole.

For a single isolated band, this relation reduces to a particularly transparent form. The hopping amplitudes are the Fourier transform of the dispersion $\varepsilon_{n\mathbf{k}}$ of band n

$$t^n_{\mathbf{0R}} = \langle w_{n\mathbf{0}}|\hat{\mathcal{H}}|w_{n\mathbf{R}}\rangle = \frac{V_{\text{cell}}}{(2\pi)^d}\int_{\text{BZ}} d\mathbf{k}\, e^{-i\mathbf{k}\cdot\mathbf{R}}\varepsilon_{n\mathbf{k}}, \tag{1.37}$$

and the band dispersion is recovered as

$$\varepsilon_{n\mathbf{k}} = \sum_{\mathbf{R}} e^{i\mathbf{k}\cdot\mathbf{R}} t^n_{\mathbf{0R}}. \tag{1.38}$$

Thus, if all hopping amplitudes are retained, the Wannier representation gives an exact tight-binding model reproducing the original band structure.

1.2 Topological band theory

It was eventually recognized that insulating band structures can be topologically different. Intuitively, a topological distinction means that one object cannot be adiabatically deformed into another without encountering a singular transformation, for example it is not possible to continuously transform a sphere into a torus without creating a hole. Therefore, the sphere and the torus belong to different topological classes. By contrast, a sphere can be smoothly deformed into a cube, and the two objects are thus said to be topologically equivalent. In general, however, establishing whether two geometric objects are topologically equivalent is not always straightforward, especially in higher dimensions. For two-dimensional closed surfaces, the Gauss-Bonnet theorem provides a rigorous criterion that relates the integral of the Gaussian curvature $\mathbf{\Omega}$ over the surface of a geometric object S to an non-negative integer number g

$$\frac{1}{2\pi}\int_S \mathbf{\Omega}\cdot d\boldsymbol{\sigma} = 2(1-g). \tag{1.39}$$

The integer g, called genus, counts the number of holes in the geometric object (see Figure 1.2). It is known as *topological invariant* since it does not change under smooth deformations, and therefore provides a classification of closed surfaces.

Insulating band structures can be classified in an analogous way, with the Gaussian curvature replaced by geometric quantities defined in the reciprocal space. In the spirit of the geometric examples above, two insulating systems belonging to different topological classes cannot be continuously deformed into one another. In this context, a continuous deformation corresponds to an adiabatic change of the Hamiltonian and the impossibility of connecting two distinct topological phases is reflected in the fact that they must be separated by a gap-closing point, that is, by a semi-metallic state in which the band gap vanishes. The origin of these topological properties in the band theory stems from the fact that the BZ can be considered as a closed manifold on which Bloch wavefunctions labeled by $\mathbf{k}$ are defined, and the topological classification arises from the possibility (or not) of smoothly evolving these states, especially their phases, on the whole BZ manifold.

In particular, the phase accumulated by a quantum state during an adiabatic evolution was actually disregarded in quantum mechanics until the 1984, when Berry [17] showed that a quantum state undergoing a cyclic evolution acquires a phase factor of purely geometric origin which is, in principle, observable. Geometric quantities, such as the Berry phase and the Chern number, are the main object of this section, with their applications to the band theory of solids and the way they are used as topological invariants in the classification of insulators.

A fundamental consequence of a non-trivial topology of the bulk wavefunctions, characterized by a nonzero topological invariant, is the appearance of robust conducting edge states when open boundary conditions are considered: this is the essence of the *bulk–boundary correspondence*. In a finite insulating system, boundary states can lie inside the bulk energy gap and are exponentially localized at the edges of the sample. In a trivial insulator, such edge states can be removed by continuously deforming the Hamiltonian without closing the bulk gap. In contrast, in a topological phase, gapless edge modes connect the valence and conduction bands, thus giving rise to conducting channels at the boundary. These modes cannot be removed unless the bulk gap closes or the symmetries inducing topology are broken. In this sense, the edge states are said to be topologically protected.

1.2.1 Berry phase and Chern number

Consider a Hamiltonian depending on some parameter $\boldsymbol{\xi}$, which satisfies the Schrödinger equation

$$\hat{H}(\boldsymbol{\xi})\,|\psi(\boldsymbol{\xi})\rangle = E(\boldsymbol{\xi})\,|\psi(\boldsymbol{\xi})\rangle\,, \tag{1.40}$$

where the eigenstate $|\psi(\boldsymbol{\xi})\rangle$ is defined only up to a phase, because of gauge freedom

$$|\psi(\boldsymbol{\xi})\rangle \to e^{i\alpha(\boldsymbol{\xi})}\,|\psi(\boldsymbol{\xi})\rangle\,. \tag{1.41}$$

Moving in the parameter space, we can have two solutions at two different points $\boldsymbol{\xi}_1$ and $\boldsymbol{\xi}_2$, and between them we can define the relative phase $\Delta\phi_{12}$

$$\Delta\phi_{12} = -\arg\big\langle\psi(\boldsymbol{\xi}_1)\big|\psi(\boldsymbol{\xi}_2)\big\rangle = -\mathrm{Im}\ln\big\langle\psi(\boldsymbol{\xi}_1)\big|\psi(\boldsymbol{\xi}_2)\big\rangle, \tag{1.42}$$

where the function $\arg(z)$ is a multi-valued function that returns the phase of a complex number z as $\theta+2\pi n$, with $n\in\mathbb{Z}$. We note that the relative phase $\Delta\phi_{12}$ is not invariant under transformation in Eq. (1.41) applied to the states $|\psi(\boldsymbol{\xi}_1)\rangle$ and $|\psi(\boldsymbol{\xi}_2)\rangle$. For this reason, a more interesting quantity can be defined for a closed loop of N points in the parameter space, such that $\boldsymbol{\xi}_{N+1}\equiv\boldsymbol{\xi}_1$,

$$\phi^{(N)} = \sum_{j=1}^{N}\Delta\phi_{j,j+1} = -\sum_{j=1}^{N}\arg\big\langle\psi(\boldsymbol{\xi}_j)\big|\psi(\boldsymbol{\xi}_{j+1})\big\rangle = -\sum_{j=1}^{N}\mathrm{Im}\ln\big\langle\psi(\boldsymbol{\xi}_j)\big|\psi(\boldsymbol{\xi}_{j+1})\big\rangle \tag{1.43}$$

which is the discrete *Berry phase*. It has a well-defined continuum limit, obtained by increasing the density of points along the loop in the parameter space. We describe a loop $\mathcal{C}$ as a curve in parameter space, parametrized as $\boldsymbol{\xi}(t)$ with $t\in[0,1)$ and $\boldsymbol{\xi}(1)=\boldsymbol{\xi}(0)$. Then, by infinitely varying the parameters from $\boldsymbol{\xi}$ to $\boldsymbol{\xi}+d\boldsymbol{\xi}$, we have that

$$\begin{aligned}\ln\Big(\big\langle\psi(\boldsymbol{\xi})\big|\psi(\boldsymbol{\xi}+d\boldsymbol{\xi})\big\rangle\Big) &= \ln\Big(\big\langle\psi(\boldsymbol{\xi})\big|\,\Big[\big|\psi(\boldsymbol{\xi})\big\rangle + d\boldsymbol{\xi}\,\big|\nabla_{\boldsymbol{\xi}}\psi(\boldsymbol{\xi})\big\rangle + \cdots\Big]\Big)\\ &= \ln\Big(1 + d\boldsymbol{\xi}\cdot\big\langle\psi(\boldsymbol{\xi})\big|\nabla_{\boldsymbol{\xi}}\psi(\boldsymbol{\xi})\big\rangle\Big) + \cdots \simeq d\boldsymbol{\xi}\cdot\big\langle\psi(\boldsymbol{\xi})\big|\nabla_{\boldsymbol{\xi}}\psi(\boldsymbol{\xi})\big\rangle.\end{aligned} \tag{1.44}$$

The relative phase between two neighboring states on the curve $\mathcal{C}$ is, to the first order in $d\boldsymbol{\xi}$,

$$\Delta\phi = -\mathrm{Im}\ln\Big(\big\langle\psi(\boldsymbol{\xi})\big|\psi(\boldsymbol{\xi}+d\boldsymbol{\xi})\big\rangle\Big) = -\mathrm{Im}\Big\{\big\langle\psi(\boldsymbol{\xi})\big|\nabla_{\boldsymbol{\xi}}\psi(\boldsymbol{\xi})\big\rangle\cdot d\boldsymbol{\xi}\Big\}. \tag{1.45}$$

If the eigenstate is normalized $\big\langle\psi(\boldsymbol{\xi})\big|\psi(\boldsymbol{\xi})\big\rangle = 1$, then $\mathrm{Re}\Big\{\big\langle\psi(\boldsymbol{\xi})\big|\nabla_{\boldsymbol{\xi}}\psi(\boldsymbol{\xi})\big\rangle\Big\} = 0$ and we have that

$$\Delta\phi = i\,\big\langle\psi(\boldsymbol{\xi})\big|\nabla_{\boldsymbol{\xi}}\psi(\boldsymbol{\xi})\big\rangle\cdot d\boldsymbol{\xi} \tag{1.46}$$

is a real quantity. We define the *Berry connection*

$$\mathbf{A}(\boldsymbol{\xi}) = i\big\langle\psi(\boldsymbol{\xi})\big|\nabla_{\boldsymbol{\xi}}\psi(\boldsymbol{\xi})\big\rangle \tag{1.47}$$

which, under the transformation in Eq. (1.41), changes as

$$\mathbf{A}(\boldsymbol{\xi}) \to \mathbf{A}(\boldsymbol{\xi}) - \nabla_{\boldsymbol{\xi}}\alpha(\boldsymbol{\xi}). \tag{1.48}$$

The Berry phase is then written as the integral over the closed loop of the Berry connection

$$\phi_{\mathcal{C}} = \oint_{\mathcal{C}} \mathbf{A}(\boldsymbol{\xi}) \cdot d\boldsymbol{\xi} \tag{1.49}$$

and changes as

$$\phi_{\mathcal{C}} \to \phi_{\mathcal{C}} - \oint_{\mathcal{C}} \nabla_{\boldsymbol{\xi}} \alpha(\boldsymbol{\xi}) \cdot d\boldsymbol{\xi}, \tag{1.50}$$

where

$$\oint_{\mathcal{C}} \nabla_{\boldsymbol{\xi}} \alpha(\boldsymbol{\xi}) \cdot d\boldsymbol{\xi} = \int_0^1 \alpha'(t) dt = \alpha(\boldsymbol{\xi}(1)) - \alpha(\boldsymbol{\xi}(0)). \tag{1.51}$$

While the state $|\psi(\boldsymbol{\xi})\rangle$ at the edge of the closed loop is only required to return to the same physical state, and may therefore differ by a phase at $\boldsymbol{\xi}(1)$ and $\boldsymbol{\xi}(0)$, the gauge transformation in Eq. (1.41) must be single-valued, meaning that

$$\alpha(\boldsymbol{\xi}(1)) = \alpha(\boldsymbol{\xi}(0)) + 2\pi m \qquad \text{with } \; m \in \mathbb{Z}. \tag{1.52}$$

This implies that the Berry phase is gauge-invariant mod 2π, and as such it is an observable, although it is not the expectation value of an operator.

A further quantity can be defined from the Berry connection by taking its exterior derivative. In a three-dimensional parameter space, this corresponds to the curl of the Berry connection and defines the *Berry curvature*

$$\boldsymbol{\Omega}(\boldsymbol{\xi}) = \nabla_{\boldsymbol{\xi}} \times \mathbf{A}(\boldsymbol{\xi}), \tag{1.53}$$

which is a gauge-invariant quantity. Equivalently, in component form, the Berry curvature is described by the antisymmetric tensor

$$\Omega_{\mu\nu}(\boldsymbol{\xi}) = \partial_\mu A_\nu(\boldsymbol{\xi}) - \partial_\nu A_\mu(\boldsymbol{\xi}). \tag{1.54}$$

In analogy with the case of the Gaussian curvature, the Chern theorem ensures that the integral of the Berry curvature over a closed manifold is (2π times) an integer-valued topological invariant called *Chern number* C

$$\oint_{\Sigma} \boldsymbol{\Omega}(\boldsymbol{\xi}) \cdot d\mathbf{S} = 2\pi C. \tag{1.55}$$

The reason why the Chern number is not always zero (as we could expect, at first sight, from the Stokes' theorem, being an integral over a closed surface Σ, whose border $\partial\Sigma$ is null set) is that the Berry connection $\mathbf{A}(\boldsymbol{\xi})$ could not be globally smooth over the entire manifold Σ. Indeed, let us consider the case in which the closed surface is a sphere and suppose that the Berry connection has a singularity on the sphere. We can always divide the sphere into two open surfaces Σ_A and Σ_B, and the Chern number calculation can be separated into integrals over the two surfaces

$$C = \frac{1}{2\pi} \oint_{\Sigma} \boldsymbol{\Omega} \cdot d\mathbf{S} = \frac{1}{2\pi} \left[\int_{\Sigma_A} \boldsymbol{\Omega} \cdot d\mathbf{S} + \int_{\Sigma_B} \boldsymbol{\Omega} \cdot d\mathbf{S} \right]. \tag{1.56}$$

If we assume that the singularity lies on the Σ_B surface, given that $\mathbf{\Omega}$ is gauge-invariant, we can calculate the second integral choosing a gauge which makes the Berry connection $\mathbf{A}(\boldsymbol{\xi})$ well-defined everywhere in Σ_B and locally apply the Stokes' theorem

$$C = \frac{1}{2\pi}\left[\int_{\Sigma_A} \mathbf{\Omega}\cdot d\mathbf{S} + \int_{\Sigma_B} \tilde{\mathbf{\Omega}}\cdot d\mathbf{S}\right] = \frac{1}{2\pi}\left[\oint_{\partial\Sigma} \mathbf{A}(\boldsymbol{\xi})\cdot d\boldsymbol{\xi} - \oint_{\partial\Sigma} \tilde{\mathbf{A}}(\boldsymbol{\xi})\cdot d\boldsymbol{\xi}\right], \tag{1.57}$$

where the boundary $\partial\Sigma$ is the same, but oriented in the opposite direction, for the two surfaces. The two Berry connections differ by a gauge transformation as in Eq. (1.48), so their line integrals over the same loop return two Berry phases which differ by $2\pi m$

$$C = \frac{1}{2\pi}\left[\phi_{\partial\Sigma} - \left(\phi_{\partial\Sigma} - 2\pi m\right)\right] = m \in \mathbb{Z}. \tag{1.58}$$

Note that if the Berry curvature were well-defined over the entire sphere, no gauge transformation would be needed, and globally applying the Stokes' theorem we would find $C = 0$. The presence of a nonzero Chern number points out an obstruction to the construction of a globally smooth gauge [18].

1.2.2 Berryology of the Brillouin zone

In the band theory of solids the Bloch states have an explicit dependence on $\mathbf{k}$, which gives a natural parameter to study Berry phase effects. In particular, due to the presence of derivatives of the eigenstates, it turns out to be more suitable in calculations to deal with the periodic functions $u_{n\mathbf{k}}$ rather than the full Bloch state $\psi_{n\mathbf{k}}$. Indeed, derivatives $\nabla_{\mathbf{k}} u_{n\mathbf{k}}$ are well-defined periodic functions belonging to the same Hilbert space of $u_{n\mathbf{k}}$, contrary to $\nabla_{\mathbf{k}}\psi_{n\mathbf{k}} = e^{i\mathbf{k}\cdot\mathbf{r}}[\nabla_{\mathbf{k}} u_{n\mathbf{k}} + i\mathbf{r}u_{n\mathbf{k}}]$, where the second term grows linearly with distance from the origin making the functions non-integrable.

For a band insulator, let us consider the subspace spanned by the N_{occ} occupied bands. This subspace is assumed to be separated from the empty bands by a finite energy gap throughout the Brillouin zone. In this case, one can define the multiband, or non-Abelian[1], Berry connection [15]

$$\mathcal{A}_{mn,\mu}(\mathbf{k}) = i\left\langle u_{m\mathbf{k}} | \partial_\mu u_{n\mathbf{k}}\right\rangle, \tag{1.59}$$

where $\partial_\mu = \partial/\partial k_\mu$ and $\mathcal{A}_\mu(\mathbf{k})$ is a $N_{\text{occ}} \times N_{\text{occ}}$ matrix at each $\mathbf{k}$. The Abelian Berry connection associated with the occupied subspace is obtained by taking the trace over indices of the occupied bands

$$A_\mu(\mathbf{k}) = \operatorname{Tr}\mathcal{A}_\mu(\mathbf{k}) = i\sum_{n=1}^{N_{\text{occ}}}\left\langle u_{n\mathbf{k}} | \partial_\mu u_{n\mathbf{k}}\right\rangle, \tag{1.60}$$

[1] Since the matrices do not generally commute.

and this is the quantity that will be used throughout the text.

A first use of the Berry connection is to define the Berry phase accumulated along a closed path $\mathcal{C}$ in the Brillouin zone

$$\phi_{\mathcal{C}} = \oint_{\mathcal{C}} \mathrm{Tr}\, \boldsymbol{\mathcal{A}}(\mathbf{k}) \cdot d\mathbf{k} = \oint_{\mathcal{C}} \mathbf{A}(\mathbf{k}) \cdot d\mathbf{k}, \tag{1.61}$$

and, in the special case in which the occupied bands are nowhere degenerate among themselves and can be followed individually, it reduces to the sum of the single-band Berry phases $\phi_{\mathcal{C}}^{(n)}$.

When the closed path $\mathcal{C}$ crosses the boundary of the Brillouin zone, the states $u_{n\mathbf{k}}$ at the edges of the BZ coincide up to a phase

$$|u_{n\mathbf{k}+\mathbf{b}_j}\rangle = e^{-i\mathbf{b}_j\cdot\mathbf{r}}\, |u_{n\mathbf{k}}\rangle \tag{1.62}$$

where $\mathbf{b}_j$ are the reciprocal lattice vectors defining the BZ. This implements the *periodic gauge* defined in Eq. (1.25).

The Berry connection can also be integrated over the whole Brillouin zone. This quantity appears in the modern theory of polarization through the King-Smith and Vanderbilt formula [19]. In d dimensions the electronic contribution to the polarization can be written as

$$\mathbf{P}_{\mathrm{el}} = -\frac{fe}{(2\pi)^d} \sum_{n=1}^{N_{\mathrm{occ}}} \int_{\mathrm{BZ}} d\mathbf{k}\, i \,\langle u_{n\mathbf{k}} | \nabla_{\mathbf{k}} u_{n\mathbf{k}} \rangle \,, \tag{1.63}$$

where f is the occupation factor, usually $f = 2$ for spin-degenerate bands and $f = 1$ when spin is treated explicitly. Within the modern theory of polarization, the electronic polarization of a periodic system is not a single-valued bulk observable, but it is defined modulo a quantum [20].

The relation between Berry phases and Brillouin-zone integrals becomes particularly transparent in one dimension. In this case, the Brillouin zone is itself a closed path, and the Berry phase accumulated along this path is also known as the Zak phase [21]

$$\phi_{\mathrm{Zak}} = \oint_{\mathrm{BZ}} \mathrm{Tr}\, \mathcal{A}(k)\, dk = i \sum_{n=1}^{N_{occ}} \oint_{\mathrm{BZ}} dk\, \langle u_{nk} | \partial_k u_{nk} \rangle \,. \tag{1.64}$$

Therefore, in 1D the Brillouin-zone integral entering the polarization formula is precisely a Berry phase. The electronic polarization is then

$$P_{\mathrm{el}} = -\frac{fe}{2\pi}\, \phi_{\mathrm{Zak}} \qquad \mathrm{mod}\ e. \tag{1.65}$$

In a generic one-dimensional insulator, the Zak phase can vary continuously under smooth deformations of the Hamiltonian that preserve the bulk gap. However, in the presence of spatial symmetries, such as inversion or mirror symmetry, the electronic polarization may be quantized.

In this case, the Zak phase is restricted to discrete values, typically 0 or π modulo 2π. It can therefore act as a topological invariant, since it cannot change continuously as long as the protecting symmetry is preserved and the bulk gap remains open.

It is worth noting that, when symmetry-quantized, the Zak phase provides a $\mathbb{Z}_2$ classification. Other one-dimensional symmetry classes may display different topological classifications. For instance, systems with chiral symmetry can possess an $\mathbb{Z}$ classification, which is more naturally characterized by the winding number [**Chiu**, 22]. This case, however, falls outside the scope of the present discussion.

In addition, if the spin σ is a good quantum number, in one-dimensional systems one can compute separate spin-resolved Zak phases by restricting the Berry connection to the occupied states of each spin sector $|u^{\sigma}_{nk}\rangle$

$$\phi^{\sigma}_{\mathrm{Zak}} = i \sum_{n=1}^{N_{occ}} \oint_{\mathrm{BZ}} dk \, \langle u^{\sigma}_{nk} | \partial_k u^{\sigma}_{nk} \rangle \, . \tag{1.66}$$

The difference $\phi^{\uparrow}_{\mathrm{Zak}} - \phi^{\downarrow}_{\mathrm{Zak}}$ defines a spin-polarization-like quantity, which is often useful for diagnosing topological phases in one-dimensional systems with time-reversal symmetry when spin is conserved. A detailed discussion of time-reversal symmetry is given in Appendix A.

In higher-dimensional systems, one can also consider the curvature associated with the Berry connection $A_\mu(\mathbf{k})$ defined in Eq. (1.60). In particular, we define the Abelian Berry curvature of the occupied subspace as

$$\Omega_{\mu\nu}(\mathbf{k}) = \partial_\mu A_\nu(\mathbf{k}) - \partial_\nu A_\mu(\mathbf{k}) = -2 \, \mathrm{Im} \sum_{n=1}^{N_{\mathrm{occ}}} \big\langle \partial_\mu u_{n\mathbf{k}} \big| \partial_\nu u_{n\mathbf{k}} \big\rangle. \tag{1.67}$$

In two-dimensional insulating systems, the integral of the Berry curvature over the Brillouin zone defines the Chern number

$$C = \frac{1}{2\pi} \int_{BZ} \Omega_{xy}(\mathbf{k}) \, d\mathbf{k} = -\frac{1}{\pi} \mathrm{Im} \sum_{n=1}^{N_{occ}} \int_{BZ} \big\langle \partial_{k_x} u_{n\mathbf{k}} \big| \partial_{k_y} u_{n\mathbf{k}} \big\rangle \, dk_x dk_y. \tag{1.68}$$

Unlike the Zak phase of a generic one-dimensional insulator, the Chern number is always quantized, since it is an integer-valued quantity $C \in \mathbb{Z}$, and cannot change under smooth deformations of the Hamiltonian unless the bulk energy gap closes. A nonzero Chern number signals an obstruction to constructing a globally smooth and periodic gauge for the occupied Bloch states over the entire BZ. Equivalently, it obstructs the construction of exponentially localized Wannier functions respecting the lattice periodicity.

For our purposes, it is useful to recall that, in the presence of time-reversal (TR) symmetry, the Berry curvature of the full occupied subspace is odd in momentum (see Appendix A)

$$\Omega_{xy}(\mathbf{k}) = -\Omega_{xy}(-\mathbf{k}), \tag{1.69}$$

so its integral over the Brillouin zone vanishes. Therefore a TR-invariant insulator always has zero total Chern number, $C = 0$.

This, however, does not imply that such systems are necessarily topologically trivial. In two dimensions, TR-invariant insulators are classified by a $\mathbb{Z}_2$ topological invariant. One possible expression for this invariant is the Fu–Kane formula [23]

$$\nu = \frac{1}{2\pi}\left[\oint_{\partial\mathcal{B}_{1/2}} \mathbf{A}(\mathbf{k})\cdot d\mathbf{l} - \int_{\mathcal{B}_{1/2}} \mathbf{\Omega}(\mathbf{k})\cdot d\mathbf{S}\right] \mod 2, \tag{1.70}$$

where $\mathcal{B}_{1/2}$ denotes half of the Brillouin zone and $\partial\mathcal{B}_{1/2}$ is its boundary, oriented counterclockwise. This expression is reminiscent of the Chern number, which is obtained from the integration over the entire BZ of the Berry curvature, which is a gauge-invariant quantity. In contrast, the $\mathbb{Z}_2$ invariant also involves the Berry connection, which is gauge dependent and therefore the definition in Eq. (1.70) requires a choice of gauge. If both $\mathbf{A}$ and $\mathbf{\Omega}$ are evaluated in the same gauge, chosen to be smooth over the region $\mathcal{B}_{1/2}$, the expression would vanish by Stokes' theorem.

The non-trivial content of the $\mathbb{Z}_2$ invariant in Eq. (1.70) comes from the additional requirement that the boundary integral of $\mathbf{A}$ is computed in a gauge that respects time-reversal symmetry. A value $\nu = 1$ signals precisely the obstruction to choosing a globally smooth gauge that is simultaneously compatible with time-reversal symmetry.

In Ref. [23], Fu and Kane also proposed an equivalent formulation of the $\mathbb{Z}_2$ invariant ν in terms of "time-reversal polarization". This approach leads to the expression

$$(-1)^{\nu} = \prod_{i=1}^{4} \frac{\sqrt{\det[w(\mathbf{\Gamma}_i)]}}{\mathrm{Pf}[w(\mathbf{\Gamma}_i)]}, \tag{1.71}$$

where Pf denotes the Pfaffian and

$$w_{mn}(\mathbf{k}) = \langle u_{m,-\mathbf{k}}|\hat{\mathcal{T}}|u_{n,\mathbf{k}}\rangle \tag{1.72}$$

are the matrix elements of the time-reversal operator $\hat{\mathcal{T}}$. Here, $\mathbf{\Gamma}_i$ denote the four time-reversal-invariant momenta (TRIM) in the two-dimensional Brillouin zone, defined in Appendix A.

Although Eq. (1.71) appears to require the knowledge of the occupied wavefunctions only at four points in the BZ, it is not usually convenient for numerical implementation since the sign of the Pfaffian is not uniquely defined. This problem may be overcome in the presence of some additional symmetry. For example, in Ref. [24] it is shown that, when inversion symmetry is present, ν can be computed from the parity eigenvalues of the occupied stated at the TRIM.

1.3 Chern insulators

The first example of a topologically non-trivial insulator came with the integer quantum Hall effect (IQHE), first observed by von Klitzing *et. al.* [25] in 1980. In this phenomenon, the energy

spectrum of a two-dimensional electron gas at low temperatures and under a strong perpendicular magnetic field is quantized into Landau levels. By changing either the carrier density or the magnetic field strength, the Fermi energy can be placed in the gap between Landau levels and the system exhibits a quantized transverse conductivity

$$\sigma_{xy} = C\frac{e^2}{h} \tag{1.73}$$

where C is an integer number. This quantization was explained by Thouless *et. al.* [26], by considering a 2D electron system in a periodic potential subject to a perpendicular $\mathbf{B}$ field. By evaluating the Kubo formula for the Hall conductivity, they showed that C is actually the Chern number calculated over the magnetic Brillouin zone[2].

In the bulk of a system exhibiting the IQHE, when the Fermi energy lies between Landau levels, the electrons occupy gapped levels and do not contribute to conduction, behaving as an insulator. In a finite sample, however, the confining potential at the boundaries shifts the Landau levels upward, so that some of them cross the Fermi energy. This gives rise to states that are localized in the direction perpendicular to the edge but extended along it, causing the electrons to propagate along the boundary. Their propagation is chiral, since on a given edge they move only in one direction, while on the opposite edge they propagate in the opposite direction. These chiral edge states carry the current responsible for quantized Hall conductivity, and the difference between the number of edge modes propagating in opposite directions is equal to the Chern number, in accordance with the bulk-edge correspondence.

For years, it was tacitly assumed that a macroscopic external magnetic field was necessary to observe a quantum Hall effect. This idea was challenged by Haldane in 1988 [3] who introduced a 2D tight-binding model for Chern insulators on a honeycomb lattice and showed that a topologically non-trivial ground state, characterized by a quantized Hall conductivity and a Chern number $C = \pm 1$, can exist even in the absence of an external magnetic field. A quantum Hall effect occurring without an external magnetic field is referred to as "anomalous" and systems realizing such a state are called quantum anomalous Hall insulators (QAHIs) or Chern insulators.

1.3.1 The Haldane model

The prototypical model of a Chern insulator is the Haldane model [3], which provided the first theoretical example of a QAHI state. It is defined on a honeycomb lattice, namely a two-dimensional triangular Bravais lattice with two sites in the unit cell, labeled A and B, and

[2] In the presence of magnetic field, the Hamiltonian of the model is not strictly translationally invariant , since the potential vector $\mathbf{A}(\mathbf{r}+\mathbf{R}) \neq \mathbf{A}(\mathbf{r})$. However, by choosing an appropriate unit cell, large enough to accommodate an integer number of flux quanta eB/h, one can restore a generalized translational symmetry and recover a Bloch-like description.

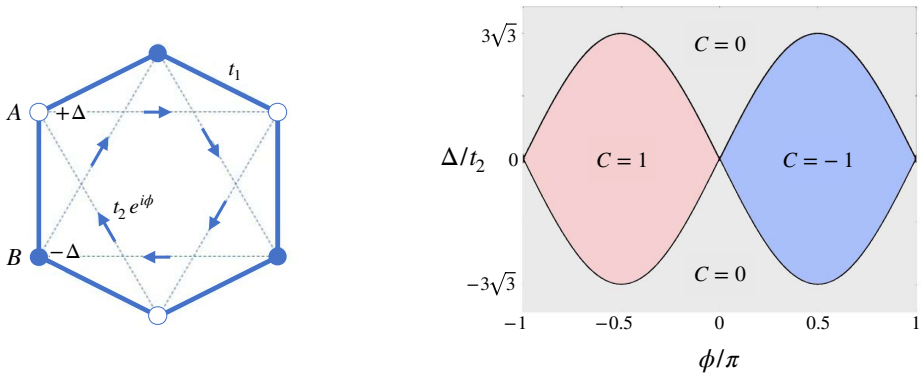


Figure 1.3: Left panel: Parameters of the Haldane model in Eq. (1.74) represented on the honeycomb lattice. The two sites of the basis are labeled A and B and have opposite on-site energy $\pm\Delta$. The first nearest-neighbors hopping t_1 involves sites of different type, the second nearest-neighbors hopping $t_2\, e^{i\phi}$ involves sites of the same type. Right panel: Topological phase diagram of the Haldane model. Three regions can be identified: two are characterized by non-trivial values of the Chern number, while the region with vanishing Chern number corresponds to a trivial band insulator. The regions are separated by the gapless points given by Eq. (1.80), shown in black lines.

describes *spinless* electrons. The tight-binding Hamiltonian reads

$$\hat{H} = -t \sum_{\langle ij \rangle} \left(\hat{c}_i^\dagger \hat{c}_j + h.c. \right) + \Delta \sum_i \epsilon_i \hat{c}_i^\dagger \hat{c}_i - t_2 \sum_{\langle\langle ij \rangle\rangle} \left(e^{-i\nu_{ij}\phi} \hat{c}_i^\dagger \hat{c}_j + h.c. \right), \tag{1.74}$$

where t is the nearest-neighbor hopping amplitude, Δ is a staggered on-site potential with $\epsilon_i = \pm 1$ depending on whether the ith site belongs to A or B sublattice, and t_2 is a next-nearest-neighbor hopping carrying a complex phase ϕ. The factor

$$\nu_{ij} = \text{sign}\, (\mathbf{d}_1 \times \mathbf{d}_2)_z = \pm 1 \tag{1.75}$$

depends on the orientation of the hopping path between next-nearest-neighbors. The different hoppings are sketched in the left panel of Figure 1.3.

The starting point of the Haldane model is the tight-binding model of graphene, which includes only the real nearest-neighbor hopping t and gives rise to two bands with gapless Dirac cones centered on the high-symmetry points $\mathbf{K}$ and $\mathbf{K}'$ in the Brillouin zone. The staggered potential Δ opens a gap at the Dirac points by breaking inversion symmetry $A \leftrightarrow B$, but the resulting insulating phase is topologically trivial. The crucial ingredient introduced by Haldane is the complex next-nearest-neighbor hopping term, which makes it possible to obtain a topologically non-trivial insulating phase[3]. This complex hopping can be interpreted as the effect of

[3]Within the two-band Haldane model, one deals with an insulator by taking the lowest band as fully occupied. By taking $\left|\frac{t_2}{t}\right| \leq \frac{1}{3}$ there is no overlap between bands, which are always separated by a finite gap when physical parameters are varied, unless they touch in $\mathbf{K}$ or $\mathbf{K}'$ point going through the semi-metallic state.

local magnetic fluxes, through the Peierls substitution [27]. However, these fluxes are arranged in a staggered pattern: some regions of the unit cell carry positive flux, while others carry negative flux. The two contributions cancel when summed over the full unit cell, so the net magnetic flux vanishes. Despite this cancellation, the local flux pattern still breaks time-reversal symmetry. Indeed, for spinless particles, the TR operator is simply the antiunitary complex-conjugation operator $\hat{\mathcal{T}} = \hat{K}$ (see Appendix A), so TR symmetry requires the Hamiltonian to be invariant under complex conjugation. Since the complex next-nearest-neighbor hopping amplitudes are mapped to their complex conjugates under $\hat{\mathcal{T}}$, the Haldane Hamiltonian is not time-reversal invariant for generic $\phi \neq 0, \pi$. As a result, the Haldane model realizes a quantum Hall phase with a finite Chern number despite the absence of an external magnetic field.

In momentum space, the Haldane model is described by a Bloch Hamiltonian $H(\mathbf{k})$ acting in the sublattice basis. In terms of the Pauli matrices τ_i and of the identity matrix τ_0, it can be written as

$$H(\mathbf{k}) = \epsilon(\mathbf{k})\,\tau_0 + \sum_{i=x,y,z} d_i(\mathbf{k})\,\tau_i, \tag{1.76}$$

where the coefficients $\epsilon(\mathbf{k})$ and $d_i(\mathbf{k})$ can be found in Ref. [3]. In particular, we are interested in the form that Eq. (1.76) acquires when expanded around the two inequivalent Dirac points $\mathbf{K}$ and $\mathbf{K}'$. We write $\mathbf{k} = \mathbf{K}_\alpha + \mathbf{q}$, where $\alpha = +1$ corresponds to $\mathbf{K}$, $\alpha = -1$ corresponds to $\mathbf{K}'$, and $|\mathbf{q}| \ll 1$. To linear order in $\mathbf{q}$, the Hamiltonian takes the massive Dirac form

$$H_\alpha(\mathbf{q}) = v_F\,(\alpha q_x \tau_x + q_y \tau_y) + M_\alpha \tau_z, \tag{1.77}$$

where v_F is the Fermi velocity and

$$M_\alpha = \Delta + \alpha\, 3\sqrt{3}\, t_2 \sin\phi \tag{1.78}$$

is usually referred to as the Dirac mass, or topological mass. Equation (1.78) shows that the two masses associated with $\mathbf{K}$ and $\mathbf{K}'$ can acquire opposite signs. This relative sign change corresponds to a band inversion at one of the two Dirac points and is the key mechanism leading to a non-vanishing Chern number.

At the points $\mathbf{K}$ and $\mathbf{K}'$ themselves, $\mathbf{q} = 0$ and the kinetic Dirac terms vanish, so that the Hamiltonian becomes proportional to τ_z

$$H_\alpha(0) = M_\alpha \tau_z = \begin{pmatrix} \Delta + \alpha\, 3\sqrt{3}\, t_2 \sin\phi & 0 \\ 0 & -\left(\Delta + \alpha\, 3\sqrt{3}\, t_2 \sin\phi\right) \end{pmatrix}. \tag{1.79}$$

From this, we can see that the gap at $\mathbf{K}$ and $\mathbf{K}'$ is equal to $2|M_\alpha|$: when one of the masses vanishes, the gap closes at the corresponding Dirac point. Then, the equation

$$\Delta = \pm 3\sqrt{3}\, t_2 \sin\phi \tag{1.80}$$

identify the semi-metallic lines in parameter space. Across these gap-closing lines, the sign of one Dirac mass changes and the Chern number of the occupied band changes accordingly. In particular, as shown in the right panel of Figure 1.3, the Haldane model exhibits phases with Chern number $C = 0, \pm 1$, corresponding to a trivial insulator and to quantum anomalous Hall insulators, respectively. As in the integer quantum Hall effect, the boundary of a QAHI hosts chiral edge states in accordance with the value of the Chern number, so that in the Haldane model chiral edge modes propagate in opposite directions for the two cases $C = \pm 1$.

1.4 Time-reversal protected topological insulators

In Chern insulators, time-reversal symmetry must be broken in order to obtain a non-vanishing Chern number. Indeed, as follows from Eq. (1.69), in a TR-invariant system the Berry curvature is odd in momentum space, so that its integral over the Brillouin zone, i.e., the Chern number, vanishes.

This does not imply, however, that TR-invariant systems are necessarily topologically trivial. On the contrary, some topological phases exist precisely because certain symmetries are preserved. These phases are known as symmetry-protected topological (SPT) phases: they cannot be adiabatically deformed into a trivial insulator without closing the bulk gap, as long as the protecting symmetry is maintained.

A paradigmatic example is the quantum spin Hall insulator (QSHI), a two-dimensional topological insulator protected by time-reversal symmetry. In this case, the total Chern number is forced to vanish, which allows, in principle, for the occupied Bloch states to be described by a gauge that is smooth and periodic throughout the Brillouin zone. However, in the QSHI phase it is impossible to choose such a gauge while simultaneously preserving the time-reversal constraint [23]. This obstruction gives rise to a $\mathbb{Z}_2$ classification, which distinguishes trivial insulators from topological ones according to whether the corresponding invariant is even or odd.

A useful way to formulate the $\mathbb{Z}_2$ invariant, more practical than the original Fu–Kane expressions given in Eqs. (1.70) and (1.71), is to decompose the occupied Hilbert space of a QSHI into two subspaces that are mapped into each other by the time-reversal operator $\hat{\mathcal{T}}$. Within each subspace, TR symmetry is effectively broken, so that one can define individual Chern numbers C_1 and C_2. Time-reversal symmetry imposes that these contributions are equal in magnitude and opposite in sign

$$C_1 = -C_2, \tag{1.81}$$

so that the total Chern number vanishes. Nevertheless, the parity of one of these Chern numbers

remains well defined and provides the $\mathbb{Z}_2$ topological invariant as

$$\nu = \frac{C_1 - C_2}{2} \mod 2. \tag{1.82}$$

Such a decomposition of the occupied Hilbert space is straightforward when the system possesses additional structure, for example mirror symmetry [28] or conservation of the spin component S_z [29]. More general decompositions based solely on TR symmetry have also been developed [30], but are made challenging by the peculiarity of $\hat{\mathcal{T}}$ to be an antiunitary operator (see Appendix A).

In the following, we focus on $\mathbb{Z}_2$ invariants expressed in terms of *spin Chern numbers*. In the specific case in which the spin component S_z is conserved, the Hilbert space can be decomposed into spin-up and spin-down sectors, each behaving as an independent Chern insulator, whose Chern numbers satisfy

$$C_\uparrow = -C_\downarrow. \tag{1.83}$$

In this regime, the system exhibits helical edge states, namely counter-propagating edge modes carrying opposite spin. As a consequence, there is no net charge Hall current, while the spin Hall conductivity is quantized according to

$$\sigma^s_{xy} = \frac{C_\uparrow - C_\downarrow}{2}\frac{e}{2\pi} = C_\uparrow \frac{e}{2\pi}. \tag{1.84}$$

Thus, in the spin-conserving limit, the spin Hall conductivity is proportional to an integer spin Chern number which may assume any integer value. However, such an integer classification relies on the additional conservation of S_z and is not stable under generic TR-symmetric perturbations. Indeed, when terms that do not conserve S_z are allowed (such as the spin-orbit coupling introduced in Eq. (1.10) which generally mixes spin sectors), only the parity of the spin Chern number remains topologically meaningful: phases with odd spin Chern number belong to the same non-trivial QSHI phase, while those with even spin Chern number are topologically trivial.

Moreover, the name "quantum spin Hall insulator" may suggest that the spin Hall conductivity is always quantized, but this is not true when the spin S_z is not conserved [15]. Nevertheless, the QSHI phase remains well defined as long as TR symmetry is preserved and the bulk gap does not close[4].

Actually, spin Chern numbers can be rigorously defined beyond the spin-conserving case following Prodan's approach [31]. The key idea is to consider the spin operator projected onto the occupied subspace

$$\hat{P}_z(\mathbf{k}) = \hat{P}_{occ}(\mathbf{k})\, \hat{S}_z\, \hat{P}_{occ}(\mathbf{k}), \tag{1.85}$$

[4] In the more general case of S_z not being conserved, the edge states protected by TR symmetry are no longer modes with definite opposite S_z, but rather Kramers pairs of helical edge states, which may have momentum-dependent spin texture.

where $\hat{S}_z$ is the total spin operator and $\hat{P}_{occ}(\mathbf{k})$ is the ground-state projector at the $\mathbf{k}$-point

$$\hat{P}_{occ}(\mathbf{k}) = \sum_{n=1}^{N_{occ}} |u_{n\mathbf{k}}\rangle \langle u_{n\mathbf{k}}| \,. \tag{1.86}$$

By diagonalizing the operator in Eq. (1.85), its spectrum can be decomposed into subspaces with positive and negative eigenvalues. The Chern numbers computed separately on these two subspaces, denoted by C_+ and C_-, define generalized spin Chern numbers. These quantities are integer-valued topological invariants and remain unchanged under continuous deformations, but they require that not only the insulating gap of the Hamiltonian, but also the spectral gap of the projected spin operator, remain open at each $\mathbf{k}$-point. Under these conditions, the generalized spin Chern numbers can be computed and their parity can still be used to characterize the QSHI phase in the absence of S_z conservation. Notably, this approach could in principle be used also for systems with a small breaking of TR symmetry, as in the TR-symmetry-broken quantum spin Hall effect [32].

1.4.1 The Kane–Mele model

The concept of QSHI was introduced in 2005 by Kane and Mele [4, 5] who, with the original idea of describing the low-energy electronic structure of graphene, extended the Haldane model to *spinful* electrons with spin-orbit coupling while preserving TR symmetry.

In its simplest form, the Kane–Mele (KM) model conserves the spin component S_z, so that spin-up and spin-down electrons are described by two time-reversed copies of the Haldane model. The corresponding Hamiltonian is

$$\hat{H}_0 = \Delta \sum_i \epsilon_i \hat{c}_i^\dagger \hat{c}_i + t \sum_{\langle ij \rangle} \big(\hat{c}_i^\dagger \hat{c}_j + h.c.\big) + \lambda_{SO} \sum_{\langle\langle ij \rangle\rangle} \big(i\, \nu_{ij}\, \hat{c}_i^\dagger \sigma_z \hat{c}_j + h.c.\big), \tag{1.87}$$

where $\hat{c}_i^\dagger = \big(\hat{c}_{i\uparrow}^\dagger, \hat{c}_{i\downarrow}^\dagger\big)$, and the summation over spin indices is understood. The first term describes a staggered potential Δ, with $\epsilon_i = \pm 1$ on the two sublattices of the honeycomb lattice, the second is the usual nearest-neighbor hopping, and the third is a spin-dependent next-nearest-neighbor hopping which describes an intrinsic spin-orbit coupling. This last term is the analogue of the complex next-nearest-neighbor hopping in the Haldane model, with a phase $\phi = \frac{\pi}{2}$, now endowed with a spin dependence through the Pauli matrix σ_z. Again, $\nu_{ij} = \text{sign}(\mathbf{d}_1 \times \mathbf{d}_2)_z = \pm 1$ depends on the orientation of the two next-nearest-neighbor bonds. Since both the imaginary unit i and the Pauli matrix σ_z change sign under TR transformation, the Hamiltonian $\hat{H}_0$ is TR invariant.

A more general TR-invariant Hamiltonian is obtained by including the Rashba spin-orbit

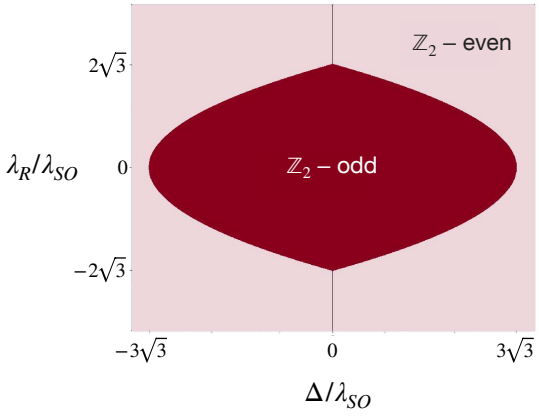


Figure 1.4: Topological phase diagram of the Kane–Mele model. Two regions can be identified: one is characterized by an odd value of the $\mathbb{Z}_2$ invariant and describes a quantum spin Hall insulator, the other has an even value of the $\mathbb{Z}_2$ invariant and indicates a trivial band insulator.

coupling

$$\begin{aligned}\hat{H} = \Delta \sum_i \epsilon_i \hat{c}_i^\dagger \hat{c}_i + t \sum_{\langle ij \rangle} \left(\hat{c}_i^\dagger \hat{c}_j + h.c.\right) + \lambda_{SO} \sum_{\langle\langle ij \rangle\rangle} \left(i\, \nu_{ij}\, \hat{c}_i^\dagger \sigma_z \hat{c}_j + h.c.\right) \\ + \lambda_R \sum_{\langle ij \rangle} \left(i\, \hat{c}_i^\dagger (\boldsymbol{\sigma} \times \mathbf{d}_{ij})_z \hat{c}_j + h.c.\right)\end{aligned} \tag{1.88}$$

where $\mathbf{d}_{ij}$ is the vector connecting nearest-neighbor sites. This term may arise, for example, in the presence of a perpendicular electric field or a substrate. Unlike the intrinsic spin-orbit coupling, the Rashba term mixes spin sectors, so that S_z is no longer conserved, even though TR symmetry remains preserved. Because the model has two sublattices and two spin states, its band structure consists of four bands. As for the Haldane model, the topological phase transition occurs when the bulk gap closes at the Dirac points $\mathbf{K}$ and $\mathbf{K}'$. In the absence of Rashba coupling, the gap at the Dirac points is

$$E_g = \left|6\sqrt{3}\lambda_{SO} - 2\Delta\right|, \tag{1.89}$$

so that

$$\Delta < 3\sqrt{3}\lambda_{SO} \tag{1.90}$$

corresponds to the QSHI phase, whereas for

$$\Delta > 3\sqrt{3}\lambda_{SO} \tag{1.91}$$

it is adiabatically connected to a trivial band insulator. When $\lambda_R \neq 0$, the QSHI phase survives over a finite region of parameter space as long as the bulk gap remains open. In particular, for

$$\lambda_R < 2\sqrt{3}\lambda_{SO} \tag{1.92}$$

the system is adiabatically connected to the QSHI phase at $\lambda_R = 0$, as shown Figure 1.4.

Therefore, at least in principle, graphene is a QSHI. In practice, however, it behaves as a Dirac semimetal, as its gap is extremely small. This is a consequence of the weakness of spin-orbit coupling in carbon C, which is a very light element. The KM mechanism is nevertheless relevant for other two-dimensional unary honeycomb-like materials made of group IV elements, often referred to as Xenes, such as silicene, germanene, and stanene [33, 34]. Here, the presence of heavier elements enhances spin-orbit coupling and is expected to produce larger topological gaps.

Most experimentally realized QSHIs, however, are based on a different physical mechanism. In particular, the first experimentally realized example, described by the Bernevig–Hughes–Zhang (BHZ) model discussed in the following section, relies on band inversion. In this case, bands with different orbital character exchange their order in energy. Nevertheless, spin-orbit coupling remains essential since it plays a crucial role in producing the inverted band structure and stabilizing the resulting topological insulating phase.

1.4.2 The Bernevig–Hughes–Zhang model

Shortly after the proposal of Kane and Mele, Bernevig and Zhang suggested that the QSHI phase could be realized in semiconductor systems [35]. In a subsequent work, Bernevig, Hughes, and Zhang [6] predicted that this phase should occur in HgTe/CdTe quantum wells, anticipating the 2007 experimental observation of a quantized, sample-width independent conductance in these systems [36].

Their model, known as the BHZ model, describes a two-dimensional $\mathbb{Z}_2$ insulator arising from band inversion in semiconductor heterostructures. The starting point is the observation that CdTe and HgTe have different band orderings near the Γ point, at the center of the Brillouin zone, as shown in Figure 1.5. In CdTe the band structure is normal, with the s-like Γ_6 band lying above the p-like Γ_8 band. In HgTe, by contrast, the ordering is inverted, because relativistic and spin-orbit effects are much stronger in this heavier compound, so that the Γ_8 band lies above the Γ_6 band. In a HgTe/CdTe quantum well, quantum confinement allows one to tune between these two regimes by varying the thickness d of the HgTe layer. For thin wells the system behaves as an ordinary insulator, whereas above a critical thickness d_c the band structure becomes inverted and the system enters the QSHI phase.

Near the Γ point, the low-energy physics of the quantum well is captured by two orbital sectors of opposite parity, usually denoted by $E1$ and $H1$. Each of them comes with a time-reversal partner, so that the minimal basis contains two Kramers pairs

$$\{|E1,+\rangle,\ |H1,+\rangle,\ |E1,-\rangle,\ |H1,-\rangle\}. \tag{1.93}$$

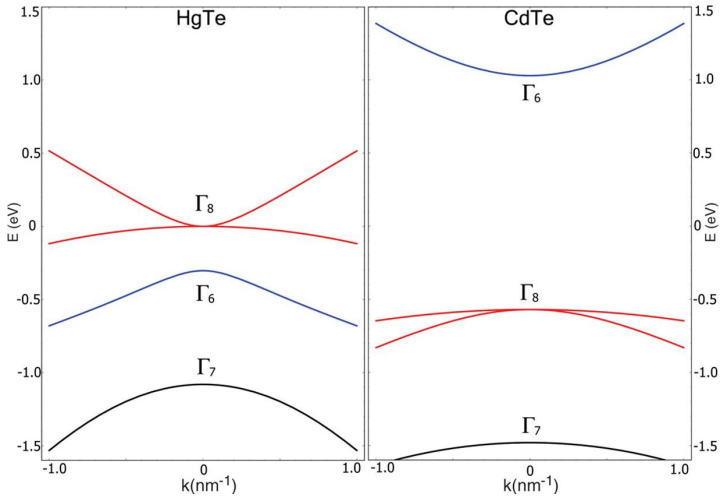


Figure 1.5: Figure adapted from Ref. [6]. Bulk energy bands of HgTe and CdTe near the Γ point.

Here + and − label the two TR-related sectors, which can be regarded as spin sectors. The corresponding Bloch Hamiltonian is therefore a 4×4 matrix. Considering the most general 4×4 Hamiltonian compatible with time-reversal and inversion symmetry, and keeping only the leading terms in a $\mathbf{k} \cdot \mathbf{p}$ expansion around Γ, one obtains the continuum BHZ Hamiltonian

$$H_{\mathrm{BHZ}}(\mathbf{k}) = \begin{pmatrix} h(\mathbf{k}) & 0 \\ 0 & h^*(-\mathbf{k}) \end{pmatrix}, \tag{1.94}$$

with

$$h(\mathbf{k}) = \epsilon(\mathbf{k})\,\tau_0 + A\,k_x\,\tau_x - A\,k_y\,\tau_y + M(\mathbf{k})\,\tau_z, \tag{1.95}$$

where

$$\epsilon(\mathbf{k}) = C - D(k_x^2 + k_y^2), \qquad M(\mathbf{k}) = M - B(k_x^2 + k_y^2). \tag{1.96}$$

Here the Pauli matrices $\boldsymbol{\tau}$ act in the orbital subspace spanned by $E1$ and $H1$. The term proportional to τ_z plays the role of a momentum-dependent Dirac mass $M(\mathbf{k})$, which controls the bulk gap and its inversion. By contrast, the terms proportional to τ_x and τ_y are off-diagonal in the orbital basis, and therefore describe momentum-dependent hybridization between the two orbital sectors.

Because the two blocks in Eq. (1.94) are related by TR symmetry, their Chern numbers are opposite. Nevertheless, when the system is in the inverted regime, the parity of the Chern number of one block is odd, and the full system is characterized by a non-trivial $\mathbb{Z}_2$ invariant.

For our purposes, rather than using the full continuum $\mathbf{k} \cdot \mathbf{p}$ description, it is convenient to introduce a minimal square-lattice regularization that contains the essential symmetry and

topological structure of the BHZ model. This is obtained by replacing the odd momentum terms with periodic functions, $k_x \to \sin k_x$ and $k_y \to \sin k_y$, and the even quadratic terms k_x^2 and k_y^2 with cosine functions over the Brillouin zone. Moreover, the term proportional to $\epsilon(\mathbf{k})$, which only shifts the bands without affecting the topology, is omitted.

Neglecting spin-mixing corrections, the Hamiltonian remains block diagonal in the two time-reversal-related spin sectors. Retaining only the minimal terms compatible with inversion, time-reversal, and C_4 symmetry, one obtains the Bloch Hamiltonian for the BHZ model on the square lattice

$$H(\mathbf{k}) = [M - t(\cos k_x + \cos k_y)]\sigma_0 \otimes \tau_z + \lambda \sin k_x \, \sigma_z \otimes \tau_x - \lambda \sin k_y \, \sigma_0 \otimes \tau_y \tag{1.97}$$

where the Pauli matrices $\boldsymbol{\tau}$ act in the orbital subspace, while $\boldsymbol{\sigma}$ act in the spin sector. The corresponding spectrum reads

$$E(\mathbf{k}) = \pm\sqrt{\left[M - t(\cos k_x + \cos k_y)\right]^2 + \lambda^2(\sin^2 k_x + \sin^2 k_y)}, \tag{1.98}$$

with each band being doubly degenerate because of TR symmetry. Hence the system is gapped unless both the mass term and the hybridization term vanish simultaneously. Since this requires $\sin k_x = \sin k_y = 0$, gap closings can occur only at TRIM

$$\Gamma = (0,0), \qquad X = (\pi,0), \qquad Y = (0,\pi), \qquad \mathbf{M} = (\pi,\pi). \tag{1.99}$$

At these points the hybridization terms vanish identically, so the phase boundaries are determined solely by the mass term $M - t(\cos k_x + \cos k_y)$. This gives the critical values $\frac{M}{t} = 2,\, 0,\, 0,\, -2$, at Γ, X, Y, and $\mathbf{M}$, respectively. Therefore, while the bulk gap generally depends on both M/t and λ, the topological phase transitions are controlled only by the ratio M/t. In particular, for $|M/t| < 2$ the mass term changes sign in the Brillouin zone, signaling band inversion and the onset of the QSHI phase.

Finally, the real-space expression of the BHZ model on the square lattice can be obtained through Fourier transformation

$$\begin{aligned}\hat{H} = M \sum_{j,\eta,\sigma} \eta \, \hat{c}^\dagger_{j,\eta,\sigma}\hat{c}_{j,\eta,\sigma} - \frac{1}{2}\Big(t \sum_{j,\boldsymbol{\mu},\eta,\sigma} \eta \, \hat{c}^\dagger_{j+\boldsymbol{\mu},\eta,\sigma}\hat{c}_{j,\eta,\sigma} \\ + \lambda \sum_{j,\eta,\sigma} \eta \, \hat{c}^\dagger_{j+\mathbf{y},\eta,\sigma}\hat{c}_{j,-\eta,\sigma} + \lambda \sum_{j,\eta,\sigma} i s_\sigma \hat{c}^\dagger_{j+\mathbf{x},\eta,\sigma}\hat{c}_{j,-\eta,\sigma} + h.c.\Big),\end{aligned} \tag{1.100}$$

where j labels the sites of the square lattice, $\boldsymbol{\mu} = \mathbf{x}, \mathbf{y}$ denotes the positive nearest-neighbor directions, $\eta = \pm 1$ labels the two orbital sectors, $\sigma = \uparrow, \downarrow$ the spin projection, and $s_\uparrow = +1$. In this form, the parameter M is the on-site potential staggered on the two orbitals, while t and λ describe, respectively, the intra-orbital and inter-orbital nearest-neighbor hoppings that reproduce the Dirac-like structure of the Bloch Hamiltonian in Eq. (1.97).

1.5 Topology beyond the non-interacting crystalline limit

The discussion so far has been entirely formulated within the single-particle framework of a clean crystalline system. In this setting, translational symmetry allows the Hamiltonian to be block-diagonal in crystal momentum and the many-body ground state is simply the Slater determinant of Eq. (1.12). The topology of non-interacting fermionic systems is determined by the global structure of the occupied Bloch states over the Brillouin zone and, crucially, by the symmetries of the Hamiltonian.

The sections above already illustrate how symmetry constraints give rise to distinct topological phases in the non-interacting limit. In Chern insulators such as the Haldane model, time-reversal symmetry is explicitly broken, allowing for a non-zero Chern number. By contrast, the Kane–Mele and BHZ models preserve time-reversal symmetry and realize a $\mathbb{Z}_2$ topological insulator, which is an example of a symmetry-protected topological (SPT) phase, in which the trivial and non-trivial phases cannot be adiabatically connected without either closing the bulk gap or breaking the protecting symmetry.

These examples are part of the broader classification of non-interacting topological phases [37–39] which is based on the spatial dimensionality of the system and on the presence or absence of three internal symmetries: time-reversal $\hat{T}$, particle-hole $\hat{C}$ and chiral $\hat{S}$ symmetry. Their possible combinations define the ten Altland–Zirnbauer symmetry classes [40], each associated in every spatial dimension with a definite topological classification. We also mention that, beyond this tenfold way, additional phases can be protected by spatial symmetries such as inversion, mirror or rotation. These phases, generally referred to as crystalline topological insulators [41], depend on the symmetries of the underlying lattice in addition to the internal ones. Disorder and interactions, whose effects on topological insulators are the main focus of this thesis, invalidate this framework in different ways.

Disorder preserves the single-particle description, and as long as the relevant protecting symmetries are preserved and the system remains insulating, with either a spectral or mobility gap, the corresponding topological phase can survive[5]. However, disorder breaks translational symmetry, requiring the usual momentum-space formulation to be replaced by single-point or real-space approaches in order to characterize the topology, as discussed in Chapter 2.

Interaction, on the other hand, invalidates the independent-particle approximation itself and therefore requires a genuinely many-body framework, which is developed in Chapter 5. In the following, we briefly discuss the broader perspective provided by interacting topological phases.

The object to be topologically characterized is, in this case, a correlated wavefunction that

[5]Disorder can break some of the spatial symmetries mentioned above and thereby potentially destroy crystalline topological phases. In some cases, however, these symmetries may be restored on average, allowing the topological phase to remain well defined as a statistical topological insulator [42].

cannot be reduced to a set of occupied single-particle Bloch states. Nevertheless, several of the concepts introduced in the non-interacting regime admit natural many-body generalizations: Berry phases and, in higher dimensions, topological invariants such as the Chern number, can be defined by adiabatically transporting the many-body ground state along a closed path in parameter space [43, 44] or through its response to twisted boundary conditions [45, 46]. In Chapter 5 we introduce a class of such many-body invariants [47, 48], derived from the modern theory of macroscopic polarization [19, 20], and use them to investigate the fate of the topological phases of the one- and two-dimensional BHZ models as interactions are introduced.

In general, an SPT phase identified in the non-interacting limit is robust against sufficiently weak interactions: as long as the bulk gap remains open and the protecting symmetries are preserved, a non-trivial phase remains distinct from a trivial one and can be regarded as the interacting continuation of its non-interacting counterpart.

Interactions, however, can modify the topological classification itself. The paradigmatic example is class BDI in one dimension, protected by time-reversal and particle-hole symmetry, whose non-interacting invariant takes values in $\mathbb{Z}$ but is reduced to $\mathbb{Z}_8$ once interactions are included [49]. Moreover, interactions can stabilize topological phases with no free-fermion counterpart at all. The invariant inherited from the non-interacting limit is therefore not, by itself, a complete characterization of the interacting phase, and complementary diagnostics are needed.

Boundary properties offer valuable insight in this respect, through the search for degenerate edge modes which may carry fractionalized charge or spin quantum numbers. A well-known example is the Haldane phase of the spin-1 antiferromagnetic Heisenberg chain [50], whose open ends host effective spin-1/2 degrees of freedom, resulting in a fourfold ground-state degeneracy in the thermodynamic limit [51, 52]. A further tool is provided by entanglement-based quantities, such as the entanglement spectrum [53, 54], which are defined directly from the many-body ground state and probe its topological structure without requiring open boundaries. Complementary non-local observables, such as string and parity order parameters, have also been proposed to characterize interacting topological phases in one dimension with spin-charge separation [55]. The latter will be used in Chapter 6 to complement the characterization of the physical nature of the interacting topological phase of the one-dimensional BHZ model.

Chapter 2

Topological invariants in disordered systems

Topological invariants are geometrical properties of the electronic structure and are most naturally formulated in reciprocal space for crystalline non-interacting systems. In this setting, the Bloch theorem allows the single-particle eigenstates to be labeled by the crystal momentum $\mathbf{k}$ and the topology of an insulating phase is encoded in the evolution of the occupied Bloch states $|u_{n\mathbf{k}}\rangle$. A paradigmatic example is the Chern number, which is obtained by integrating the Berry curvature over the Brillouin zone.

In numerical calculations, the Brillouin zone is sampled on a finite mesh of $\mathbf{k}$-points and geometric quantities are replaced by discretized expressions, usually written in terms of overlaps between occupied Bloch states at neighboring momenta. When crystalline symmetries are present, topological invariants can sometimes be computed more directly from symmetry eigenvalues at high-symmetry points in the Brillouin zone. In all these formulations, however, the existence of a well-defined crystal momentum plays a central role.

This reciprocal-space description relies on the translational invariance of the system, but real materials are never perfect and can be affected by disorder that breaks the lattice periodicity. In such cases, $\mathbf{k}$ is no longer a good quantum number and standard Bloch-based expressions for topological invariants cannot be applied directly. Nevertheless, translational invariance is not a prerequisite for the existence of a topological phase.

In disordered systems, topology can still be associated with the global structure of the occupied states, provided that a bulk spectral gap, or more generally a mobility gap, remains open and the protecting symmetries are preserved. Under these conditions, the topological phase and its associated boundary states remain stable against disorder. Conversely, in some cases disorder can even promote a topological phase starting from a clean trivial insulator, giving rise to the

so-called topological Anderson insulator (TAI) [56–58]. More broadly, non-crystalline systems, such as quasicrystals [59–64] and amorphous materials [65–70], are known to exhibit topologically non-trivial phases. These examples show that, although topology is most naturally formulated in reciprocal space for periodic systems, it is ultimately a property of the occupied electronic states and can persist beyond the crystalline setting.

For these reasons, considerable effort has been devoted to the development of methods capable of detecting topological phases in inhomogeneous or disordered systems. Without attempting to provide a complete review, we mention scattering-matrix methods [71, 72], the switch-function formalism [73–75], the entanglement spectrum [76, 77], as well as real-space topological indices such as the Bott index [78–80] and the spectral localizer [81, 82]. In particular, the Bott index and spectral localizer quantify, in different ways, the obstruction in the topological insulators to simultaneously diagonalizing position and Hamiltonian operators, which would instead be possible in a trivial phase. Another approach is based on the concept of spillage [83], where the topological character of a non-crystalline system is inferred by comparing its occupied subspace with that of a crystalline reference structure, whose topology can be determined using standard momentum-space methods.

In this chapter, we focus on two complementary strategies for diagnosing topology in disordered systems. The first aims at defining global topological invariants through *single-point* formulas within the supercell framework [7, 8]. In this approach, a finite disordered sample is periodically repeated in real space, restoring translational invariance at the supercell scale and recovering the notion of a Brillouin zone, which collapses to a single $\mathbf{k}$-point in the thermodynamic limit. The second strategy formulates topology directly in real space by means of *local topological markers* [9–11]. These markers assign a spatially resolved topological quantity to each region of the sample and can be applied under both open and periodic boundary conditions. For both single-point invariants and local markers, we discuss formulations for Chern and $\mathbb{Z}_2$ topological phases, with the latter expressed in terms of spin Chern numbers within Prodan's approach introduced in Section 1.4.

2.1 Single-point topological invariants in supercell framework

Let us consider a d-dimensional periodic lattice whose primitive unit cell contains N_b basis sites or orbitals. For a tight-binding model defined on this lattice, the Bloch Hamiltonian $H(\mathbf{k})$ is an $N_b \times N_b$ matrix at each crystal momentum $\mathbf{k}$ in the Brillouin zone. Diagonalizing $H(\mathbf{k})$ therefore gives N_b energy eigenvalues at each $\mathbf{k}$, corresponding to N_b energy bands.

The same clean lattice can equivalently be described by choosing a larger unit cell. If the unit cell is enlarged by a factor L along each primitive direction, then the resulting supercell

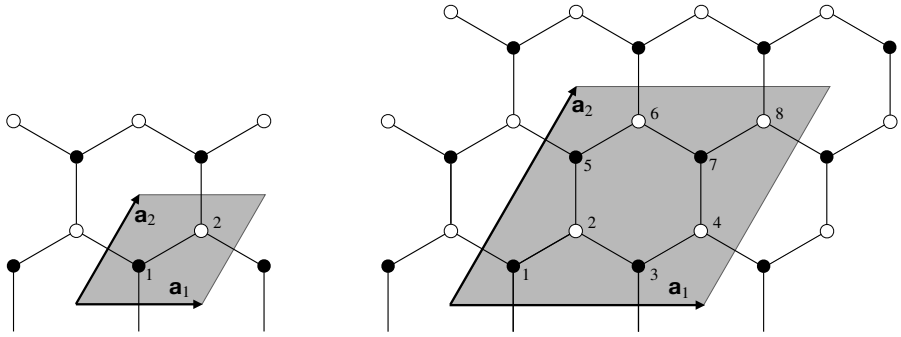


Figure 2.1: Schematic construction of a supercell in the honeycomb lattice. The left panel shows the primitive unit cell, containing $N_b = 2$ basis sites, with primitive lattice vectors $\mathbf{a}_1$ and $\mathbf{a}_2$. The right panel shows a supercell of linear size $L = 2$, which contains $N_{\text{orb}} = L^2 N_b = 8$ lattice sites.

contains

$$N_{\text{orb}} = L^d N_b \tag{2.1}$$

orbitals. In this representation, the Bloch Hamiltonian is a $N_{\text{orb}} \times N_{\text{orb}}$ matrix, and the number of bands increases from N_b to N_{orb}. This increase, however, does not correspond to additional physical degrees of freedom. Indeed, since the real-space unit cell is L^d times larger than the primitive one, the corresponding Brillouin zone is reduced in volume by the same factor. The energy bands of the primitive-cell description are therefore folded into the reduced Brillouin zone associated with the supercell. In this way, the same spectrum is represented as a larger number of bands defined over a smaller region of reciprocal space.

For a perfectly periodic system, this construction is only a change of representation reflecting the arbitrariness in the choice of unit cell. Its usefulness becomes clearer when disorder is introduced into the system. In this case, translational invariance with respect to the primitive lattice vectors of the underlying clean lattice is lost. Nevertheless, a finite disordered sample of linear size L can be identified as a supercell and periodically repeated, thereby defining an artificial periodic lattice, or *superlattice*. Translational invariance is then restored at the supercell scale, allowing Bloch's theorem to be applied in the reduced Brillouin zone of the superlattice. Thus, while for a clean lattice the use of supercell merely provides an alternative representation of the same Bloch problem, for a disordered system the supercell construction has a more substantial role, since it provides an artificial periodic approximation that makes a $\mathbf{k}$-space description possible.

This framework is particularly natural in tight-binding models, where disorder can be introduced directly at the lattice level: examples include random on-site potentials, modified hopping amplitudes, vacancies, or more general structural defects. Once a specific disordered configu-

ration is fixed within the supercell, periodic boundary conditions are imposed at the supercell scale, and the corresponding Bloch Hamiltonian can be diagonalized at **k**-points belonging to the reduced Brillouin zone.

A key observation is that, in the thermodynamic limit of infinite supercells $L \to \infty$, the reduced Brillouin zone collapses to the Γ point at its center. For sufficiently large supercells, much of the relevant information can therefore often be extracted from the Bloch Hamiltonian evaluated at this single point. This idea also underlies the common practice, in electronic-structure calculations for realistic systems, of considering very large simulation cells together with single-**k**-point sampling. The chosen point is typically Γ, although alternative choices, such as the Baldereschi point [84], can sometimes provide a more efficient sampling of the Brillouin zone.

From a physical point of view, the supercell construction is equivalent to imposing Born–von Karman boundary conditions on the finite disordered sample. If the supercell is sufficiently large, the artificial periodicity is introduced at length scales that are much larger than the relevant physical ones, such as the disorder correlation length. In this regime, quantities computed in large supercells from single-**k**-point calculations and averaged over disorder realizations are expected to reproduce the properties of the disordered system in the thermodynamic limit.

This approach provides the foundation for defining topological invariants in non-crystalline systems within the supercell framework. In the limit of very large supercells, the reduced Brillouin zone shrinks around Γ, leading to single-point formulas in which information on the topology of the system is extracted from the eigenstates of the supercell Hamiltonian at this unique point. In this section, we first review the single-point formula for the Chern number [7] in disordered systems and then discuss its extension to time-reversal-invariant $\mathbb{Z}_2$ topological insulators, in terms of single-point spin Chern numbers [8].

2.1.1 Single-point Chern number

In a periodic system, the Chern number of a two-dimensional quantum anomalous Hall insulator can be expressed in terms of the Berry curvature as

$$C = \frac{1}{2\pi} \int_{\mathrm{BZ}} \Omega_{xy}(\mathbf{k})\, d\mathbf{k} \tag{2.2}$$

$$= -\frac{1}{\pi} \mathrm{Im} \sum_{n=1}^{N_{occ}} \int_{BZ} \left\langle \partial_{k_x} u_n(\mathbf{k}) \middle| \partial_{k_y} u_n(\mathbf{k}) \right\rangle dk_x dk_y. \tag{2.3}$$

In numerical calculations, this integral is commonly evaluated on a discretized Brillouin zone and the resulting Chern number is an exact integer number, even for a relatively coarse **k**-mesh. However, this procedure still requires diagonalizing the Bloch Hamiltonian at each point of the

mesh, and it can become computationally demanding within a supercell approach for dealing with non-crystalline systems.

Ceresoli and Resta [7] showed that, in the limit of large supercell, the Chern number of a two-dimensional insulating system can instead be obtained from a single $\mathbf{k}$-point calculation, through the formula[6]

$$C^{asym} = -\frac{1}{\pi}\mathrm{Im}\sum_{n=1}^{N_{\mathrm{occ}}}\langle\tilde{u}_n(\mathbf{b}_1)|\tilde{u}_n(\mathbf{b}_2)\rangle \tag{2.4}$$

which requires the diagonalization of the supercell Bloch Hamiltonian only at the Γ point.

Let $\mathbf{b}_1$ and $\mathbf{b}_2$ be the reciprocal lattice vectors of the supercell, and let $|u_n(\Gamma)\rangle$, with $n = 1,\dots,N_{\mathrm{occ}}$, denote the occupied Bloch states at Γ point. The expression in Eq. (2.4) can then be understood as the Berry-curvature integrand of Eq. (2.2) evaluated at $\mathbf{k} = \Gamma$. Indeed, as the supercell size increases, the reduced Brillouin zone shrinks around Γ and the momentum derivatives entering in the Berry curvature in Eq. (2.3) can be approximated to finite differences as

$$|\partial_{k_j}u_n(\Gamma)\rangle = \frac{1}{|\mathbf{b}_j|}\big(\,|u_n(\mathbf{b}_j)\rangle - |u_n(\Gamma)\rangle\,\big). \tag{2.5}$$

The states $|u_n(\mathbf{b}_j)\rangle$ at the boundary of the reduced Brillouin zone can be calculated from the Γ-point states by imposing the periodic gauge in Eq. (1.25), without further diagonalizations

$$|u_n(\mathbf{b}_j)\rangle = e^{-i\mathbf{b}_j\cdot\hat{\mathbf{r}}}\,|u_n(\Gamma)\rangle\,. \tag{2.6}$$

However, finite differences are sensitive to erratic phase factors in the eigenvectors coming from numerical diagonalization. To remove this issue, the states at the boundary in Eq. (2.5) are substituted with the corresponding *dual states* with respect to $|u_n(\Gamma)\rangle$. For a generic momentum $\mathbf{k}$, these are defined as

$$|\tilde{u}_n(\mathbf{k})\rangle = \sum_{n'=1}^{N_{occ}} S^{-1}_{n'n}(\mathbf{k})\,|u_{n'}(\mathbf{k})\rangle\,, \tag{2.7}$$

where

$$S_{nn'}(\mathbf{k}) = \langle u_n(\Gamma)|u_n(\mathbf{k})\rangle \tag{2.8}$$

is the overlap matrix between the occupied states at Γ and at $\mathbf{k}$. This dual-state construction implements the finite-difference version of the covariant derivative [85–87] and is a device to approximate numerical derivatives, removing arbitrary gauge choices. We note that, although a

[6] We mention that the single-point formula for the Chern number reported here, and to which we will refer in the following calculations, is the one provided in Ref. [7] up to a geometrical prefactor associated with the chosen convention for the reciprocal vectors and the Brillouin-zone coordinates. In a non-orthogonal reciprocal basis, the prefactor must account for the area of the parallelogram spanned by the reciprocal lattice vectors $\mathbf{b}_1$ and $\mathbf{b}_2$.

non-trivial Chern number prevents the choice of a globally periodic gauge for the Bloch wavefunctions, here the periodic gauge is imposed only temporarily to build each $|u_n(\mathbf{b}_j)\rangle$ from the states $|u_n(\Gamma)\rangle$. These are then effectively replaced by the corresponding dual states, which implement the parallel-transport gauge enforced by the covariant derivative, as discussed in Appendix B.

Lastly, in Eq. (2.4) we emphasize with the superscript '*asym*' the implicit choice made in Eq. (2.5), which corresponds to the right-hand derivative. In fact, an alternative choice is the symmetric derivative, which we report here in the covariant formulation

$$\big|\tilde{\partial}_{k_\alpha} u_n(\Gamma)\big\rangle = \frac{1}{2|\mathbf{b}_\alpha|}\big(\,\big|\tilde{u}_n(-\mathbf{b}_\alpha)\big\rangle - \big|\tilde{u}_n(\mathbf{b}_\alpha)\big\rangle\,\big), \tag{2.9}$$

that leads to the symmetric formula for the single-point Chern number

$$C^{(sym)} = -\frac{1}{4\pi}\mathrm{Im}\sum_{n=1}^{N_{occ}}\big(\,\big\langle\tilde{u}_n(-\mathbf{b}_1)\big| - \big\langle\tilde{u}_n(\mathbf{b}_1)\big|\,\big)\big(\,\big|\tilde{u}_n(-\mathbf{b}_2)\big\rangle - \big|\tilde{u}_n(\mathbf{b}_2)\big\rangle\,\big). \tag{2.10}$$

The quantities defined in Eqs. (2.4) and (2.10) are not exactly quantized at finite supercell sizes. Instead, they converge to the integer topological invariant with increasing supercell size L, because the single-point approximation around Γ becomes progressively more accurate. The symmetric formula typically converges faster than the asymmetric one, making it possible in practical applications to approach the thermodynamic value with smaller supercells. Although the symmetric formula requires storing four dual states rather than two, this additional memory cost is negligible compared with the computational gain obtained from using smaller supercells, especially in terms of diagonalization of the $N_{orb} \times N_{orb}$ Bloch Hamiltonian at Γ, where N_{orb} scales as L^2.

2.1.2 Single-point spin Chern number

In Ref. [8], we generalized the single-point evaluation of topological invariants within the supercell framework to quantum spin Hall insulators. In particular, we implement a single-point formula for the spin Chern number based on the Prodan's approach [31] introduced in Section 1.4. This allows us to extend the classification of disordered $\mathbb{Z}_2$ insulators from a Γ-point calculation, even when S_z is not conserved.

Within the supercell framework, we diagonalize the Bloch Hamiltonian only at the Γ point and obtain the occupied eigenstates $|u_n(\Gamma)\rangle$. The projected spin operator introduced in Eq. (1.85) is then evaluated at Γ as

$$\hat{P}_z(\Gamma) = \hat{P}_\Gamma\,\hat{S}_z\,\hat{P}_\Gamma, \tag{2.11}$$

where $\hat{S}_z$ is the total spin operator and $\hat{P}_\Gamma$ is the projector onto the occupied states at Γ

$$\hat{P}_\Gamma = \sum_{n=1}^{N_{occ}} |u_n(\Gamma)\rangle\,\langle u_n(\Gamma)|\,. \tag{2.12}$$

Then, once the spin projected operator $\hat{P}_z(\Gamma)$ is constructed, we diagonalize it and obtain its eigenstates $|v_\lambda(\Gamma)\rangle$

$$\hat{P}_z(\Gamma)\,|v_\lambda(\Gamma)\rangle = s_\lambda\,|v_\lambda(\Gamma)\rangle\,. \tag{2.13}$$

If S_z is conserved, the spectrum of $\hat{P}_z(\Gamma)$ consists only of two values $s_\lambda = \pm 1/2$. In this case, one can select a spin sector by choosing the eigenstates associated with either $s_\lambda = +1/2$ or $s_\lambda = -1/2$. In the presence of spin-mixing terms in the Bloch Hamiltonian, S_z is no longer conserved. Nevertheless, the spectrum of $\hat{P}_z(\Gamma)$ may still split into two groups of eigenvalues, one positive and the other negative, separated by a gap around zero. This is actually the situation that we will mostly encounter in our applications, even in the presence of relatively strong Rashba spin-orbit coupling, which mixes the spin sectors. Therefore, in the presence of a finite gap in the $\hat{P}_z(\Gamma)$ spectrum, we define the two generalized spin sectors as

$$\lambda_+ = \{\lambda : s_\lambda > 0\}, \qquad \lambda_- = \{\lambda : s_\lambda < 0\}. \tag{2.14}$$

For each spin sector λ_σ, we apply the procedure described in Section 2.1.1 for calculating the single-point Chern number considering the states $|v_\lambda(\Gamma)\rangle$ with $\lambda \in \lambda_\sigma$. First, the states at the boundary of the BZ are generated from the Γ-point states by imposing the periodic gauge

$$|v_\lambda(\mathbf{b}_j)\rangle = e^{-i\mathbf{b}_j\cdot\hat{\mathbf{r}}}\,|v_\lambda(\Gamma)\rangle\,. \tag{2.15}$$

Then, we replace these states with the dual states

$$|\tilde{v}_\lambda(\mathbf{b}_j)\rangle = \sum_{\mu\in\lambda_\sigma} S^{-1}_{\mu\lambda}(\mathbf{b}_j)\,|v_\mu(\mathbf{b}_j)\rangle \tag{2.16}$$

where we define the overlap matrix

$$S_{\lambda\mu}(\mathbf{b}_j) = \langle v_\lambda(\Gamma)|v_\mu(\mathbf{b}_j)\rangle. \tag{2.17}$$

The single-point spin Chern number is then evaluated using the asymmetric

$$C^{(asym)}_\sigma = -\frac{1}{\pi}\mathrm{Im}\sum_{\lambda\in\lambda_\sigma}\big\langle\tilde{v}_\lambda(\mathbf{b}_1)\big|\tilde{v}_\lambda(\mathbf{b}_2)\big\rangle \tag{2.18}$$

or the symmetric formula

$$C^{(sym)}_\sigma = -\frac{1}{4\pi}\mathrm{Im}\sum_{\lambda\in\lambda_\sigma}\big(\,\big\langle\tilde{u}_\lambda(-\mathbf{b}_1)\big| - \big\langle\tilde{u}_\lambda(\mathbf{b}_1)\big|\,\big)\big(\,\big|\tilde{u}_{\lambda-\mathbf{b}_2}\big\rangle - \big|\tilde{u}_{\lambda\mathbf{b}_2}\big\rangle\,\big), \tag{2.19}$$

where, again, the symmetric formula for the single-point spin Chern number converges faster than the asymmetric one.

2.2 Local topological markers

The supercell approach provides a way to extend the computation of topological invariants to disordered systems while preserving periodic boundary conditions. However, this construction still assigns a global invariant to the entire supercell. This can become inadequate when the system is intrinsically inhomogeneous, for instance in the presence of an interface between regions with different topological character. In this case, the bulk topology changes across the interface and, since a topological invariant cannot change under deformations of the Hamiltonian that do not close the band gap, metallic boundary states must appear at the interface separating the trivial from the topological regions. In such a situation, the full system cannot be described in a meaningful way by a global topological invariant, which would not provide any information on where the change of topological character occurs, nor would it resolve the coexistence of distinct topological regions within the same sample.

This motivates the use of real-space diagnostics capable of locally resolving topological properties. The underlying observation is that topology, although usually formulated in reciprocal space for periodic systems, is ultimately a property of the ground-state electronic structure. As such, in view of Kohn's principle of "nearsightedness" [88], it should admit not only a real-space description but also a local formulation, in the sense that the topological character at a given point of the system should be inferred solely from the knowledge of the ground state in a neighborhood of the region of interest. One may therefore expect to be able to assign to each point of an inhomogeneous sample a quantity that describes the topology in its surroundings, thereby distinguishing topological and trivial domains within the same system.

This idea was first made explicit by Bianco and Resta [9], who showed that, in finite systems, the Chern number can be mapped onto real space through a local Chern marker $\mathcal{C}(\mathbf{r})$. When averaged over a sufficiently large region deep inside the bulk, this marker reproduces the usual integer Chern number. Closed to boundaries, interfaces, or defects, it instead captures the spatial variation of the topological character.

Local topological markers of this kind offer a natural framework for investigating systems where translational symmetry is absent, such as heterostructures, amorphous materials, or crystals with disorder and vacancies. Moreover, in some cases, they can be related to experimentally accessible probes, such as local circular dichroism [89].

In this section, we first introduce the original formulation of the local Chern marker for systems with open boundary conditions (OBC) [9] and then discuss its extension to $\mathbb{Z}_2$ topological insulators. We subsequently show how analogous real-space markers can be formulated for systems with periodic boundary conditions (PBC) by exploiting the same ingredients that enter the single-point formulas introduced in Section 2.1.

2.2.1 Local Chern and $\mathbb{Z}_2$ markers in finite systems

Bianco and Resta [9] showed that, for a crystalline QAHI, the Chern number can be rewritten as the real-space trace

$$C = \frac{1}{2\pi}\int_{\mathrm{BZ}} \mathrm{Tr}\,\Omega_{xy}(\mathbf{k})\,d\mathbf{k} = -\frac{4\pi}{A}\,\mathrm{Im}\,\mathrm{Tr}_A\Big\{\hat{P}\hat{x}(\hat{\mathbb{1}}-\hat{P})\hat{y}\Big\} \tag{2.20}$$

or, equivalently, as

$$C = \frac{4\pi}{A}\,\mathrm{Im}\,\mathrm{Tr}_A\Big\{\big[\hat{P}\hat{x}\hat{P},\hat{P}\hat{y}\hat{P}\big]\Big\}. \tag{2.21}$$

Here, A is the area of the unit cell, Tr_A denotes the trace over this area, $\hat{P}$ is the ground-state projector

$$\hat{P} = \frac{A}{4\pi^2}\sum_{n=1}^{N_{occ}}\int_{BZ} d\mathbf{k}\,|\psi_n(\mathbf{k})\rangle\langle\psi_n(\mathbf{k})|, \tag{2.22}$$

and $\hat{x}$ and $\hat{y}$ are the Cartesian components of the position operator $\hat{\mathbf{r}}$, which are well-defined operators in OBCs, whereas their use in PBCs requires a different treatment[7], as we will see in the following section.

Eqs. (2.20) and (2.21) should be understood as bulk expression. Indeed, for a sufficiently large finite system, when the trace Tr_A is taken over a unit cell far from the boundaries, the real-space expression reproduces the Chern number of the corresponding periodic system.

A key observation in Ref. [9] is that, if the trace is instead taken over the entire finite sample, the result must vanish. This follows from the commutator appearing in Eq. (2.21), whose trace on a finite-dimensional manifold is identically zero. This means that the global topology is always trivial within OBCs. The information on the topology of a finite system is recovered by evaluating *locally* the real-space operator. This leads to the definition of the local Chern marker

$$\begin{aligned}\mathcal{C}(\mathbf{r}) &= -4\pi\,\mathrm{Im}\langle\mathbf{r}|\hat{\mathcal{P}}\hat{x}(\hat{\mathbb{1}}-\hat{\mathcal{P}})\hat{y}|\mathbf{r}\rangle \\ &= 4\pi\,\mathrm{Im}\,\langle\mathbf{r}|\hat{\mathcal{P}}[\hat{x},\hat{\mathcal{P}}][\hat{y},\hat{\mathcal{P}}]|\mathbf{r}\rangle\end{aligned} \tag{2.23}$$

where with $\hat{\mathcal{P}}$ we indicate the projector onto the occupied state of the Hamiltonian diagonalized in real space, under open boundary conditions.

The local Chern number can then be obtained by calculating the macroscopic average of $\mathcal{C}(\mathbf{r})$, that is, taking the trace per unit of area in a region around the point $\mathbf{r}$ in real space. In a crystalline system, this essentially corresponds to taking the trace Tr_A over the unit cell

[7] Strictly speaking, at variance with $\hat{\mathbf{r}}$ which is ill-defined in PBCs, the combinations $\hat{P}\hat{x}(\hat{\mathbb{1}}-\hat{P})\hat{y}$ and $\big[\hat{P}\hat{x}\hat{P},\hat{P}\hat{y}\hat{P}\big]$, appearing in Eqs. (2.20) and (2.21), respectively, are well defined and regular also under PBCs. In practice, however, these operators are not directly accessible. They are usually constructed by first calculating the components of $\hat{\mathbf{r}}$ in a proper basis and then multiplying them by the projection operator $\hat{P}$. It is precisely this intermediate use of $\hat{\mathbf{r}}$ that leads to difficulties with this formulation in PBCs.

containing the point $\mathbf{r}$. If $\mathbf{r}$ lies in the bulk region, the macroscopic average of $\mathcal{C}(\mathbf{r})$ reproduces the Chern number C, while close to the boundaries the marker develops compensating contributions, so that the sum of $\mathcal{C}(\mathbf{r})$ over the entire finite sample vanishes, consistently with the global trace argument.

The same construction can also be applied to non-crystalline systems. In that case, the notion of a trace over a unit cell may not be longer available, but one can still define a physically meaningful local Chern number by averaging $\mathcal{C}(\mathbf{r})$ over a sufficiently large real-space region in the bulk of the sample. This makes the local Chern marker a useful diagnostic of topology in finite, disordered, amorphous, or otherwise inhomogeneous systems.

It is then natural to extend the idea of local markers to QSHIs [10]. A straightforward route to obtain a local formulation of the $\mathbb{Z}_2$ invariant is provided by the spin-Chern construction, following Prodan's approach [31]. Indeed, the idea of splitting the space of occupied states into two subspaces according to the positive and negative eigenvalues of the projected spin operator can be applied to local spin Chern markers (LSCM) as

$$\mathcal{C}_\sigma(\mathbf{r}) = 4\pi\,\mathrm{Im}\langle\mathbf{r}|\hat{\mathcal{P}}_\sigma[\hat{x},\hat{\mathcal{P}}_\sigma][\hat{y},\hat{\mathcal{P}}_\sigma]|\mathbf{r}\rangle, \qquad \sigma = \pm. \tag{2.24}$$

More explicitly, $\hat{\mathcal{P}}_\sigma$ denotes the projector onto the states $|\phi_\lambda\rangle$ with positive ($\sigma = +$) or negative ($\sigma = -$) eigenvalues s_λ that diagonalize the spin projected operator $\hat{\mathcal{P}}\,\hat{S}_z\,\hat{\mathcal{P}}$, namely

$$\hat{\mathcal{P}}_\sigma = \sum_{\lambda\,:\,\mathrm{sign}(s_\lambda)=\sigma} |\phi_\lambda\rangle\langle\phi_\lambda|. \tag{2.25}$$

We again stress that such formulation is naturally suited mainly to OBCs, as it requires the explicit evaluation of operators $\hat{x}$ and $\hat{y}$, which are ill-defined within PBCs.

The local $\mathbb{Z}_2$ marker can be then defined as

$$\nu(\mathbf{r}) = \frac{\mathcal{C}_+(\mathbf{r}) - \mathcal{C}_-(\mathbf{r})}{2} \mod 2. \tag{2.26}$$

where its macroscopic average over a bulk region gives a local diagnosis of the $\mathbb{Z}_2$ topology. This construction is particularly convenient because it is expressed entirely in real space and can therefore be applied to finite and non-crystalline systems, in close analogy with the LCM. However, it relies on the existence of a spectral gap in the projected spin operator $\hat{\mathcal{P}}\,\hat{S}_z\,\hat{\mathcal{P}}$, even if it is not a fundamental requirement for a QSHI. For this reason, Ref. [10] also proposed a more general $\mathbb{Z}_2$ local marker that is solely based on TR symmetry, without relying on the spin operator, thereby extending this real-space strategy to a broader class of disordered topological systems.

2.2.2 Local Chern and $\mathbb{Z}_2$ markers in periodic systems

The development of local topological markers has changed the view that working in reciprocal space is essential to obtain information on the topology of the system. These real-space quantities make it possible to investigate topological phases in systems that, like real materials, are finite, inhomogeneous, and disordered. They have also enabled the study of topological phases in amorphous and quasicrystalline systems. Nevertheless, PBCs are often the method of choice in electronic structure calculations. Not only they provide the most natural framework to study perfect crystals, but they are also commonly used to reduce finite size-effects in non-crystalline systems. In the latter case, large periodic simulation cells are employed, and physical quantities are typically checked for convergence with respect to the supercell size. As discussed in Section 2.1, within the supercell framework, a sufficiently large unit cell often allows the Brillouin-zone sampling to be reduced to the single Γ point.

The purpose of Ref. [11] is to construct a space-resolved Chern marker also for periodic systems. The main difficulty in doing this comes from the explicit presence of the position operators $\hat{x}$ and $\hat{y}$ in the local topological markers presented in Section 2.2.1, since these operators are well defined only under OBCs. To overcome this problem, the authors exploit the single-point formula for the Chern number introduced in Ref. [7] and reviewed in Section 2.1.1, obtaining a local Chern marker that can be rigorously evaluated in PBCs.

In particular, in Ref. [11] the single-point Chern number in Eq. (2.4) is first rewritten as a trace

$$C^{(asym)} = -\frac{1}{\pi}\mathrm{Im}\mathrm{Tr}\Big\{\sum_{n=1}^{N_{occ}} \big|\tilde{u}_n(\mathbf{b}_1)\big\rangle\big\langle\tilde{u}_n(\mathbf{b}_2)\big|\Big\}. \tag{2.27}$$

One then defines

$$\tilde{P}_{\mathbf{b}_2,\mathbf{b}_1} = \sum_{n=1}^{N_{occ}} \big|\tilde{u}_n(\mathbf{b}_1)\big\rangle\big\langle\tilde{u}_n(\mathbf{b}_2)\big| \tag{2.28}$$

which, in general, is not a projector, but it can be expressed in terms of the projectors

$$\hat{P}_{\mathbf{b}_j} = \sum_{n=1}^{N_{occ}} \big|\tilde{u}_n(\mathbf{b}_j)\big\rangle\big\langle\tilde{u}_n(\mathbf{b}_j)\big| \tag{2.29}$$

as

$$\tilde{P}_{\mathbf{b}_2,\mathbf{b}_1} = \hat{P}_{\mathbf{b}_2}\hat{P}_\Gamma\hat{P}_{\mathbf{b}_1}. \tag{2.30}$$

Here, $\hat{P}_\Gamma$ is the projector onto the occupied states at Γ defined in Eq. (2.12), while $|\tilde{u}_n(\mathbf{b}_j)\rangle$ are the dual states introduced in Eq. (2.6) and obtained solely from the knowledge of $|u_n(\Gamma)\rangle$. Therefore, also in this case, a single diagonalization of the Hamiltonian at the Γ point is required.

Using the cyclic property of the trace, the single-point Chern number is then written as

$$C^{(asym)} = -\frac{1}{2\pi}\mathrm{Im}\mathrm{Tr}\Big\{\big[\hat{P}_{\mathbf{b}_1},\hat{P}_{\mathbf{b}_2}\big]\,\hat{P}_\Gamma\Big\}. \tag{2.31}$$

The local Chern number in PBCs is finally obtained by taking the macroscopic average (i.e., the local trace per unit of area) of the PBC local Chern marker

$$\mathcal{C}^{(asym)}(\mathbf{r}) = -\frac{1}{2\pi}\,\mathrm{Im}\,\langle\mathbf{r}|\big[\hat{P}_{\mathbf{b}_1},\hat{P}_{\mathbf{b}_2}\big]\,\hat{P}_\Gamma|\mathbf{r}\rangle. \tag{2.32}$$

A symmetric formulation, which converges faster with the supercell size, is given by

$$\mathcal{C}^{(sym)}(\mathbf{r}) = -\frac{1}{8\pi}\,\mathrm{Im}\,\langle\mathbf{r}|\Big(\big[\hat{P}_{\mathbf{b}_1},\hat{P}_{\mathbf{b}_2}\big]+\big[\hat{P}_{-\mathbf{b}_1},\hat{P}_{-\mathbf{b}_2}\big]-\big[\hat{P}_{-\mathbf{b}_1},\hat{P}_{\mathbf{b}_2}\big]-\big[\hat{P}_{\mathbf{b}_1},\hat{P}_{-\mathbf{b}_2}\big]\Big)\,\hat{P}_\Gamma|\mathbf{r}\rangle. \tag{2.33}$$

The crucial point is that these formulas contain the operator $\hat{\mathbf{r}}$ only as an exponent in $e^{i\mathbf{b}_j\cdot\hat{\mathbf{r}}}$, which is used to construct the dual states in Eq. (2.6). This is known to be the appropriate way to treat the position operator in PBCs [44, 90] and is related to the modern theory of polarization based on the Berry phase [20].

This construction can be generalized to QSHIs, as done in Ref. [10], by applying the same projector-based formulation to the single-point spin Chern numbers introduced in Ref. [8]. The strategy is to replace the projectors $\hat{P}_\Gamma$ and $\hat{P}_{\mathbf{b}_j}$ entering in the PBC local Chen marker with the corresponding projectors $\hat{P}^\sigma_\Gamma$ and $\hat{P}^\sigma_{\mathbf{b}_j}$ for each spin sectors σ. In particular, these spin sectors are obtained by diagonalizing the spin projected operator $\hat{P}_z(\Gamma) = \hat{P}_\Gamma\hat{S}_z\hat{P}_\Gamma$ introduced in Section 2.1.2. Being $|v_\lambda(\Gamma)\rangle$ its eigenstates, with eigenvalues s_λ, the projector onto the spin sector σ at the Γ point is

$$\hat{P}^\sigma_\Gamma = \sum_{\lambda\,:\,\mathrm{sign}(s_\lambda)=\sigma} |v_\lambda(\Gamma)\rangle\,\langle v_\lambda(\Gamma)| \tag{2.34}$$

while at the BZ boundaries one defines

$$\hat{P}^\sigma_{\mathbf{b}_j} = \sum_{\lambda\,:\,\mathrm{sign}(s_\lambda)=\sigma} |\tilde{v}_\lambda(\mathbf{b}_j)\rangle\,\langle\tilde{v}_\lambda(\mathbf{b}_j)| \tag{2.35}$$

where the dual states $|\tilde{v}_\lambda(\mathbf{b}_j)\rangle$ are defined in Eq. (2.16) and are constructed solely from the eigenstates $|v_\lambda(\Gamma)\rangle$.

The PBC local spin Chern markers are then obtained by replacing, in the PBC local Chern marker in Eqs. (2.31) and (2.33), the full projectors with the projectors onto the spin sectors

$$\mathcal{C}^{(asym)}_\sigma(\mathbf{r}) = -\frac{1}{2\pi}\,\mathrm{Im}\,\langle\mathbf{r}|\big[\hat{P}^\sigma_{\mathbf{b}_1},\hat{P}^\sigma_{\mathbf{b}_2}\big]\,\hat{P}^\sigma_\Gamma|\mathbf{r}\rangle, \tag{2.36}$$

$$\mathcal{C}^{(sym)}_\sigma(\mathbf{r}) = -\frac{1}{8\pi}\,\mathrm{Im}\,\langle\mathbf{r}|\Big(\big[\hat{P}^\sigma_{\mathbf{b}_1},\hat{P}^\sigma_{\mathbf{b}_2}\big]+\big[\hat{P}^\sigma_{-\mathbf{b}_1},\hat{P}^\sigma_{-\mathbf{b}_2}\big]-\big[\hat{P}^\sigma_{-\mathbf{b}_1},\hat{P}^\sigma_{\mathbf{b}_2}\big]-\big[\hat{P}^\sigma_{\mathbf{b}_1},\hat{P}^\sigma_{-\mathbf{b}_2}\big]\Big)\,\hat{P}^\sigma_\Gamma|\mathbf{r}\rangle. \tag{2.37}$$

When the spectrum of the projected spin operator $\hat{P}_z(\Gamma)$ has a finite gap, these PBC local spin-Chern markers can be used to define the local $\mathbb{Z}_2$ marker in PBCs as the semidifference of the two spin-sector markers, taken modulo 2.

Finally, we mention that Ref. [10] also proposes a more general $\mathbb{Z}_2$ local marker, suitable for PBCs, that is based only on TR symmetry. However, in our analysis of disordered QSHIs, we will always rely on the spin-Chern formulation, since we will never encounter a closing of the spectral gap of the $\hat{P}_z(\Gamma)$ operator that would prevent its use.

Chapter 3

Fluctuations and correlations of local topological order parameters in disordered two-dimensional topological insulators

Topological insulators are commonly introduced as phases of matter that cannot be characterized by a conventional local order parameter, and therefore lie outside the conventional Landau paradigm based on spontaneous symmetry breaking [18]. Their classification relies instead on topological invariants, namely global quantities determined by the structure of the ground-state wavefunction. In crystalline systems, translational symmetry makes it possible to define these invariants in reciprocal space, where they encode the evolution of the occupied Bloch states across the entire Brillouin zone.

However, real materials are always finite, inhomogeneous, and may host different kinds of defects, ranging from weak disorder to vacancies and structural amorphization. These perturbations break translational symmetry, so that the Brillouin zone is no longer well defined. In the previous chapter, we introduced two approaches to address this issue. The first one, discussed in Section 2.1, consists in recovering an effective momentum-space formulation by introducing large disordered supercells that are periodically repeated. Within this framework, one can assign a global topological index to a disordered configuration through single-point formulas for topological invariants [7, 8]. The second and complementary strategy is offered by real-space formulations, introduced in Section 2.2. Local topological markers provide a spatially resolved description of the topological character of a system and can be applied under both open and periodic boundary conditions [9–11]. In this sense, they introduce a notion of *locality* into the

study of topological phases, revealing how topology is redistributed and modified by boundaries, disorder, interfaces and structural inhomogeneities.

Disorder, however, is not just a technical complication that requires a reformulation of topological diagnostics, but can also play an active physical role in topological systems. A paradigmatic example is provided by the integer quantum Hall effect, where disorder broadens Landau levels into bands. Most states in these Landau bands are localized and do not contribute to longitudinal transport, allowing the Hall conductivity to remain quantized over a finite energy range and producing the plateau observed experimentally. Still, near the center of each disorder-broadened band, extended states appear and mediate the transition between adjacent plateaus.

More generally, topological phases can remain stable in the presence of moderate amounts of disorder, as long as the protecting symmetries are preserved and the spectral or mobility gap does not close. In some cases, disorder can even induce topological behavior, as in the topological Anderson insulator (TAI) [56–58], where a trivial system with a small energy gap becomes topological due to disorder-induced renormalization of the effective band parameters. Recently, a material-independent mechanism has been proposed in which engineered vacancy concentrations can drive topological phase transitions in otherwise trivial semiconductors [91].

From this perspective, disorder could be regarded as a physical knob for tuning the topological character of a material. This makes disorder-driven topological phase transitions a central problem in the study of realistic topological systems. In particular, it raises the fundamental question of whether this kind of transition can be described in terms of concepts analogous to those employed in conventional critical phenomena.

In recent years, finite-size scaling analyses have been applied to local topological markers, focusing on disorder-driven [92] and mass-driven [93] topological phase transitions, mainly under open boundary conditions. In these studies, however, a global description is effectively recovered by considering the macroscopically averaged value of the marker at the center of the sample. The full spatial information contained in the markers, and in particular their fluctuations and correlations, remains largely unexplored.

In this chapter, we adopt a different viewpoint, in which local topological markers are interpreted as *bona fide* local order parameters for disorder-driven topological phase transitions. Largely based on Ref. [12], in the following we study topological phase transitions in the presence of different types of disorder in paradigmatic tight-binding models: the Haldane model for Chern insulators and the Kane–Mele model for QSHIs. We use single-point invariants to identify the transitions at the global level and then investigate the role of fluctuations and spatial correlations of local topological markers, especially under periodic boundary conditions, showing that they carry the signatures expected from a local order parameter across a disorder-driven transition.

The numerical evaluation of single-point invariants and local topological markers is performed

using the `StraWBerryPy` Python package [94]. This code is part of the Wannier-function software ecosystem [95] and is interfaced with widely used tight-binding engines, including `TBmodels` [96, 97] and `PythTB` [98].

3.1 Fluctuations and correlation function of local Chern marker

We consider the Haldane model [3] for Chern insulators, introduced in Section 1.3.1, in the presence of both Anderson disorder and lattice vacancies. Unless stated otherwise, the first nearest-neighbor hopping is real and fixed to $t = -4$, while the second nearest-neighbor hopping is complex, with amplitude $|t_2/t| = 1/4$ and phase $\phi = -\pi/2$.

Anderson disorder is introduced through a random on-site potential

$$\hat{H}_{\text{dis}} = \sum_i w_i \, \hat{c}_i^\dagger \hat{c}_i, \qquad w_i \in \left[-\frac{W}{2}, \frac{W}{2}\right] \tag{3.1}$$

where W denotes the disorder strength and the random variables w_i are drawn from a uniform distribution. Vacancies are instead modeled by randomly removing a certain fraction ρ_v of sites from the lattice. This amounts to deleting, in the real-space Hamiltonian, all the corresponding on-site terms, together with the hopping elements connecting the removed sites to first and second nearest-neighbors.

We use the single-point Chern number in Eq. (2.10) to identify the topological phase transitions at the global level, and the local Chern markers in periodic and open boundary conditions, Eqs. (2.33) and (2.23), to analyze the real-space structure of the topological response to disorder.

In the presence of disorder, indeed, the local Chern markers fluctuate from site to site. To extract the physically relevant local topology, we perform a macroscopic average over all primitive cells within a radial cutoff r_c. This coarse graining suppresses short-scale disorder-induced fluctuations away from criticality, while preserving the large-scale fluctuations that emerge near a phase transition. This behavior, together with the Chern-Chern correlation function and its correlation length, which peaks at the transition, corroborates the interpretation of local topological markers as genuine local order parameters for disorder-driven topological phase transitions.

3.1.1 Disorder-driven transition from QAHI to trivial insulator

We first consider the case in which the pristine Haldane model is in the topological phase, with Chern number $C = 1$ and on-site term $\Delta/t = 1.25$. For weak Anderson disorder the system remains topological, whereas, at sufficiently large disorder strength, Anderson localization occurs and drives the system into a trivial phase with Chern number $C = 0$. The transition between the two insulating phases is rather sharp, as it can be seen in the left panel of Figure 3.1, which shows

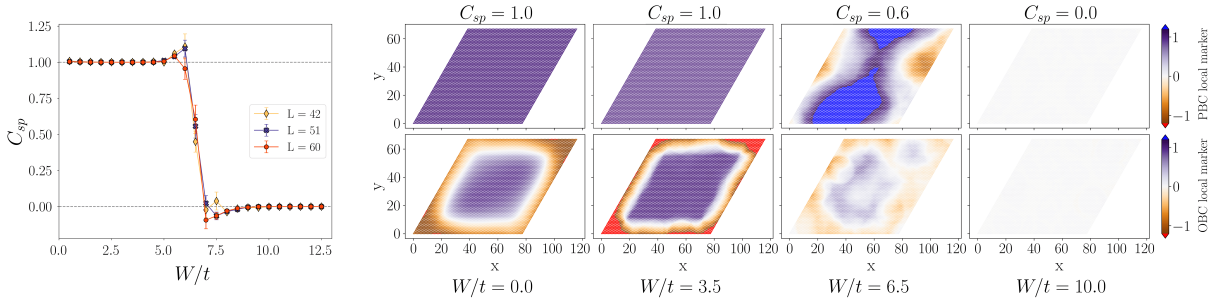


Figure 3.1: QAHI→trivial phase transition driven by Anderson disorder in the Haldane model ($\Delta/t = 1.25$). Left panel: single-point Chern number (C_{sp}) calculations as a function of the disorder strength W in units of the nearest-neighbor hopping t. The points and error bars correspond to the average and standard deviation over $N_{\text{samples}} = 300$ realizations. Right panel: PBC (top row) and OBC (bottom row) Chern marker maps for the linear size $L = 78$ (12168 sites) for various values of W; the single-point Chern number corresponding to the maps is displayed above. The disordered on-site terms are the same in PBCs and OBCs. The color (gray) scale displays values in $[-1.2, 1.2]$, values outside the range are marked in red (lower than -1.2) and blue (larger than 1.2).

the single-point Chern number C_{sp} as a function of W/t, calculated in supercells of increasing linear size L.

The right panel of Figure 3.1 shows real-space maps of the local Chern marker computed with both PBCs and OBCs for $L = 78$, corresponding to 12168 lattice sites. The value assigned to each site is obtained by averaging the marker over all primitive cells within a radial cutoff $r_c = 20$, measured in units of the lattice parameter. The maps show that, even when the disorder amplitude is comparable with the on-site term of the pristine model, the local topology remains essentially homogeneous. This feature is preserved throughout most of the transition, and the main exception occurs close to the critical point, where the single-point Chern number deviates from integer values and strong real-space fluctuations appear. In this regime, finite-size effects become more pronounced, especially in finite samples. Indeed, the OBC simulations return rather different topological maps with respect to their PBC counterparts, even if all the on-site terms are equal and only the boundary conditions are changed.

We now analyze the length scale of the fluctuations of the local topological marker. The left panel of Figure 3.2 shows PBC maps of the local Chern marker computed for increasing cutoff radii, from $r_c = 2$ to $r_c = 30$. We compare three representative regimes: the topological phase with $C_{sp} = 1.0$ at $W/t = 5$, the trivial phase with $C_{sp} = 0.0$ at $W/t = 10$, and the transition region with $C_{sp} = 0.6$ at $W/t = 6.5$.

For small values of r_c, the local marker displays microscopic fluctuations in all phases. Increasing r_c corresponds to coarse graining the local Chern markers over larger regions. In both the topological and trivial phases, short-range fluctuations are rapidly averaged out, and the system appears topologically uniform already for relatively small cutoffs, such as $r_c = 10$. By

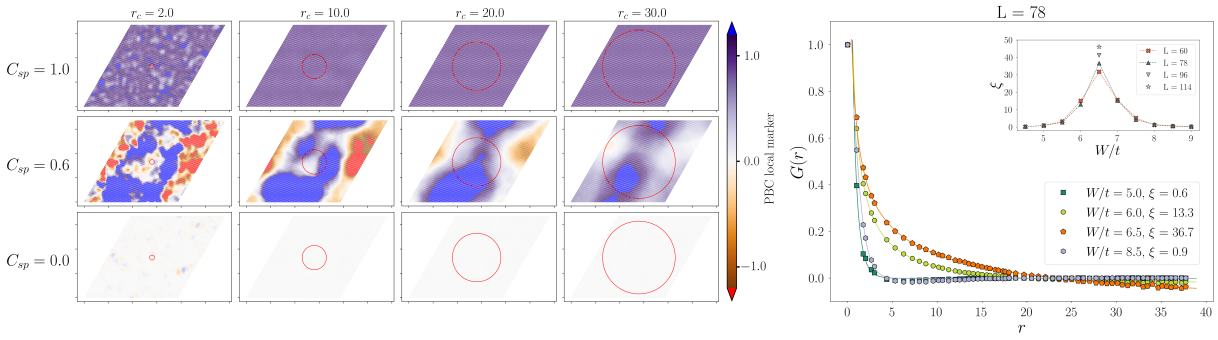


Figure 3.2: Macroscopic average and Chern-Chern correlation function. Left panel: PBC Chern marker maps for three different values of the disorder strength W/t, which correspond to three different values of the single-point Chern number ($C_{sp} = 1.0$ for $W/t = 5$, $C_{sp} = 0.6$ for $W/t = 6.5$ and $C_{sp} = 0.0$ for $W/t = 10$). Maps are drawn for increasing values of the cutoff r_c over which the macroscopic average is performed. The cutoff r_c is marked by the radius of the red circle centered in the middle of the sample. Short-scale fluctuations of the topological marker average out in the topological and trivial phase, while large-scale fluctuations remain at the transition. Right panel: the Chern-Chern correlation function (Eq. 3.2) computed at different disorder strengths, averaged over $N_{\text{samples}} = 200$ realizations with linear size $L = 78$. The correlation length ξ is obtained by fitting with the Ornstein-Zernike formula (Eq. 3.4); the inset reports ξ as a function of W/t for system sizes $L = 60$ and $L = 78$, additional values for $L = 96, 114$ are shown at $W/t = 6.5$ only.

contrast, close to the critical region, large-scale fluctuations persist even when the macroscopic average is performed over rather large regions (e.g., $r_c = 30$).

To characterize the spatial range of these fluctuations, we introduce the connected radial correlation function of the local Chern marker

$$G(r) = \langle \mathcal{C}_0 \mathcal{C}_r \rangle_{\text{samples}} - \langle \mathcal{C}_0 \rangle^2_{\text{samples}} , \tag{3.2}$$

where the mean $\langle \dots \rangle_{\text{samples}}$ is taken over N_{samples} disorder realizations at fixed disorder strength. The one- and two-point correlations are normalized as

$$\langle \mathcal{C}_0 \mathcal{C}_r \rangle_{\text{samples}} = \left\langle \frac{1}{N_r} \frac{\sum_{i,j} \delta(r - r_{ij}) \mathcal{C}^s_i \mathcal{C}^s_j}{\sigma^2_s} \right\rangle_{\text{samples}} \tag{3.3}$$

with N_r being the number of sites j at distance r from site i, $\mathcal{C}^s_i$ are the local Chern markers at site i in the realization s, $\langle \mathcal{C}_i \rangle_s$ is the mean value of the local Chern number over the system (which coincides with the single-point Chern number) and $\sigma^2_s = \langle \mathcal{C}^2_i \rangle_s - \langle \mathcal{C}_i \rangle^2_s$ is the corresponding variance.

In the right panel of Figure 3.2 we report the correlation function $G(r)$ for several disorder strengths, including the values used for the local Chern maps in the left panel. The correlation function is fitted with an Ornstein-Zernike form [99, 100]

$$G(r) \sim r^{-p} e^{-r/\xi} \tag{3.4}$$

from which the correlation length ξ and the power-law exponent p are extracted.

In both the topological and trivial phases, the correlation length is in general very short, comparable with the lattice scale, no matter the large W that might be present. This is related to the fact that, in these regimes, the local Chern marker displays only weak fluctuations around its quantized value, namely around 1 in the topological phase and around 0 in the trivial phase. As the transition is approached, instead, $G(r)$ acquires longer tails and the correlation length increases dramatically. We note that the large values ($\xi \approx 30 - 50$) obtained very close to the transition may not provide fully reliable estimates, precisely because these lengths are comparable with the simulation cell ($L = 78$). To assess this finite-size effect, in the inset we show results up to $L = 114$ (corresponding to 25992 sites), for which the fitted ξ remains lower than half of the cell length. Moreover, close to the transition, the power-law exponent extracted from the fit is approximately $p \simeq 1/2$.

It is also worth mentioning that, while the local topological order parameter sharply distinguishes the two phases, its fluctuations and correlations display the same behavior on both sides of the transition and are characterized by the same exponent p and length ξ.

3.1.2 Topological Anderson insulator transitions

We now turn to the disorder-driven transition into the topological Anderson insulator (TAI) phase [56–58]. In this case, the pristine system is trivial but lies sufficiently close to the semimetallic point at the topological phase boundary. A moderate amount of disorder can then drive the trivial system into a topological phase, the TAI, while stronger disorder eventually destroys this phase and leads to a trivial Anderson insulator.

This behavior can be understood qualitatively in terms of a disorder-induced renormalization of the topological mass M_α defined in Eq. (1.78). Elastic scattering due to on-site Anderson disorder produces a self-energy correction to the clean Hamiltonian [57]. As pointed out in Ref. [101], this correction effectively shifts the topological mass by a negative contribution δM. The renormalized mass

$$\widetilde{M}_\alpha = M_\alpha + \delta M, \tag{3.5}$$

can therefore change sign even when the bare mass corresponds to a trivial phase. In the weak-disorder regime, this mechanism can be described within effective-medium theory, for instance using the self-consistent Born approximation [57, 101].

The destruction of the TAI at stronger disorder has a different origin and cannot be captured by the same weak-disorder effective-medium picture. Instead, it is associated with the crossing of a mobility edge and the onset of Anderson localization [57], similarly to the QAHI→trivial transition discussed above. Thus, the TAI phase is bounded by two distinct disorder-driven

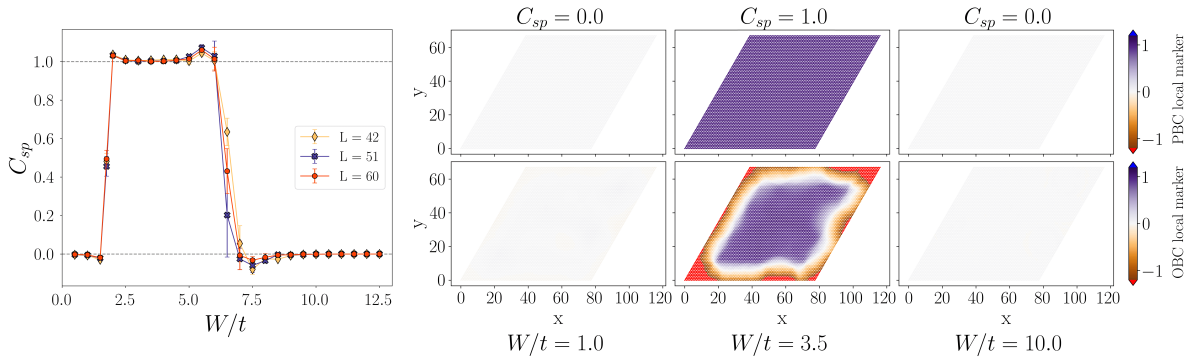


Figure 3.3: Trivial→TAI→trivial phase transitions driven by Anderson disorder in the Haldane model ($\Delta/t = 1.375$); the disorder-induced phase with $C_{sp} = 1.0$ is the topological Anderson insulator (TAI). Plots are arranged as in Figure 3.1. The local topology is homogeneous for all phases, independently of the disorder strength, except at the two phase transitions where the fluctuations become large, as signaled by the large variance of the single-point Chern numbers.

transitions: a weak-disorder transition from a trivial insulator to a topological phase, and a strong-disorder transition from the TAI to a trivial Anderson insulator.

In Figure 3.3, we show numerical results for this scenario in the Haldane model, starting from a pristine trivial system with $C = 0$ and $\Delta/t = 1.375$, while all other parameters are kept as above. The figure reports both the single-point Chern number C_{sp} and real-space maps of the local Chern marker in PBCs and OBCs, computed with $r_c = 10$. The single-point Chern number clearly displays the disorder-induced trivial→TAI transition, followed by the TAI→trivial transition at stronger disorder strength. The local Chern maps show that, once the marker is averaged over a length scale that is larger than the Chern-Chern correlation length, the local topology is homogeneous inside each phase. As in the direct QAHI→trivial transition discussed above, large fluctuations appear near both phase boundaries. These fluctuations are reflected in the increased variance of the single-point Chern number over disorder realizations and are associated with the growth of the correlation length.

3.1.3 Vacancy-driven transition

We now consider a different type of disorder, namely randomly distributed lattice vacancies. A density of vacancies is introduced in the Haldane model by randomly removing a fraction ρ_v of lattice sites. This perturbation is qualitatively different from a random on-site potential, but it still drives a disorder-induced topological phase transition once the vacancy concentration exceeds a critical value.

In Figure 3.4 we report numerical simulations for the the Haldane model as a function of

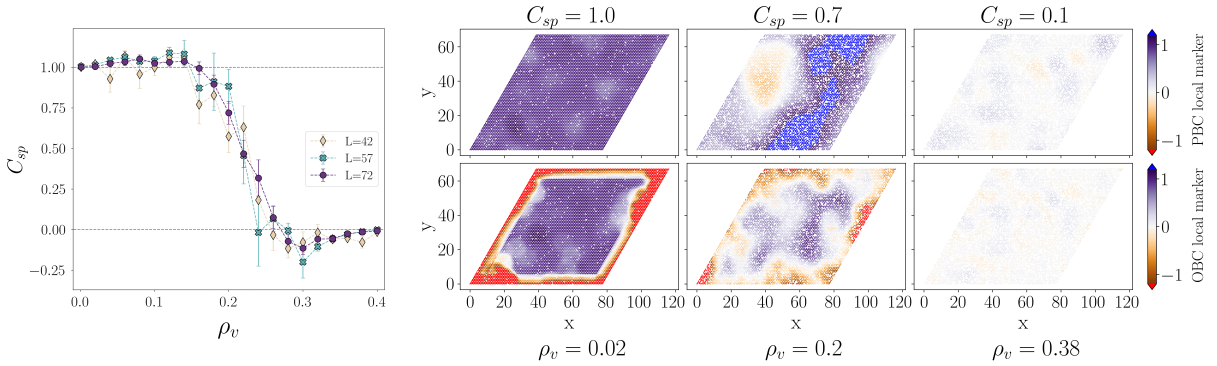


Figure 3.4: Topological phase transition in the Haldane model ($\Delta = 0$) driven by the presence of vacancies, with relative density ρ_v. Plots are arranged as in Figs. 3.1 and 3.3. The macroscopic average is performed within a radial cutoff $r_c = 6$ and yields a rather uniform topological landscape, except in the neighborhood of the phase transition where it becomes patchy and strongly affected by finite-size effects.

ρ_v. The pristine system is in the topological phase, with $\Delta = 0$ and $\phi = -\pi/8$. The left panel of Figure 3.4 reports the single-point Chern number for different lattice sizes, $L = 42$, 52, and 72. For small vacancy densities the system remains in the QAHI phase, whereas for large ρ_v it becomes trivial. The transition occurs at about 20% of removed sites.

The right panel shows PBC and OBC maps of the local Chern marker in three representative regimes: the topological phase with few vacancies at $\rho_v = 0.02$, the critical region $\rho_v = 0.2$, and the trivial phase at high vacancy density $\rho_v = 0.38$. The vacancy-driven transition displays the same qualitative phenomenology observed for Anderson disorder. Away from the transition, the local topology is spatially homogeneous after coarse graining. Near the critical vacancy density, instead, the local Chern marker develops large fluctuations and spatial patches, while finite-size and boundary effects become more pronounced.

3.2 Fluctuations and correlations in quantum spin Hall insulators

Although the previous section focused on Chern numbers and QAHIs, our framework can be extended to quantum spin Hall insulators (QSHIs), whose topology is described by a $\mathbb{Z}_2$ invariant protected by time-reversal symmetry.

In particular, we consider the Kane-Mele model [4, 5] on the honeycomb lattice, introduced in Section 1.4.1, in the presence of Anderson disorder as defined in Eq. (3.1). In the pristine case, the real nearest-neighbor hopping is set to $t = 1$. The intrinsic Kane-Mele spin-orbit coupling (SOC) is a complex next-nearest-neighbor hopping with a spin-dependent amplitude

$\lambda_{SO} = 0.05$, proportional to the Pauli matrix σ_z. The staggered on-site potential Δ is such that $\Delta/\lambda_{SOC} = 3$, while the Rashba SOC term, a complex nearest-neighbor hopping with off-diagonal spin components, is set to $\lambda_R/\lambda_{SOC} = 1$. For this set of parameters, the pristine system is in the topological QSHI phase.

We globally characterize the topology of the system via the single-point spin Chern number [8] given in Eq. (2.10). The corresponding single-point $\mathbb{Z}_2$ index, denoted by ν_{sp}, is obtained as the half-difference, modulo 2, of the spin Chern numbers associated with the two spin sectors. At the local level, we employ the local spin Chern marker [10] under periodic boundary conditions given by Eq. (2.37). The corresponding PBC local $\mathbb{Z}_2$ marker is given by

$$\nu(\mathbf{r}) = \frac{C_+(\mathbf{r}) - C_-(\mathbf{r})}{2} \mod 2. \tag{3.6}$$

The spin Chern numbers and markers used here follow Prodan's approach [31, 102], which relies on the spectral decomposition of spin operator projected onto the occupied states, namely PS_zP. This construction is well posed provided that this operator has a finite spectral gap around zero. This gap generally remains open even when S_z is not conserved, as occurs in the presence of Rashba spin-orbit coupling. However, the existence of a topological insulating phase does not, in general, guarantee that this projected-spin gap is finite. We therefore explicitly check that the gap of PS_zP does not close in any of the simulations discussed here. Additionally, the spin Chern marker is particularly convenient because it converges rapidly with system size and is numerically more practical than a local $\mathbb{Z}_2$ marker based solely on TR symmetry [10]. For these reasons, we use the single-point spin Chern number and the spin Chern marker to study disorder-driven phase transitions in the Kane-Mele model. Nevertheless, the conclusions drawn from the fluctuation and correlation analysis are more general and would equally hold for the TR-based $\mathbb{Z}_2$ markers, which may be useful in scenarios where the spin Chern marker is ill-defined.

The disordered KM model undergoes topological phase transitions which are analogous to those observed in the Haldane model, namely the disorder-driven transition from a QSHI to a trivial Anderson insulator as well as the emergence of a TAI [103]. In the following, however, we do not show the single-point topological $\mathbb{Z}_2$ invariant as a function of the Anderson disorder strength, an analysis that, however, can be found in Ref. [8]. Instead, in Figure 3.5, we show real-space maps for the local $\mathbb{Z}_2$ marker $\nu(\mathbf{r})$ in PBCs, computed for increasing cutoff radii (red circles) ranging from $r_c = 2$ to $r_c = 30$. We compare three representative regimes: the QSHI phase with $\nu_{sp} = 1.0$ at $W/t = 3$, the transition region with $\nu_{sp} = 0.5$ at $W/t = 4$, and the trivial phase with $\nu_{sp} = 0.0$ at $W/t = 6.8$. In constructing these maps, a macroscopic average is first taken over a cutoff radius r_c, followed by a modulo 2 operation applied to each marker on the map as dictated by the definition of the $\mathbb{Z}_2$ invariant in Eq. (3.6). Finally, the results are mapped into the range $[0, 1]$ to aid in visualization.

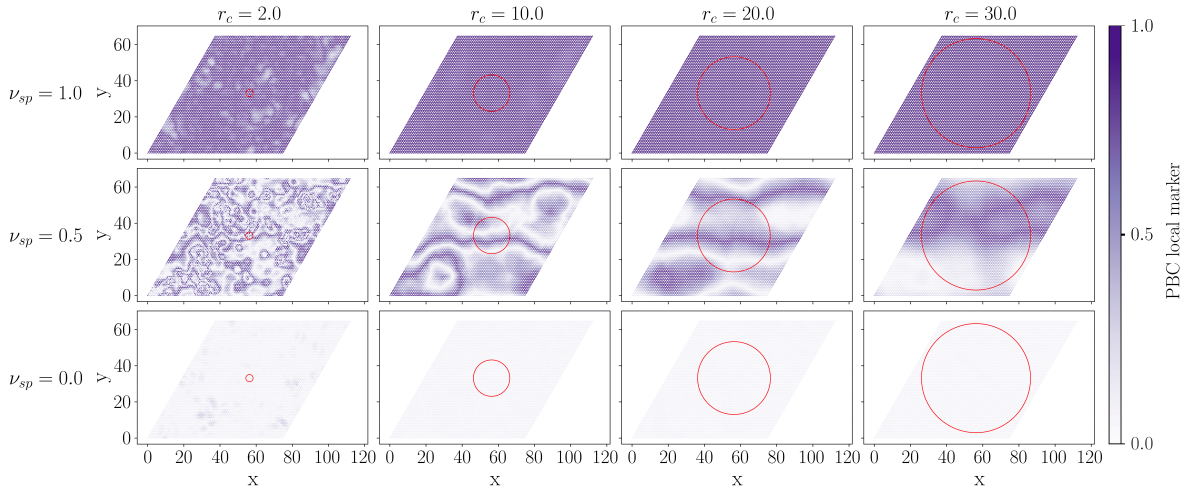


Figure 3.5: Macroscopic average of the local $\mathbb{Z}_2$ marker in QSHIs. Real-space maps for the spin Chern marker in PBC are shown for three different values of the disorder strength W/t that is added to the Kane-Mele model (linear size $L = 75$), corresponding to three different values of the single-point spin Chern number ($\nu_{sp} = 1.0$ for $W/t = 3$, $\nu_{sp} = 0.5$ for $W/t = 4$ and $\nu_{sp} = 0.0$ for $W/t = 6.8$). The maps are drawn for increasing values of the radial cutoff r_c within which the macroscopic average is performed. The cutoff r_c is marked by the radius of the red circle centered in the middle of the sample. Short-scale fluctuations of the topological marker average out in the topological and trivial phase, while large-scale fluctuations remain at the transition.

For small values of r_c, the local marker displays microscopic fluctuations, which are very strong close to the phase transition. By averaging over larger regions, essentially coarse graining the topological markers, short-scale fluctuations disappear both in the topological and trivial phase: already at $r_c = 10$ these disordered systems appear topologically uniform. On the contrary, sufficiently close to the phase transition we observe large-scale fluctuations that persist even if the macroscopic average is performed over rather large regions (e.g., $r_c = 30$).

The same machinery also allows one to define a spin Chern–spin Chern correlation function, in direct analogy with the Chern-Chern correlation function of Eq. (3.2). By fitting its behavior with the Ornstein-Zernike form in Eq. (3.4), one can extract both the correlation length ξ and the power-law exponent p associated with the critical decay. This provides a unified way to compare disorder-driven transitions in QAHIs and QSHIs, as we are going to discuss in the following section.

3.3 Critical exponents from topological correlation functions

The generality of our findings suggests that the power-law decay exponent p could serve as a critical exponent for disorder-driven topological phase transitions.

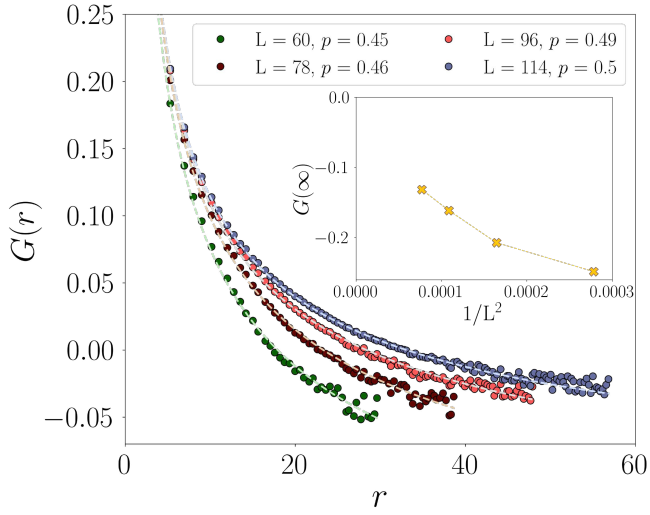


Figure 3.6: Correlation function $G(r)$ for different cell sizes L in the Haldane model ($\Delta/t = 1.25$, $\phi = -\frac{\pi}{2}$) at the disorder-driven transition with $W/t = 6.5$. Dashed lines are obtained by power-law fitting with Eq. 3.7, from which a critical exponent $p \simeq \frac{1}{2}$ is consistently obtained for all sizes. The fitting also yields $G(\infty)$, which is shown in the inset to vanish in the thermodynamic limit.

Before comparing the critical decay of topological correlation functions across different models and disorder-driven transitions, we comment on finite-size effects. These effects become particularly important close to criticality, where the correlation length can become comparable with the linear size of the simulation cell. As a consequence, the long-distance behavior of $G(r)$ may be affected even in large (but finite) supercells. This is illustrated in Figure 3.6 for the QAHI→trivial transition in the Haldane model, but the same behavior is also observed for the other transitions. At large distances, the correlation function may become slightly negative and approach a finite offset, denoted by $G(\infty)$. This behavior is a finite-size artifact caused by the very long correlation length near the transition, which induces spurious correlations between periodic images. In the thermodynamic limit, $G(\infty)$ vanishes and $G(r)$ becomes positive definite at all distances. To account for this effect, we fit the correlation function at criticality using

$$G(r) = G(\infty) + \frac{c}{r^p}, \tag{3.7}$$

where c, p, and $G(\infty)$ are fitting parameters. The inset of Figure 3.6 shows that $G(\infty)$ decreases with increasing system size, consistently with its interpretation as a finite-size offset. Moreover, the exponent extracted from the fit depends only weakly on system size and converges toward $p \simeq 1/2$ for the Haldane topological→trivial transition.

Having identified and accounted for this finite-size offset, we now compare the critical power-law decay of $G(r)$ for several disorder-driven transitions in the Haldane and Kane-Mele models.

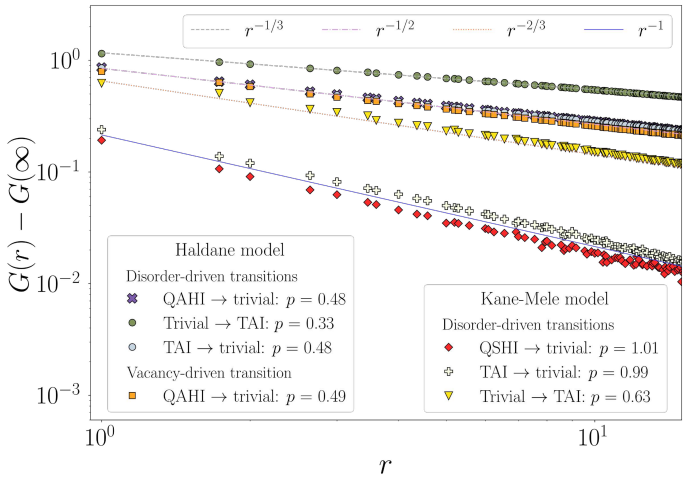


Figure 3.7: Power-law decay of the correlation function $G(r)$ for several disorder-driven topological phase transitions in the Haldane and Kane-Mele models. The dashed lines represent power laws r^{-p} for rational values of p. All topological→trivial transitions are characterized by exponents that do not depend on the type of disorder but only on the symmetry class: p is about 1/2 in QAHIs and 1 in QSHIs. The trivial→TAI transition is characterized by a different exponent, about 1/3 in QAHIs and 2/3 in QSHIs. The parameters of the Haldane model ($L = 96$, except for the case of vacancies where $L = 57$) are reported in the previous figures. Here we list the parameters of the Kane-Mele model ($L = 72$): the QSHI→trivial transition occurs at about $W/t = 4$ with $\Delta/\lambda_{SOC} = 3$; the trivial→TAI and the TAI→trivial occur respectively at about $W/t = 1.4$ and $W/t = 4$ with $\Delta/\lambda_{SOC} = 5.3$.

In Figure 3.7, we plot the shifted correlation function $G(r) - G(\infty)$, which removes the finite-size offset and makes the slopes in the log-log plot clearer. This allows us to determine whether different transitions share the same exponent p, extracted from the fit with Eq. (3.7).

Remarkably, all topological→trivial transitions are characterized by the same exponent p which does not depend on the type of disorder (namely, Anderson disorder or vacancies), but it depends on the symmetry class. In QAHIs, the topological→trivial transitions are characterized by $p \simeq 1/2$, whereas in QSHIs the corresponding exponent is $p \simeq 1$. Notably, the trivial→TAI transitions display a different exponent with respect to the topological→trivial cases: in QAHIs we find $p \simeq 1/3$, while in QSHIs $p \simeq 2/3$. Thus, the power-law decay of the topological correlation function provides a possible fingerprint for distinguishing disorder-induced TAI transitions from transitions out of a topological phase driven by Anderson localization. Interestingly, the ratio between the QSHI and QAHI exponents is approximately 2 for both classes of transitions.

Chapter 4

Towards realistic topological materials: monolayer jacutingaite with defects

The realization of robust topological phases in realistic materials has become one of the central directions in the field of topological matter. Beyond their fundamental scientific interest, topological insulators have been proposed as platforms for several technological applications. In particular, the helical edge states of a quantum spin Hall insulator (QSHI) provide spin-momentum-locked transport channels in which elastic backscattering is forbidden by time-reversal symmetry. This makes QSHIs promising candidates for low-dissipation electronics, spintronics, and topological quantum computing. For these purposes, however, a realistic QSHI must display a sufficiently large bulk gap, so as to ensure stability against temperature, disorder, and structural defects, while ideally allowing for external control of its topological phase.

Achieving sizable topological gaps in two-dimensional QSHIs has motivated the exploration of materials beyond graphene, for which the Kane–Mele (KM) model was originally intended, but where the intrinsic spin-orbit coupling (SOC) of carbon is too weak to produce an experimentally robust gap. In this respect, buckled honeycomb systems, generally referred to as Xenes [33, 34], have attracted considerable attention, since the presence of heavier elements can enhance SOC. A paradigmatic example is germanene, which has been shown to host a QSHI state with a gap large enough to support topological properties up to room temperature [104, 105]. Moreover, in some of these systems, the topological phase can be controlled by an external electric field [104–106].

Within this search for large-gap, stable, and possibly electrically tunable QSHIs, monolayer of jacutingaite (Pt_2HgSe_3) has emerged as a particularly promising candidate [13]. First-principles

calculations have shown that its low-energy electronic structure closely resembles the KM model, while the presence of heavy elements such as Hg and Pt gives rise to a sizable topological gap. The same study also highlighted the competing roles of SOC and crystal-symmetry breaking in determining the structural stability of the monolayer, and showed that the topological phase can be switched by applying moderate and realistic electric fields. However, the low formation energy of Hg vacancies suggests that real samples of monolayer jacutingaite may be prone to vacancy disorder. At the same time, owing to the intrinsic robustness of topological phases, a moderate concentration of such defects is not expected to immediately destroy the QSHI state.

This chapter is devoted to the study of vacancy-induced effects in the monolayer of jacutingaite. We first introduce the theoretical and computational tools required to describe realistic materials starting from first-principles calculations. After this methodological introduction, we present original results on the effect of Hg vacancies. We begin with an *ab initio* characterization of an isolated Hg vacancy, focusing on the defect states appearing inside the bulk gap. We then move to an effective-Hamiltonian description based on Wannier models derived from first-principles calculations, which allows us to access larger supercells and finite concentrations of randomly distributed vacancies. By applying some of the topological diagnostics for disordered systems introduced in Chapter 2, we investigate the robustness of the QSHI phase and estimate the critical concentration of Hg vacancies at which the topological phase is eventually lost.

4.1 First-principles electronic structure calculations

In the previous chapters, we have seen how tight-binding models provide a controlled framework to investigate the effects of disorder in electronic systems. In particular, the use of large supercells makes it possible to introduce disorder either through random spatial modulations of local potentials and hopping amplitudes, or by explicitly removing, substituting, or modifying selected lattice sites. This approach is especially useful because it allows one to access large system sizes and to study disorder-induced effects in a systematic way.

When the goal is to describe realistic materials, however, the effective tight-binding model must be closely connected to the underlying electronic structure of the system. This requires, on the one hand, determining Hamiltonian parameters that faithfully reproduce the relevant bands of the material. On the other hand, it is necessary to verify that the phenomenology obtained from the disordered tight-binding model is consistent with the actual response of the material when defects or disorder are introduced explicitly at the atomic scale.

Both aspects can be addressed by means of first-principles, or *ab initio*, methods which allow one to compute the electronic band structure directly from the atomic structure and chemical composition of a material. In the following, we briefly outline how the electronic structure of

realistic materials is computed from first principles within the framework of density-functional theory. We then discuss how these calculations can provide a microscopic starting point for the construction of effective tight-binding models, for instance through the Wannierization procedure. The resulting Wannier Hamiltonians reproduce the relevant low-energy bands and provide material-specific hopping amplitudes and on-site energies. Finally, we review a band-unfolding procedure that can be applied to both first-principles and tight-binding supercell calculations. This method makes it possible to compare the electronic band structure of a disordered system with that of the corresponding crystalline reference system in the primitive Brillouin zone, thereby identifying how disorder modifies the electronic structure of the pristine material.

4.1.1 Density-functional theory

As discussed in Section 1.1, within the Born–Oppenheimer and frozen nuclei approximations, the many-body Hamiltonian of interacting electrons and nuclei can be reduced to an electronic Hamiltonian for a fixed nuclear configuration

$$\mathcal{H}_{\mathrm{el}} = \sum_{i=1}^{N_e} \left[\frac{\mathbf{p}_i^2}{2m_e} + V_{\mathrm{ext}}(\mathbf{r}_i) \right] + \frac{1}{2} \sum_{i \neq j} \frac{e^2}{|\mathbf{r}_i - \mathbf{r}_j|}. \tag{4.1}$$

This problem still contains the full electron-electron interaction and remains exponentially complex in the number of electrons.

Density-functional theory (DFT) provides a practical reformulation of this problem by changing the basic variable used to describe the ground state. Instead of attempting to determine the many-body wavefunction $\Psi(\mathbf{r}_1, \ldots, \mathbf{r}_{N_e})$, which depends on $3N_e$ spatial coordinates, DFT reformulates the problem in terms of the electronic density

$$n(\mathbf{r}) = N_e \int |\Psi(\mathbf{r}, \mathbf{r}_2, \ldots, \mathbf{r}_{N_e})|^2 \, d\mathbf{r}_2 \ldots d\mathbf{r}_{N_e}. \tag{4.2}$$

The density contains much less information than the full wavefunction, as it depends only on the three spatial coordinates of $\mathbf{r}$. Nevertheless, it is sufficient, in principle, to determine the ground-state properties of the system.

Indeed, the formal basis of DFT is provided by the Hohenberg–Kohn (HK) theorems [107], which establish that, for a given external potential $V_{\mathrm{ext}}(\mathbf{r})$, the ground-state energy is a functional $E[n]$ of the electronic density $n(\mathbf{r})$ and that the exact ground-state density minimizes this functional. The interacting many-body problem can therefore be recast, in principle exactly, as a variational minimization over the density rather than over the full many-body wavefunction.

The HK theorems, however, do not provide a practical prescription for constructing the exact energy functional $E[n]$. A computationally useful formulation was introduced by Kohn

and Sham [108], whose idea was that of finding an auxiliary non-interacting system constrained to reproduce the same ground-state density as the original interacting problem. Within this Kohn–Sham (KS) framework, the energy functional is written as

$$E[n] = T[n] + \int d\mathbf{r}\, V_{\text{ext}}(\mathbf{r}) n(\mathbf{r}) + E_{\text{H}}[n] + E_{\text{XC}}[n], \tag{4.3}$$

where $T[n]$ is the kinetic energy functional, $V_{\text{ext}}(\mathbf{r})$ is the external potential generated by the nuclei and

$$E_{\text{H}}[n] = \frac{e^2}{2} \int d\mathbf{r} \int d\mathbf{r}' \frac{n(\mathbf{r}) n(\mathbf{r}')}{|\mathbf{r} - \mathbf{r}'|} \tag{4.4}$$

is the Hartree energy describing the classical electrostatic repulsion of a continuous electron density $n(\mathbf{r})$. The remaining term $E_{\text{XC}}[n]$ is the exchange-correlation functional, which contains all many-body effects beyond the classical Hartree contribution.

By minimizing the energy functional with respect to the density $n(\mathbf{r})$, one obtains the Kohn–Sham equations

$$\left[-\frac{\nabla^2}{2m_e} + V_{\text{KS}}(\mathbf{r}) \right] \psi_i(\mathbf{r}) = \varepsilon_i \psi_i(\mathbf{r}), \tag{4.5}$$

where the effective potential $V_{\text{KS}}(\mathbf{r}) \equiv V_{\text{KS}}[n(\mathbf{r})]$ is a functional of the electronic density and can be decomposed as

$$V_{\text{KS}}(\mathbf{r}) = V_{\text{ext}}(\mathbf{r}) + V_{\text{H}}(\mathbf{r}) + V_{\text{XC}}(\mathbf{r}). \tag{4.6}$$

The Hartree potential is obtained as the functional derivative of the Hartree energy

$$V_{\text{H}}(\mathbf{r}) = \frac{\delta E_{\text{H}}[n]}{\delta n(\mathbf{r})} = e^2 \int d\mathbf{r}' \frac{n(\mathbf{r}')}{|\mathbf{r} - \mathbf{r}'|}, \tag{4.7}$$

and the exchange-correlation potential is defined as

$$V_{\text{XC}}(\mathbf{r}) = \frac{\delta E_{\text{XC}}[n]}{\delta n(\mathbf{r})}. \tag{4.8}$$

The KS formalism thus replaces the original interacting many-body problem in Eq. (4.1) with the auxiliary non-interacting problem for the Hamiltonian in Eq. (4.5), which we denote by H_{KS}. The corresponding occupied orbitals define the ground-state density

$$n(\mathbf{r}) = \sum_{i \in \text{occ}} |\psi_i(\mathbf{r})|^2, \tag{4.9}$$

which, by construction, coincides with the electronic density of the original interacting system. The density obtained from the KS orbitals can be inserted back into the Kohn–Sham potential $V_{\text{KS}}[n(\mathbf{r})]$ and the equations are solved self-consistently by iterating this procedure until the input and output densities agree within a chosen tolerance.

As already mentioned, non-trivial topology is often driven by the presence of spin-orbit coupling. In particular, SOC effects are enhanced in materials containing heavy atomic elements, where the large nuclear charge produces strong electric fields close to the atomic cores, significantly influencing the electronic motion. Within DFT framework, SOC can be included in a spin-dependent Kohn–Sham description, where the single-particle orbitals become spinors and the Hamiltonian H_{KS} can be schematically written as

$$\left[-\frac{\nabla^2}{2m} + V_{\text{ext}} + V_{\text{H}} + V_{\text{XC}} + \mathbf{W}_{\text{XC}} \cdot \boldsymbol{\sigma} + V_{\text{SOC}}\right] \begin{pmatrix} \psi_i^{\uparrow} \\ \psi_i^{\downarrow} \end{pmatrix} = \varepsilon_i \begin{pmatrix} \psi_i^{\uparrow} \\ \psi_i^{\downarrow} \end{pmatrix}. \tag{4.10}$$

Here V_{XC} and $\mathbf{W}_{\text{XC}}$ denote the scalar and spin-dependent parts of the exchange-correlation potential, respectively, while V_{SOC} takes the form introduced in Eq. (1.10)

$$V_{SOC} = \frac{\hbar}{4m_e^2c^2}\boldsymbol{\sigma} \cdot \nabla V(\mathbf{r}) \times \mathbf{p}, \tag{4.11}$$

where $V(\mathbf{r}) = -e\phi(\mathbf{r})$ is the electrostatic potential experienced by an electron.

Then, since the Kohn–Sham problem is an effective single-particle problem, the concepts introduced in Section 1.1 can be applied. In particular, for a crystalline system the KS potential has the periodicity of the lattice, and the solutions can be classified according to Bloch's theorem by wavevectors $\mathbf{k}$ belonging to the Brillouin zone. The corresponding Kohn–Sham eigenvalues $\varepsilon_{n\mathbf{k}}$ are therefore commonly represented as an *ab initio* electronic band structure. These eigenvalues provide a highly useful description of the electronic structure and are widely used to analyze band gaps, band inversions, and the effect of spin-orbit coupling in realistic materials. However, they do not rigorously correspond to the exact excitation energies of the original many-body system. Indeed, DFT is formulated to describe the ground-state density of the neutral system, whereas electron addition or removal involves charged excitations and the associated redistribution and screening of the electronic density. As a consequence, standard DFT approximations often underestimate band gaps. A more accurate description of quasiparticle energies can be obtained within many-body perturbation theory, for instance through the G_0W_0 approximation [109, 110], where one starts from a reference DFT calculation and computes corrections to the Kohn–Sham eigenvalues by including the many-body self-energy associated with the screened Coulomb interaction.

Numerical implementation of DFT: exchange-correlation functionals, plane waves and pseudopotentials

The KS formulation is formally exact, but the correct exchange-correlation functional $E_{\text{XC}}[n]$ is unknown and must be approximated in practical calculations. A common choice is the local-density approximation (LDA), in which the exchange-correlation energy depends only on the

local value of the density

$$E_{\mathrm{XC}}^{\mathrm{LDA}}[n] = \int n(\mathbf{r})\epsilon_{\mathrm{XC}}\big(n(\mathbf{r})\big)d\mathbf{r}. \tag{4.12}$$

where $\epsilon_{\mathrm{XC}}(n)$ is the exchange-correlation energy per electron of a homogeneous electron gas with density n. A more flexible class of approximations is provided by generalized-gradient approximations (GGA), where the functional also depends on gradients of the density. A widely used example is the Perdew–Burke–Ernzerhof (PBE) functional [111].

In order to solve the Kohn–Sham equations numerically, the single-particle orbitals $\psi_{n\mathbf{k}}(\mathbf{r})$ must be expanded in a suitable basis. In our DFT calculations, we employ a plane-wave basis, which is particularly convenient for periodic systems, as implemented in the `Quantum ESPRESSO` code [112–114]. In practice, this basis is truncated by introducing a kinetic-energy cutoff, meaning that only plane waves with kinetic energy below a chosen threshold are retained in the expansion. Moreover, the use of periodic boundary conditions in DFT calculations naturally leads to a reciprocal-space description. Physical quantities are then evaluated through integrals over the Brillouin zone, which are approximated in practice by sums over a finite grid of $\mathbf{k}$ points. The density of this grid and the kinetic-energy cutoff are two key convergence parameters. They must be properly chosen to ensure that quantities such as total energies, band gaps, and band dispersions are stable within the desired numerical accuracy.

A direct description of all electrons in a material, however, would be very demanding in a plane-wave basis. Near the nuclei, the potential varies rapidly and the wavefunctions of core electrons display strong spatial oscillations. Accurately representing these features would require a very large number of plane waves and, therefore, a very large cutoff energy. This difficulty is overcome through the pseudopotential approximation, in which only valence electrons are treated explicitly, while the nuclei together with the core electrons are replaced by an effective ionic potential. These pseudopotentials reproduce the interaction felt by the valence electrons outside the core region, while leading to smooth pseudo-wavefunctions inside it. As a result, both the number of explicitly treated electrons and the number of plane waves needed in the calculation are greatly reduced, making plane-wave DFT calculations computationally feasible. In norm-conserving pseudopotentials [115], the pseudo-wavefunctions are constructed so that, outside a chosen core radius, they reproduce the corresponding "all-electron" wavefunctions, while preserving the same norm inside the core region.

4.1.2 Wannier interpolation and *ab initio* tight-binding models

While DFT provides a microscopic description of the electronic structure starting from the fundamental physical properties and atomic composition of a material, the construction of reliable effective models that capture the relevant low-energy physics remains of great importance. This

is especially useful when one needs to evaluate electronic properties on very dense Brillouin-zone meshes or to build large supercells, which would be computationally demanding at the full DFT level.

As discussed in Section 1.1.2, Wannier functions provide a natural localized basis for constructing tight-binding Hamiltonians. Here we discuss how they can be obtained from first-principles calculations, leading to *ab initio* tight-binding models that retain the accuracy of DFT within a compact real-space representation.

Starting from a Bloch eigenstate $|\psi_{n\mathbf{k}}\rangle$ solving the KS equations, the Wannier function $|w_{n\mathbf{R}}\rangle$ associated with the lattice vector $\mathbf{R}$ can be constructed through the Fourier transformation introduced in Eq. (1.26). However, each Bloch state is defined only up to a $\mathbf{k}$-dependent phase factor $e^{i\varphi_n(\mathbf{k})}$. Different choices of this phase correspond to different gauges and lead to Wannier functions with different degrees of localization.

More generally, for a set of J bands coming from the DFT calculation, that may be connected among themselves by degeneracies but that are separated from all lower and higher bands, the Wannier functions are defined as [16]

$$|w_{n\mathbf{R}}\rangle = \frac{1}{N_{\mathbf{k}}} \sum_{\mathbf{k}} e^{-i\mathbf{k}\cdot\mathbf{R}} \, |\psi^W_{n\mathbf{k}}\rangle \tag{4.13}$$

where the Bloch-like state $|\psi^W_{n\mathbf{k}}\rangle$ are obtained by mixing the original Bloch eigenstates within the chosen subspace

$$|\psi^W_{n\mathbf{k}}\rangle = \sum_{m=1}^{J} U^{(\mathbf{k})}_{mn} \, |\psi_{m\mathbf{k}}\rangle \qquad \text{for} \quad n = 1, \ldots, J. \tag{4.14}$$

Here, $U^{(\mathbf{k})}$ is a $J \times J$ unitary matrix generalizing the notion of gauge transformation to the multiband case: at each $\mathbf{k}$ point the Bloch states can be mixed without changing the physical subspace they span. The superscript W for the Bloch-like state denotes the Wannier gauge, in contrast to the Hamiltonian gauge in which the Kohn–Sham effective Hamiltonian is diagonal and the states are the original eigenstates $|\psi_{m\mathbf{k}}\rangle$. Different choices of $U^{(\mathbf{k})}$ therefore define different Wannier gauges and, consequently, different real-space Wannier functions.

The aim of the maximally-localized Wannier function (MLWF) construction is to exploit this gauge freedom to obtain orbitals that are as localized as possible in real space. In the Marzari–Vanderbilt (MV) approach [16, 116] the matrices $U^{(\mathbf{k})}$ are chosen by minimizing the total quadratic spread

$$\Omega = \sum_{n} \left[\langle w_{n\mathbf{0}} | r^2 | w_{n\mathbf{0}} \rangle - |\langle w_{n\mathbf{0}} | \mathbf{r} | w_{n\mathbf{0}} \rangle|^2 \right]. \tag{4.15}$$

The resulting MLWFs are centered around well-defined positions and often resemble atomic-like orbitals. Their localization makes them particularly suitable for constructing real-space tight-binding Hamiltonians, whose matrix elements decay rapidly with distance.

The construction described above applies directly to isolated groups of bands, such as the fully occupied bands of an insulator. However, in many situations the bands of interest are not separated from the rest of the spectrum. This occurs, for instance, for metallic systems, low-lying conduction bands, or whenever one wants to describe simultaneously valence and conduction bands in a certain energy window. In these cases, the J target bands are said to be entangled with the others.

To treat entangled bands, one first defines an "outer energy window" [117]. At each $\mathbf{k}$-point, this energy window contains $\mathcal{J}_{\mathbf{k}}$ Bloch eigenstates, with $\mathcal{J}_{\mathbf{k}} \geq J$. From these states, an orthonormal set of J Bloch states is obtained at each $\mathbf{k}$-point by constructing

$$|\tilde{\psi}_{n\mathbf{k}}\rangle = \sum_{m=1}^{\mathcal{J}_{\mathbf{k}}} \tilde{V}_{mn}^{(\mathbf{k})} |\psi_{m\mathbf{k}}\rangle \qquad \text{for} \quad n = 1, \ldots, J \tag{4.16}$$

where $\tilde{V}^{(\mathbf{k})}$ is a $\mathcal{J}_{\mathbf{k}} \times J$ semi-unitary matrix satisfying $\tilde{V}^{(\mathbf{k})\dagger}\tilde{V}^{(\mathbf{k})} = \mathbb{1}_{J\times J}$. This disentanglement step selects the optimal J-dimensional subspace of states within the outer energy window at each $\mathbf{k}$. After this, the MV procedure can be applied by minimizing the total quadratic spread of the Wannier functions given by Eq. (4.13). In this case the Wannier-gauge states are

$$|\psi_{n\mathbf{k}}^{W}\rangle = \sum_{j=1}^{\mathcal{J}_{\mathbf{k}}} V_{jn}^{(\mathbf{k})} |\psi_{j\mathbf{k}}\rangle \,, \tag{4.17}$$

where $V^{(\mathbf{k})} = \tilde{V}^{(\mathbf{k})}U^{(\mathbf{k})}$ is the $\mathcal{J}_{\mathbf{k}} \times J$ matrix encoding both disentanglement step, which selects the optimal subspace, and the localization step, which fixes the gauge within that subspace[8].

Once the matrices $V^{(\mathbf{k})} = \tilde{V}^{(\mathbf{k})}U^{(\mathbf{k})}$ have been obtained $\big($for an isolated group of bands they reduce to $V^{(\mathbf{k})} = U^{(\mathbf{k})}\big)$, the Kohn–Sham Hamiltonian H_{KS} can be expressed in the basis of Wannier-gauge Bloch states. We first denote by H the Hamiltonian gauge, in which the Bloch states $|\psi_{n\mathbf{k}}\rangle$ diagonalize the KS Hamiltonian

$$\big(H_{KS}^{H}\big)_{mn}(\mathbf{k}) = \varepsilon_{n\mathbf{k}}\delta_{mn}. \tag{4.18}$$

The Hamiltonian in the Wannier gauge is then obtained as

$$H_{KS}^{W}(\mathbf{k}) = V^{(\mathbf{k})\dagger}\, H_{KS}^{H}(\mathbf{k})\, V^{(\mathbf{k})}. \tag{4.19}$$

[8] In some situations, one wants to construct Wannier functions that exactly reproduce the original *ab initio* bands within a limited energy range, for example around the Fermi level when studying transport properties, while remaining as localized as possible. However, in the disentanglement procedure the Kohn–Sham eigenstates within the outer energy window are mixed, so the selected subspace does not necessarily preserve the original bands exactly throughout the window. This issue can be addressed by introducing a second energy window, called the "inner" or "frozen" window, contained within the outer window. The spread minimization is then performed under the constraint that the KS states lying inside the frozen window are retained exactly in the selected subspace [117].

By Fourier transforming $H^W_{KS}(\mathbf{k})$ one obtains the real-space matrix elements

$$H_{mn}(\mathbf{R}) = \frac{1}{N_{\mathbf{k}}} \sum_{\mathbf{k}} e^{-i\mathbf{k}\cdot\mathbf{R}} \big(H^W_{KS}\big)_{mn}(\mathbf{k}) \tag{4.20}$$

which can be easily identified with the KS Hamiltonian matrix elements between MLWFs

$$H_{mn}(\mathbf{R}) = \langle w_{m\mathbf{0}} | H_{KS} | w_{n\mathbf{R}} \rangle. \tag{4.21}$$

The set of matrix elements $H_{mn}(\mathbf{R})$ defines the *ab initio* Wannier Hamiltonian, namely a tight-binding Hamiltonian in which the on-site energies and hopping amplitudes are computed directly from the first-principles Kohn–Sham Hamiltonian through projection onto the Wannier basis, instead of being treated as empirical parameters. Since MLWFs are localized in real space, these matrix elements typically decay rapidly with $|\mathbf{R}|$, making it possible to truncate the Hamiltonian to a finite range of hoppings while preserving the relevant DFT bands with high accuracy.

Wannier interpolation is then performed by transforming the real-space Hamiltonian $H_{mn}(\mathbf{R})$ back to momentum space. However, owing to the finite *ab initio* $\mathbf{k}$-mesh, the Wannier functions are artificially periodic over the Born–von Karman supercell associated with this mesh. As a consequence, the hopping matrix elements inherit the same periodicity

$$H_{mn}(\mathbf{R} + \mathbf{T}) = H_{mn}(\mathbf{R}), \tag{4.22}$$

for any supercell lattice vector $\mathbf{T}$. To minimize spurious effects due to this artificial periodicity, one should choose, for each hopping, the shortest vector connecting the Wannier center $\mathbf{r}_m$ of orbital m in the home cell $\mathbf{0}$ to the Wannier center $\mathbf{R} + \mathbf{r}_n$ of orbital n in the cell at $\mathbf{R}$. In practice, this amounts to considering the displacement vector

$$\mathbf{R} + \mathbf{T} + \mathbf{r}_n - \mathbf{r}_m \tag{4.23}$$

that lie inside the Wigner–Seitz (WS) supercell centered at the Wannier center $\mathbf{r}_m$ [118]. If the displacement vector lies on the boundary of the Wigner–Seitz supercell, then all equivalent vectors lying on the other boundaries of the WS supercell are retained with equal weight, in order to avoid artificial symmetry breaking.

The interpolated Hamiltonian at an arbitrary momentum $\mathbf{q}$ is then written as

$$H_{mn}(\mathbf{q}) = \sum_{\mathbf{R}\in \mathrm{WS}} \frac{1}{N_{\mathbf{R},mn}} \sum_{l=1}^{N_{\mathbf{R},mn}} e^{i\mathbf{q}\cdot\left(\mathbf{R}+\mathbf{T}^l_{\mathbf{R},mn}\right)} H_{mn}(\mathbf{R}), \tag{4.24}$$

where $\mathbf{T}^l_{\mathbf{R},mn}$ are the supercell lattice vectors for which the displacement vectors in Eq. (4.23) are the shortest vectors connecting the two Wannier centers. The integer $N_{\mathbf{R},mn}$ counts how

many such equivalent vectors exist. For hoppings strictly inside the Wigner–Seitz supercell one has $N_{\mathbf{R},mn} = 1$, while $N_{\mathbf{R},mn} > 1$ for vectors lying on the boundary.

Finally, diagonalizing $H_{mn}(\mathbf{q})$ gives the Wannier-interpolated band energies at any desired momentum point. By construction, they reproduce the original *ab initio* band structure at the $\mathbf{k}$-points of the original DFT mesh[9]. At intermediate $\mathbf{q}$-points, the accuracy of the interpolation depends on the density of the original mesh and on the localization of the Wannier functions.

In our practical implementation, starting from a DFT calculation performed with `Quantum ESPRESSO` [113], the information required for the "Wannierization" procedure, such as the Kohn–Sham eigenvalues and the overlaps between Bloch states, is passed to the `Wannier90` [118] code through the `PW2Wannier90` interface. The `Wannier90` code constructs the MLWFs and returns the corresponding real-space Wannier Hamiltonian.

4.1.3 Bands unfolding

In the previous sections, we introduced two complementary descriptions of electronic band structures. Within the DFT framework, the Kohn–Sham equations are solved for a periodic system, providing eigenstates that are labeled by a Bloch momentum $\mathbf{k}$ and may be expanded, for instance, in a plane-wave basis. The corresponding eigenvalues define the electronic band structure. In the Wannier representation, the same *ab initio* electronic structure is recast into a localized basis, yielding tight-binding Hamiltonians that efficiently interpolate the *ab initio* bands throughout the Brillouin zone. In both descriptions, as long as the system is described by the primitive periodicity of the underlying crystal, the calculation and interpretation of the band structure are straightforward.

The situation becomes less direct when supercells are introduced, as is often necessary to describe realistic non-crystalline systems. In DFT calculations, the disordered system is usually treated as a large supercell that is periodically repeated in space. Similarly, in a Wannier-based tight-binding description, one can construct a real-space supercell Hamiltonian and modify it to include the desired defect or disorder pattern.

The price to pay is that, since the supercell Brillouin zone is smaller than the primitive-cell one, the electronic bands are folded into this reduced Brillouin zone, producing a denser spectrum with many more bands. As a result, comparison with the pristine crystal, described by the primitive periodicity, becomes less transparent: in the supercell band structure defined in the reduced Brillouin zone it is difficult to identify which features are inherited from the original bands and which ones are induced by defects or disorder.

Band unfolding provides a way to represent the supercell spectrum in the Brillouin zone of the primitive cell. The eigenvalues obtained from the supercell calculation are mapped onto an

[9] In the presence of disentanglement, this exact agreement is guaranteed only within the frozen energy window.

effective band structure [119, 120], where each supercell eigenstate is assigned a spectral weight according to the amount of primitive-cell Bloch character it retains. This provides a common framework to compare pristine and disordered systems, both in first-principles calculations and in Wannier-based tight-binding models.

Let $\mathbf{k}$ be the wavevector in the primitive-cell Brillouin zone and $\mathbf{K}$ a wavevector in the supercell Brillouin zone. Since the supercell Brillouin zone is smaller, several primitive-cell momenta might be folded onto the same supercell momentum. A primitive-cell momentum $\mathbf{k}$ is said to fold onto $\mathbf{K}$ if there exists a reciprocal lattice vector $\mathbf{G}$ such that

$$\mathbf{K} = \mathbf{k} - \mathbf{G}. \tag{4.25}$$

Conversely, a given supercell momentum $\mathbf{K}$ corresponds to a set of primitive-cell momenta

$$\mathbf{k}_i = \mathbf{K} + \mathbf{G}_i, \qquad i = 1, \ldots, N_{\mathbf{K}}. \tag{4.26}$$

The main observation is in fact that the vectors $\mathbf{K}$ and $\mathbf{G}$ are unique for a given $\mathbf{k}$, while a given $\mathbf{K}$ can be obtained from a number $N_{\mathbf{K}}$ of different pairs $(\mathbf{k}_i, \mathbf{G}_i)$. This leads to the property that any supercell eigenstate $|\psi_{m\mathbf{K}}\rangle$ can be expressed as a combination of primitive-cell eigenstates $|\psi_{n\mathbf{k}_i}\rangle$

$$|\psi_{m\mathbf{K}}\rangle = \sum_{i=1}^{N_{\mathbf{K}}} \sum_{n} F(\mathbf{k}_i, n; \mathbf{K}, m) |\psi_{n\mathbf{k}_i}\rangle. \tag{4.27}$$

The central idea of unfolding is to quantify how much primitive-cell Bloch character at momentum $\mathbf{k}_i$ is contained in a given supercell eigenstate $|\psi_{m\mathbf{K}}\rangle$. This is achieved by projecting $|\psi_{m\mathbf{K}}\rangle$ onto the subspace spanned by the primitive-cell Bloch states $|\psi_{n\mathbf{k}_i}\rangle$

$$P_{m\mathbf{K}}(\mathbf{k}_i) = \sum_{n} \left| \langle \psi_{n\mathbf{k}_i} | \psi_{m\mathbf{K}} \rangle \right|^2 . \tag{4.28}$$

The quantity $P_{m\mathbf{K}}(\mathbf{k}_i)$ is therefore the spectral weight of the supercell state $|\psi_{m\mathbf{K}}\rangle$ at the primitive-cell momentum $\mathbf{k}_i$ and measures the contribution of states with Bloch character $\mathbf{k}_i$ to the supercell eigenstate. From these spectral weights one can construct a spectral function of the continuous variable E as

$$A(\mathbf{k}_i, E) = \sum_{m,\mathbf{K}} P_{m\mathbf{K}}(\mathbf{k}_i)\, \delta\big(E - E_m(\mathbf{K})\big), \tag{4.29}$$

where $E_m(\mathbf{K})$ are the supercell eigenvalues. This spectral function, possibly averaged over different disorder realizations, defines the effective band structure in the primitive-cell Brillouin zone.

In the following, the spectral function associated with supercell band structures obtained from DFT calculations is obtained by using the plane-wave bands unfolding technique [120], including

SOC, as implemented in the `bands_unfold.x` code of the `EPW/ZG` module [121] of `Quantum ESPRESSO`. For supercell band structures obtained from tight-binding models, the unfolding is instead performed using the `WannierTools` package [122].

4.2 Hg vacancies in a monolayer of jacutingaite

Jacutingaite (Pt_2HgSe_3) is a naturally occurring layered mineral, first discovered in 2008 [123] and later synthesized artificially [124]. In recent years, it has attracted considerable attention because of its rich topological character. In its bulk form, jacutingaite is an example of a dual topological material, in which a three-dimensional weak topological character coexists with crystalline topological properties signaled by a non-trivial mirror Chern number. This dual topology can be understood in terms of a Kane–Mele model extended to include out-of-plane interlayer couplings [125]. When reduced to a single layer, jacutingaite exhibits an even closer connection with Kane–Mele physics. Although it is a ternary compound and differs in several respects from Xenes, its mercury Hg atoms form the characteristic buckled honeycomb structure of these systems.

In 2018, extensive first-principles calculations predicted that monolayer jacutingaite is a QSHI with a sizable band gap, estimated from many-body G_0W_0 calculations to be approximately 0.5 eV [13]. The low-energy physics around the Fermi level of the pristine monolayer is accurately described by an *ab initio* tight-binding Hamiltonian written in the basis of 4 maximally localized Wannier functions. These functions are constructed from the highest occupied and lowest unoccupied bands obtained from DFT calculations, as discussed in Section 4.1.2. The resulting MLWFs display mainly the character of Hg s-orbital, hybridized with the d orbitals of the three nearest-neighbor Pt atoms. Notably, the MLWFs are centered on the Hg atoms and therefore inherit their buckled honeycomb arrangement.

The full Wannier Hamiltonian accurately reproduces the highest occupied valence band and lowest unoccupied conduction band, as shown in the left panel of Figure 4.1. Moreover, retaining hopping terms up to second-nearest neighbors in the Wannier Hamiltonian is already sufficient to capture the qualitative low-energy physics. This truncation leads to a generalized Kane–Mele model of the form [13]

$$H = t \sum_{\langle ij\rangle\alpha} c^\dagger_{i\alpha} c_{j\alpha} + it_2 \sum_{\langle\langle ij\rangle\rangle\alpha\beta} \nu_{ij}\, c^\dagger_{i\alpha} \sigma^z_{\alpha\beta} c_{j\beta} + t_2' \sum_{\langle\langle ij\rangle\rangle\alpha} c^\dagger_{i\alpha} c_{j\alpha} + it_2'' \sum_{\langle\langle ij\rangle\rangle\alpha\beta} u_{ij} (\mathbf{s}\times\mathbf{d}_{ij})^z_{\alpha\beta} c^\dagger_{i\alpha} c_{j\beta}. \tag{4.30}$$

Here t, t_2, t_2' and t_2'' are the hopping amplitudes up to second-nearest neighbors. The factor $\nu_{ij} = \pm 1$ depends on the orientation of the two bonds connecting second-neighbor sites, $u_{ij} = \pm 1$ distinguishes the two inequivalent sites of the bucked honeycomb lattice, and $\mathbf{d}_{ij}$ is the unit

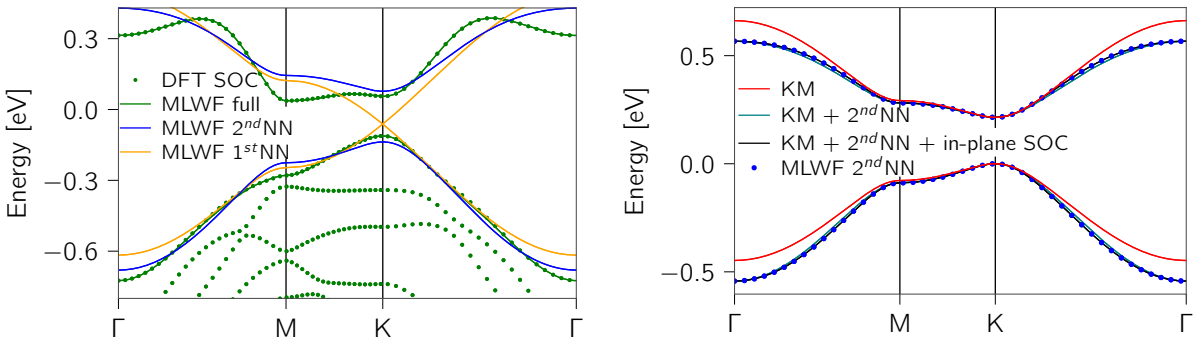


Figure 4.1: Image adapted from Ref. [13]. Left panel: band structure obtained from the MLWF Hamiltonian derived from DFT calculations with SOC and truncated at different hopping cutoffs. The full MLWF Hamiltonian (green line) accurately interpolates the highest occupied and lowest unoccupied DFT bands (green dots). Keeping only first NN hoppings (yellow line) closes the gap into a Dirac point; including second NN hoppings (blue line) opens a gap at **K**. Right panel: band structures of the generalized Kane–Mele Hamiltonian in DFT calculations. The pure Kane–Mele model, with t and t_2 terms only, reproduces the band dispersion and the gap at **K** (red). The real second NN hopping term t_2' breaks particle-hole symmetry and mainly affects the bands near Γ, while the additional in-plane SOC term t_2'', allowed by the broken planar mirror symmetry of the buckled lattice, vanishes at **K** and remains negligible along the high-symmetry path.

vector connecting second-nearest-neighbor sites. The four terms describe, respectively, a real first nearest-neighbor (1st NN) hopping, the intrisic Kane–Mele SOC between second nearest-neighbors (2nd NN), a real 2nd NN hopping and an "in-plane" SOC between 2^{nd} NN. The first two terms are already present in the spin-diagonal Kane–Mele model of Eq. (1.87). The real 2nd NN hopping is also allowed by time-reversal symmetry. The last term, instead, is an additional SOC contribution specific to buckled geometries: it is absent in planar honeycomb lattices such as graphene, but becomes allowed once in-plane mirror symmetry is broken. The calculation of the $\mathbb{Z}_2$ invariant for the tight-binding model in Eq. (4.30), with parameters extracted from first-principles DFT calculations, returns that the system is in the QSHI phase.

In Ref. [13], the formation of Hg, Pt, and Se vacancies in monolayer jacutingaite was also investigated by computing the corresponding formation energies. Among these defects, the Hg vacancy was found to have the lowest formation energy, approximately 0.5 eV. This value is rather small compared with typical vacancy formation energies in other two-dimensional materials, where even the lowest-energy vacancies are often of the order of 1 eV or larger.

The low formation energy of Hg vacancies indicates that these defects may be relevant in realistic samples of monolayer jacutingaite and that particular care should be taken during synthesis to prevent their formation. Nevertheless, because topological phases are generally robust against weak to moderate perturbations, a finite concentration of Hg vacancies is not expected

to immediately suppress the QSHI state.

The purpose of the following analysis is to study the response of the monolayer of jacutingaite to Hg vacancies and to estimate the critical vacancy concentration at which the topological phase is eventually lost. To this end, we first perform DFT calculations on a $3 \times 3 \times 1$ supercell containing a single Hg vacancy, which provide a first-principles characterization of the vacancy-induced defect states. We then use the effective tight-binding descriptions introduced above, namely the full Wannier Hamiltonian and the generalized Kane–Mele model of Eq. (4.30), to benchmark the single-vacancy spectrum and to extend the analysis to larger supercells and finite vacancy concentrations.

4.2.1 *Ab initio* characterization of a single Hg vacancy

We first investigate the effect of an isolated Hg vacancy in a monolayer of jacutingaite at the DFT level. The calculations are performed using plane waves and pseudopotentials, as implemented in the `Quantum ESPRESSO` package [112–114]. We employ optimized norm-conserving Vanderbilt (ONCV) pseudopotentials [126] from the PseudoDojo library [127]. The exchange-correlation functional is treated within the PBE approximation [111]. Since spin-orbit coupling plays a central role in the topological properties of the material, the calculations are performed within a fully relativistic non-collinear framework.

Starting from the pristine monolayer, we construct a $3 \times 3 \times 1$ supercell containing 108 atoms: 36 Pt, 18 Hg, and 54 Se atoms. A single Hg atom is then removed from the supercell, and the resulting defective structure is relaxed through a structural optimization using the BFGS algorithm, as implemented in the `relax` routine of `Quantum ESPRESSO`.

The vacancy formation energy is defined as

$$E_f = E_{\mathrm{def}} + E_{\mathrm{atom}} - E_{\mathrm{prist}}, \tag{4.31}$$

where E_{def} is the total energy of the relaxed defective system, E_{prist} is the total energy of the corresponding pristine supercell, and E_{atom} is the energy of the isolated removed atom. From self-consistent field (SCF) calculations performed at the single Γ point in the supercell framework, we obtain that the formation energy of Hg is

$$E_f = 0.568\,\mathrm{eV}, \tag{4.32}$$

in good agreement with the value $E_f \simeq 0.5\,\mathrm{eV}$ reported in Ref. [13].

In addition, we test whether the Hg vacancy may induce magnetism. To this end, we perform spin-polarized non-collinear calculations initialized with random magnetic moments on the atoms surrounding the vacancy, in particular on the Pt and Hg sites. For these magnetic calculations, we

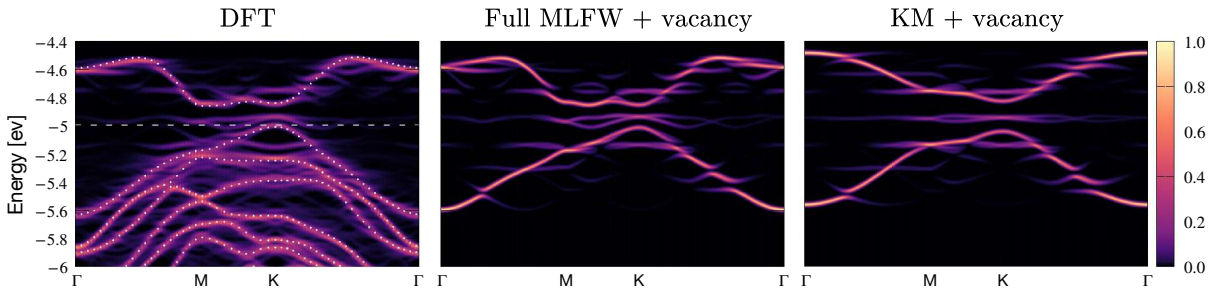


Figure 4.2: Effective band structures of $3 \times 3 \times 1$ supercells in the presence of a single defect, unfolded back onto the Brillouin zone of the primitive cell. The color scale indicates the unfolded spectral function $A(\mathbf{k}, E)$ defined in Eq. (4.29). Left panel: spectral function obtained from DFT calculations for a supercell of monolayer of jacutingaite with a single Hg vacancy. The white dots indicate the band structure of the pristine system computed in the primitive cell. The dashed gray line indicates the Fermi energy of the defective system. The vacancy induces defect states inside the topological gap. Middle panel: unfolded spectral function obtained from the full Wannier Hamiltonian with one removed Hg-centered Wannier site. Right panel: corresponding result for the generalized Kane–Mele model with hopping terms up to second-nearest neighbors.

use LDA pseudopotentials, since fully relativistic non-collinear calculations including spin-orbit coupling are found to be difficult to converge with generalized-gradient approximations such as PBE. All calculations converge to a non-magnetic solution with vanishing total magnetization. We therefore find no evidence of vacancy-induced magnetism associated with an isolated Hg vacancy in monolayer of jacutingaite.

We then analyze the electronic structure of the defective system using the band-unfolding procedure described in Section 4.1.3. The left panel of Figure 4.2 shows the spectral function $A(\mathbf{k}, E)$ obtained from the DFT calculation of the $3 \times 3 \times 1$ supercell containing a single Hg vacancy. For comparison, the band structure of the pristine monolayer of jacutingaite, computed in the primitive cell, is shown as white dots. The unfolded spectral function clearly reveals the appearance of defect states inside the topological gap.

The emergence of such in-gap states is consistent with the general observation that vacancies in topological insulators can induce localized defect states inside the bulk gap [128]. A useful intuitive picture is to regard the vacancy as a hole in the topological medium. Since this hole can be viewed as a locally trivial region embedded in a topological system, edge-like states are expected to circulate around its boundary. As the radius of the hole is gradually reduced, the energy separation between these confined edge states increases, and most of them are pushed into the bulk bands. However, a finite number of states can remain trapped inside the gap, giving rise to vacancy-induced bound states, as the hole evolves into a point-like defect[10].

[10]We mention that the spectral response to a localized impurity in an otherwise clean system has been proposed as a diagnostic of non-trivial topology [129, 130]. A potential scattering impurity introduced in the bulk of an

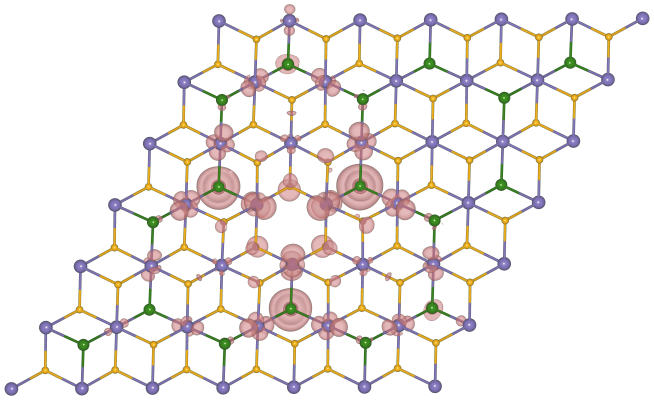


Figure 4.3: Isosurface plot of one of the two maximally localized Wannier functions (MLWFs) constructed from the in-gap defect states appearing in a $3 \times 3 \times 1$ supercell of a monolayer of jacutingaite with a single Hg vacancy. The MLWFs are obtained through a disentanglement procedure. They are mainly localized on the Hg atoms (green) nearest to the removed Hg site, where they display predominantly *s*-orbital character, with additional contributions from the *d*-orbitals of the surrounding Pt atoms (violet).

We investigate the localization properties of the in-gap defect states induced by a single Hg vacancy in the monolayer of jacutingaite, by constructing two maximally localized Wannier functions from the two bands appearing inside the bulk gap. The isosurface of one of these Wannier functions is shown in Figure 4.3. We observe that the resulting Wannier functions mainly have *s*-orbital character on the Hg atoms closest to the removed Hg site, together with contributions from the *d*-orbitals of the surrounding Pt atoms.

An estimate of the degree of localization of the defect states is provided by the total quadratic spread Ω of the Wannier functions, introduced in Eq. (4.15). This quantity is the sum of the individual spreads Ω_n of the two Wannier functions and is found to be $\Omega \simeq 195\,\text{Å}^2$.[11] Since the two Wannier functions have the same spread, this corresponds to an effective spatial extension $\sqrt{\Omega_n} \simeq 10\,\text{Å}$ for each Wannier function. This length scale is smaller than, but comparable to, the linear size of the simulation cell, which is approximately 22 Å. A more detailed characterization of the spatial decay of the defect states would therefore require larger simulation cells, in order to reduce finite-size effects. Indeed, under periodic boundary conditions, the periodic images of the vacancy-induced states may be artificially coupled if the supercell is not sufficiently large. This interpretation is supported by the finite dispersion of the in-gap defect states visible in the DFT electronic structure shown in the left panel of Figure 4.2. Since a direct first-principles study of larger defective supercells would be computationally very demanding, we turn in the following

insulator may generate bound states whose energies lie in the gap between the bulk bands. The key observation is that, for topologically non-trivial states, impurity-induced bound states can occur for arbitrary impurity strength, whereas this behavior is not generally expected in topologically trivial phases, where in-gap bound states are absent for strong impurities.

[11] We note that this value of the total quadratic spread is very close to its gauge-invariant part $\Omega_I \simeq 190\,\text{Å}^2$, which provides a lower bound on how localized the Wannier functions can become within the chosen subspace in the Marzari–Vanderbilt construction of maximally localized Wannier functions.

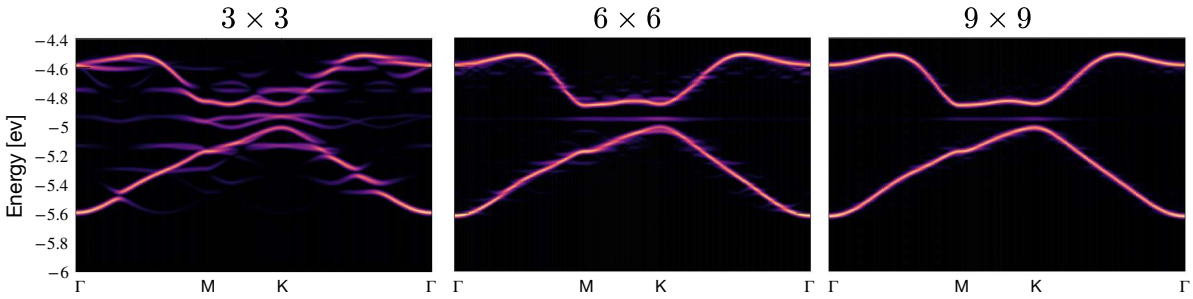


Figure 4.4: Evolution of the unfolded spectral function obtained from the full Wannier Hamiltonian with one removed Hg-centered Wannier site, for increasing supercell size. From left to right, we show the results for supercells of linear size $L = 3$, $L = 6$, and $L = 9$, corresponding to 17, 71, and 161 remaining sites after the vacancy is introduced. The $L = 3$ case, already shown in the middle panel of Figure 4.2, is reported here again for comparison. The defect state induced by the removed site becomes increasingly flat inside the bulk gap as the supercell size is increased. The single-point $\mathbb{Z}_2$ invariants associated with these configurations are $\nu_{sp} = 1.181$, 1.097, and 1.039, respectively, showing that the invariant converges towards 1 as the system size increases.

to effective Hamiltonian descriptions, which allow us to access larger system sizes.

4.2.2 Vacancy effects within effective tight-binding models

We proceed by exploiting the tight-binding description of the monolayer of jacutingaite provided by the 4-bands Wannier Hamiltonians introduced in Ref. [13] and reviewed at the beginning of this section. Specifically, we consider both the full Wannier model and the generalized Kane–Mele model of Eq. (4.30), in which hopping terms are retained up to second-nearest neighbors. In both cases, we construct a supercell of linear size $L = 3$ and model the Hg vacancy by removing one Hg-centered lattice site. The resulting band structures are then unfolded back onto the Brillouin zone of the primitive cell and compared with the DFT electronic structure in the presence of the single Hg vacancy in Figure 4.2.

The full Wannier Hamiltonian, shown in the middle panel of Figure 4.2, accurately reproduces the structure of the vacancy-induced defect states with respect to the DFT calculation. The generalized Kane–Mele model, in the right panel, still captures the qualitative appearance of the in-gap defect states, although with some deviations in the detailed spectral features.

This approach is particularly useful because it allows us to get an insight into the finite-size origin of the dispersion of the in-gap defect states. Indeed, within the tight-binding framework, it is straightforward to compute the unfolded spectral function from the full Wannier Hamiltonian with one removed Wannier site while progressively increasing the supercell size. As shown in Figure 4.4, the vacancy-induced defect states become increasingly flat inside the bulk gap as the supercell size is increased. This behavior confirms that the dispersion observed in smaller

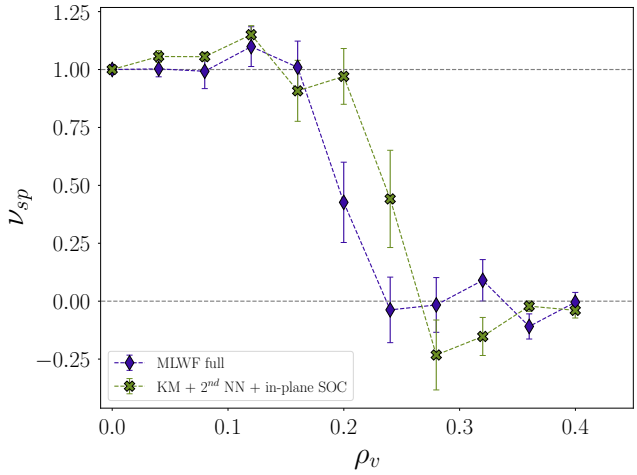


Figure 4.5: Vacancy-driven topological phase transition in a monolayer of jacutingaite. The single-point $\mathbb{Z}_2$ invariant ν_{sp} is shown as a function of the vacancy concentration ρ_v for two tight-binding descriptions: the full MLWF Hamiltonian and the generalized Kane–Mele model including real second-neighbor hopping and in-plane SOC, given in Eq. (4.30). The points and error bars correspond to the average and standard deviation over $N_{samples} = 300$. For small vacancy concentrations, both models remain in the QSHI phase, while increasing ρ_v drives a transition to a topologically trivial regime. The critical concentration is approximately 20% of removed sites for a supercell of linear size $L = 54$ containing 5832 sites in the clean limit.

supercells arises from the artificial coupling between periodic images of the vacancy.

Having verified the reliability of the tight-binding models in the single-vacancy limit, we finally use them to study finite vacancy concentrations. We consider both the full Wannier Hamiltonian and the generalized Kane–Mele model, and construct a large supercell of linear size $L = 54$, containing 5832 sites in the clean limit, where an increasing fraction ρ_v of lattice sites is randomly removed. In generating the vacancy configurations, we remove the same number of sites from the two sublattices of the underlying honeycomb lattice. This constraint avoids introducing a net sublattice imbalance, which would act as an additional perturbation and could therefore affect the stability of the QSHI phase independently of vacancy disorder itself. In Figure 4.5 we report the single-point $\mathbb{Z}_2$ invariant ν_{sp} computed through the single-point spin Chern numbers [8] defined in Eq. (2.19). For small vacancy concentrations, both models remains in the QSHI phase. Upon increasing ρ_v, the single-point invariant changes value, signaling a vacancy-driven topological phase transition. This occurs at approximately 20% of removed sites. Remarkably, the generalized KM model only slightly overestimates the critical vacancy density compared with the full Wannier Hamiltonian. This further confirms that, despite its simplicity, it accurately captures the low-energy physics of monolayer of jacutingaite, also in the presence of vacancy disorder.

Chapter 5

Variational Monte Carlo approach for correlated topological systems

The band theory of solids represents one of the earliest and most successful frameworks for understanding the electronic properties of materials, providing a clear distinction between metals and insulators in terms of band filling. Within this approach, which assumes a single-particle perspective, the many-body ground state is constructed by occupying the lowest-energy electronic states according to the Pauli principle, and the presence or absence of a gap at the Fermi level determines the conducting behavior. Although this approach successfully captures the qualitative physics of a wide range of materials, it fails in systems where electron–electron interactions play a dominant role, such as transition-metal oxides with partially filled $d-$ or $f-$shells. Indeed, the insulating behavior observed in these compounds, despite predictions of metallicity from band theory, motivated the seminal ideas of Mott and Peierls [131], who emphasized the crucial role of the Coulomb repulsion. In this kind of systems, interaction cannot be neglected because of the presence of very localized orbitals, and the small overlap between orbitals on neighboring atoms leads to narrow electronic bands, where the contribution from the kinetic energy is reduced and the electron–electron interactions cannot be treated as a small perturbation.

Recognizing the importance of interactions has spurred interest in the quantum many-body physics of strongly correlated systems. In this field, the focus moved from increasingly complicated systems studied via ab initio approaches, such as Density Functional Theory (DFT), toward simplified lattice models designed to capture the essential physics of correlation-driven phenomena, disregarding specific microscopic details. Representative examples include the Hubbard model and its multi-orbital generalizations, which give rise to a wide range of phenomena that go beyond the independent-particle picture.

At the same time, the theory of topological phases of matter, introduced in the previous

chapters, is deeply rooted in the properties of single-particle wavefunctions. This raises the fundamental question of how the topological phases evolve when electronic correlations become significant and how to detect them. Addressing this issue has become particularly relevant in light of recent experimental advances, such as moiré materials (e.g., twisted bilayer graphene [132]), where narrow bands and strong interactions coexist with nontrivial band topology, leading to rich and unconventional phase diagrams.

From a theoretical perspective, the study of interacting quantum systems is challenged by the exponential growth of the Hilbert space, which makes exact solutions unfeasible in most cases. This has motivated the development of numerical approaches capable of capturing the essential physics of correlated states. In this context, Variational Monte Carlo (VMC) provides a powerful framework to investigate ground-state properties of interacting fermionic systems, allowing for the inclusion of correlation effects through appropriately designed wavefunctions.

This chapter is devoted to the theoretical tools for studying correlated topological systems. We begin by introducing the Hamiltonian description of interacting systems, starting from the general multi-orbital framework given by the Hubbard-Kanamori model, and then narrowing down the single-band Hubbard model. In this context, we discuss the strong coupling limit described by the Heisenberg model, and we discuss the construction of physically motivated many-body wavefunctions. We then present the Jastrow factor as a key ingredient to enhance correlations within variational wavefunctions. Subsequently, we review ground-state probes for distinguishing metallic and insulating behavior in interacting systems, along with many-body topological markers that characterize topology beyond the single-particle picture. Finally, we outline the Variational Monte Carlo framework employed throughout this work.

5.1 Hamiltonian models for interacting electronic systems

In this section, we outline how the effects of Coulomb interaction can be incorporated into a tight-binding Hamiltonian formulation. In particular, our aim is not to provide a comprehensive review, but rather to present the essential concepts needed for our study of electronic correlations in the BHZ model, both in one- and two-dimensions, which will be addressed in the next chapter. Since this model features two orbital degrees of freedom, we begin by presenting the multi-orbital Hubbard model, commonly referred to as the Hubbard-Kanamori model. We then exploit the conceptual simplicity of the single-orbital case, the well-known Hubbard model, to capture the key features and fundamental physics of strongly correlated systems. In particular, we examine the strong-coupling limit, which leads to the Heisenberg model and serves as a pedagogical foundation for subsequent analysis. We also introduce the framework for treating correlation effects through appropriately designed variational wavefunctions, such as the Gutzwiller wavefunction.

In order to include Coulomb interactions in a tight-binding lattice model, the interaction potential must be expressed within the second-quantization formalism. The general Hamiltonian describing electrons interacting in a solid was introduced in the first chapter in Eq. (1.6) and, in second-quantization, can be written as

$$\hat{\mathcal{H}} = \hat{\mathcal{H}}_0 + \hat{\mathcal{H}}_{int} = \sum_{\sigma} \int d\mathbf{r}\, \hat{\Psi}^{\dagger}_{\sigma}(\mathbf{r}) \left[-\frac{\hbar^2}{2m_e}\nabla^2 + V(\mathbf{r}) \right] \hat{\Psi}_{\sigma}(\mathbf{r}) \tag{5.1}$$

$$+ \frac{1}{2} \sum_{\sigma,\sigma'} \int d\mathbf{r}\, d\mathbf{r}'\, \hat{\Psi}^{\dagger}_{\sigma}(\mathbf{r}) \hat{\Psi}^{\dagger}_{\sigma'}(\mathbf{r}') U(\mathbf{r}-\mathbf{r}') \hat{\Psi}_{\sigma'}(\mathbf{r}') \hat{\Psi}_{\sigma}(\mathbf{r}). \tag{5.2}$$

where $V(\mathbf{r})$ is the ionic potential experienced by an electron at position $\mathbf{r}$, arising from the presence of nuclei whose positions are fixed in space under the so-called *frozen nuclei approximation*, thereby defining a lattice of N sites. Moreover, $U(\mathbf{r}-\mathbf{r}') = \frac{e^2}{|\mathbf{r}-\mathbf{r}'|}$ is the Coulomb interaction between electrons in $\mathbf{r}$ and $\mathbf{r}'$, while $\hat{\Psi}^{\dagger}_{\sigma}(\mathbf{r})$ and $\hat{\Psi}_{\sigma}(\mathbf{r})$ are the field operators that create and annihilate a fermionic particle with spin σ at the point $\mathbf{r}$. If we assume that electrons are almost localized at each site of the lattice, as it happens in the strongly correlated materials, we can consider the basis of Wannier functions defined in Eq. (1.26)

$$w_{m\sigma}(\mathbf{r}-\mathbf{R}_i) = \frac{1}{N} \sum_{\mathbf{k}\in \mathrm{BZ}} e^{-i\mathbf{k}\cdot\mathbf{R}_i} \psi_{m\mathbf{k}\sigma}(\mathbf{r}) \tag{5.3}$$

associated at each lattice site $\mathbf{R}_i$ and expressed in terms of the Bloch wavefunctions $\psi_{m\mathbf{k}\sigma}(\mathbf{r}) = e^{i\mathbf{k}\cdot\mathbf{r}}\, u_{m\mathbf{k}\sigma}(\mathbf{r})$ which diagonalize the non-interacting part of the Hamiltonian $\mathcal{H}_0$. In the basis of Wannier functions, the fermionic field operators can be expanded as

$$\begin{aligned} \hat{\Psi}^{\dagger}_{\sigma}(\mathbf{r}) &= \sum_{i,m} w^{*}_{m\sigma}(\mathbf{r}-\mathbf{R}_i)\, \hat{c}^{\dagger}_{im\sigma} \\ \hat{\Psi}_{\sigma}(\mathbf{r}) &= \sum_{i,m} w_{m\sigma}(\mathbf{r}-\mathbf{R}_i)\, \hat{c}_{im\sigma} \end{aligned} \tag{5.4}$$

where $\hat{c}^{\dagger}_{im\sigma}$ ($\hat{c}_{im\sigma}$) creates (annihilates) an electron with spin σ in the m-th Wannier orbital centered at site $\mathbf{R}_i$. In this representation, the Hamiltonian describing the many-body system can be written as

$$\hat{\mathcal{H}} = \sum_{\substack{i,j \\ m,m',\sigma}} t^{mm'}_{ij}\, \hat{c}^{\dagger}_{im\sigma} \hat{c}_{jm'\sigma} + \frac{1}{2} \sum_{\substack{i,j,k,l \\ m,m',n,n'}} \sum_{\sigma,\sigma'} V^{mm'nn'}_{ijkl}\, \hat{c}^{\dagger}_{im\sigma} \hat{c}^{\dagger}_{jm'\sigma'} \hat{c}_{kn\sigma'} \hat{c}_{ln'\sigma} \tag{5.5}$$

where

$$t^{mm'}_{ij} = \int d\mathbf{r}\, w^{*}_{m\sigma}(\mathbf{r}-\mathbf{R}_i) \left[-\frac{\hbar^2}{2m_e}\nabla^2 + V(\mathbf{r}) \right] w_{m'\sigma}(\mathbf{r}-\mathbf{R}_j) \tag{5.6}$$

is the hopping amplitude[12] between orbitals m' and m at lattice sites j and i, respectively, and

$$V_{ijkl}^{mm'nn'} = \int d\mathbf{r} \int d\mathbf{r}'\, w_{m\sigma}^{*}(\mathbf{r}-\mathbf{R}_i) w_{m'\sigma'}^{*}(\mathbf{r}'-\mathbf{R}_j)\, U(\mathbf{r}-\mathbf{r}')\, w_{n\sigma'}(\mathbf{r}-\mathbf{R}_k) w_{n'\sigma}(\mathbf{r}'-\mathbf{R}_l) \quad (5.7)$$

represents the Coulomb interaction matrix element between two electrons.

This tight-binding model is described by an infinite number of parameters, since it does not include any screening effects, and hoppings and interactions are considered between sites at every distance. But, dealing with localized orbitals, it is reasonable to expect that the hopping amplitudes $t_{ij}^{mm'}$ decay exponentially with the distance between sites i and j. Therefore, to a good approximation, the kinetic energy can be truncated to nearest-neighbor hoppings only. Similarly, the Coulomb interaction between electrons at different sites decreases rapidly with the distance and is dominated by the on-site contribution, which can be written as

$$V_{ijkl}^{mm'nn'} = U^{mm'nn'} \delta_{ij}\delta_{ik}\delta_{il}, \quad (5.8)$$

where we drop the site indices and for every lattice site $\mathbf{R}_i \equiv \mathbf{R}$

$$U^{mm'nn'} = \int d\mathbf{r} \int d\mathbf{r}'\, w_{m\sigma}^{*}(\mathbf{r}-\mathbf{R}) w_{m'\sigma'}^{*}(\mathbf{r}'-\mathbf{R})\, U(\mathbf{r}-\mathbf{r}')\, w_{n\sigma'}(\mathbf{r}-\mathbf{R}) w_{n'\sigma}(\mathbf{r}'-\mathbf{R}). \quad (5.9)$$

5.1.1 The multi-orbital Hubbard-Kanamori Hamiltonian

The number of independent parameters for the local interaction given by Eq. (5.9) were further reduced in the original work by Kanamori [133], yielding the following subset of on-site integrals:

$$U = \int d\mathbf{r}\, d\mathbf{r}' \sum_{\sigma,\sigma'} |w_{m\sigma}(\mathbf{r})|^2\, U(\mathbf{r}-\mathbf{r}')\, |w_{\sigma' m}(\mathbf{r}')|^2, \quad (5.10)$$

$$U' = \int d\mathbf{r}\, d\mathbf{r}' \sum_{\sigma,\sigma'} |w_{m\sigma}(\mathbf{r})|^2\, U(\mathbf{r}-\mathbf{r}')\, |w_{m'\sigma'}(\mathbf{r}')|^2, \quad (5.11)$$

$$J = \int d\mathbf{r}\, d\mathbf{r}' \sum_{\sigma,\sigma'} w_{m\sigma}^{*}(\mathbf{r}) w_{m'\sigma'}^{*}(\mathbf{r}')\, U(\mathbf{r}-\mathbf{r}')\, w_{m'\sigma}(\mathbf{r}) w_{m\sigma'}(\mathbf{r}'), \quad (5.12)$$

$$J' = \int d\mathbf{r}\, d\mathbf{r}' \sum_{\sigma,\sigma'} w_{m\sigma}^{*}(\mathbf{r}) w_{m\sigma'}^{*}(\mathbf{r}')\, U(\mathbf{r}-\mathbf{r}')\, w_{m'\sigma}(\mathbf{r}) w_{m'\sigma'}(\mathbf{r}'). \quad (5.13)$$

[12] There is no dependence of the hopping amplitude $t_{ij}^{mm'}$ on the spin σ since no spin-orbit coupling is considered in Eq. (5.1).

The full many-body atomic Hamiltonian in second quantization, at each site $\mathbf{R}$, then takes the form [134][13]

$$\begin{aligned}\hat{\mathcal{H}}_{int} = U\sum_{m}\hat{n}_{m\uparrow}\hat{n}_{m\downarrow} + U'\sum_{m\neq m'}\hat{n}_{m\uparrow}\hat{n}_{m'\downarrow} + (U'-J)\sum_{m<m',\sigma}\hat{n}_{m\sigma}\hat{n}_{m'\sigma} \\ - J\sum_{m\neq m'}\hat{c}^{\dagger}_{m\uparrow}\hat{c}_{m\downarrow}\hat{c}^{\dagger}_{m'\downarrow}\hat{c}_{m'\uparrow} + J'\sum_{m\neq m'}\hat{c}^{\dagger}_{m\uparrow}\hat{c}^{\dagger}_{m\downarrow}\hat{c}_{m'\downarrow}\hat{c}_{m'\uparrow}\end{aligned} \tag{5.14}$$

where $\hat{n}_{m\sigma} = \hat{c}^{\dagger}_{m\sigma}\hat{c}_{m\sigma}$. The first three terms involve only density-density interactions, between electrons with opposite spins in the same orbital (U), opposite spins in different orbitals (U') and parallel spins in different orbitals ($U'-J$). The last two terms describe processes in which two electrons in different orbitals flip the spin (J) or hop together from an orbital to another (J'), respectively.

The case in which the Hamiltonian in Eq. (5.14) is most commonly applied is the one of d orbitals of transition-metal oxides, where a cubic crystal field splits the fivefold-degenerate d shell into a threefold-degenerate t_{2g} manifold and a twofold-degenerate e_g manifold. For d orbitals, the full rotational invariance in the orbital space constrains the interaction parameters, leading to the relation

$$U' = U - 2J. \tag{5.15}$$

Moreover, since the Wannier functions can be chosen real, the exchange and pair-hopping amplitudes are identical $J = J'$.

The interaction Hamiltonian can be equivalently rewritten in a compact form in terms of the total charge, total spin, and orbital pseudospin operators

$$\hat{N} = \sum_{m,\sigma}\hat{n}_{m\sigma}, \qquad \hat{\boldsymbol{S}} = \frac{1}{2}\sum_{m\sigma\sigma'}\hat{c}^{\dagger}_{m\sigma}\boldsymbol{\sigma}_{\sigma\sigma'}\hat{c}_{m\sigma'}, \qquad \hat{\boldsymbol{T}} = \frac{1}{2}\sum_{m,m',\sigma}\hat{c}^{\dagger}_{m\sigma}\boldsymbol{\tau}_{mm'}\hat{c}_{m'\sigma}, \tag{5.16}$$

where $\boldsymbol{\sigma}$ are the Pauli matrices in spin space and $\boldsymbol{\tau}$ are generators of the $SU(\mathrm{M})$ symmetry in orbital space ($\mathrm{M} = 3$ for t_{2g} and $\mathrm{M} = 2$ for e_g).

For the t_{2g} manifold ($m = xy, yz, zx$) the interaction takes the form

$$\hat{\mathcal{H}}^{(t_{2g})}_{int} = \frac{U-3J}{2}\hat{N}(\hat{N}-1) - 2J\hat{\boldsymbol{S}}^2 - \frac{J}{2}\hat{\boldsymbol{T}}^2 + \frac{5J}{2}\hat{N}. \tag{5.17}$$

For the e_g manifold, it reads

$$\hat{\mathcal{H}}^{(e_g)}_{int} = (U-J)\frac{\hat{N}(\hat{N}-1)}{2} + 2J(T_x^2 + T_z^2) - J\hat{N}, \tag{5.18}$$

[13]This formulation of an interacting Hamiltonian is consistent with the Hund's rules, which aim to determine the ground-state electronic configuration for a multi-orbital atom, which, in order, maximizes the total spin S, maximizes the total angular momentum L, for less(more) than half-filling minimizes(maximizes) $|L-S|$.

where $\hat{\boldsymbol{T}}$, in this case, is the pseudospin-1/2 operator in the space of orbitals $3z^2-r^2$ and x^2-y^2.

Although these Hamiltonians are derived for d orbitals, they provide a rotationally invariant and physically accurate description of on-site Coulomb interactions in multi-orbital systems. A common strategy for investigating electronic correlation effects, both in realistic materials and in simplified toy models, is to first identify the relevant bands and construct an effective non-interacting Hamiltonian within the corresponding orbital subspace. Once the low-energy physics and degrees of freedom are established, the Coulomb electron–electron interactions are introduced in a form that preserves the symmetries and physical constraints of the system.

5.1.2 The single-band Hubbard model

The single-band Hubbard model represents the minimal theoretical framework in condensed matter physics to describe Coulomb interacting electrons on a lattice, introduced in a series of seminal works in the 1960s [133, 135, 136]. The model describes a d-dimensional lattice of N sites, each of which can host at most two electrons with opposite spin. Although it does not incorporate Hund's-rule effects, the Hubbard model provides a clean setting to study interaction-driven localization and captures the essential physics of strongly correlated systems. The model is defined by the Hamiltonian

$$\hat{\mathcal{H}} = -t \sum_{\langle i,j\rangle,\sigma} \hat{c}^{\dagger}_{i\sigma}\hat{c}_{j\sigma} + U \sum_{i} \hat{n}_{i\uparrow}\hat{n}_{i\downarrow}. \tag{5.19}$$

The non-interacting part is reduced to the hopping t between nearest-neighboring lattice sites, while the effect of the Coulomb interaction is to penalize double occupation by an energy cost $U > 0$. The kinetic and interaction terms do not commute and therefore cannot be simultaneously diagonalized. Indeed, the hopping term can be diagonalized in momentum space by delocalized states in the form of plane waves, giving rise to a single energy band of width $W = 2td$. On the contrary, at $t = 0$ or equivalently $U/t = \infty$, the Hubbard Hamiltonian is diagonal in real space, and any state constructed by placing electrons on the sites of the lattice is an eigenstate with energy $E = UN_d$, where N_d is the number of doubly occupied sites. The ground state is highly degenerate; in particular, at half-filling (when the number of electrons $N_e = N$) it has exactly one electron per site and degeneracy equal to 2^N, corresponding to all possible configurations with one up or down spin at each site. Therefore, spin excitations are gapless, whereas moving an electron from a site to another creates a doubly occupied site, so that charge excitations are gapped with an energy gap equal to U. This insulating behavior is induced by electron correlation, differs from that of a band insulator, as evidenced by the distinct behavior of the charge and spin channels, and takes the name of *Mott insulator*.

Despite its simplicity, solving the Hubbard model is highly nontrivial. Aside from the to two limiting case discussed above, exact results are available only in a few special cases: when

small system sizes are considered and are accessible via exact diagonalization (ED); the infinite-dimensional case, where Dynamical mean-field theory (DMTF) becomes exact; the specific case of $U/t = \infty$ and $N_e = L - 1$ (a single hole), where the ground state is a ferromagnet in any dimension d [137]; in one dimension ($d = 1$), where the Bethe *Ansatz* [138] yields exact results for the ground-state energy and other thermodynamics quantities, although correlation functions remain difficult to compute. In particular, in $d = 1$, no Mott transition takes place, since for $U > 0$ the ground state is always an insulator at half-filling ($N_e = L$) [139], while it is metallic for $N_e \neq L$. Beyond these special situations, the ground-state properties of the Hubbard model in $d > 1$, for generic filling and interaction U/t are not known. Remarkably, numerically exact Monte Carlo simulations without a sign problem are available at half-filling on bipartite lattices in $d > 1$ for any value of U/t [140, 141]. However, in a generic d-dimensional lattice, starting from the non-interacting system which is metallic at half-filing and increasing U/t, it is natural to expect an interaction-driven transition to the Mott insulator at a certain critical interaction strength U_c ($U_c = 0$ for the exactly solvable model in $d = 1$).

Although the Mott transition is not associated with spontaneous symmetry-breaking, in most cases the metal-insulator transition is accompanied by the emergence of long-range order, most notably antiferromagnetic order. The tendency towards antiferromagnetic order can be understood by performing a strong-coupling expansion with $U/t \gg 1$. We start from the highly degenerate manifold of states that minimize the Coulomb repulsion U with one electron per site (no double occupations) and treat the kinetic term t perturbatively. While first-order processes create energetically unfavorable doubly occupied sites, at second-order two neighboring electrons with opposite spins may profit from a virtual hopping process that creates a doubly occupied lattice site, which is not possible for two parallel neighboring spins because of Pauli exclusion principle. This mechanism generates an effective antiferromagnetic super-exchange interaction $J = 4t^2/U$ and the model that captures this spin dynamics is the *Heisenberg model*

$$\hat{\mathcal{H}} = J \sum_{\langle i,j \rangle} \hat{\mathbf{S}}_i \cdot \hat{\mathbf{S}}_j \tag{5.20}$$

where $\hat{\mathbf{S}}_i = (\hat{S}_i^x, \hat{S}_i^y, \hat{S}_i^z)$ is the spin-1/2 operator at site i with components

$$\hat{S}_i^x = \frac{1}{2}(\hat{c}_{i\uparrow}^\dagger \hat{c}_{i\downarrow} + \hat{c}_{i\downarrow}^\dagger \hat{c}_{i\uparrow}), \tag{5.21}$$

$$\hat{S}_i^y = \frac{1}{2i}(\hat{c}_{i\uparrow}^\dagger \hat{c}_{i\downarrow} - \hat{c}_{i\downarrow}^\dagger \hat{c}_{i\uparrow}), \tag{5.22}$$

$$\hat{S}_i^z = \frac{1}{2}(\hat{c}_{i\uparrow}^\dagger \hat{c}_{i\uparrow} - \hat{c}_{i\downarrow}^\dagger \hat{c}_{i\downarrow}). \tag{5.23}$$

The antiferromagnetic ($J > 0$) Heisenberg Hamiltonian captures the low-energy spin properties of the Hubbard model at half-filling in the strong-coupling limit $U/t \to \infty$, where charge fluctuations are completely suppressed. The corresponding ground state is smoothly connected to the Mott insulating phase of the Hubbard model. In order to recover a more realistic insulating state, which still has charge fluctuations, it is necessary to relax the strict single-occupancy constraint and allow for a finite density of doubly occupied sites. A physically transparent way to achieve this is through the Gutzwiller wavefunction (GWF) [136], which is constructed by applying a correlation operator to a non-interacting fermionic ground state $|\Phi_0\rangle$

$$|\Psi_G\rangle = \hat{\mathcal{P}}_G |\Phi_0\rangle \tag{5.24}$$

where the Gutzwiller projector

$$\hat{\mathcal{P}}_G = \exp\left[-g \sum_i \hat{n}_{i\uparrow}\hat{n}_{i\downarrow}\right] \tag{5.25}$$

is expressed in terms of a single variational parameter $g > 0$ that depends on U. For $g = 0$, $|\Psi_G\rangle$ reduces to the non-interacting ground state and is exact for $U = 0$. In the opposite limit, for $g = \infty$ the *fully-projected* Gutzwiller state corresponds to an insulator in the atomic limit $U/t = \infty$, where all doubly occupied configurations are completely suppressed. For finite U/t, the probability of finding configurations with large N_d decreases with increasing g.

Despite its conceptual simplicity, the GWF is analytically difficult to treat: the correlation operator acts in the configuration space, whereas the non-interacting ground state $|\Phi_0\rangle$ is naturally expressed in momentum space. As a consequence, applying the Gutzwiller projector to $|\Phi_0\rangle$ effectively requires evaluating a Slater determinant for each configuration of the electrons in the lattice, each weighted by the correlation factor $\exp[-gN_d]$ corresponding to that configuration. In practice, this makes it necessary to rely on numerical methods or further approximations. Notably, within the so-called Gutzwiller approximation (GA) (which neglects the configuration-dependent amplitudes arising from the determinants and instead assigns the same weight to all configurations with the same number of double occupancies N_d, thereby ignoring spatial correlation of the spins given by the Slater determinant), Brinkman and Rice [142] predicted a metal-insulator transition at a finite U/t in the Hubbard model. However, later studies based on exact analytic treatments of the GWF in one dimension [143] and variational Monte Carlo simulations (which do not rely on the GA) [144–146], clarified that the Gutzwiller correlation factor is not sufficient to stabilize a Mott insulator in any finite dimension. At half filling, the insulating state is recovered only in the atomic limit $U/t = \infty$, where the variationally optimized GWF has $g = \infty$. For any finite value of U/t, the optimal value of g is finite and the resulting state is metallic. This can be understood in terms of charge excitations, which at half-filling take

the form of doublons (doubly occupied sites) and holons (empty sites), carrying positive and negative charge, respectively. A finite value of g penalizes the creation of these objects but does not prevent their motion once they are formed, so charge transport remains possible. Only in the fully projected limit $g = \infty$ there is no conduction, since the creation of empty and doubly occupied sites is completely forbidden.

5.2 The Jastrow factor

We have discussed that a simple Gutzwiller wavefunction is insufficient to describe a realistic Mott insulator, where the presence of a gap in the charge excitations does not forbid the possibility of having charge fluctuations. A straightforward generalization of the Gutzwiller wavefunction is given by the inclusion of long-range terms in the correlator that is applied to the non-interacting wavefunction $|\Phi_0\rangle$

$$\hat{\mathcal{J}}_d = \exp\left[-\frac{1}{2}\sum_{i,j} v_{i,j}\hat{n}_i\hat{n}_j\right] \tag{5.26}$$

known as the density-density Jastrow factor[14]. The coefficients $v_{i,j}$ represent a pseudo-potential controlling density correlations. For translationally invariant models, such as the Hubbard model, $v_{i,j}$ depends only on the relative distance between the sites i and j, while the on-site term $v_{i,i}$ reduces to the Gutzwiller parameter g.

It has been shown that the inclusion of long–range Jastrow terms can turn a non-interacting metallic state $|\Phi_0\rangle$ into an insulating state that does not break any lattice symmetry, corresponding to the Mott insulator, in one and two dimensions [150–152]. Physically, the long–range tail of the Jastrow factor induces binding between holons and doublons, suppressing charge transport while still allowing local density fluctuations. In particular, denoting the Fourier transform of the translationally invariant pseudo-potential $v_{i,j}$ by v_q, a gapless (metallic) phase is described by having $v_q \approx 1/|\mathbf{q}|$ for $|\mathbf{q}| \to 0$ in any dimension d; by contrast, a fully gapped (insulating) phase is obtained in $d = 1$ with $v_q \approx 1/|\mathbf{q}|^2$ for $|\mathbf{q}| \to 0$, since this behavior induces an exponential decay of the density-density correlations. In $d = 2, 3$ a holon-doublon bound-state is generated by $v_q \approx \beta/|\mathbf{q}|^d$ for a sufficiently large value of β, but these behaviors are not sufficient to have a fully gapped phase, since a residual power-law behavior in the density-density correlations is still present.

[14] The Jastrow wave function was introduced in 1955 [147] to describe strongly-correlated systems on the continuum and found one of its first and most important applications in the description of the ground state of ^{4}He [148]. With their formula which relates the Jastrow and the density structure factor, Reatto and Chester [149] proved that, in order to correctly reproduce the structure of liquid Helium, a long-range component of the Jastrow factor is required.

It is also useful to introduce here the possibility of defining a spin-spin Jastrow factor

$$\hat{\mathcal{J}}_s = \exp\left[-\frac{1}{2}\sum_{i,j} u_{i,j}\hat{S}^z_i\hat{S}^z_j\right] \tag{5.27}$$

which has provided strong evidence of being very accurate for quantum-spin systems, such as the Heisenberg model in Eq. (5.20), when applied on top of classical spin-states. In particular, in the spin$-1/2$ case it reproduces the correct spin-correlation functions when applied to the Néel state with antiferromagnetic order in the x-direction [153], and (more interestingly for our purposes) recent studies [154] have shown that, in the spin-1 case, such a spin-Jastrow wavefunction can successfully describe the Haldane phase. In the latter case, it is important to stress that the Jastrow factor is parametrized by a two-body pseudo-potential $u_{i,j}$ and therefore explicitly encodes pairwise spin-spin correlations. For this reason, its ability to describe phases characterized by genuine many–body order is highly nontrivial. In particular, as we will see, the non-local string correlation characterizing the Haldane phase depends on the configuration of all spins between two distant sites and is not explicitly contained in a purely two-body correlator.

5.3 Ground-state probes of electronic and topological properties

The characterization of a quantum phase requires identifying the physical properties that distinguish it from other phases. In the systems considered in this thesis, two features are particularly important. The first concerns the electronic response of the system, namely whether the ground state describes an insulator, and whether charge or spin excitations are gapless. The second concerns its topological character, namely whether insulating states that share the same symmetries can nevertheless be distinguished by a bulk topological invariant.

Within the band-theory framework, both aspects can be addressed in terms of single-particle Bloch states. The metallic or insulating character is inferred from the energy spectrum: if the Fermi level crosses one or more bands, the system is metallic, whereas if it lies within a gap separating occupied and empty bands, the system is insulating. The topological properties of a non-interacting insulator are instead encoded in the geometry of the occupied Bloch states, through quantities such as Berry phases, Chern numbers, or $\mathbb{Z}_2$ invariants.

In an interacting system, however, this single-particle description is no longer sufficient. The low-energy excitations are not, in general, described by independent electrons promoted to higher-energy Bloch bands, and the topology of the many-body state cannot always be inferred from the occupied eigenstates of a Bloch Hamiltonian. Therefore, both the electronic and the topological characterization of the system must be reformulated in terms of many-body quantities.

At zero temperature, the distinction between a metal and an insulator can be formulated in terms of transport properties: metals exhibit a finite dc conductivity, which instead vanishes for

insulators. A direct calculation of the conductivity, however, generally requires the knowledge of the low-energy many-body excitation spectrum. Similarly, many-body topological invariants can be defined through twisted boundary conditions or Green's functions, but these approaches may require information beyond a single ground-state wavefunction.

Since our approach is based on the determination of an optimal ground-state wavefunction (see Section 5.4), it is necessary to identify diagnostics that can be evaluated directly on the ground state. The aim of this section is therefore to introduce ground-state probes for both electronic and topological properties. In particular, we first discuss how the long-wavelength behavior of static correlation functions can be used to infer the presence or absence of charge and spin gaps. We then introduce a many-body marker, related to the modern theory of polarization, whose phase provides information about the topology of correlated insulating states.

5.3.1 Feynman construction for charge and spin excitations

Starting from the ground state $|\Psi\rangle$ of a many-body system of N electrons with energy E_0, it is possible to construct simple variational states for the lowest-energy excitations. For instance, let us recall the Feynman single-mode approximation, originally formulated in the context of collective excitations in liquid Helium [155, 156].

Adapting this construction to a lattice system, a variational charge-excited state Ψ_q is given by

$$|\Psi_{\mathbf{q}}\rangle = \hat{n}_{\mathbf{q}} |\Psi\rangle \tag{5.28}$$

where

$$\hat{n}_{\mathbf{q}} = \sum_j e^{i\mathbf{q}\cdot\mathbf{r}_j} \hat{n}_j \tag{5.29}$$

is the Fourier transformation of the local electron density operator $\hat{n}_j$. The variational estimator of the excitation energy-gap is then given by

$$\Delta_{\mathbf{q}} = E_{\mathbf{q}} - E_0 = \frac{\langle\Psi_{\mathbf{q}}| \hat{\mathcal{H}} - E_0 |\Psi_{\mathbf{q}}\rangle}{\langle\Psi_{\mathbf{q}}|\Psi_{\mathbf{q}}\rangle} = \frac{\langle\Psi| \hat{n}_{-\mathbf{q}}[\hat{\mathcal{H}}, \hat{n}_{\mathbf{q}}] |\Psi\rangle}{N_{\mathbf{q}}\langle\Psi|\Psi\rangle} \tag{5.30}$$

where

$$N_{\mathbf{q}} = \frac{\langle\Psi| \hat{n}_{-\mathbf{q}}\hat{n}_{\mathbf{q}} |\Psi\rangle}{\langle\Psi|\Psi\rangle} \tag{5.31}$$

is the static density structure factor.

Whenever the interaction terms in the Hamiltonian contain density-density interactions that commute with $\hat{n}_{-\mathbf{q}}$, the commutator in Eq. (5.30) involves the kinetic term only. In this case, in the limit of $\mathbf{q} \to 0$ the excitation energy behaves as [157]

$$\Delta_{\mathbf{q}} \approx \frac{\text{const} \times \mathbf{q}^2}{N_{\mathbf{q}}}. \tag{5.32}$$

Therefore, the small-$\mathbf{q}$ behavior of the static structure factor calculated on the ground state provides information about the energy spectrum being insulating or not. If

$$N_{\mathbf{q}} \propto |\mathbf{q}| \qquad \text{for} \qquad |\mathbf{q}| \to 0, \tag{5.33}$$

the charge excitation spectrum is gapless, consistently with metallic behavior. Conversely, if

$$N_{\mathbf{q}} \propto |\mathbf{q}|^2 \qquad \text{for} \qquad |\mathbf{q}| \to 0, \tag{5.34}$$

the Feynman construction yields a finite charge gap, indicating an insulating state. It is important to note that, in this latter case, the possibility of other gapless excitations cannot be excluded.

An analogous construction can be made for spin excitations by considering the variational state

$$|\tilde{\Psi}_{\mathbf{q}}\rangle = \hat{s}_{\mathbf{q}} |\Psi\rangle , \tag{5.35}$$

where

$$\hat{s}_{\mathbf{q}} = \sum_j e^{i\mathbf{q}\cdot\mathbf{r}_j} \hat{S}^z_j \tag{5.36}$$

is the Fourier transformation of the local spin operator

$$\hat{S}^z_j = \frac{1}{2}(\hat{c}^\dagger_{j\uparrow}\hat{c}_{j\uparrow} - \hat{c}^\dagger_{j\downarrow}\hat{c}_{j\downarrow}). \tag{5.37}$$

The behavior at small momenta (or, equivalently, at large wavelengths) of the static spin structure factor

$$S_{\mathbf{q}} = \frac{\langle\Psi|\, \hat{s}_{-\mathbf{q}}\hat{s}_{\mathbf{q}} \,|\Psi\rangle}{\langle\Psi|\Psi\rangle} \tag{5.38}$$

reveals the nature of the energy spectrum in the spin excitations.

In this way, the charge and spin structure factors provide diagnostics of the low-energy properties that can be evaluated directly on the ground state, or on a variational approximation to it. The small-$\mathbf{q}$ behavior of the charge structure factor allows one to distinguish between metallic and insulating behavior in the charge sector, while the spin structure factor provides information on the presence of gapless spin excitations.

5.3.2 Topological invariants for interacting systems

A many-body formulation of topological invariants was already introduced in the early studies of the integer quantum Hall effect. In this approach, the Chern number is obtained by imposing twisted boundary conditions on the ground-state wavefunction and integrating over the corresponding boundary phases [46]. This construction replaces the integration over the single-particle crystal momentum $\mathbf{k}$ with an integration over the twist angle $\boldsymbol{\theta}$ defining the boundary conditions,

making the method applicable to many-body wavefunctions. However, it requires the determination of the ground state for different boundary conditions and the evaluation of derivatives of the many-body wavefunction, which pose challenges for numerical implementations.

In one spatial dimension, the Density-Matrix Renormalization Group (DMRG) has been employed to compute the density profile of systems with open boundary conditions. In this setting, the presence of states that are exponentially localized at the edges of the chain can, in principle, provide an indication of the topological nature of the ground state [158]. However, this approach is not entirely satisfactory, particularly in the view of working with periodic boundary conditions, where edge states are absent by construction. This highlights the need for a bulk invariant capable of distinguishing between trivial and topological insulating phases in interacting systems.

Alternative strategies rely on the analysis of the poles and zeros of the interacting single-particle Green's function $G(\omega, \mathbf{k})$ [159, 160], or on the construction of an effective Hamiltonian from $G(0, \mathbf{k})$ [161], which is related to the zero-frequency self-energy Σ

$$H_{eff}(\mathbf{k}) = -G^{-1}(\omega = 0, \mathbf{k}) = H_0(\mathbf{k}) + \Sigma(\omega = 0). \tag{5.39}$$

Still, these types of approach are not always practical, since the Green's function is not directly accessible with many ground-state methods (such as DMRG and quantum Monte Carlo), or they require computing the self-energy $\Sigma(\omega)$ using methods like Dynamical Mean-Field Theory (DMFT), which is exact in infinite dimensions and approximate in two and three dimensions. We also mention that the real-space Chern markers, introduced for non-interacting systems with open-boundary conditions in the Chapter 2, have been extended, within DMFT, to include the effects of electron-electron interactions [162].

In this thesis, we adopt a different approach based on the many-body marker proposed by Resta and Sorella [47], which is closely related to the modern theory of polarization [19, 20]. In systems with periodic boundary conditions (PBC), which constitute the standard framework in condensed matter theory, the usual position operator $\hat{x}$ is not a well-defined operator within the Hilbert space of periodic states, since its action takes a state outside this space. However, the exponential of the position operator is a well-defined operator [44]. Let us consider a one-dimensional system of length $L = Na$, where a is the lattice spacing and N is the number of sites, with periodic boundary conditions. One can introduce the many-body operator

$$\hat{Z} = \exp\left(i\frac{2\pi}{L} \sum_{j=1}^{N} x_j \hat{n}_j \right), \tag{5.40}$$

and its expectation value over the many-body ground state

$$z = \langle\Psi|\,\hat{Z}\,|\Psi\rangle = \langle\Psi|\exp\left(i\frac{2\pi}{L}\sum_{j=1}^{N} x_j\hat{n}_j\right)|\Psi\rangle\,. \tag{5.41}$$

The quantity z is complex. Its modulus is related to the degree of localization of the many-body ground state and can be used, in the thermodynamic limit, to distinguish localized insulating states from delocalized metallic ones [47]. In the following, instead, we will mainly use the phase of z, which defines a many-body Berry phase, or equivalently the electronic polarization modulo a quantum, and can therefore distinguish between topologically inequivalent insulating states.

5.3.2.1 Berry phase for correlated systems

In one-dimensional insulating systems, the phase of z is directly related to the electronic polarization (in units of the electric charge e) through the Berry phase ϕ [44]

$$P_{\rm el} = \frac{\phi}{2\pi} = \frac{1}{2\pi}\mathrm{Im}\log z. \tag{5.42}$$

This relation can be explicitly demonstrated in the non-interacting case, where the ground state can be written as the Slater determinant of Bloch wavefunctions $\psi_{nk}(x) = e^{ikx}u_{nk}(x)$

$$\Psi(x_1,\ldots,x_{N_e}) = \frac{1}{\sqrt{N_e!}}\sum_P \xi_P \prod_{i=1}^{N_e}\psi_{P\{\alpha_i\}}(x_i) \tag{5.43}$$

where P denotes permutations of the single-particle states $\alpha_i = (n_i, k_i)$ and ξ_P is the sign of the permutation. Applying the many-body operator $\hat{Z}$ in Eq. (5.40) to the Slater determinant in Eq. (5.43) the results is, again, a Slater determinant of Bloch wavefunctions. Therefore, one finds that the expectation value z can be expressed as the overlap of two Slater determinants

$$z = \frac{1}{N_e!}\sum_{P,Q}\xi_P\,\xi_Q\prod_{i=1}^{N_e}\int_0^L dx_i\,\psi_{P\{\alpha_i\}}(x_i)e^{i\frac{2\pi}{Na}x_i}\psi_{Q\{\alpha_i\}}(x_i). \tag{5.44}$$

If we look at the one-coordinate expectation value, in general we have

$$\int_0^L dx\,\psi^*_{nk_p}(x)\,e^{i\frac{2\pi}{Na}x}\psi_{mk_q}(x) \tag{5.45}$$

with k_p and k_q two of the equally spaced Bloch vectors defined in the Brillouin zone

$$k_p = \frac{2\pi}{Na}p \quad \text{for} \quad p = 0,\ldots N-1. \tag{5.46}$$

Due to the orthogonality properties of the Bloch wavefunctions, the one-coordinate expectation value in Eq. (5.45) vanishes except when $k_p = k_q + \frac{2\pi}{Na}$, that is, for $p = q+1$. From this, we find

that the permutation P has the same sign as Q if N is odd and the opposite sign of Q if N is even, so that $\xi_P\,\xi_Q = (-1)^{N-1}$.

Therefore, we have that Eq. (5.45) can be written as

$$\delta_{k_p,k_q+\frac{2\pi}{Na}} \int_0^L dx\, u^*_{nk_p}(x)\, u_{mk_q}(x) = \delta_{k_p,k_q+\frac{2\pi}{Na}}\, \delta_{n,m}\, \langle u_{nk_p}|u_{mk_q}\rangle \tag{5.47}$$

and then we get

$$z = (-1)^{N-1} \prod_{i=1}^{N_e} \left\langle u_{n_i,k_i+\frac{2\pi}{Na}} \middle| u_{n_i,k_i} \right\rangle = \prod_{n=1}^{N_{occ}} \prod_{j=1}^{N} \left\langle u_{n,k_j+\frac{2\pi}{Na}} \middle| u_{n,k_j} \right\rangle \tag{5.48}$$

where we have assumed that the system is an insulator with N_{occ} fully occupied bands.

The overlap between periodic functions $\left\langle u_{n,k_j+\frac{2\pi}{Na}} \middle| u_{n,k_j} \right\rangle$ can be explicitly evaluated for $N \gg 1$, such that $\frac{2\pi}{Na} = \delta k$, yielding

$$\begin{aligned}
z &= (-1)^{N-1} \exp\left\{ \sum_{n=1}^{N_{occ}} \sum_{j=1}^{N} \log \langle u_{n,k_j+\delta k}|u_{n,k_j}\rangle \right\} \\
&= (-1)^{N-1} \exp\left\{ \sum_{n=1}^{N_{occ}} \sum_{j=1}^{N} \log\Big[\Big(\langle u_{n,k_j}| + \delta k_j\, \langle \partial_{k_j} u_{n,k_j}| \Big) |u_{n,k_j}\rangle \Big] \right\} \\
&= (-1)^{N-1} \exp\left\{ \sum_{n=1}^{N_{occ}} \sum_{j=1}^{N} \log\Big[1 + \delta k_j\, \langle \partial_{k_j} u_{n,k_j}|u_{n,k_j}\rangle \Big] \right\} \\
&\simeq (-1)^{N-1} \exp\left\{ \sum_{n=1}^{N_{occ}} \sum_{j=1}^{N} \delta k_j\, \langle \partial_{k_j} u_{n,k_j}|u_{n,k_j}\rangle \right\} \simeq (-1)^{N-1} \exp\left\{ \sum_{n=1}^{N_{occ}} \oint_{BZ} dk \langle \partial_k u_{nk}|u_{nk}\rangle \right\}.
\end{aligned}$$

Finally we find that, in one-dimensional insulating systems of non-interacting electrons, the expectation value of the $\hat{Z}$ operator is related to the Zak phase ϕ_{Zak} given in Eq. (1.64) by

$$z = (-1)^{N-1} e^{-i\phi_{\text{Zak}}}. \tag{5.49}$$

Since $\hat{Z}$ is a many-body operator, this construction naturally extends to interacting systems. Indeed, the quantization of the phase of z is a robust feature with respect to the addition of interactions, as long as the symmetries protecting the topological phase are preserved. In particular, for interacting centrosymmetric 1D insulators [163], one finds $z = 1$ or -1 (up to a size-dependent overall sign), which allows to distinguish topologically distinct phases.

Furthermore, for one-dimensional systems with time-reversal symmetry, this method allows to distinguish between $\mathbb{Z}_2$-even and $\mathbb{Z}_2$-odd insulators by calculating the expectation value of the spin-resolved many-body operator

$$\hat{Z}_\sigma = \exp\left(i \frac{2\pi}{Na} \sum_{j=1}^{N} x_j \hat{n}_{j,\sigma} \right) \tag{5.50}$$

where $\hat{n}_{j,\sigma}$ is the spin-projected electron density operator at the j-th site, located in x_j. In analogy with the case above, the expectation value z_σ of the spin-resolved many-body operator $\hat{Z}_\sigma$ is related to the spin-resolved Zak phase defined in Eq. (1.66).

5.3.2.2 Many-body marker for correlated $\mathbb{Z}_2$ topological insulators

Inspired by the operator in Eq. (5.50), Ref. [48] extended the method to two-dimensional $\mathbb{Z}_2$ time-reversal invariant insulators, providing a clear and practical criterion to distinguish between trivial and topological phases. It has already been discussed in Section 1.4 that, in the non-interacting limit, this class of systems can be characterized by the parity of the spin Chern number calculated over the occupied states of a single spin sector (either up or down) and that this approach can be extended even when the total spin operator $\hat{S}_z$ does not commute with the Hamiltonian.

In Ref. [48], the many-body operator $\hat{Z}_\sigma$ is generalized to finite clusters of any geometry and dimension as

$$\hat{Z}_\sigma(\delta\mathbf{k}) = \exp\left(i\,\delta\mathbf{k}\cdot\sum_{j=1}^{N}\mathbf{R}_j\,\hat{n}_{j,\sigma}\right) \tag{5.51}$$

where $\delta\mathbf{k}$ is a wavevector quantized according to the lattice geometry. For a square lattice with N sites, choosing $\delta k_x = \delta k_y = \frac{2\pi}{L}$ (where L is the linear dimension of the lattice) and defining the ratio

$$\rho_\sigma = \frac{\langle\Psi|\hat{Z}_\sigma(\delta k_x,\delta k_y)|\Psi\rangle}{\langle\Psi|\hat{Z}_\sigma(\delta k_x,0)|\Psi\rangle\langle\Psi|\hat{Z}_\sigma(0,\delta k_y)|\Psi\rangle} \tag{5.52}$$

one finds that, in the non-interacting limit where $|\Psi\rangle$ is a Slater determinant of Bloch states, this expression reduces to

$$\begin{aligned}
\rho_\sigma &= \prod_{\mathbf{q}}\frac{\langle u_{\mathbf{q}+\delta k_x,\sigma}|u_{\mathbf{q}-\delta k_y,\sigma}\rangle}{\langle u_{\mathbf{q}+\delta k_x,\sigma}|u_{\mathbf{q},\sigma}\rangle\langle u_{\mathbf{q},\sigma}|u_{\mathbf{q}-\delta k_y,\sigma}\rangle} \\
&= \prod_{\mathbf{q}}\Big[1-\delta k_x\delta k_y\big(\langle\partial_{q_x}u_{\mathbf{q},\sigma}|\partial_{q_y}u_{\mathbf{q},\sigma}\rangle - \langle\partial_{q_x}u_{\mathbf{q},\sigma}|u_{\mathbf{q},\sigma}\rangle\langle u_{\mathbf{q},\sigma}|\partial_{q_y}u_{\mathbf{q},\sigma}\rangle\big)\Big] \\
&= \exp\left\{-\int_{BZ}dq_xdq_y\big(\langle\partial_{q_x}u_{\mathbf{q},\sigma}|\partial_{q_y}u_{\mathbf{q},\sigma}\rangle - \langle\partial_{q_x}u_{\mathbf{q},\sigma}|u_{\mathbf{q},\sigma}\rangle\langle u_{\mathbf{q},\sigma}|\partial_{q_y}u_{\mathbf{q},\sigma}\rangle\big)\right\}.
\end{aligned}$$

The exponent can be identified as the integral over the Brillouin zone of the Berry curvature over the manifold of occupied states with spin σ, that is $-i\pi$ times the spin Chern number

$$\rho_\sigma = |\rho_\sigma|\exp\left(i\pi C_\sigma\right). \tag{5.53}$$

Depending on the symmetries of the model, ρ_σ may in general be complex, especially for finite system sizes. However, as shown in Ref. [48], its phase remains very close to either 0 or π, with

the quantization improving as the system size increases, even in the presence of interaction. This provides a simple and robust identification of the topological nature of the many-body ground state.

5.4 Variational Monte Carlo framework

Technological advancements in the 20th century have revealed fascinating physical phenomena such as superconductivity [164], superfluidity [165], and the fractional quantum Hall effect [166], which could not be adequately explained by simple mean-field theories and instead require an explicit treatment of electron–electron interactions. The choice of the method for studying strongly correlated systems is largely dictated by the dimensionality. Approaches in which the entire Hamiltonian matrix is stored in the computer are known as Exact Diagonalization (ED) methods. These methods provide exact and unbiased results and are therefore widely used as benchmarks, but their applicability is limited to small system sizes due to the exponential growth of the Hilbert space ($N_e \lesssim 20$ when iterative Lanczos-type approaches are used to obtain only the ground state and the low-energy excitations, instead of the full spectrum).

In one dimension, DMRG [167] is recognized as the dominant approach, yielding extremely accurate results to describe the ground state, especially for gapped systems, while analytical approaches such as bosonization [168] and the Renormalization Group [169] provide deep theoretical insight.

In two dimensions, the problem becomes more challenging: ED is restricted to very small clusters but remains crucial for benchmarking; DMRG is still useful on narrow cylinder geometries but becomes computationally expensive, and tensor network methods such as Projected Entangled Pair States (PEPS) [170], although designed for 2D systems, yet remain costly. Quantum Monte Carlo [171] can also be extremely powerful and scalable in 2D, but is limited by the sign problem in many relevant cases, such as many frustrated or fermionic systems. Mean-field approaches such as the Hartree–Fock method provide a simple and computationally inexpensive starting point, but generally fail to capture strong correlation effects. Extensions such as DMFT [172] incorporate local quantum fluctuations and are particularly successful in higher dimensions, although they neglect non-local correlations that are essential in low-dimensional systems.

In this context, Variational Monte Carlo (VMC) [173] represents a powerful and flexible approach, particularly appealing in both 1D and 2D, as it allows one to study large system sizes without encountering a sign problem, and to employ systematically improvable variational wavefunctions. For these reasons, it constitutes the method of choice in this work and will be discussed in detail in the following.

In this section, we begin by introducing the variational principle. We show how the expectation values of quantum operators with respect to a variational wavefunction can be evaluated within a Monte Carlo approach, based on sampling configurations from a given probability distribution, and we briefly recap the Metropolis algorithm employed for this purpose. Next, we introduce the Jastrow-Slater variational wavefunction, which will be used in the following chapters. Finally, we present the Stochastic reconfiguration method for optimizing the variational wavefunction, allowing for an accurate approximation of the interacting ground state within a chosen variational *Ansatz*.

5.4.1 Variational principle

In order to approximate the ground state of a many-body system, the VCM method takes advantage of the variational principle. For a general Hamiltonian $\hat{H}$, we consider a trial variational state $|\Psi_{var}\rangle$ that aims to approximate the true ground state $|\Psi_0\rangle$ of $\hat{H}$. The variational energy E_{var} is defined as the expectation value of the Hamiltonian over $|\Psi_{var}\rangle$

$$E_{var} = \frac{\langle \Psi_{var} | \hat{H} | \Psi_{var} \rangle}{\langle \Psi_{var} | \Psi_{var} \rangle}. \tag{5.54}$$

A key observation is that this quantity is bounded from below by the exact ground-state energy E_0. This can be shown by expanding the variational state in the basis of the Hamiltonian eigenstates, $|\Psi_{var}\rangle = \sum_n \langle \phi_n | \Psi_{var} \rangle |\phi_n\rangle$. Substituting this expansion into Eq. (5.54), the variational energy can be rewritten as

$$E_{var} = \sum_n E_n \frac{|\langle \phi_n | \Psi_{var} \rangle|^2}{\langle \Psi_{var} | \Psi_{var} \rangle} = E_0 + \sum_{n \neq 0} (E_n - E_0) \frac{|\langle \phi_n | \Psi_{var} \rangle|^2}{\langle \Psi_{var} | \Psi_{var} \rangle} \geq E_0. \tag{5.55}$$

This result expresses the *variational principle*, which provides a systematic method for approximating the ground-state wavefunction of a given Hamiltonian.

In principle, if one could vary $|\Psi_{var}\rangle$ over the entire Hilbert space and minimize the variational energy, then the lowest value would be E_0 and the corresponding state would coincide with the exact ground state of $\hat{H}$. In practice, however, such a procedure is not feasible for many-body systems, since the Hilbert space grows exponentially with the system size. Therefore, one restricts the search to a suitable subspace of the Hilbert space by introducing an *Ansatz* for the variational wavefunction. This corresponds to selecting a specific functional form for the wavefunction that depends on a set of variational parameters θ. Within this framework, a specific variational wavefunction $|\Psi_\theta\rangle$ is chosen and its parameters θ are optimized to minimize the corresponding variational energy E_θ.

Once the variational principle is established, the main challenge is to compute the variational energy efficiently. The analytical evaluation of Eq. (5.54) is only possible in a few cases, like

for example when $|\Psi_{var}\rangle$ is an uncorrelated Slater determinant constructed from single-electron orbitals. Otherwise, we have to devise a numerical technique to compute the variational energy, together with the energy derivatives with respect to the variational parameters, in order to determine the lowest-energy solution.

In the following, we will consider the case where the Hilbert space is discrete, since we will focus on interacting electrons on the lattice. We fix a complete many-body basis of states $\{|x\rangle\}$, where each element is specified by giving the positions (lattice site and orbital occupation) and the component of the spin along the z-axis of every electron. If the basis is taken to be orthogonal and normalized, then we can define the completeness relation $\sum_x |x\rangle \langle x| = \mathbb{1}$. Then, in general, given a variational state $|\Psi_\theta\rangle$ and a quantum operator $\hat{\mathcal{A}}$ the expectation value can be written as

$$\frac{\langle \Psi_\theta | \hat{\mathcal{A}} | \Psi_\theta \rangle}{\langle \Psi_\theta | \Psi_\theta \rangle} = \sum_x \frac{\langle \Psi_\theta | x \rangle \langle x | \hat{\mathcal{A}} | \Psi_\theta \rangle}{\langle \Psi_\theta | \Psi_\theta \rangle} = \sum_x \frac{|\langle x | \Psi_\theta \rangle|^2}{\langle \Psi_\theta | \Psi_\theta \rangle} \frac{\langle x | \hat{\mathcal{A}} | \Psi_\theta \rangle}{\langle x | \Psi_\theta \rangle}. \tag{5.56}$$

We can define the amplitude of the variational wavefunction on the state $|x\rangle$

$$\Psi_\theta(x) = \langle x | \Psi_\theta \rangle \tag{5.57}$$

and the following quantity

$$P_\theta(x) = \frac{|\Psi_\theta(x)|^2}{\langle \Psi_\theta | \Psi_\theta \rangle} \tag{5.58}$$

can be interpreted as a probability, since it is a non-negative quantity for all states $|x\rangle$ and is normalized $\sum_x P(x) = 1$. Moreover, we define the local observable

$$\mathcal{A}_l^\theta(x) = \frac{\langle x | \hat{\mathcal{A}} | \Psi_\theta \rangle}{\langle x | \Psi_\theta \rangle} = \sum_{x'} \langle x | \hat{\mathcal{A}} | x' \rangle \frac{\langle x' | \Psi_\theta \rangle}{\langle x | \Psi_\theta \rangle} = \sum_{x'} \langle x | \hat{\mathcal{A}} | x' \rangle \frac{\Psi_\theta(x')}{\Psi_\theta(x)}. \tag{5.59}$$

Notably, only the ratio between two amplitudes $\Psi_\theta(x')/\Psi_\theta(x)$ enters the computation of local observables, thereby allowing the use of unnormalized states. Using the definitions above, the expectation value of a quantum operator can be rewritten as the statistical average of the local observable $\mathcal{A}_l^\theta(x)$ over the probability distribution $P_\theta(x)$

$$\frac{\langle \Psi_\theta | \hat{\mathcal{A}} | \Psi_\theta \rangle}{\langle \Psi_\theta | \Psi_\theta \rangle} = \sum_x P_\theta(x) \mathcal{A}_l^\theta(x). \tag{5.60}$$

This quantity can be evaluated through a stochastic estimation, by calculating the local observable over M "representative" configurations $\{x_i\}$ which are randomly generated according to the desired probability $P_\theta(x)$

$$\frac{\langle \Psi_\theta | \hat{\mathcal{A}} | \Psi_\theta \rangle}{\langle \Psi_\theta | \Psi_\theta \rangle} \approx \frac{1}{M} \sum_{i=1}^{M} \mathcal{A}_l^\theta(x_i). \tag{5.61}$$

According to the central limit theorem, the statistical error made in this estimate of the expectation value scales as $\frac{1}{\sqrt{M}}$, independently of the dimension of the original Hilbert space, so it provides a controlled approximation method to compute the expectation values. It is also worth noting that evaluating the local observable in Eq. (5.59) for a given configuration x_i generally involves a sum over an exponentially large number of configurations $\{x'\}$. However, physically relevant observables are typically local, and the number of configurations x' such that $\langle x_i|\,\hat{\mathcal{A}}\,|x'\rangle \neq 0$ scales polynomially with the system size.

5.4.2 The Metropolis algorithm

To sample configurations $\{x_i\}$ from a probability distribution $P_\theta(x)$ we employ the Metropolis algorithm to create Markov chains of configurations.

A Markov chain is a sequence of configurations generated stochastically, where each configuration in the sequence is obtained from the previous one by making random changes. Any Markov chain is characterized by a transition (conditional) probability $T_\theta(x_{i+1}|x_i)$ of randomly generating a configuration x_{i+1} starting from configuration x_i. It can be shown that a sufficient condition to ensure that, regardless of the initial configuration, the sequence will eventually converge to the correct distribution $P_\theta(x)$ is the so-called *detailed balance* condition

$$P_\theta(x_i)\,T_\theta(x_{i+1}|x_i) = P_\theta(x_{i+1})\,T_\theta(x_i|x_{i+1}) \qquad \forall\ x_i. \tag{5.62}$$

The Metropolis-Hastings algorithm [174, 175] indicates a specific choice for the $T_\theta(x_{i+1}|x_i)$. As a first step, it splits the transition probability into two processes

$$T_\theta(x_{i+1}|x_i) = k(x_{i+1}|x_i)\,A_\theta(x_{i+1}, x_i), \tag{5.63}$$

where $k(x_{i+1}|x_i)$ is the proposal kernel, which proposes the new configuration x_{i+1} given x_i, and $A_\theta(x_{i+1}, x_i)$ is the acceptance probability for accepting the proposal x_{i+1}. Then, the simplest choice of acceptance probability that satisfies the detailed balance condition is given by

$$A_\theta(x_{i+1}, x_i) = \min\left\{1, \frac{P_\theta(x_{i+1})\,k(x_i|x_{i+1})}{P_\theta(x_i)\,k(x_{i+1}|x_i)}\right\}. \tag{5.64}$$

In most cases, as in the original work by Metropolis *et al.* [174] and as we will consider in our implementation, it is useful to consider symmetric proposal kernels $k(x_{i+1}|x_i) = k(x_i|x_{i+1})$, and this further simplifies the acceptance probability

$$A_\theta(x_{i+1}, x_i) = \min\left\{1, \frac{P_\theta(x_{i+1})}{P_\theta(x_i)}\right\}. \tag{5.65}$$

A crucial point is that this algorithm applied to the VMC permits to know the probability distribution $P_\theta(x)$, and so the variational wavefunction $\Psi_\theta(x)$, up to a normalization constant, since only the ratio $P_\theta(x_{i+1})/P_\theta(x_i)$ appears in the acceptance probability relation. Indeed, in performing a Metropolis step in the construction of Markov chains of configurations $\{x_i\}$, it is sufficient to evaluate the variational wavefunction in the two configurations x_{i+1} and x_i and compute the ratio

$$\frac{P_\theta(x_{i+1})}{P_\theta(x_i)} = \left| \frac{\Psi_\theta(x_{i+1})}{\Psi_\theta(x_i)} \right|^2 . \tag{5.66}$$

Drawing a random number p uniformly distributed in $[0, 1)$, if $p < P_\theta(x_{i+1})/P_\theta(x_i)$, then the new configuration x_{i+1} is accepted; otherwise, it is rejected.

5.4.3 The Jastrow-Slater wavefunction

Our *Ansatz* for the variational wavefunction is the Jastrow-Slater wavefunction, which consists of applying the Jastrow factor to the non-interacting ground state of a fermionic auxiliary Hamiltonian $\hat{H}_{aux}$ which can be written as a Slater determinant $|\Phi_0\rangle$. In particular, the variational wavefunction is defined as

$$|\Psi_{JS}\rangle = \hat{\mathcal{J}}_s \, \hat{\mathcal{J}}_d \, \hat{\mathcal{P}}_{\{S^z=0\}} \, |\Phi_0\rangle \, , \tag{5.67}$$

where $\hat{\mathcal{J}}_s$ and $\hat{\mathcal{J}}_d$ are the multi-orbital generalizations of the spin-spin and density-density Jastrow factors introduced in Section 5.2

$$\hat{\mathcal{J}}_d = \exp\left[-\frac{1}{2} \sum_{i,j} \sum_{\alpha,\beta} v_{i,j}^{\alpha,\beta} \hat{n}_{i,\alpha} \hat{n}_{j,\beta} \right], \tag{5.68}$$

$$\hat{\mathcal{J}}_s = \exp\left[-\frac{1}{2} \sum_{i,j} \sum_{\alpha,\beta} u_{i,j}^{\alpha,\beta} \hat{S}_{i,\alpha}^z \hat{S}_{j,\beta}^z \right], \tag{5.69}$$

where the pseudo-potentials $u_{i,j}^{\alpha,\beta}$ and $v_{i,j}^{\alpha,\beta}$ are variational parameters, whose total number scales as $O(N^2)$. For a translationally invariant model, the pseudo-potentials depend only on the spatial distance between sites i and j, thus the number of parameters reduces $O(N)$. In addition, we set $v_{i,j}^{\alpha,\beta} = v_{i,j}^{\beta,\alpha} = v_{i,j}^{inter}$ and $u_{i,j}^{\alpha,\beta} = u_{i,j}^{\beta,\alpha} = u_{i,j}^{inter}$ for $\alpha \neq \beta$ and fix the intra-orbital terms to be the same for the different orbitals, that is $v_{i,j}^{\alpha,\beta} = v_{i,j}^{intra}$ and $u_{i,j}^{\alpha,\beta} = u_{i,j}^{intra}$ for $\alpha = \beta$.

Furthermore, $\mathcal{P}_{\{S^z=0\}}$ is the projection onto the subspace with $S^z_{\text{tot}} = \sum_{i,\alpha} \hat{S}^z_{i,\alpha} = 0$, which enforces the conservation of the total spin S^z.

Finally, $|\Phi_0\rangle$ is the Slater determinant constructed from single-particle orbitals that diagonalize a non-interacting auxiliary Hamiltonian $\hat{H}_{aux} = \sum_{i,j} \tilde{h}_{i,j} \hat{c}_i^\dagger \hat{c}_j$, depending on a set of variational parameters $\tilde{h}_{i,j}$ that can be used to impose symmetries on the variational wavefunction.

One advantage of considering such a wavefunction within the VMC approach is that the calculations can be made extremely efficient. In particular, whenever the Jastrow factors are diagonal in the chosen basis of states $\{|x\rangle\}$, the wavefunction amplitude reads

$$\Psi_{JS}(x) = \langle x|\Psi_{JS}\rangle = \mathcal{J}_s(x)\,\mathcal{J}_d(x)\,\langle x|\Phi_0\rangle\,. \tag{5.70}$$

Here, $\mathcal{J}(x)$ denotes the value of a Jastrow operator on the configuration $|x\rangle$, i.e., $\hat{\mathcal{J}}\,|x\rangle = \mathcal{J}(x)\,|x\rangle$, and the configurations $|x\rangle$ are sampled among those that conserve the total spin $S^z = 0$. Since the Jastrow factors are diagonal in the basis $\{|x\rangle\}$, $\mathcal{J}(x)$ can be evaluated in $O(N^2)$ operations; in contrast, applying $\hat{\mathcal{J}}\,|x\rangle$ in a non-diagonal representation would generate an exponentially large number of states. Furthermore, the computation of $\langle x|\Phi_0\rangle$ typically requires $O(N^3)$ operations due to the determinant.

Evaluating the variational wavefunction on the configuration $|x\rangle$ is fundamental for constructing the Markov chains of configurations and for calculating the local observable in Eq. (5.59) Indeed the ratio between amplitudes on two configurations is required both in the evaluation of the probability of accepting a Monte Carlo step

$$\frac{P(x')}{P(x)} = \left|\frac{\Psi_{JS}(x')}{\Psi_{JS}(x)}\right|^2, \tag{5.71}$$

and in the sum over configuration x' in the local observable

$$\mathcal{A}_l(x) = \sum_{x'} \langle x|\,\hat{\mathcal{A}}\,|x'\rangle\,\frac{\Psi_{JS}(x')}{\Psi_{JS}(x)}. \tag{5.72}$$

In Appendix C, it is shown how the computational cost of this ratio can be reduced, through a *fast-update* algorithm for the Jastrow-Slater wavefunction, yielding $O(N^2)$ scaling for the determinant and $O(N)$ for the Jastrow factors.

5.4.4 The Stochastic Reconfiguration optimization method

Up to now, we have focused on how to stochastically estimate the expectation values of quantum operators with respect to a certain variational wavefunction. It is important to note that this is performed with fixed variational parameters. In the following, we will focus on how these parameters are optimized to obtain the wavefunction that minimizes the variational energy. Specifically, we will discuss the *Stochastic Reconfiguration* method [176, 177], which is a gradient-based approach.

In a gradient-based optimization approach, the fundamental ingredient is the evaluation of the gradient of the variational energy E_θ with respect to the p parameters, namely $F_\alpha = -\partial E_\theta/\partial\theta_\alpha$

with $\alpha = 1, \dots, p$. From previous sections, by combining Eqs. (5.56) and (5.59), the expectation value of the Hamiltonian $\hat{H}$ with respect to the variational state $|\Psi_\theta\rangle$ can be written ad

$$E_\theta = \frac{\langle\Psi_\theta|\hat{H}|\Psi_\theta\rangle}{\langle\Psi_\theta|\Psi_\theta\rangle} = \sum_{x,x'} \langle x|\, \hat{H}\, |x'\rangle\, \frac{\Psi^*_\theta(x)\Psi_\theta(x')}{\langle\Psi_\theta|\Psi_\theta\rangle}. \tag{5.73}$$

By performing the derivative of the previous equation with respect to the parameter θ_α and assuming real valued parameters[15], it can be shown that the expression for the gradient of the variational energy is

$$F_\alpha = -\frac{\partial E_\theta}{\partial \theta_\alpha} = -2\,\Re\Big\{ \frac{\langle\Psi_\theta|\hat{H}\hat{O}^\alpha|\Psi_\theta\rangle}{\langle\Psi_\theta|\Psi_\theta\rangle} - \frac{\langle\Psi_\theta|\hat{H}|\Psi_\theta\rangle}{\langle\Psi_\theta|\Psi_\theta\rangle} \frac{\langle\Psi_\theta|\hat{O}^\alpha|\Psi_\theta\rangle}{\langle\Psi_\theta|\Psi_\theta\rangle} \Big\} \tag{5.74}$$

where we have introduced the local operator $\hat{O}^\alpha$ defined by diagonal matrix elements $O^\alpha(x)$ which are the logarithmic derivatives of the wavefunction $\Psi_\theta(x)$ with respect to the variational parameter θ_α

$$\langle x|\hat{O}^\alpha|x'\rangle = \delta_{x,x'} O^\alpha(x)\,, \tag{5.75}$$

$$O^\alpha(x) = \frac{1}{\Psi_\theta(x)} \frac{\partial \Psi_\theta(x)}{\partial \theta_\alpha} = \frac{\partial \ln \Psi_\theta(x)}{\partial \theta_\alpha}. \tag{5.76}$$

The expression in Eq. (5.74) for F_α highlights the fact that the gradient of the energy can be seen as a correlation function between the Hamiltonian $\hat{H}$ and the local operator $\hat{O}^\alpha$. By denoting with $\langle\cdot\rangle = \frac{\langle\Psi_\theta|\,\cdot\,|\Psi_\theta\rangle}{\langle\Psi_\theta|\Psi_\theta\rangle}$ the expectation value of a generic operator over the state $|\Psi_\theta\rangle$, we have

$$F_\alpha = -2\,\Re\Big\{ \frac{\langle\Psi_\theta|\hat{H}\big[\hat{O}^\alpha - \langle\hat{O}^\alpha\rangle\big]|\Psi_\theta\rangle}{\langle\Psi_\theta|\Psi_\theta\rangle} \Big\} = -2\,\Re\Big\{ \frac{\sum_x \langle\Psi_\theta|\hat{H}|x\rangle\, \langle x|\big[\hat{O}^\alpha - \langle\hat{O}^\alpha\rangle\big]|\Psi_\theta\rangle}{\langle\Psi_\theta|\Psi_\theta\rangle} \Big\} \tag{5.77}$$

$$= -2\,\Re\Big\{ \sum_x E^*_l(x)\big[O^\alpha_l(x) - \langle\hat{O}^\alpha\rangle\big] \frac{|\Psi_\theta(x)|^2}{\langle\Psi_\theta|\Psi_\theta\rangle} \Big\} \tag{5.78}$$

where $E_l(x)$ is the local energy, i.e., the local observable for the operator $\hat{H}$ with respect to $|\Psi_\theta\rangle$ defined in Eq. (5.59). Note that the local energy can be complex when calculated on a single configuration $|x\rangle$. Analogously, $O^\alpha_l(x)$ denotes the local observable associated with the operator $\hat{O}^\alpha$. Then, F_α can be stochastically evaluated as

$$F_\alpha \approx -2\,\Re\Big\{ \frac{1}{M} \sum_{i=1}^{M} E^*_l(x_i)\big[O^\alpha_l(x_i) - \langle\hat{O}^\alpha\rangle\big] \Big\}, \tag{5.79}$$

with

$$\langle\hat{O}^\alpha\rangle \approx \frac{1}{M} \sum_{i=1}^{M} O^\alpha_l(x_i). \tag{5.80}$$

[15] If the variational wave function is defined with complex-valued parameters, the latter can be treated as couples of independent real-valued parameters.

The knowledge of the energy gradient allows us to employ the gradient-descent method to update the variational parameters θ_α, for $\alpha = 1, \dots, p$, as

$$\theta'_\alpha = \theta_\alpha + \delta\theta_\alpha = \theta_\alpha + \gamma\, F_\alpha, \tag{5.81}$$

where γ is an arbitrary small constant, known as the learning rate. We show that the gradient-descent method converges to a minimum of the energy, where $F_\alpha = 0$. Indeed, for a small variation of the variational parameters, the variational energy $E_{\theta'}$, calculated on the wavefunction $|\Psi_{\theta'}\rangle$ with the updated parameters θ'_α, can be expanded to linear order in γ

$$E_{\theta'} = E_\theta + \sum_{\alpha=1}^{p} \frac{\partial E_\theta}{\partial \theta_\alpha}\delta\theta_\alpha + O(\gamma^2) = E_\theta - \gamma \sum_{\alpha=1}^{p} F_\alpha^2 + O(\gamma^2). \tag{5.82}$$

Therefore, for sufficiently small γ, we find that the parameter update given by Eq. (5.81) yields a decrease in the energy

$$E_{\theta'} - E_\theta = -\gamma \sum_{\alpha=1}^{p} F_\alpha^2 \leq 0 \tag{5.83}$$

with the equality held only when $F_\alpha = 0$. Thus, by iteratively applying the parameter update, the energy decreases monotonically, ensuring convergence to a minimum.

Within the plain gradient-descent method, the variation of the parameters $\boldsymbol{\delta\theta} = (\delta\theta_1, \dots, \delta\theta_p)$ is parallel to the energy gradient $\boldsymbol{F} = (F_1, \dots, F_p)$. This argument is well justified when the wavefunction depends linearly on the parameters, but it may become inefficient when the dependence is highly non-linear, as in the Jastrow factors. In such situations, a small change in some variational parameters can lead to a significant change in the wavefunction and physical quantities, whereas variations in other parameters may only weakly affect the wavefunction. To overcome this issue, the convergence to the minimum of the variational energy can be improved by updating the parameters in a non-uniform way, effectively reweighting their contributions. This is the central idea of the Stochastic Reconfiguration (SR) method, which accelerates convergence by applying a preconditioning matrix to the gradient F_α.

In addition to estimating F_α as in the plain gradient-descent case, one also needs to compute the matrix $\mathbf{S}$, which defines a metric in the space of wavefunctions $|\Psi_\theta\rangle$. It is defined as

$$S_{\alpha\beta} = \Re\left\{ \frac{\langle\Psi_\theta|\left[\hat{O}^{\alpha\dagger} - \langle\hat{O}^\alpha\rangle^*\right]\left[\hat{O}^\beta - \langle\hat{O}^\beta\rangle\right]|\Psi_\theta\rangle}{\langle\Psi_\theta|\Psi_\theta\rangle} \right\} = \Re\left\{ \langle\hat{O}^{\alpha\dagger}\hat{O}^\beta\rangle - \langle\hat{O}^\alpha\rangle^* \langle\hat{O}^\beta\rangle \right\} \tag{5.84}$$

$$\approx \Re\left\{ \frac{1}{M}\sum_{i=1}^{M} Q_l^{\alpha\beta}(x_i) - \langle\hat{O}^\alpha\rangle\langle\hat{O}^\beta\rangle \right\}, \tag{5.85}$$

where $Q_l^{\alpha\beta}(x_i)$ denotes the local value of the observable $\hat{Q}^{\alpha\beta} = \hat{O}^{\alpha\dagger}\hat{O}^\beta$.

The matrix $S_{\alpha\beta}$ can be interpreted as a covariance matrix of the operators $\hat{O}^\alpha$ evaluated on the wavefunction $|\Psi_\theta\rangle$, and it is positive semi-definite by definition. However, it is possible for $S_{\alpha\beta}$ to have very small or even vanishing eigenvalues, for instance when there is a redundancy in the wavefunction parametrization. To ensure that the matrix $S_{\alpha\beta}$ is invertible, a regularization is required, for example by adding a small bias ϵ to the diagonal elements

$$\tilde{S}_{\alpha\beta} = S_{\alpha\beta} + \epsilon\,\delta_{\alpha\beta}. \tag{5.86}$$

The Stochastic Reconfiguration method can then be implemented by performing gradient-descent using $\tilde{S}^{-1}_{\alpha\beta}$ as a preconditioner

$$\theta'_\alpha = \theta_\alpha + \gamma \sum_\beta \tilde{S}^{-1}_{\alpha\beta} F_\beta. \tag{5.87}$$

Because of the positive semi-definiteness of $\tilde{S}_{\alpha\beta}$, also its inverse $\tilde{S}^{-1}_{\alpha\beta}$ is positive semi-definite, ensuring that the variational energy decreases monotonically within the SR framework as well.

Chapter 6

Interaction-induced phases in the Bernevig-Hughes-Zhang model

Topological phases in solid-state systems have been widely studied, especially in one and two spatial dimensions, in the regime of non-interacting electrons, where the classification of topologically distinct phases hinges on topological invariants, integer numbers that can be computed from the eigenstates of single-particle Hamiltonians. At the same time, the electron-electron interaction may have strong effects in low dimensions, leading to a variety of phenomena that cannot be captured within the independent-electron picture; well-established examples are Tomonaga-Luttinger [178] or Luther-Emery [179] liquids in one dimension and Mott insulators [180] or the fractional quantum Hall effect [166] in two dimensions. Recently, a boost in the field has been given by the discovery of Moiré materials (e.g., twisted bilayer graphene [132]), which revealed the presence of a wide variety of phases when varying the filling factor of the Moiré bands [181]. Actually, these are examples in which strong electron correlation exists on top of a band structure that features topological properties, thus giving general motivation to understand the fate of topological insulators beyond the band theory, namely when the Coulomb repulsion is included. A central challenge is to assess the possibility that unconventional (not mediated by phonons) superconductivity may emerge from a correlated topological insulator upon doping. Another significant, and more focused, objective is to examine the impact of electron-electron interactions on a topological insulator. In this framework, it is of great interest to study the nature of phase transitions between trivial, topological, and Mott insulators, potentially involving additional phases that may intrude on them. In fact, in the case of non-interacting fermions, the transition between a topological insulator and a trivial gapped phase is generally continuous, characterized by a single semi-metallic point at which the band gap closes, provided that the symmetries protecting the topology of the system are preserved.

Recently, several studies have investigated the role of electronic correlations in two-dimensional topological insulators, including the Kane–Mele [182–188] and Bernevig–Hughes–Zhang (BHZ) models [189–192]. These works have shown that on-site interactions can strongly affect the stability of topological phases and may substantially modify the nature of the transition between trivial and topological insulators. In particular, for sufficiently strong interactions, this transition can become first order [191–193].

At the same time, one-dimensional systems have attracted increasing interest. Despite their reduced dimensionality, they can host a variety of topological phases closely related to those found in higher-dimensional systems, while being more accessible from a numerical point of view. This makes them a valuable setting for studying the interplay between topology and electronic correlations, as the reduced complexity of 1D systems simplifies analysis. In this direction, interacting Su–Schrieffer–Heeger [194, 195] and one-dimensional BHZ [158, 196] models have been studied using exact diagonalization (ED) and density-matrix renormalization group (DMRG) methods.

In this chapter, we present a variational Monte Carlo study of the BHZ model in the presence of strong electron–electron interactions, using a Jastrow–Slater wavefunction. We first consider the one-dimensional version of the model, which is interesting in its own right and, at the same time, provides a useful benchmark for the variational approach. The insights gained in this setting are then used as a starting point for the two-dimensional problem, where numerically exact methods such as ED and DMRG become much less affordable, while variational Monte Carlo offers a flexible and scalable framework to investigate the strongly correlated regime.

The one-dimensional results, presented in Section 6.1, are largely based on Ref. [14]. Our numerical calculations, based on a Jastrow–Slater variational wavefunction and corroborated by DMRG, reveal a rich phase diagram in which electronic correlations do not simply renormalize the non-interacting picture, but give rise to new emergent phases. We then extend our method to the two-dimensional case in Section 6.2, where long-range ordered phases can be stabilized, and report the emergence of an excitonic insulating phase, consistent with previous studies based on different methods.

6.1 The interacting one-dimensional BHZ model

We study a one-dimensional fermionic model with two orbitals per site, as the one introduced in Refs. [158, 196]. We consider a chain of length L (in units of lattice spacing a), i.e., with L sites, where the non-interacting Hamiltonian corresponds to the 1D version of the BHZ model [6]

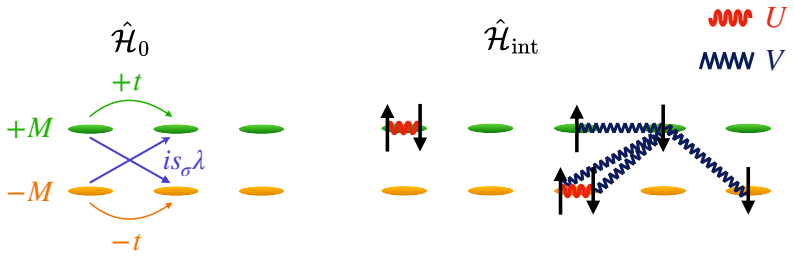


Figure 6.1: Illustration of the terms defining the Hamiltonian in Eq. (6.3) under investigation. The two orbitals on each site are represented by yellow and green ellipses; on the left part, on-site energies ($\pm M$), intra-orbital ($\pm t$), and inter-orbital ($is_\sigma\lambda$) hoppings are depicted; on the right part, intra-orbital (U) and nearest-neighbor (V) interactions are shown.

presented in Section 1.4.2 and reads

$$\hat{\mathcal{H}}_0 = \sum_{j=1}^{L}\sum_{\eta,\sigma}\left[M\,\eta\,\hat{n}_{j,\eta,\sigma} + (t\,\eta\,\hat{c}^\dagger_{j+1,\eta,\sigma}\hat{c}_{j,\eta,\sigma} + is_\sigma\lambda\,\hat{c}^\dagger_{j+1,\eta,\sigma}\hat{c}_{j,-\eta,\sigma} + \text{h.c.})\right], \tag{6.1}$$

where $\hat{c}^\dagger_{j,\eta,\sigma}$ ($\hat{c}_{j,\eta,\sigma}$) is the creation (annihilation) operator of an electron at the j-th site on the orbital $\eta = \pm 1$ and with spin σ, while $\hat{n}_{j,\eta,\sigma} = \hat{c}^\dagger_{j,\eta,\sigma}\hat{c}_{j,\eta,\sigma}$ is the corresponding local density operator. Here, $s_\uparrow = +1$ and $s_\downarrow = -1$. In addition, the density per orbital is defined by $\hat{n}_{j,\eta} = \sum_\sigma \hat{n}_{j,\eta,\sigma}$, while the total density on site j is $\hat{n}_j = \sum_{\eta,\sigma}\hat{n}_{j,\eta,\sigma}$. Following Ref. [158], the interacting part contains an intra-orbital on-site interaction U and a nearest-neighbor density-density repulsion V

$$\hat{\mathcal{H}}_{\rm int} = U\sum_{j=1}^{L}\sum_{\eta}\hat{n}_{j,\eta,\uparrow}\hat{n}_{j,\eta,\downarrow} + V\sum_{j=1}^{L}\hat{n}_j\hat{n}_{j+1}. \tag{6.2}$$

Specifically, Ref. [158] investigates the effect of the nearest-neighbor Coulomb interaction, which favors a charge-density-wave (CDW) insulating phase, using DMRG calculations with open boundary conditions. They show that the transition between the topological and CDW insulators becomes first-order for a sufficiently large on-site (intra-orbital) interaction. However, only a limited portion of the phase diagram was explored, leaving several aspects still to be investigated.

In the following, we consider the Hamiltonian

$$\hat{\mathcal{H}}_{1D} = \hat{\mathcal{H}}_0 + \hat{\mathcal{H}}_{\rm int} \tag{6.3}$$

with periodic-boundary conditions at half filling, i.e., with a fixed total number of electrons $N_e = 2L$, and restrict the analysis to $M \geq 0$ and $t > 0$. The main results of the study can be summarized as follows.

- (i) The inclusion of a finite U on top of the topological insulator gives rise to the Haldane state (where each orbital is singly occupied and the low-energy sector is described by a spin $S = 1$ chain); notably, the spin string-order parameter is already finite for $U = 0$.
- (ii) An insulating phase with *gapless* spin excitations intrudes between trivial and topological phases at finite values of U; this intermediate phase is particularly interesting since it cannot be derived within a simple strong-coupling limit.
- (iii) The presence of a nearest-neighbor interaction V induces density disproportionations: when V dominates all the other energy scales, a fully gapped CDW is obtained, adiabatically connected to the atomic limit in which sites with 4 electrons alternate with empty sites (this phase is dubbed CDW_{4-0}); in addition, in a region around $V/U \approx 1/4$ and $M/U \approx 1/2$, a different CDW exists and can be adiabatically connected to the atomic limit in which sites with 3 electrons alternate with singly-occupied sites; here, the spin degrees of freedom are governed by an effective spin $S = 1/2$ Heisenberg Hamiltonian, thus leading to *gapless* spin excitations (this phase is dubbed CDW_{3-1}).

These results are demonstrated by using Jastrow-Slater wavefunction and variational Monte Carlo techniques introduced in Section 5.4; furthermore, DMRG calculations on the same clusters have been performed, corroborating the Monte Carlo results.

6.1.1 The symmetries of the model

The model of Eq. (6.3) is invariant under a few local transformations. The first one is the (anti-unitary) time reversal (TR) symmetry, defined by

$$\mathcal{T}_R\, \hat{c}^\dagger_{j,\eta,\uparrow}\, \mathcal{T}_R^{-1} = +\hat{c}^\dagger_{j,\eta,\downarrow}, \tag{6.4}$$

$$\mathcal{T}_R\, \hat{c}^\dagger_{j,\eta,\downarrow}\, \mathcal{T}_R^{-1} = -\hat{c}^\dagger_{j,\eta,\uparrow}. \tag{6.5}$$

The second one is a (unitary) spin-flip, with a sign depending on the orbital (SF+η sign)

$$\mathcal{F}\, \hat{c}^\dagger_{j,\eta,\uparrow}\, \mathcal{F}^{-1} = \eta\, \hat{c}^\dagger_{j,\eta,\downarrow}, \tag{6.6}$$

$$\mathcal{F}\, \hat{c}^\dagger_{j,\eta,\downarrow}\, \mathcal{F}^{-1} = \eta\, \hat{c}^\dagger_{j,\eta,\uparrow}. \tag{6.7}$$

At half filling, the Hamiltonian is also invariant under a (unitary) particle-hole transformation, with orbital flip (η-PH)

$$\mathcal{P}\, \hat{c}^\dagger_{j,\eta,\sigma}\, \mathcal{P}^{-1} = \hat{c}_{j,-\eta,\sigma}. \tag{6.8}$$

In addition, the Hamiltonian in Eq. (6.3) is invariant under a $U(1)$ spin symmetry

$$\mathcal{U}\, \hat{c}^\dagger_{j,\eta,\sigma}\, \mathcal{U}^{-1} = e^{i\theta_\sigma}\, \hat{c}^\dagger_{j,\eta,\sigma}, \tag{6.9}$$

and lattice symmetries, notably translation (T) and inversion with a sign depending on the orbital (I+η sign)

$$\mathcal{T}\,\hat{c}^{\dagger}_{j,\eta,\sigma}\,\mathcal{T}^{-1} = \hat{c}^{\dagger}_{j+1,\eta,\sigma}, \tag{6.10}$$

$$\mathcal{I}\,\hat{c}^{\dagger}_{j,\eta,\sigma}\,\mathcal{I}^{-1} = \eta\,\hat{c}^{\dagger}_{L+2-j,\eta,\sigma}. \tag{6.11}$$

6.1.2 The non-interacting and the "atomic" limit

In the presence of periodic-boundary conditions, the non-interacting Hamiltonian in Eq. (6.1) can be diagonalized by a Fourier transformation. In momentum space, the corresponding Bloch Hamiltonian $H_0(k)$ can be written in terms of Pauli matrices in the spin $\boldsymbol{\sigma}$ and orbital $\boldsymbol{\tau}$ spaces

$$H_0(k) = [2t\cos(k) + M]\tau_z \otimes \sigma_0 + 2\lambda\sin(k)\tau_x \otimes \sigma_z, \tag{6.12}$$

where σ_0 denotes the 2×2 identity matrix. Since $H_0(k)$ is diagonal in the spin sector, it decomposes into two independent blocks, one for each spin projection. The two blocks are related by TR symmetry and have the same energy spectrum

$$E_k = \pm\sqrt{[2t\cos(k) + M]^2 + [2\lambda\sin(k)]^2}. \tag{6.13}$$

At half filling, corresponding to two electrons per site on average, the lower bands are completely occupied and trivial and topological phases are obtained for $M/t > 2$ and $M/t < 2$, respectively. These two cases can be distinguished by the spin-resolved Zak phase ϕ^{σ}_{Zak} calculated by considering the eigenstates of either the spin up or down blocks of $H_0(k)$. Indeed, because of TR symmetry, the total Zak phase computed on the full occupied states is trivial, while the Zak phase of a single spin sector can still detect the band topology [21]. In particular, one finds that $\phi^{\sigma}_{\mathrm{Zak}} = 0$ in the trivial phase, whereas $\phi^{\sigma}_{\mathrm{Zak}} = \pi$ in the topological one (modulus 2π).

It is instructive to consider the "atomic" limit of the 1D BHZ model, i.e., the case with no hopping terms ($t = \lambda = 0$) and in the presence of strong couplings U and V. The phase diagram for the half-filled case is shown in Figure 6.2.

Here, four distinct states are obtained: two of them have uniform density (i.e., two electrons on each site), while the other two have density disproportionations. For moderate values of V and large on-site energy M, a Trivial insulator is stabilized, with two electrons in the same orbital (the one having a negative on-site energy). When M is small, the ground state has one electron on each orbital, thus having an exponentially large degeneracy (2^{2L}) due to the spin component of each electron. Between these two cases, the CDW_{3-1} state is stabilized; also here a large degeneracy is present (2×2^{L}), due to the singly occupied orbitals and the two-fold degeneracy due to translations. Finally, for large V interactions, the CDW_{4-0} state becomes the

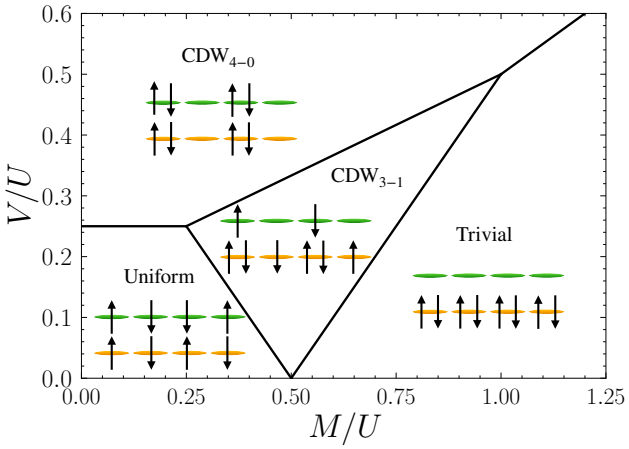


Figure 6.2: Phase diagram in the atomic limit, with $t = \lambda = 0$. The Uniform and Trivial phases have two electrons on each site; in the former, electrons occupy different orbitals (with an arbitrary spin configuration), while in the latter they reside in the same orbital (the one with the lowest on-site energy). The other two phases (CDW_{4-0} and CDW_{3-1}) have non-uniform density patterns; within the CDW_{4-0}, sites with 4 electrons alternate with empty sites, and in the CDW_{3-1} there is an alternation between sites with 1 and 3 electrons (and an arbitrary spin configuration). In this case, all transition lines are first-order.

lowest-energy configuration; this state is fully gapped, while being two-fold degenerate due to the breaking of translation symmetry.

In order to fully specify the strong-coupling phase diagram, we have to assess the spin state in the two regions (Uniform and CDW_{3-1}) where an exponential degeneracy is present at $t = \lambda = 0$. This goal can be accomplished by using second-order perturbation theory in the hopping amplitudes t and λ, giving rise to Heisenberg-like models, written in terms of the orbital-resolved spin$-1/2$ operators

$$\hat{S}^{\alpha}_{j,\eta} = \frac{1}{2} \sum_{\sigma,\sigma'} \hat{c}^{\dagger}_{j,\eta,\sigma} \tau^{\alpha}_{\sigma,\sigma'} \hat{c}^{\dagger}_{j,\eta,\sigma'} \tag{6.14}$$

where τ^{α} indicates one of the three Pauli matrices for $\alpha = x$, y, and z.

Let us first consider the CDW_{3-1} phase, defined by the inequalities $|U - 2M| < 2V$ and $U + 2M > 6V$, where each site j hosts a total spin $S = 1/2$. The ground-state energy per site at $t = \lambda = 0$ is $E_0 = 3V + \frac{U}{2} - M$. Virtual hoppings of amplitude t, which do not modify the global orbital occupancy, are always possible, giving a constant contribution to the energy per site $\Delta E_t = -\frac{2t^2}{3V}$. Analogously an inter-orbital hopping of amplitude $is_{\sigma}\lambda$ from a doubly occupied orbital to an empty one gives a constant energy per site $\Delta E_{\lambda} = -\frac{2\lambda^2}{3V-U+2M}$. Instead, the inter-orbital hopping of the same amplitude $is_{\sigma}\lambda$ between singly occupied orbitals favors antiferromagnetic ordering and gives a term in the effective spin Hamiltonian reproducing the

usual spin-1/2 Heisenberg model

$$\hat{\mathcal{H}}_{CDW_{3-1}} = J_{3-1} \sum_{j=1}^{L} \left[\hat{\mathbf{S}}_j \cdot \hat{\mathbf{S}}_{j+1} - \frac{1}{4} \right], \tag{6.15}$$

where $\hat{\mathbf{S}}_j = \hat{\mathbf{S}}_{j,+} + \hat{\mathbf{S}}_{j,-}$ is the total spin operator on the j-th site and

$$J_{3-1} = \frac{2\lambda^2}{U - 2M + 3V} + \frac{2\lambda^2}{U + 2M - 5V}. \tag{6.16}$$

This form of the effective Hamiltonian justifies the presence of gapless spin excitations in CDW_{3-1} phase.

The case of the Uniform region is different, since there are two $S = 1/2$ spins on different orbitals. The energy per site at $t = \lambda = 0$ is $E_0 = 4V$ and the two inequalities $U > 4V$ and $U > 2V + 2M$ hold in this phase. Every virtual hopping between neighboring sites favors antiferromagnetic ordering both on the same orbital and on different orbitals giving an effective Hamiltonian of the form

$$\hat{\mathcal{H}}_U = J \sum_{j=1}^{L} \sum_{\eta} \left[\hat{\mathbf{S}}_{j,\eta} \cdot \hat{\mathbf{S}}_{j+1,\eta} - \frac{1}{4} \right] + J' \sum_{j=1}^{L} \sum_{\eta} \left[\hat{\mathbf{S}}_{j,\eta} \cdot \hat{\mathbf{S}}_{j+1,-\eta} - \frac{1}{4} \right] \tag{6.17}$$

with

$$J = \frac{4t^2}{U - V} \qquad \text{and} \qquad J' = \frac{2\lambda^2}{U - V - 2M} + \frac{2\lambda^2}{U - V + 2M}. \tag{6.18}$$

The ground state of this model can be easily figured out in the classical limit, where the alignment of the two spins on different orbitals at the same site is energetically favored, suggesting the picture of an effective spin-1 model governing the low-energy behavior of the system. This conclusion can be made rigorous, following the argument detailed in Ref. [197], along the special line

$$\lambda = t \sqrt{1 - \frac{4M^2}{(U - V)^2}}. \tag{6.19}$$

In this case, the amplitudes of the two terms in Eq. (6.17) coincide, the total spin on each site $\hat{\mathbf{S}}_j$ commutes with $\hat{\mathcal{H}}_U$ and the ground state belongs to the subspace where the two spins form a triplet on each site. This implies that, in the low-energy sector, the Hamiltonian $\mathcal{H}_U$ maps into a spin-1 Heisenberg chain, whose ground state is known to exhibit string order and gapped excitation spectrum (Haldane phase) [198].

In the following, we set $t = \lambda = 1$ and show how these four states evolve by varying M, U, and V.

6.1.3 The variational wavefunction

In this work, we use the multi-orbital Jastrow-Slater wavefunction as it is defined in Section 5.4.3

$$|\Psi_{JS}\rangle = \hat{\mathcal{J}}_s\, \hat{\mathcal{J}}_d\, \hat{\mathcal{P}}_{\{S^z=0\}}\, |\Phi_0\rangle \tag{6.20}$$

where $\mathcal{J}_s$ and $\mathcal{J}_d$ are the spin-spin and density-density Jastrow factors of Eqs. (5.68) and (5.69) that induce correlation effects onto the non-interacting Slater determinant $|\Phi_0\rangle$. This is obtained as the ground state of the auxiliary (quadratic) Hamiltonian, which contains three terms

$$\hat{\mathcal{H}}_{\text{aux}} = \hat{\mathcal{H}}_{\text{band}} + \hat{\mathcal{H}}_{\text{CDW}} + \hat{\mathcal{H}}_{\text{AF}}. \tag{6.21}$$

The first one contains the "mass" term and the intra- and inter-orbital hoppings (including an on-site inter-orbital one)

$$\begin{aligned} \hat{\mathcal{H}}_{\text{band}} &= \sum_{j=1}^{L} \sum_{\eta,\sigma} \big[\tilde{M}\, \eta\, \hat{n}_{j,\eta,\sigma} + \tilde{\lambda}_{0,\sigma} \hat{c}^{\dagger}_{j,\eta,\sigma} \hat{c}_{j,-\eta,\sigma} && (6.22) \\ &+ \sum_{k=1,2} (\tilde{t}_k\, \eta\, \hat{c}^{\dagger}_{j+k,\eta,\sigma} \hat{c}_{j,\eta,\sigma} + \text{h.c.}) + (\tilde{\lambda}_{k,\eta,\sigma}\, \hat{c}^{\dagger}_{j+k,\eta,\sigma} \hat{c}_{j,-\eta,\sigma} + \text{h.c.}) \big]. && (6.23) \end{aligned}$$

Here $\tilde{M}$, $\tilde{\lambda}_{0,\sigma}$, $\tilde{t}_k$ (with $\tilde{t}_1 \equiv t$, fixed to define the energy scale), and $\tilde{\lambda}_{k,\eta,\sigma}$ are variational parameters, which allow a renormalization of the band structure. The last two terms in Eq. (6.21) are given by

$$\begin{aligned} \hat{\mathcal{H}}_{\text{CDW}} &= \Delta \sum_{j=1}^{L} (-1)^j\, \hat{n}_j, && (6.24) \\ \hat{\mathcal{H}}_{\text{AF}} &= h \sum_{j=1}^{L} (-1)^j \sum_{\eta} \eta\, (\hat{c}^{\dagger}_{j,\eta,\uparrow} \hat{c}_{j,\eta,\downarrow} + \text{h.c.}), && (6.25) \end{aligned}$$

where Δ and h are additional variational parameters. In particular, the former one is important to induce CDW order in the non-interacting wavefunction; by contrast, the (fictitious) anti-ferromagnetic magnetic field h is useful to construct an accurate *Ansatz* in the large-U limit, recovering the results of the $S = 1$ Heisenberg model [154].

We note that, although h introduces a magnetic field at the level of the variational *Ansatz*, the projector $\hat{\mathcal{P}}_{\{S^z=0\}}$ prevents the breaking of TR symmetry. Indeed, when TR acts on top of the Hamiltonian $\hat{\mathcal{H}}_{\text{AF}}$ in Eq. (6.69), it maps $h \to -h$, and the two ground states are related by

$$|\Phi_0^{-h}\rangle = e^{-i\pi \sum_i \hat{S}^z_i}\, |\Phi_0^{h}\rangle\,. \tag{6.26}$$

The projector onto the subspace with fixed magnetization M can be written as

$$\hat{\mathcal{P}}_{\{S^z=M\}} = \delta\Big(\sum_i \hat{S}^z_i - M\Big) = \int d\theta\, e^{i\theta \left(\sum_i \hat{S}^z_i - M\right)}, \tag{6.27}$$

therefore, upon applying the projector for $M = 0$, one obtains

$$\hat{\mathcal{P}}_{\{S^z=0\}} |\Phi_0^{-h}\rangle = \int d\theta \, e^{i(\theta-\pi)\sum_i \hat{S}_i^z} |\Phi_0^h\rangle = \hat{\mathcal{P}}_{\{S^z=0\}} |\Phi_0^h\rangle \,, \tag{6.28}$$

where, in the last step, we performed a shift of the integration variable. This shows that the projected ground state is invariant under TR.

Moreover, the presence of the spin-spin Jastrow factor of Eq. (6.63) is crucial to prevent the onset of a true magnetic ordering, similarly to what happens in the spin-1 Heisenberg chain [154].

The optimization of the variational parameters (which also include the pseudo-potentials $v_{i,j}^{\alpha,\beta}$ and $u_{i,j}^{\alpha,\beta}$) and the evaluation of the physical properties, such as variational energy and correlation functions, are performed, as reviewed in Section 5.4, by using Markov chains obtained with a Metropolis algorithm (see 5.4.2) and through a Stochastic Reconfiguration approach (see 5.4.4).

6.1.4 Numerical results

We present the numerical results, which are obtained through the variational Monte Carlo approach on the Jastrow-Slater wavefunction. Our variational Monte Carlo results are compared to DMRG calculations in which we take a matrix-product state (which has no translational symmetry and is defined with open-boundary conditions, although the Hamiltonian is always defined with periodic-boundary conditions) and optimize it by means of the algorithm implemented in the ITensor library [199] up to a bond dimension $\chi = 1600$; the accuracy of the calculations is verified by evaluating the variance of the total energy, which is always below $0.0025t^2$.

We start from the case with $V = 0$, showing how the intra-orbital Hubbard-U interaction modifies the non-interacting trivial and topological phases. Then, we consider the effect of the nearest-neighbor repulsion V.

6.1.4.1 The case with $V = 0$

The ground-state phase diagram in the (M, U) plane is shown in Figure 6.3 and contains three different phases. The first one is a trivial insulator, which can be connected to both the non-interacting limit with $M/t > 2$ and the Trivial state described within the atomic limit. The second one is a topological insulator, connected to the non-interacting state obtained for $M/t < 2$ and the Uniform state described in the atomic limit. Interestingly, we find evidence for a third uniform phase, which intrudes in a narrow region between trivial and topological phases for $U > 0$. Here, by looking at the structure factors, our numerical calculations give evidence for gapless spin excitations at $q = 0$ (while they are gapped at $q = \pi$), even though we cannot exclude the presence of a tiny gap. By contrast, density excitations are gapped, indicating an insulating character.

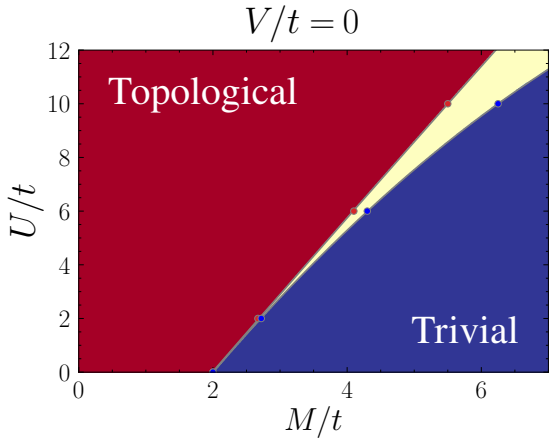


Figure 6.3: Phase diagram of the 1D BHZ model of Eq. (6.3) in the (M, U) plane for $V = 0$ (and $t = \lambda$), as obtained using the Jastrow-Slater wavefunction. Topological (red) and trivial (blue) states are distinguished by the value of the phase of the many-body marker in Eq. (6.34) (0 or π, respectively). For finite values of the intra-orbital interaction U, an intermediate (pale yellow) region is found, with vanishing values of the modulus of the many-body marker. This insulating state sustains gapless spin excitations.

Now, we are going to describe the detailed calculations that allow us to determine the properties summarized in Figure 6.3.

First, we investigate the effect of the intra-orbital interaction onto the topological state with $M/t < 2$. Remarkably, by increasing the intra-orbital Hubbard-U interaction (within the region $M/U \lesssim 0.5$), this state evolves continuously into the ground state of the spin-1 Heisenberg model, discussed in the strong-coupling regime in Section 6.1.2. The latter is characterized by having a non-vanishing spin string-order parameter [198]. Within the electronic model, we can define the non-local correlation function

$$C_s^{\text{string}}(r) = \frac{1}{L}\sum_{j=1}^{L}\langle \hat{S}_j^z \exp\left(i\pi \sum_{l=j+1}^{j+r-1} \hat{S}_l^z\right)\hat{S}_{j+r}^z\rangle, \tag{6.29}$$

where $\langle \dots \rangle$ indicates the expectation value over the approximate ground state, obtained by variational Monte Carlo or DMRG approaches. Then, for phases which are gapped in the spin sector, the spin string-order parameter is given by the $r \to \infty$ limit of the correlation function in Eq. (6.29).

Our variational approach based on the Jastrow-Slater wavefunction gives an accurate description of the strong-coupling limit. The results obtained for $M/t = 0.5$ with increasing intra-orbital U are presented in Figure 6.4, where we set the energy scale $J = 4t^2/U$ in agreement with Eq. (6.18) for $V = 0, M/U \to 0$ and $t = \lambda$. Here, the extrapolated variational energy per site

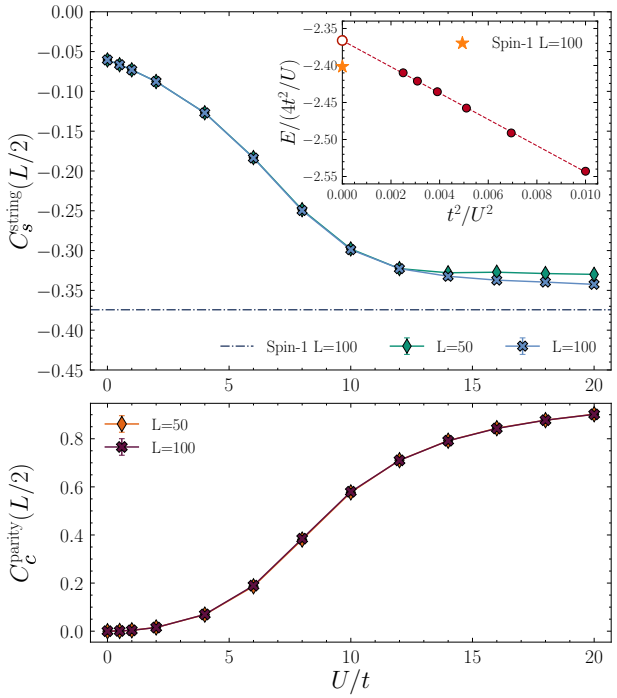


Figure 6.4: Comparison between Jastrow-Slater results in the strong-coupling limit and DMRG calculations for the spin-1 Heisenberg model. Upper panel: Spin string correlations in Eq. (6.29) at the maximum distance $C_s^{\mathrm{string}}(L/2)$ as a function of the intra-orbital interaction U/t, for $L = 50$ and $L = 100$ sites, at fixed on-site term $M/t = 0.5$ and $V = 0$. The value of the string-order parameter for the spin-1 Heisenberg model, obtained by DMRG calculations for system size $L = 100$, is also reported (dashed line). The Jastrow-Slater energy per site (in unit of $4t^2/U$) as a function of t^2/U^2 is shown in the inset, compared with the DMRG result for the spin-1 Heisenberg model on a chain $L = 100$. Lower panel: The same as in the upper panel, but for the charge parity correlations in Eq. (6.32) at the maximum distance $C_c^{\mathrm{parity}}(L/2)$.

(for $L = 100$) is $E/J = -2.366(1)$, which compares well with that of the spin-1 model (including the constant term) $E/J = -2.4015$ as obtained from the DMRG calculation. This latter result, computed for the $L = 100$ spin-1 chain with periodic boundary conditions, is numerically identical to the one extrapolated in the thermodynamic limit [200]. Remarkably, the spin string-order parameter $C_s^{\mathrm{string}}(L/2)$ is finite not only in the strong-coupling regime but also down to $U = 0$, as shown in Figure 6.4.

For comparison, we now consider the trivial phase, which corresponds to $M/t > 2$ in the non-interacting limit. While the Trivial insulator depicted in Fig. 6.2 in the atomic limit has a vanishing spin string-order parameter, a finite value of $C_s^{\mathrm{string}}(L/2)$ can occur in the non-interacting trivial phase. Moreover, this behavior persists upon introducing interaction: the correlated trivial phase continuously connected to the non-interacting trivial phase can also exhibit a finite spin string-order parameter for $U > 0$ (see Table 6.1). Therefore, a finite spin string-order parameter, by itself, cannot serve as a diagnostic of the topological phase. The fact that a spin string-order parameter may be finite in a non-interacting tight-binding model has been discussed in Ref. [201].

Similarly to Eq. (6.29), for phases which are gapped in the charge sector, it is possible to define a charge string-order parameter [55, 202, 203] as the $r \to \infty$ limit of the correlation

	Topological at $U = 0$	Trivial at $U \geq 0$	Topological at $U > 0$	Intermediate
$C_s^{\text{string}}(L/2)$	✓	✓	✓	×
$C_c^{\text{string}}(L/2)$	0	0	0	✓
$C_s^{\text{parity}}(L/2)$	✓	✓	✓	×
$C_c^{\text{parity}}(L/2)$	0	✓	✓	0

Table 6.1: Qualitative behavior of the non-local string and parity order parameters across the different phases. A ✓ indicates that the corresponding order parameter remains finite, 0 indicates a vanishing value in the thermodynamic limit, while a × indicates that the corresponding spin (s) or charge (c) sector is gapless, so that the associated non-local order parameter is not well defined.

function

$$C_c^{\text{string}}(r) = \frac{1}{L}\sum_{j=1}^{L}\langle \hat{N}_j \exp\left(i\pi \sum_{l=j+1}^{j+r-1} \hat{N}_l\right)\hat{N}_{j+r}\rangle, \tag{6.30}$$

where we define

$$\hat{N}_j = \hat{n}_j - 2. \tag{6.31}$$

The results obtained within the Jastrow–Slater approach for the charge string-order parameter, reported in Table 6.1, indicate that it vanishes in the thermodynamic limit for both the trivial and topological phases, in both the non-interacting and correlated regimes.

In addition, we evaluate the charge parity-order parameter [55, 202, 203], which provides information about electron localization due to strong interactions. For that, we define the non-local correlation function

$$C_c^{\text{parity}}(r) = \frac{1}{L}\sum_{j=1}^{L}\langle \exp\left(i\pi \sum_{l=j+1}^{j+r} \hat{N}_l\right)\rangle. \tag{6.32}$$

As before, for gapped phases the parity-order parameter is obtained from the limit $r \to \infty$. In the strong-coupling limit, we have that $C_c^{\text{parity}}(r) = 1$, since each site is doubly occupied with no fluctuations. By contrast, in the non-interacting topological phase (i.e., $U = 0$ and $M/t < 2$) the parity-order parameter vanishes. The results shown in the lower panel in Figure 6.4 strongly indicate that $C_c^{\text{parity}}(L/2)$ becomes finite as soon as the intra-orbital interaction is finite.

Finally, we consider the spin parity correlation function

$$C_s^{\text{parity}}(r) = \frac{1}{L}\sum_{j=1}^{L}\langle \exp\left(i\pi \sum_{l=j+1}^{j+r} \hat{S}_l^z\right)\rangle, \tag{6.33}$$

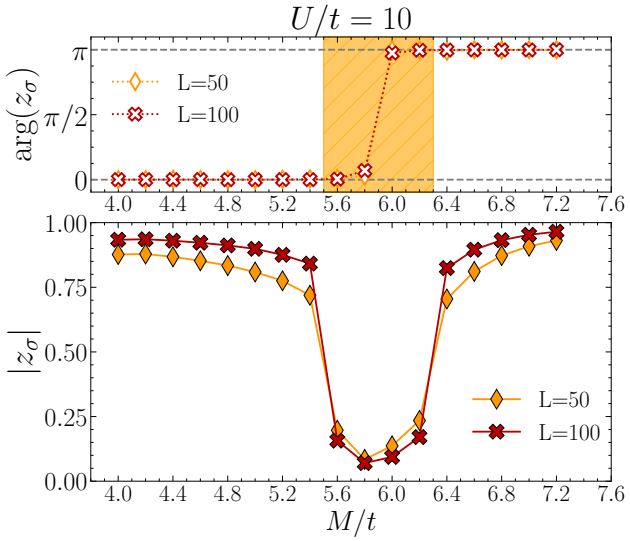


Figure 6.5: The Jastrow-Slater results for many-body marker of Eq. (6.34) at $V = 0$ and $U/t = 10$. In the upper panel, the phase of the many-body marker is shown. The yellow strip indicate the region where the modulus of the many-body marker is vanishing, as shown in the lower panel.

and the corresponding non-local order parameter, which remains finite for both the trivial and topological phases, in both the non-interacting and correlated regimes (see Table 6.1).

Taken together, the behavior of the string and parity correlation functions provides evidence that the non-interacting topological insulator is adiabatically connected to the strong-coupling regime described by the spin-1 Heisenberg model. In particular, the persistence of the relevant non-local order parameters upon increasing the interaction strength is consistent with the absence of a phase transition connecting these two limits.

Now, we move on to describe how the (continuous) transition between the topological and trivial phases is affected by the presence of interactions $U > 0$. To this end, we use the spin-resolved many-body marker introduced in Eq. (5.50) calculated on the optimized Jastrow-Slater wavefunction

$$z_\sigma = \langle \exp\left(i\frac{2\pi}{L} \sum_{j=1}^{L} x_j \hat{n}_{j,\sigma} \right) \rangle. \tag{6.34}$$

In the absence of local order parameters distinguishing different phases of matter, this many-body marker provides valuable information about the nature of the many-body wavefunction [48].

As we have seen in Section 5.3.2.1, for the non-interacting model it is possible to show that

$$z_\sigma = (-1)^{L-1} e^{i\phi_\sigma}, \tag{6.35}$$

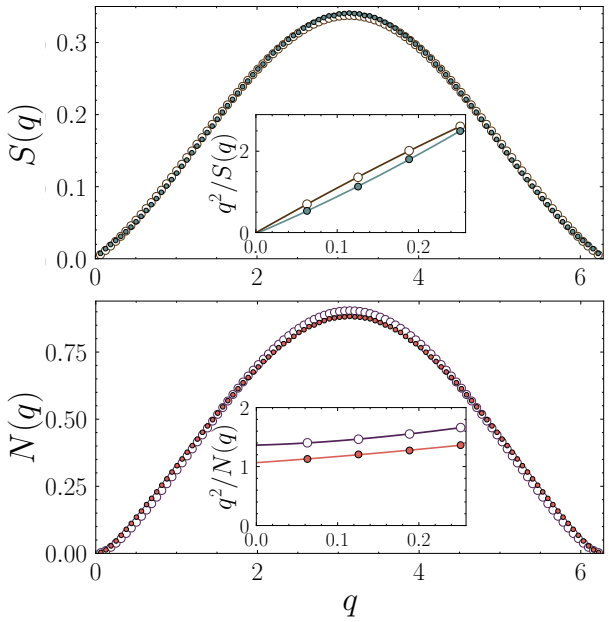


Figure 6.6: Spin (upper panel) and density (lower panel) structure factors in the intermediate phase (between topological and trivial insulators), for $L = 100$ sites at $V = 0$, $U/t = 10$, and $M/t = 5.9$, obtained by the Jastrow-Slater wavefunction (full points). The DMRG results are also reported for comparison (empty points). The insets show the ratios $q^2/S(q)$ and $q^2/N(q)$ for small momenta, in order to emphasize the linear or quadratic behavior of the structure factors.

where ϕ_σ indicates the spin-resolved Zak phase. Therefore, the transition at $M/t = 2$ can be detected by a jump in the phase of z_σ, from 0 to π for even system sizes L. The TR symmetry in Eq. (6.4) ensures that $z_\downarrow = z_\uparrow^*$. In addition, as long as either the η-PH in Eq. (6.8) or the I+η sign symmetry in Eq. (6.11) is preserved, a *real* value of z_σ is guaranteed and the sign of z_σ can therefore be used to distinguish between topological and trivial states also in the interacting case.

In our calculation, we find that, away from the transition, $\arg(z_\sigma)$ clearly distinguishes two interacting phases with different topology. In the upper panel of Figure 6.3, the topological and trivial phases are identified by the phase of z_σ being 0 or π, respectively. Between the two phases, however, the modulus $|z_\sigma|$ vanishes upon increasing the system size, as shown in the lower panel of Figure 6.5 for $U/t = 10$, and in this regime the sign of z_σ is no longer a reliable diagnostic. The region where the modulus of the many-body marker vanishes is marked in pale yellow in the phase diagram in Figure 6.3.

In order to clarify the nature of this intermediate phase and assess the existence of gapless excitations, we consider the density and spin structure factors

$$N(q) = \frac{1}{L}\sum_{j=1}^{L} e^{iqr}\langle \hat{n}_j \hat{n}_{j+r}\rangle, \tag{6.36}$$

$$S(q) = \frac{1}{L}\sum_{j=1}^{L} e^{iqr}\langle \hat{S}^z_j \hat{S}^z_{j+r}\rangle, \tag{6.37}$$

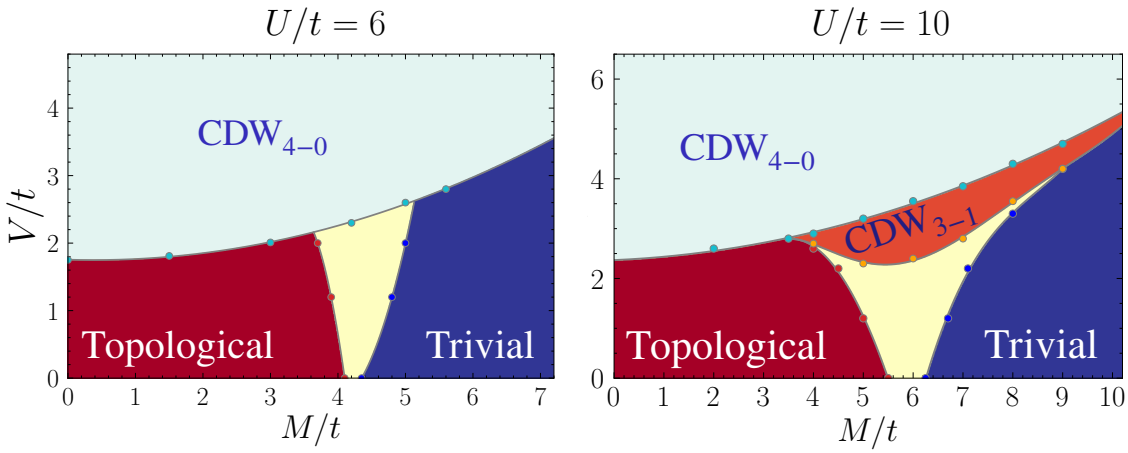


Figure 6.7: Phase diagram of the 1D BHZ model of Eq. (6.3) in the (M, V) plane for $U/t = 6$ (left panel) and $U/t = 10$ (right panel) (for $t = \lambda$), as obtained using the Jastrow-Slater wavefunction. Besides the topological (red), trivial (blue), and intermediate (pale yellow) phases, observed in the case with $V = 0$, as shown in Figure 6.3, a fully gapped CDW (pale blue) exits for both values of U/t, for large-enough values of V/t. For $U/t = 10$ a CDW_{3-1} with gapless spin excitations (orange) is stabilized, between the intermediate and the fully gapped CDW phases.

where $\hat{n}_j$ and $\hat{S}^z_j$ are the total density and spin operators on the j-th site, respectively. In fact, gapless excitations at $q = 0$ are marked by a linear behavior of these quantities for $q \to 0$ [150, 156], as reported in Section 5.3.1; a singularity at a finite q would also imply a gapless mode at that momentum. A standard example is given by the spin-1/2 Heisenberg chain, where $S(q) \propto q$ at small momenta and $S(\pi) \propto \ln(L)$. For both topological and trivial phases shown in the phase diagram of Figure 6.3, $N(q)$ and $S(q)$ do not possess any singularity, with a quadratic behavior for small values of the momenta (not shown), in agreement with the fact that both density and spin excitations are gapped, as in the non-interacting limit. By contrast, a different scenario appears within the intermediate phase, where the modulus of the many-body marker z_σ is vanishing. As shown in Figure 6.6, while the density structure factor maintains a completely smooth behavior, indicating an insulating character of the state, the spin structure factor has a linear behavior at small momenta, e.g. $S(q) \propto q$, signaling the existence of *gapless* excitations. Nevertheless, the situation is strikingly different from the standard 1D Heisenberg model, since there is neither a diverging peak nor a kink at $q = \pi$.

In addition, in Table 6.1 we report the qualitative behavior of non-local string and parity order parameters in the intermediate phase. We focus on the charge sector, where the system is gapped in this phase. We find that the intermediate phase is characterized by a finite charge string-order parameter, in contrast to both the trivial and topological phases, while the charge parity-order parameter vanishes.

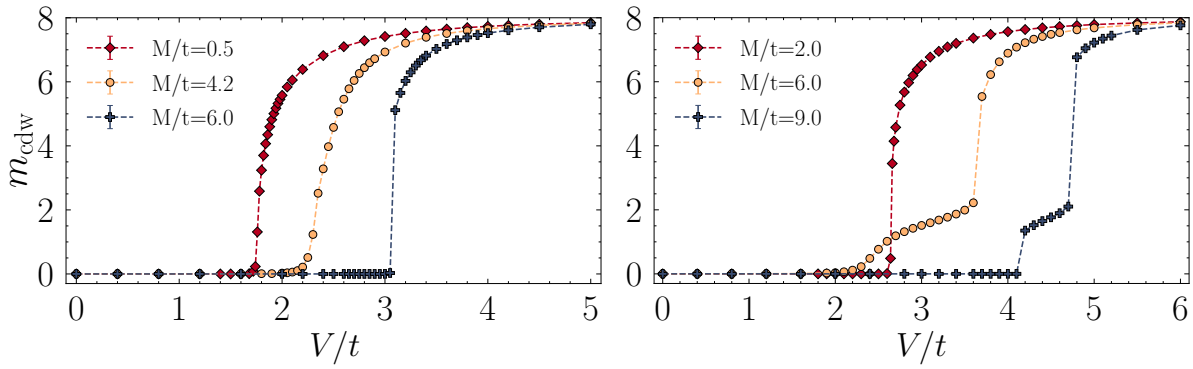


Figure 6.8: The Jastrow-Salter results for the CDW order parameter $m_{\rm cdw}$ in Eq. (6.38) as a function of V/t for $L = 50$ sites at $U/t = 6$ (left panel) and $U/t = 10$ (right panel).

6.1.4.2 The case with $V > 0$

Let us move to the case with $V > 0$. In this case, we consider two values of the intra-orbital interaction $U/t = 6$ and $U/t = 10$ and show the phase diagram in the (M, V) plane, see Figure 6.7. The first observation is that a (not too large) nearest-neighbor repulsion V enlarges the stability region of the intermediate phase. Most importantly, two additional phases settle down. The first is a fully gapped CDW, which appears for sufficiently large values of V; it breaks the translational symmetry by one lattice spacing and is adiabatically connected to the CDW_{4-0} that has been discussed in Section 6.1.2. The second one is an insulating CDW, still breaking the translational symmetry but sustaining gapless spin excitations, connected to the CDW_{3-1} presented in Section 6.1.2. Although local densities are non-integer for finite values of U and V, we refer to these insulators as CDW_{4-0} and CDW_{3-1}. In all cases, the presence of a density disproportionation is marked by the local order parameter that is computed from density-density correlations in real space:

$$m_{\rm cdw} = \lim_{L\to\infty} |\tilde{N}(L/2) - \tilde{N}(L/2-1)|, \tag{6.38}$$

where

$$\tilde{N}(r) = \frac{1}{L}\sum_{j=1}^{L}\langle \hat{n}_j \hat{n}_{j+r}\rangle. \tag{6.39}$$

In the atomic limit, the values of the local parameter for the CDW_{4-0} and CDW_{3-1} are $m_{\rm cdw} = 8$ and 2, respectively.

For the values of U/t considered in Figure 6.8, the transition between the topological insulator and the fully gapped CDW is continuous. By contrast, a first-order transition (with a jump in $m_{\rm cdw}$) is clearly detected when the intra-orbital Hubbard interaction is increased further, e.g.,

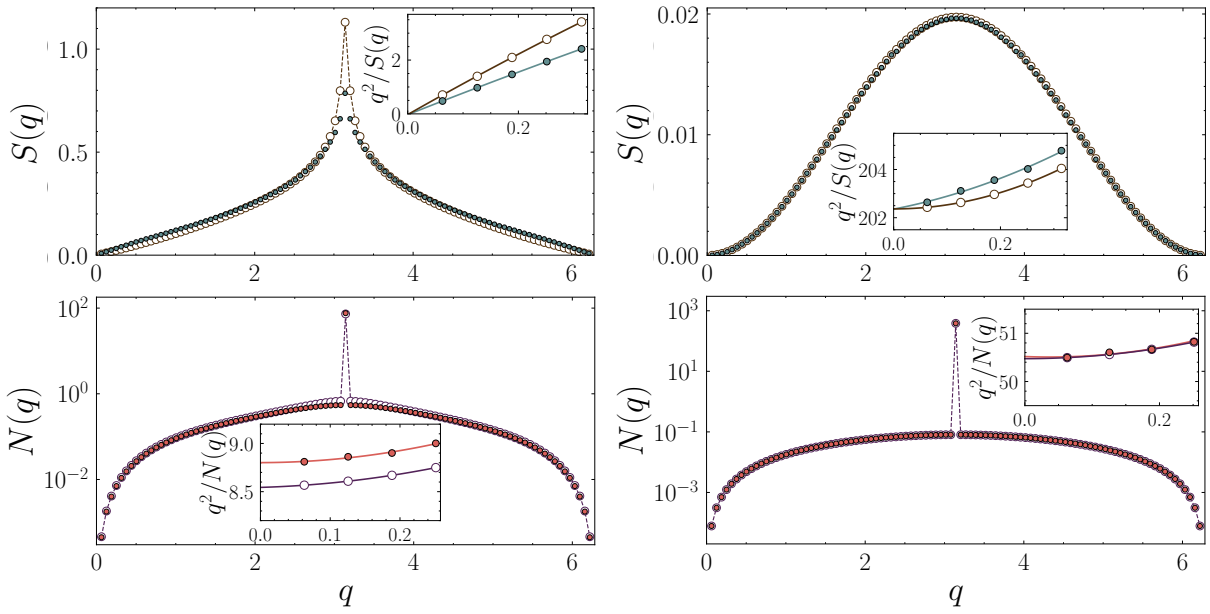


Figure 6.9: The same as in Figure 6.6 for the CDW_{3-1} phase (left panel), with $L = 100$ sites at $V/t = 3$, $U/t = 10$ and $M/t = 6$ and for the CDW_{4-0} phase (right panel), with $L = 100$ sites at $V/t = 5$, $U/t = 10$ and $M/t = 6$. Notice the logarithmic scale in the y axis in the lower panels, taken for showing the huge value of $N(\pi)$.

$U/t = 14$ (not shown). This result is in agreement with DMRG calculations (on chains with open-boundary conditions) of Ref. [158].

For $U/t = 6$, the intermediate region (where the modulus of the many-body marker is vanishing) is characterized by a vanishingly small CDW order parameter up to moderate values of V. For this value of the on-site repulsion, no sign of the CDW_{3-1} is detected. Then, by increasing further the nearest-neighbor interaction, a continuous transition to a fully gapped CDW is observed. Furthermore, the transition between the trivial and the CDW_{4-0} insulator is most likely first-order.

The situation changes for $U/t = 10$, where the CDW_{3-1} phase appears in a rather wide region of the phase diagram, in between the intermediate insulating phase and the CDW_{4-0} one. The presence of the CDW_{3-1} phase can be detected from m_{cdw}, which shows a "step-like" behavior when increasing V. Most importantly, the spin structure factor $S(q)$ in the CDW_{3-1} acquires singularities at $q = 0$ and π, thus signaling the existence of gapless modes, see left panel in Figure 6.9. Here, the presence of a huge peak in the density structure factor at $q = \pi$ is the hallmark of the insurgence of charge disproportionation [i.e., $N(\pi) \approx m_{\mathrm{cdw}} L$]. From our variational calculations, the transition between the intermediate state and the CDW_{3-1} is most likely continuous, as deduced from the smooth behavior of m_{cdw} in Figure 6.8; instead, the transition from gapless to gapped CDW phases looks first-order, with a sudden jump in

$m_{\rm cdw}$ (from our data, however, we cannot exclude a second-order transition, with a small critical exponent). Remarkably, within the CDW_{3-1} the value of $m_{\rm cdw}$ is always smaller than the "saturation" limit (i.e., $m_{\rm cdw} = 2$). We emphasize that the latter quantity cannot be used to distinguish between CDW_{3-1} and CDW_{4-0}, which also show qualitatively similar (smooth) density-density structure factors $N(q)$, which can be compared in the lower panels of Figure 6.9. By contrast, these two CDW phases can be distinguished by the presence of singularities in $S(q)$: while the fully gapped CDW_{4-0} has a smooth spin-spin structure factor, the gapless CDW_{3-1} displays singularities for both $q = 0$ and $q = \pi$, as compared in the upper panels of Figure 6.9.

6.2 The interacting two-dimensional BHZ model

While we have seen that electron-electron correlations can have a nontrivial interplay with topology already in one dimension, strong interactions in two dimensions may additionally favor spontaneous symmetry breaking and the formation of long-range-ordered states.

We therefore extend our analysis to an interacting two-orbital Hubbard model on a two-dimensional square lattice with $L \times L$ sites, described by the Hamiltonian

$$\hat{\mathcal{H}}_{2D} = \hat{\mathcal{H}}_0 + \hat{\mathcal{H}}_{\rm int}. \tag{6.40}$$

The non-interacting part is the paradigmatic BHZ model for a quantum spin Hall insulator [35], introduced in Section 1.4.2. In real space, it reads

$$\begin{aligned}\hat{\mathcal{H}}_0 = M \sum_{\mathbf{R},\eta,\sigma} \eta\, \hat{c}^\dagger_{\mathbf{R},\eta,\sigma}\hat{c}_{\mathbf{R},\eta,\sigma} - \frac{1}{2}\Bigg[t \sum_{\mathbf{R},\boldsymbol{\mu},\eta,\sigma} \eta\, \hat{c}^\dagger_{\mathbf{R}+\boldsymbol{\mu},\eta,\sigma}\hat{c}_{\mathbf{R},\eta,\sigma} \\ + \lambda \sum_{\mathbf{R},\eta,\sigma} \eta\, \hat{c}^\dagger_{\mathbf{R}+\mathbf{y},\eta,\sigma}\hat{c}_{\mathbf{R},-\eta,\sigma} + \lambda \sum_{\mathbf{R},\eta,\sigma} i s_\sigma \hat{c}^\dagger_{\mathbf{R}+\mathbf{x},\eta,\sigma}\hat{c}_{\mathbf{R},-\eta,\sigma} + h.c.\Bigg],\end{aligned} \tag{6.41}$$

where $\mathbf{R}$ runs over the sites of the square lattice, $\eta = \pm$ labels the two orbitals on each site, while $\sigma = \uparrow, \downarrow$ is the spin degree of freedom, with $s_\uparrow = +1$ and $s_\downarrow = -1$. The vectors $\mathbf{x}$ and $\mathbf{y}$ are the primitive lattice vectors of the square lattice, and the sum over $\boldsymbol{\mu}$ runs over the positive displacements connecting each site to its nearest-neighbour sites, i.e. $\boldsymbol{\mu} = \mathbf{x}, \mathbf{y}$.

In momentum space, the Hamiltonian can be written as a 4×4 matrix in terms of Pauli matrices acting in the spin $\boldsymbol{\sigma}$ and orbital $\boldsymbol{\tau}$ spaces

$$H_0(\mathbf{k}) = [M - t(\cos k_x + \cos k_y)]\, \sigma_0 \otimes \tau_z + \lambda \sin k_x\, \sigma_z \otimes \tau_x - \lambda \sin k_y\, \sigma_0 \otimes \tau_y. \tag{6.42}$$

Since $H_0(\mathbf{k})$ is a block diagonal in the spin sector, the energy spectrum is doubly degenerate and, for each spin component, is given by

$$E_{\mathbf{k}} = \pm\sqrt{[M - t(\cos k_x + \cos k_y)]^2 + \lambda^2 \left(\sin^2 k_x + \sin^2 k_y\right)}. \tag{6.43}$$

At half filling, corresponding to two electrons per site on average, the two lower bands are fully occupied and the system is insulating, except at the gap-closing points occurring at TR-invariant momenta, as discussed in Section 1.4.2. For $t > 0$, the system realizes a QSHI phase for $|M/t| < 2$, with the exception of $M = 0$, where the bulk gap closes, whereas it is topologically trivial for $|M/t| > 2$. In the following, we consider $M > 0$ and $t > 0$.

In the non-interacting limit the two insulating phases can be distinguished by the spin Chern numbers C_σ defined in Section 1.4. Since the BHZ Hamiltonian conserves the spin component S_z, these invariants can be computed as the integral over the Brillouin zone of the Berry curvature of the occupied states in each spin sector. In particular, the parity of C_σ is odd in the QSHI phase and even in the trivial one.

The role of electronic correlations in the BHZ model has been addressed in a number of works, especially in the presence of both Hubbard and Hund interactions described by the Hubbard–Kanamori Hamiltonian discussed in Section 5.1.1. Most studies rely on DMFT and related approaches, and show that interactions can substantially enrich the phase diagram of the model. In particular, upon increasing the interaction strength, a trivial band insulator may first undergo a transition into a quantum spin Hall phase at intermediate coupling, before eventually entering a Mott insulating phase in the strongly interacting regime [189, 191, 192]. The transition from the trivial band insulator to the interaction-induced quantum spin Hall phase has been found to be first order for sufficiently large interactions [192].

More recently, excitonic phases have also been reported in interacting BHZ models. These phases spontaneously break the time-reversal symmetry that protects the quantum spin Hall state and may appear between the correlated quantum spin Hall insulator and the trivial insulating phase [204–206]. Moreover, studies of the BHZ model with purely intra-band Hubbard interactions have revealed the possible emergence of antiferromagnetic topological insulating phases [190, 207], while DMFT calculations have further suggested that such an antiferromagnetic topological insulator may intrude between the quantum spin Hall and Mott insulating phases in the presence of strong Coulomb interaction [208].

In this section, we consider the density-density part of the two-orbital Kanamori interaction introduced in Eq. (5.14), setting $J = J' = 0$. The interaction Hamiltonian is therefore

$$\hat{\mathcal{H}}_{\text{int}} = U \sum_{\mathbf{R},\eta} \hat{n}_{\mathbf{R},\eta,\uparrow} \hat{n}_{\mathbf{R},\eta,\downarrow} + U' \sum_{\mathbf{R},\sigma,\sigma'} \hat{n}_{\mathbf{R},+,\sigma} \hat{n}_{\mathbf{R},-,\sigma'}. \tag{6.44}$$

Here, U is the intra-orbital Hubbard repulsion, while U' is the inter-orbital density-density interaction. Despite its relatively simple form, this interaction is sufficient to capture the essential correlation effects on the BHZ model in two dimensions, allowing us to investigate, within

our variational Monte Carlo approach based on Jastrow–Slater wavefunctions, several of the correlation-driven phases discussed above.

The main results of the study can be summarized as follows.

- (i) The sole intra-orbital interaction U drives the system into an *antiferromagnetic* phase with magnetic order along the z direction. When the non-interacting system is in the QSHI phase, this transition occurs above a critical value of U/t. Conversely, when the system is initially trivial, increasing U/t first drives the system into a correlated QSHI phase, before eventually inducing the antiferromagnetic phase. The transition into the antiferromagnetic phase appears to be first order.
- (ii) The presence of both intra- and inter-orbital interactions $U' = U$, generally favors a transition towards a trivial insulating phase. However, for small values of the mass parameter M/t, when starting from a QSHI phase, the system first enters an insulating phase characterized by finite *excitonic* correlations, known ad excitonic insulator (EI).

6.2.1 The symmetries of the non-interacting model

The non-interacting BHZ Hamiltonian of Eq. (6.42) is invariant under a few symmetry transformations. The first one is time-reversal (TR) symmetry which protects the topological phase and, in real space, acts on the fermionic creation operators as

$$\mathcal{T}\,\hat{c}^\dagger_{\mathbf{R},\eta,\uparrow}\,\mathcal{T}^{-1} = +\hat{c}^\dagger_{\mathbf{R},\eta,\downarrow}, \tag{6.45}$$

$$\mathcal{T}\,\hat{c}^\dagger_{\mathbf{R},\eta,\downarrow}\,\mathcal{T}^{-1} = -\hat{c}^\dagger_{\mathbf{R},\eta,\uparrow}. \tag{6.46}$$

Since the Hamiltonian contains only spin-diagonal terms, it conserves the z-component of the total spin

$$\hat{S}^z = \frac{1}{2}\sum_{\mathbf{R},\eta}\left(\hat{c}^\dagger_{\mathbf{R},\eta,\uparrow}\hat{c}_{\mathbf{R},\eta,\uparrow} - \hat{c}^\dagger_{\mathbf{R},\eta,\downarrow}\hat{c}_{\mathbf{R},\eta,\downarrow}\right). \tag{6.47}$$

and the model is invariant under $U(1)$ spin rotations around the z axis, generated by $\hat{S}^z$

$$\mathcal{U}\,\hat{c}^\dagger_{\mathbf{R},\eta,\sigma}\,\mathcal{U}^{-1} = e^{i\theta_\sigma}\,\hat{c}^\dagger_{\mathbf{R},\eta,\sigma}. \tag{6.48}$$

In addition to this continuous symmetry, the model is invariant under a unitary discrete transformation that exchanges the two spin sectors

$$\mathcal{Z}\,\hat{c}^\dagger_{\mathbf{R},\eta,\sigma}\,\mathcal{Z}^{-1} = (-1)^{R_x}\,\hat{c}^\dagger_{\mathbf{R},\eta,-\sigma}. \tag{6.49}$$

This transformation flips the spin projection along the z axis,

$$\mathcal{Z}\,\hat{S}^z\,\mathcal{Z}^{-1} = -\hat{S}^z, \tag{6.50}$$

and satisfies $\mathcal{Z}^2 = 1$, generating therefore a unitary $\mathbb{Z}_2$ symmetry.

The model is also invariant under lattice translations

$$\mathcal{T}_x \, \hat{c}^\dagger_{\mathbf{R},\eta,\sigma} \, \mathcal{T}_x^{-1} = \hat{c}^\dagger_{\mathbf{R}+\mathbf{x},\eta,\sigma}, \tag{6.51}$$

$$\mathcal{T}_y \, \hat{c}^\dagger_{\mathbf{R},\eta,\sigma} \, \mathcal{T}_y^{-1} = \hat{c}^\dagger_{\mathbf{R}+\mathbf{y},\eta,\sigma}. \tag{6.52}$$

If the two orbitals have opposite parity, as encoded by the orbital index η, the Hamiltonian is further invariant under inversion. Choosing the inversion center at the origin, this transformation can be written as

$$\mathcal{I} \, \hat{c}^\dagger_{\mathbf{R},\eta,\sigma} \, \mathcal{I}^{-1} = \eta \, \hat{c}^\dagger_{-\mathbf{R},\eta,\sigma}. \tag{6.53}$$

6.2.2 Strong-coupling limit

It is useful to analyze the strong-coupling regime of the two-dimensional BHZ model. We first consider the case in which only the intra-orbital Hubbard interaction

$$\hat{H}_U = U \sum_{\mathbf{R},\eta} \hat{n}_{\mathbf{R},\eta,\uparrow} \hat{n}_{\mathbf{R},\eta,\downarrow} \tag{6.54}$$

is present. In the atomic limit, obtained for $t = \lambda = 0$, there are three relevant local configurations at half filling. Two of them correspond to two electrons occupying the same orbital on each site, denoted by $(2,0)$ and $(0,2)$, depending on whether the $+$ or the $-$ orbital is occupied. The third configuration, denoted by $(1,1)$, has one electron in each orbital and will also be referred to as the Uniform configuration. Their energies are

$$E_{1,1} = 0, \qquad E_{2,0} = U + 2M, \qquad E_{0,2} = U - 2M. \tag{6.55}$$

Since we consider $M > 0$, the lowest-energy doubly occupied configuration is $(0,2)$. Therefore, for $M/U > 0.5$, the atomic ground state is the configuration $(0,2)$, in the following named as the Trivial state, which is unique. By contrast, for $M/U < 0.5$, the energetically favored configuration is the Uniform configuration $(1,1)$, that is a highly degenerate state, since the spin orientation on each orbital remains arbitrary.

In order to determine the magnetic character of this state, one has to include the hopping terms perturbatively. Starting from the Uniform configuration with one electron per orbital, the leading corrections arise at second order in the hopping amplitudes. They are generated by virtual processes in which an electron hops to a neighboring orbital, creates a doubly occupied state, and then returns to the singly occupied subspace. The intra-orbital hopping t produces the usual antiferromagnetic superexchange between neighboring spins belonging to the same orbital

$$J_{\text{intra}} = \frac{t^2}{U}. \tag{6.56}$$

Similarly, the inter-orbital hopping along the $\hat{\mathbf{y}}$ direction gives rise to an antiferromagnetic exchange between different orbitals on neighboring sites

$$J_{\text{inter}} = \frac{\lambda^2}{U}. \tag{6.57}$$

The inter-orbital hopping along the $\hat{\mathbf{x}}$ direction is instead qualitatively different, because of the spin-dependent amplitude $i\sigma\lambda$. This factor changes the relative sign between processes in which the same electron hops back and forth and processes in which two electrons are exchanged. As a consequence of this, the corresponding superexchange is anisotropic in spin space: the z component enters with the opposite sign with respect to the x and y components.

The resulting strong-coupling Hamiltonian is the Heisenberg-like model

$$\begin{aligned}\hat{H}_{\text{eff}} = J_{\text{intra}} \sum_{\mathbf{R},\boldsymbol{\mu},\eta} \left(\hat{\mathbf{S}}_{\mathbf{R},\eta} \cdot \hat{\mathbf{S}}_{\mathbf{R}+\boldsymbol{\mu},\eta} - \frac{1}{4} \right) + J_{\text{inter}} \sum_{\mathbf{R},\eta} \left(\hat{\mathbf{S}}_{\mathbf{R},\eta} \cdot \hat{\mathbf{S}}_{\mathbf{R}+\hat{\mathbf{y}},-\eta} - \frac{1}{4} \right) \\ + J_{\text{inter}} \sum_{\mathbf{R},\eta} \left(\hat{S}^z_{\mathbf{R},\eta} \hat{S}^z_{\mathbf{R}+\hat{\mathbf{x}},-\eta} - \hat{S}^x_{\mathbf{R},\eta} \hat{S}^x_{\mathbf{R}+\hat{\mathbf{x}},-\eta} - \hat{S}^y_{\mathbf{R},\eta} \hat{S}^y_{\mathbf{R}+\hat{\mathbf{x}},-\eta} - \frac{1}{4} \right)\end{aligned} \tag{6.58}$$

in terms of the orbital-resolved spin$-1/2$ operators

$$\hat{S}^{\alpha}_{\mathbf{R},\eta} = \frac{1}{2} \sum_{\sigma,\sigma'} \hat{c}^{\dagger}_{\mathbf{R},\eta,\sigma} \tau^{\alpha}_{\sigma,\sigma'} \hat{c}^{\dagger}_{\mathbf{R},\eta,\sigma'} \tag{6.59}$$

where τ^{α} indicates one of the three Pauli matrices for $\alpha = x$, y, and z.

The first term in Eq. (6.58) is the standard antiferromagnetic Heisenberg exchange between nearest-neighbor spins in the same orbital. The second term has the same $SU(2)$-symmetric form, but couples different orbitals along the $\hat{\mathbf{y}}$ direction. The third term, instead, is anisotropic and explicitly breaks the full $SU(2)$ spin-rotation symmetry. This reduced symmetry is already present in the non-interacting BHZ Hamiltonian, where the spin-dependent hopping proportional to $i\sigma\lambda$ selects the z spin axis and breaks $SU(2)$ down to rotations around z. Thus, both the non-interacting model and the effective strong-coupling Hamiltonian conserve S^z_{tot}, but not the full spin vector $\hat{\mathbf{S}}_{\text{tot}}$. The residual spin symmetry of Eq. (6.58) is therefore $U(1) \times \mathbb{Z}_2$, where the $U(1)$ factor corresponds to rotations around the z axis, while the $\mathbb{Z}_2$ factor corresponds to the discrete inversion of the z spin component.

The classical magnetic state can be inferred directly from Eq. (6.58). The intra-orbital exchange favors antiferromagnetic order separately within each orbital sector, while the inter-orbital exchange along the $\hat{\mathbf{y}}$ direction tends to align the two antiferromagnetic order parameters associated with the two orbitals. However, since both terms are $SU(2)$-symmetric, they do not fix the orientation of the corresponding order parameter. The anisotropic exchange along $\hat{\mathbf{x}}$, instead, selects the z axis as the energetically favored direction. This results in a classical

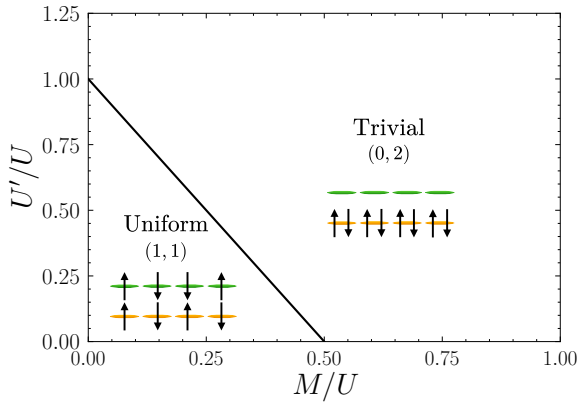


Figure 6.10: Phase diagram in the atomic limit, with $t = \lambda = 0$. The Uniform $(1,1)$ and Trivial $(2,0)$ phases have two electrons on each site; in the former, electrons occupy different orbitals (with an arbitrary spin configuration), while in the latter they reside in the orbital with the lowest on-site energy.

ground state with two parallel spins on the same site and antiferromagnetic order along z. This Ising-like state has two degenerate Néel configurations, related by $S^z \to -S^z$; choosing one of them spontaneously breaks the residual $\mathbb{Z}_2$ symmetry, while the $U(1)$ symmetry around the z axis remains unbroken.

We now include the inter-orbital density-density interaction in the strong-coupling analysis

$$\hat{H}_{U'} = U' \sum_{\mathbf{R}} \hat{n}_{\mathbf{R},+} \hat{n}_{\mathbf{R},-}. \tag{6.60}$$

The energies of the relevant local configurations become

$$E_{1,1} = U', \qquad E_{2,0} = U + 2M, \qquad E_{0,2} = U - 2M. \tag{6.61}$$

Therefore, for $M > 0$, the Uniform configuration $(1,1)$ is the atomic ground state provided that

$$U' < U - 2M. \tag{6.62}$$

The inter-orbital interaction U' does not lift the degeneracy of the $(1,1)$ manifold, but only contributes a constant energy per site. Moreover, within second-order perturbation theory, it does not affect the virtual hopping processes responsible for the spin exchange, since its contribution to the energy is unchanged between the initial and intermediate states. Hence, as long as the condition in (6.62) is satisfied, the effective spin Hamiltonian in Eq. (6.58) remains the appropriate low-energy description also in the presence of U'.

By contrast, when this condition is violated, the Trivial configuration $(0,2)$ becomes the lowest-energy atomic state, as shown in Figure 6.10. Along the boundary $U' = U - 2M$, the

Uniform and Trivial configurations become degenerate, and more generally, near this boundary, both the orbital-polarized state $(0,2)$ and the spin-degenerate manifold $(1,1)$ contribute to the low-energy physics. Moreover, at $M=0$, the configuration $(2,0)$ also becomes degenerate and must be included in the low-energy manifold.

The resulting effective theory is therefore no longer a pure spin model, but rather a coupled spin-orbital model which can be formulated in terms of pseudospin degrees of freedom acting on the enlarged local Hilbert space. In this regime, Ref. [205] predicts that the competition between the orbital-polarized atomic states $(0,2)$ and $(2,0)$, and the singly occupied multiplet $(1,1)$ can drive an excitonic instability. This is associated with an order parameter of the form $\langle \hat{c}^\dagger_{\mathbf{R},\eta,\sigma}\hat{c}_{\mathbf{R},-\eta,\sigma'}\rangle$. This expectation value describes a coherent hybridization between the two orbitals, corresponding to the creation of a particle in one orbital together with a hole in the other. It therefore has the structure of an inter-orbital particle-hole pair. A finite value of the order parameter signals that these particle-hole pairs acquire macroscopic phase coherence and condense, giving rise to an excitonic insulating state.

6.2.3 The variational wavefunction

We employ the multi-orbital Jastrow-Slater wavefunction introduced in Section 5.4.3 and already used in the one-dimensional BHZ model

$$|\Psi_{JS}\rangle = \hat{\mathcal{J}}_s\,\hat{\mathcal{J}}_d\,\hat{\mathcal{P}}_{\{S^z=0\}}\,|\Phi_0\rangle \tag{6.63}$$

where $\mathcal{J}_s$ and $\mathcal{J}_d$ are the spin-spin and density-density Jastrow factors of Eqs. (5.68) and (5.69) that induce correlation effects onto the non-interacting Slater determinant $|\Phi_0\rangle$, and $\mathcal{P}_{\{S^z=0\}}$ is the projection onto the subspace with $S^z_{\text{tot}} = \sum_{\mathbf{R},\eta} S^z_{\mathbf{R},\eta} = 0$, which enforces the conservation of the total spin S^z.

The main difference with respect to the 1D case lies in the choice of the auxiliary Hamiltonian from which the non-interacting Slater determinant $|\Phi_0\rangle$ is obtained. Indeed, the two-dimensional auxiliary Hamiltonian is formed by the terms

$$\hat{\mathcal{H}}_{\text{aux}} = \hat{\mathcal{H}}_{\text{band}} + \hat{\mathcal{H}}_{\text{Ising}} + \hat{\mathcal{H}}^{\parallel}_{\text{AF}} + \hat{\mathcal{H}}_{\text{Exciton}}. \tag{6.64}$$

The first one contains the "mass" term and the intra- and inter-orbital hoppings as appearing in the physical non-interacting BHZ Hamiltonian

$$\hat{\mathcal{H}}_{\text{band}} = \tilde{M}\sum_{\mathbf{R},\eta,\sigma}\eta\,\hat{c}^\dagger_{\mathbf{R},\eta,\sigma}\hat{c}_{\mathbf{R},\eta,\sigma} - \frac{1}{2}\Bigg[t\sum_{\mathbf{R},\boldsymbol{\mu},\eta,\sigma}\eta\,\hat{c}^\dagger_{\mathbf{R}+\boldsymbol{\mu},\eta,\sigma}\hat{c}_{\mathbf{R},\eta,\sigma} \tag{6.65}$$

$$+ \tilde{\lambda}\sum_{\mathbf{R},\eta,\sigma}\Big(\eta\,\hat{c}^\dagger_{\mathbf{R}+\mathbf{y},\eta,\sigma}\hat{c}_{\mathbf{R},-\eta,\sigma} + is_\sigma\hat{c}^\dagger_{\mathbf{R}+\mathbf{x},\eta,\sigma}\hat{c}_{\mathbf{R},-\eta,\sigma}\Big) + h.c.\Bigg], \tag{6.66}$$

where $\tilde{M}$ and $\tilde{\lambda}$ are variational parameters that allow the band structure to be renormalized by interactions, while t is kept fixed and sets the energy scale.

The remaining terms in Eq. (6.64) allow the Slater determinant to develop possible symmetry-broken orders. The first one is a staggered magnetic field along the z direction

$$\hat{\mathcal{H}}_{\text{Ising}} = b_z \sum_{\mathbf{R},\eta} (-1)^{R_x+R_y} \left(\hat{c}^\dagger_{\mathbf{R},\eta,\uparrow} \hat{c}_{\mathbf{R},\eta,\uparrow} - \hat{c}^\dagger_{\mathbf{R},\eta,\downarrow} \hat{c}_{\mathbf{R},\eta,\downarrow} \right), \tag{6.67}$$

which favors the Ising-like antiferromagnetic order suggested by the strong-coupling analysis.

In order to test whether antiferromagnetic order may instead develop in the plane perpendicular to z, we also include the variational term

$$\hat{\mathcal{H}}^{\parallel}_{\text{AF}} = b_{\parallel} \sum_{\mathbf{R},\eta} (-1)^{R_x+R_y} \left[e^{-i\phi} \hat{c}^\dagger_{\mathbf{R},\eta,\uparrow} \hat{c}_{\mathbf{R},\eta,\downarrow} + h.c. \right], \tag{6.68}$$

where $b_{\parallel}$ is the amplitude of the in-plane staggered field and ϕ fixes its direction in the xy plane.

Finally, we consider an on-site inter-orbital excitonic hybridization

$$\hat{\mathcal{H}}_{\text{Exciton}} = \lambda_e \sum_{\mathbf{R},\eta,\sigma} i s_\sigma \hat{c}^\dagger_{\mathbf{R},\eta,\sigma} \hat{c}_{\mathbf{R},-\eta,-\sigma} \tag{6.69}$$

which flips the spin and mixes different orbitals on the same site, with $s_\uparrow = +1$ and $s_\downarrow = -1$.

We note that the terms in the auxiliary Hamiltonian proportional to b_z, $b_{\parallel}$, and λ_e explicitly break time-reversal symmetry, as defined in Eq. (6.45). However, as already discussed for the one-dimensional case in Section 6.1.3, the application of the projector $\mathcal{P}_{S^z=0}$ can restore TR symmetry at the level of the variational wavefunction. Nevertheless, finite optimized values of these variational parameters remain physically meaningful: they act as auxiliary fields that enhance the corresponding long-range correlations, and therefore provide a useful way to detect possible symmetry breaking in the thermodynamic limit.

The optimization of the variational parameters, which also include the charge and spin Jastrow pseudo-potentials $v^{\alpha,\beta}_{i,j}$ and $u^{\alpha,\beta}_{i,j}$, is performed within the variational Monte Carlo framework reviewed in Section 5.4. The same framework is used to evaluate the physical observables discussed below.

6.2.4 Numerical results

We present the numerical results obtained within the variational Monte Carlo approach using the Jastrow–Slater wavefunction.

We first consider the case $U' = 0$, in order to investigate the effect of the intra-orbital Hubbard interaction U alone. This interaction modifies both the non-interacting trivial and topological phases, but, differently from the one-dimensional case, the $\mathbb{Z}_2$ many-body marker

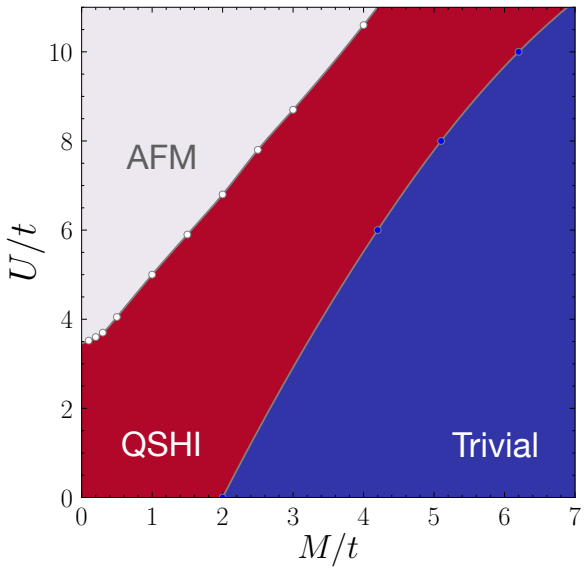


Figure 6.11: Phase diagram of the 2D BHZ model of Eq. (6.40) in the (M, U) plane for $U' = 0$ (and $t = \lambda$), as obtained using the Jastrow-Slater wavefunction. Quantum spin Hall (red) and trivial (blue) insulators are distinguished by the value of the phase of the $\mathbb{Z}_2$ many-body marker in Eq. (5.52) (π or 0, respectively). For large values of the intra-orbital interaction U, in the region $M/U \lesssim 0.5$, the antiferromagnetic phase (pink) emerges, signaled by a finite value of the magnetization order parameter in Eq. (6.70).

does not provide evidence for an intermediate phase between them. At strong coupling, the Hubbard U interaction instead drives the system into an antiferromagnetic phase ordered along the z direction. We then analyze the effect of the inter-orbital interaction by considering the case $U' = U$. In this case, we find evidence for the emergence of an insulating phase with finite excitonic correlation, which we refer to as an excitonic insulator.

6.2.4.1 The case with $U' = 0$ and the antiferromagnetic phase

The ground-state phase diagram in the (M, U) plane for $U' = 0$ is shown in Figure 6.11 and contains three different phases. The first is a trivial insulator, which is continuously connected to both the non-interacting limit with $M/t > 2$ and the Trivial configuration identified in the atomic limit. The second is the correlated QSHI, connected to the non-interacting topological state obtained for $M/t < 2$. Finally, at strong intra-orbital interaction, the system develops antiferromagnetic order along the z direction, in agreement with the strong-coupling analysis of Section 6.2.2. In the following, we describe the detailed calculations that allow us to determine the properties summarized in Figure 6.11.

The evolution with increasing U/t depends on the value of the mass term M/t. Starting

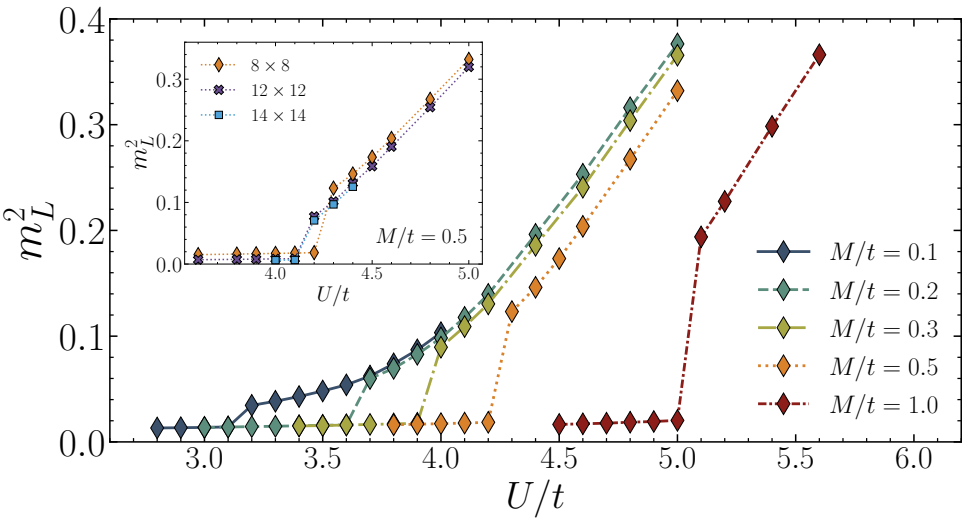


Figure 6.12: Antiferromagnetic order parameter. Main panel: the finite-size estimate of the squared staggered magnetization along the z direction, m_L^2, as a function of the intra-orbital Hubbard interaction strength U/t for a fixed 8×8 lattice and different values of the mass term M/t. Increasing M/t shifts the onset of antiferromagnetic order to larger U/t, and the transition appears to be first order. Inset: size dependence of m_L^2 at fixed $M/t = 0.5$, comparing 8×8, 12×12 and 14×14 lattices.

from the non-interacting QSHI regime at $M/t < 2$, the system eventually enters the antiferromagnetic phase. Although the variational wavefunction allows for an in-plane antiferromagnetic field, the energetically favored solution in this phase is always characterized by ordering along z. When starting from the non-interacting trivial regime at $M/t > 2$, the interaction first induces a transition into a correlated QSHI phase, before the system eventually enters the same antiferromagnetic phase at larger values of U/t. The onset of the antiferromagnetic order is detected through the finite-size estimate of the staggered magnetization [209]

$$m_L^2 = \frac{S(\pi, \pi)}{L^2} \tag{6.70}$$

where L is the linear size of the square lattice and

$$S(\mathbf{q}) = \sum_{\mathbf{R}} e^{i\mathbf{q}\cdot\mathbf{R}} \langle \hat{S}_{\mathbf{0}}^z \hat{S}_{\mathbf{R}}^z \rangle \tag{6.71}$$

is the spin structure factor, with $\hat{S}_{\mathbf{R}}^z$ the z component of the total spin operator on the site located at $\mathbf{R}$. Figure 6.12 shows the antiferromagnetic order parameter m_L^2 as a function of the intra-orbital Hubbard interaction U/t for a square lattice of size 8×8. Upon increasing the mass term M/t, the onset of the antiferromagnetic order along the z direction is shifted to larger interaction strengths. Moreover, the transition appears to be first order, as signaled by the abrupt

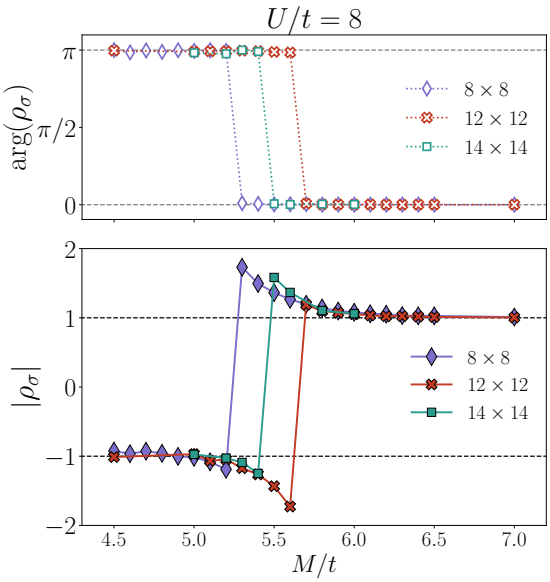


Figure 6.13: The Jastrow–Slater results for the many-body marker for two-dimensional correlated $\mathbb{Z}_2$ topological insulators given in Eq. (5.52), are shown for $U' = 0$ and $U/t = 8$. The upper panel displays the phase of the many-body marker as a function of the mass term M/t for increasing lattice sizes, while the lower panel shows the corresponding modulus. The phase distinguishes the topological phase, characterized by $\arg(\rho_\sigma) = \pi$, from the trivial phase, where $\arg(\rho_\sigma) = 0$. The data indicate a direct transition between these two insulating phases.

increase of m_L^2, especially for larger values of M/t. The inset of Figure 6.12 reports the lattice size dependence of m_L^2 for a fixed value of the mass term $M/t = 0.5$. In the non-magnetic QSHI phase the order parameter decreases with increasing system size, consistently with its vanishing in the thermodynamic limit. By contrast, in the antiferromagnetic phase, m_L^2 remains finite as the system size is increased, supporting the presence of long-range antiferromagnetic order.

We now discuss the transition between the topological and the trivial phases in the presence of interaction $U > 0$. For this purpose, we evaluate the many-body marker for correlated $\mathbb{Z}_2$ topological insulators [48] ρ_σ introduced in Eq. (5.52), on the optimized Jastrow-Slater wavefunction. In the non-interacting limit, it is possible to show that

$$\rho_\sigma = |\rho_\sigma| \exp(i\pi C_\sigma), \tag{6.72}$$

so that the phase of the marker is directly related to the spin Chern number C_σ calculated within a fixed spin sector. For a QSHI, the parity of C_σ defines the $\mathbb{Z}_2$ topological invariant.

In the presence of finite interaction strength U, the many-body marker ρ_σ is in general a complex number. Remarkably, as shown in Figure 6.13, its phase remains quantized and its modulus stays finite across the transition. This behavior allows us to identify a direct transition between the correlated QSHI phase, characterized by $\arg(\rho_\sigma) = \pi$ and corresponding to an odd spin Chern number, and the trivial phase, characterized by $\arg(\rho_\sigma) = 0$ and corresponding to an even spin Chern.

We further report that, upon computing the marker ρ_σ in the antiferromagnetic phase, its phase remains quantized and takes the value $\arg(\rho_\sigma) = 0$. This corresponds to an even value

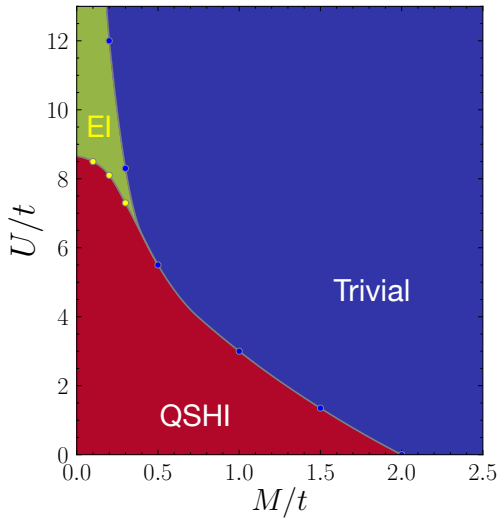


Figure 6.14: Phase diagram of the 2D BHZ model of Eq. (6.40) in the (M, U) plane for the interaction term given in Eq. (6.44), with $U' = U$ and $t = \lambda$, as obtained using the Jastrow–Slater wavefunction. Quantum spin Hall insulators (red) and trivial insulators (blue) are distinguished by the phase of the $\mathbb{Z}_2$ many-body marker defined in Eq. (5.52), which takes the values π and 0, respectively. For large values of U and small values of the mass parameter M, an excitonic insulator (green) emerges. This phase is signaled by a finite value of the excitonic correlation function defined in Eq. (6.73), evaluated at the maximum distance on the 8×8 lattice.

of the spin Chern number, suggesting that the antiferromagnetic phase is topologically trivial according to this diagnostic. Importantly, our variational wavefunction would in principle be capable of describing a phase with both a finite antiferromagnetic order parameter m_L^2 and a non-trivial value $\arg(\rho_\sigma) = \pi$. The absence of such a signal therefore indicates that, at least within the topological characterization provided by ρ_σ, the antiferromagnetic phase appearing in the phase diagram with only intra-orbital Hubbard interaction U does not display a topological character.

6.2.4.2 The case with $U' = U$ and the excitonic insulator

We finally consider the case $U' = U$, in which the intra-orbital and inter-orbital Hubbard repulsions have the same strength. In the following, we denote the total interaction simply by U. As discussed in the strong-coupling analysis of Section 6.2.2, large interactions tend to favor the Trivial local configuration. Consistently, as shown in Figure 6.14, starting from the quantum spin Hall insulating phase realized in the non-interacting limit for $M/t < 2$, increasing U generally drives the system towards a topologically trivial phase.

However, for sufficiently small values of the mass parameter M, an intermediate phase appears before the system becomes trivial. This phase is characterized by the onset of excitonic order,

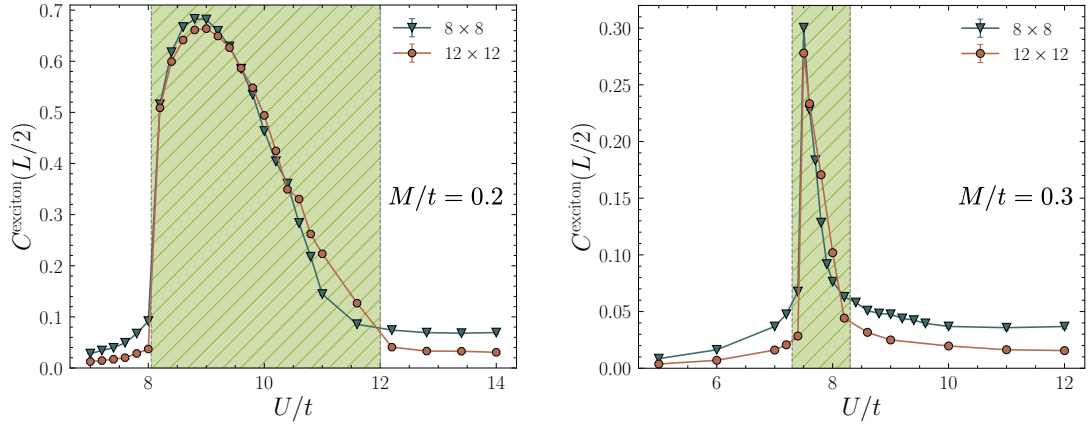


Figure 6.15: Excitonic order parameter, defined as the excitonic correlation function given in Eq. (6.73) and evaluated at the maximum distance, which on a square lattice of size $L \times L$ is $L/2$. The order parameter is shown as a function of the interaction strength U/t for fixed value of the mass parameter: $M/t = 0.2$ in the left panel and $M/t = 0.3$ in the right panel. Results are reported for two lattice sizes, 8×8 and 12×12. The green shaded regions correspond to the excitonic insulator (EI) reported as the green area in the phase diagram of Figure 6.14. These regions are identified as the range of interaction strength U/t where the excitonic order parameter remains finite with increasing system size. On the lower-U side of these regions, the transition from the QSHI, characterized by a vanishing excitonic order parameter, to the EI is most likely first-order. At large values of U/t, the transition from the EI to the trivial insulator, also characterized by a vanishing order parameter, appears to be continuous.

which we detect through the long-distance value of the excitonic correlation function

$$C^{\text{exciton}}(\mathbf{R}) = \langle \hat{\Delta}_{\mathbf{0}} \hat{\Delta}_{\mathbf{R}} \rangle, \tag{6.73}$$

where

$$\hat{\Delta}_{\mathbf{R}} = \sum_{\eta=\pm} \left(\hat{c}^{\dagger}_{\mathbf{R},\eta,\uparrow} \hat{c}_{\mathbf{R},-\eta,\downarrow} + \hat{c}^{\dagger}_{\mathbf{R},-\eta,\downarrow} \hat{c}_{\mathbf{R},\eta,\uparrow} \right). \tag{6.74}$$

The operator $\hat{\Delta}_{\mathbf{R}}$ describes a local hybridization between opposite orbitals and opposite spin projections. A finite long-distance value of $C^{\text{exciton}}(\mathbf{R})$ signals the condensation of inter-orbital particle-hole pairs, known as exciton condensate. This ordered state has been shown to be accompanied by the spontaneous breaking of spin $U(1)$, inversion and time-reversal symmetries [204].

In Figure 6.15, we show the excitonic order parameter as a function of the interaction strength U/t for two lattice sizes, considering two values of the mass term M/t. In the quantum spin Hall insulating phase, the excitonic order parameter decreases with increasing system size, consistently with the absence of long-range excitonic order. Upon increasing U/t, we observe an abrupt enhancement of the order parameter, which remains finite over a sizable range of interactions for the smallest mass considered, $M/t = 0.2$, whereas its stability region is considerably reduced for $M/t = 0.3$. In both panels of Figure 6.15, these excitonic regions are highlighted by green shaded areas and have a correspondence to the green area shown in the phase diagram of Figure 6.14.

On the lower-U side of these regions, the transition from the QSHI phase to the excitonic phase appears to be first order for both values of the mass term M/t, in agreement with the results reported in Ref. [205]. At larger values of U/t, the excitonic order parameter decreases, but in a smoother way, suggesting a continuous transition towards a topologically trivial phase, in which excitonic correlations vanish in the thermodynamic limit.

In order to further characterize the excitonic phase, we consider the density structure factor

$$N(\mathbf{q}) = \sum_{\mathbf{R}} e^{i\mathbf{q}\cdot\mathbf{R}} \langle \hat{n}_{\mathbf{0}} \hat{n}_{\mathbf{R}} \rangle, \tag{6.75}$$

where $\hat{n}_{\mathbf{R}}$ is the total density operator on the site located at $\mathbf{R}$. In the left panel of Figure 6.16, we show the density structure factors computed at $M/t = 0.2$ on a 12×12 square lattice, for increasing values of U/t. The values of U/t span the sequence of phases from the QSHI phase to the excitonic phase and, finally, to the trivial phase.

As discussed in Section 5.3.1, gapless excitations at $\mathbf{q} = 0$ are associated with a linear behavior of the structure factor in the limit $\mathbf{q} \to 0$ [150, 156]. Similarly, a singularity at a finite momentum would indicate the presence of a gapless mode at that momentum. In the excitonic phase, $N(\mathbf{q})$ is smooth around (π, π) and displays a quadratic behavior at small momenta. This indicates that the excitonic phase retains an insulating character. The same behavior is observed in the trivial phase.

We observe a slightly different behavior in the QSHI phase, close to the transition. While deep inside the topological phase the density structure factor is clearly quadratic at small momenta (not shown here), a more linear-like dependence appears as the transition towards the excitonic phase is approached, for increasing U/t. This may suggest the emergence of low-energy charge excitations and would be compatible with a transition from the QSHI to the excitonic insulator which is mediated by a gap closing. However, this interpretation is not conclusive, since a more accurate analysis on larger system sizes would be required to reliably resolve the small-$\mathbf{q}$ behavior. We also mention that Ref. [204] predicts that the transition from the QSHI to the EI, as well as the one from the EI to the trivial phase, are not accompanied by a gap closing. In this scenario, the interaction-driven spontaneous breaking of time-reversal symmetry in the EI allows to connect the QSHI phase to the trivial one without crossing a gapless point.

Finally, in the right panel of Figure 6.16 we report the spin structure factor, defined in Eq. (6.71) and computed for the same parameters as the density structure factor discussed above. In this case, we observe a clear quadratic behavior at small momenta $\mathbf{q}$ in the QSHI phase, indicating that the topological system is gapped in the spin sector, also close to the transition. We further confirm that the trivial phase has a finite gap in the spin sector. A different behavior appears in the excitonic insulating phase, where the spin structure factor displays a more linear-like dependence at small momenta.

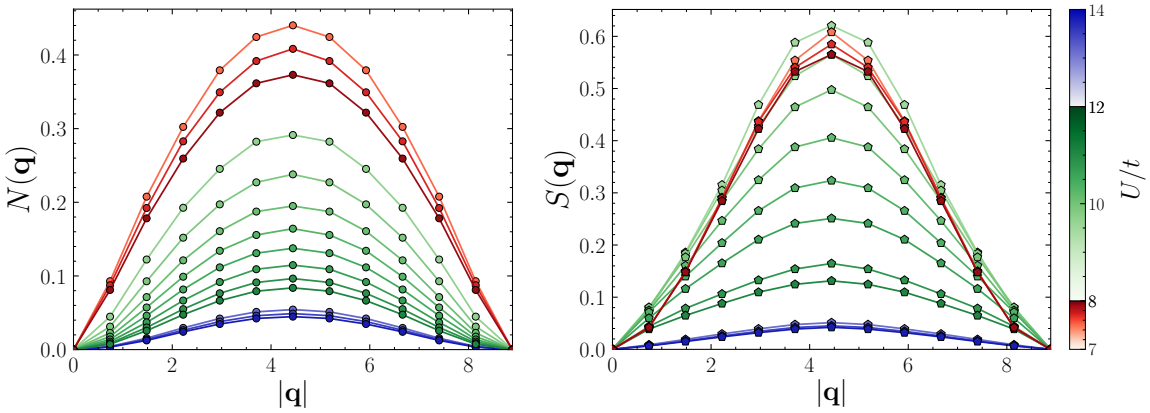


Figure 6.16: Density structure factor $N(\mathbf{q})$ (left panel) and spin structure factor $S(\mathbf{q})$ (right panel) evaluated along the diagonal direction $q_x = q_y$, for $M/t = 0.2$ on a 12×12 square lattice. Each panel shows results for several values of the interaction strength U/t, spanning the sequence of phases from the QSHI phase to the excitonic phase and, finally, to the trivial insulating phase. The color code is such that red curves correspond to the QSHI phase, green curves to the excitonic phase, and blue curves to the trivial phase, with darker shades denoting larger values of U/t. In the excitonic phase, the quadratic behavior of $N(\mathbf{q})$ at small momenta indicates its insulating character, while the more linear-like behavior of $S(\mathbf{q})$ at small momenta suggests the presence of gapless excitations in the spin sector.

This behavior suggests that the excitonic insulator, while remaining gapped in the charge sector, supports low-energy spin excitations. Such a feature is naturally interpreted as the signature of a Goldstone mode associated with the spontaneous breaking of the spin $U(1)$ symmetry. Although a finite-size scaling analysis would be needed for a definitive conclusion, the simultaneous presence of a quadratic $N(\mathbf{q})$ and a linear-like $S(\mathbf{q})$ at small-$\mathbf{q}$ provides strong evidence that the excitonic phase is an insulator with gapless spin dynamics.

Conclusions and Outlook

The aim of this thesis has been to investigate the role of disorder and strong electronic interactions in topological phases of matter. The results presented here show that these effects should not be viewed as simple perturbations of an ideal topological band structure in the non-interacting crystalline limit. Rather, they can give rise to genuinely new physical regimes and require theoretical and numerical tools capable of characterizing topology beyond the standard momentum-space framework.

The characterization of topology in disordered systems was carried out by combining single-point topological invariants within the supercell framework [7, 8] with local topological markers [9–11]. In particular, local markers make it possible to assign a spatially resolved topological quantity to each region of the sample, allowing topology to be described directly in real space. This viewpoint leads to one of the main conclusions of the thesis: although topological invariants are usually regarded as global quantities, local topological markers can act as local order parameters for disorder-driven topological phase transitions [12]. Indeed, numerical simulations on large disordered supercells of paradigmatic tight-binding models show that these markers display meaningful spatial fluctuations and correlation functions. At the transition, long-range fluctuations of these local order parameters persist, and the associated topological correlation functions exhibit critical exponents that appear to be universal across different types of disorder, such as Anderson disorder and vacancies. Importantly, these exponents remain sensitive to the nature of the transition. In particular, they distinguish between transitions in models belonging to different symmetry classes and, within a given model, between strong-disorder transitions driven by Anderson localization and disorder-induced transitions into a topological Anderson insulating phase.

This perspective provides new insight into the physics of disorder-driven topological phase transitions and opens possible directions for the systematic study of topological phases using concepts and tools inspired by statistical mechanics and quantum information theory, applied to local topological markers. In this respect, a natural future direction would be to extend the same framework to temperature-driven topological phase transitions, such as those occurring in

transition-metal dichalcogenides [210].

To move beyond canonical tight-binding models, we extended the analysis of disorder to a realistic topological material, focusing on vacancy disorder in monolayer jacutingaite (Pt_2HgSe_3). Since Hg vacancies have a very low formation energy in this material [13], they represent a particularly relevant source of disorder. By combining first-principles calculations with *ab initio* Wannier Hamiltonians, we showed that such vacancies induce in-gap defect states and assessed the stability of the quantum spin Hall insulating phase at finite vacancy concentrations.

This analysis demonstrates that the methods developed for disordered tight-binding models can be successfully transferred to realistic systems, where disorder is a physically relevant ingredient in determining the stability and evolution of topological phases. A particularly compelling avenue for future research would be to extend this analysis to bilayer jacutingaite, which is a trivial insulator in its free-standing form but can be brought close to a topological transition through encapsulation and the application of a perpendicular electric field [211]. In this context, it would be worth investigating whether Hg vacancies, or vacancy-induced disorder more generally, can provide a disorder-driven route from the trivial insulating phase to the quantum spin Hall insulating regime.

The second major theme of this thesis was the study of the effects of electronic interactions in topological insulators. This problem was addressed by using variational Monte Carlo, with a multi-orbital Jastrow–Slater wavefunction as a variational *Ansatz*. This approach offers a physically transparent way to incorporate correlation effects beyond a single-particle description and to investigate possible symmetry-breaking tendencies driven by interaction.

The interacting Bernevig–Hughes–Zhang model provides a suitable setting to investigate how electronic correlations affect quantum spin Hall insulating phases, reshape their transition toward trivial insulating regimes, and possibly stabilize additional correlated phases. This already emerges in the one-dimensional version of the model. Besides serving as a valuable benchmark for the variational approach, through comparison with DMRG calculations, the one-dimensional case reveals that interactions prevent a direct transition between the topological and trivial insulating phases. Instead, an intermediate spin-gapless insulating phase appears between them [14]. The absence of a simple weak- or strong-coupling interpretation highlights the genuinely correlated nature of this phase.

The insights gained in one dimension were then used as a starting point for the two-dimensional problem, where numerically exact methods such as exact diagonalization and DMRG become much less feasible, while VMC remains flexible and scalable. Depending on the interaction regime, the results find evidence for the stabilization of long-range ordered phases, including antiferromagnetic order and excitonic insulating behavior. In agreement with complementary investigations based on methods such as DMFT, these findings show that electronic interactions

can profoundly modify the phase diagram of topological insulators, producing phases that go beyond the simple competition between trivial and topological insulating states.

An important aspect of this work concerned the characterization of topology in interacting ground states through many-body markers inspired by the modern theory of polarization. In particular, in two dimensions, we applied a recently introduced many-body marker for interacting $\mathbb{Z}_2$ topological insulators [48]. To the best of our knowledge, this represents one of the first applications of such a marker to large-scale simulations of correlated topological systems beyond exact diagonalization. The results demonstrate that many-body markers provide a reliable diagnostic of the topological character of correlated quantum spin Hall insulators and suggest that they may become valuable tools for the broader study of interacting topological phases.

Overall, the results obtained in both one and two dimensions establish the Jastrow–Slater variational framework as a solid and versatile tool for correlated topological systems. The method is capable of capturing different interaction-driven phases while remaining computationally tractable. The availability of fast-update algorithms for this class of variational wavefunctions makes it particularly efficient for large multi-band fermionic models and therefore especially well suited to topological systems, where a multi-orbital description is often essential.

A natural continuation of this project would be to explore regimes away from half filling, which can be straightforwardly accessed within the variational Monte Carlo framework. This would make it possible to study how the interaction-driven phases identified here evolve upon doping and to assess whether superconducting tendencies may emerge from the interplay between topology and electronic correlations.

Acknowledgements

I would like to express my sincere gratitude to my supervisors, Federico Becca and Antimo Marrazzo, for their constant support throughout my research. I am especially grateful for the balance of patience and encouragement with which they guided my work, and for always being there whenever I knocked on their doors.

I would also like to warmly thank Alberto Parola, whose visits to Trieste always brought valuable scientific insights and, no less importantly, many good laughs. My sincere thanks also go to Michele Fabrizio, for many fruitful discussions, and to Daniele Coslovich, for his precious support with computational matters and for always keeping an eye on my jobs on the Bora cluster.

Finally, as a great man once taught me, "Ringrazio le persone che ho conosciuto a Trieste": thank you all for making this city so dear to me and for making it feel like home.

Appendix A

Time-reversal symmetry

The time-reversal operator $\hat{\mathcal{T}}$ reverses the direction of time evolution. As a consequence, the position operator $\hat{r}$ is unchanged, whereas the momentum operator $\hat{p}$ changes sign because it is proportional to the velocity, which is a time derivative of a TR-invariant quantity (the position operator). Consequently, the orbital angular momentum $\hat{L} = \hat{r} \times \hat{p}$ also changes sign.

$$\hat{\mathcal{T}}\,\hat{r}\,\hat{\mathcal{T}}^{-1} = \hat{r}, \qquad \hat{\mathcal{T}}\,\hat{p}\,\hat{\mathcal{T}}^{-1} = -\hat{p}, \qquad \hat{\mathcal{T}}\,\hat{L}\,\hat{\mathcal{T}}^{-1} = -\hat{L}. \tag{A.1}$$

To determine a representation for the operator $\hat{\mathcal{T}}$ we can consider its action on the commutator of $\hat{r}$ and $\hat{p}$

$$\hat{\mathcal{T}}\,[\hat{r},\hat{p}]\,\hat{\mathcal{T}}^{-1} = [\hat{\mathcal{T}}\hat{r}\hat{\mathcal{T}}^{-1}, \hat{\mathcal{T}}\hat{p}\hat{\mathcal{T}}^{-1}] = [\hat{r},-\hat{p}] = -i\hbar \tag{A.2}$$

On the other hand, since

$$[\hat{r},\hat{p}] = i\hbar, \tag{A.3}$$

it is required that

$$\hat{\mathcal{T}}\,i\,\hat{\mathcal{T}}^{-1} = -i \tag{A.4}$$

suggesting that the time-reversal operator has to be proportional to the operator of complex conjugation $\hat{K}$ that is *antilinear*

$$\hat{K}\big(\alpha\,|\psi\rangle\big) = \alpha^{*}\hat{K}\,|\psi\rangle\,. \tag{A.5}$$

An antilinear operator that preserves the norm (as we expect from a symmetry operator as time-reversal) is called *antiunitary*. Any antiunitary operator can be written in the form

$$\hat{\mathcal{T}} = \hat{U}\,\hat{K}, \tag{A.6}$$

where $\hat{U}$ is a unitary operator and $\hat{K}$ is the operator of complex conjugation.

We further require that the time-reversal operator, when applied twice, returns the original state up to a phase

$$\hat{\mathcal{T}}^2 = e^{i\theta}\mathbb{1}. \tag{A.7}$$

From calculations, one finds

$$\hat{\mathcal{T}}^2 = \hat{U}\,\hat{K}\,\hat{U}\,\hat{K} = \hat{U}\,\hat{U}^* = e^{i\theta}\mathbb{1}. \tag{A.8}$$

It can be shown [212] that the only possible values are $\theta = 0, \pi$. Therefore, we can have two cases

- $\hat{\mathcal{T}}^2 = \mathbb{1} \implies \hat{U}\,\hat{U}^* = \mathbb{1} \implies \hat{U} = \hat{U}^T \implies$ U unitary and symmetric
- $\hat{\mathcal{T}}^2 = -\mathbb{1} \implies \hat{U}\,\hat{U}^* = -\mathbb{1} \implies \hat{U} = -\hat{U}^T \implies$ U unitary and antisymmetric.

In general $\hat{\mathcal{T}}^2 = \mathbb{1}$ for integer-spin particles and $\hat{\mathcal{T}}^2 = -\mathbb{1}$ for semi-integer-spin particles.

For *spinless* fermions $\hat{\mathcal{T}}^2 = \mathbb{1}$, and the unitary part of the time-reversal operator can be taken $\hat{U} = \mathbb{1}$, so that $\hat{\mathcal{T}} = \hat{K}$, i.e. time reversal acts simply by complex conjugation of the scalar wavefunction.

For spin-1/2 fermions, time-reversal also flips the spin, since spin is an angular momentum

$$\hat{\mathcal{T}}\,\hat{\boldsymbol{\sigma}}\,\hat{\mathcal{T}}^{-1} = -\hat{\boldsymbol{\sigma}} \tag{A.9}$$

where $\hat{\boldsymbol{\sigma}} = (\hat{\sigma}_x, \hat{\sigma}_y, \hat{\sigma}_z)$ is the vector of Pauli matrices. In this case, the conventional representation of the time-reversal operator is

$$\hat{\mathcal{T}} = i\hat{\sigma}_y\hat{K} \tag{A.10}$$

which indeed satisfies Eq. (A.9) and obeys $\hat{\mathcal{T}}^2 = -\mathbb{1}$.

A.1 Time-reversal invariant Hamiltonians

As for any symmetry, a system is time-reversal invariant if its Hamiltonian $\hat{H}$ commutes with $\hat{\mathcal{T}}$

$$\hat{H}\hat{\mathcal{T}} = \hat{\mathcal{T}}\hat{H} \tag{A.11}$$

so, if $|\psi\rangle$ is an eigenstate of $\hat{H}$ with energy E, then $\hat{\mathcal{T}}\,|\psi\rangle$ is also an eigenstate of the Hamiltonian with the same energy. However, differently from ordinary symmetries that are represented by unitary and linear operators and are simultaneously diagonalized by Hamiltonian eigenvectors, antiunitary matrices are not diagonalizable in the usual sense. Therefore, Hamiltonian eigenstates

cannot, in general, be labeled by a time-reversal quantum number.
For particles with $\hat{\mathcal{T}}^2 = -\mathbb{1}$ one obtains that the states $|\psi\rangle$ and $\hat{\mathcal{T}}|\psi\rangle$ are orthogonal. Indeed,

$$\langle\psi|\hat{\mathcal{T}}\psi\rangle = \langle\hat{\mathcal{T}}^2\psi|\hat{\mathcal{T}}\psi\rangle = \langle-\psi|\hat{\mathcal{T}}\psi\rangle = -\langle\psi|\hat{\mathcal{T}}\psi\rangle \tag{A.12}$$

which implies

$$\langle\psi|\hat{\mathcal{T}}\psi\rangle = 0. \tag{A.13}$$

Thus, every energy level of a TR-invariant system with $\hat{\mathcal{T}}^2 = -1$ is at least twofold degenerate. The two degenerate states are called a Kramers pair.

A.2 Time-reversal in crystalline systems

In a crystalline system, time-reversal symmetry acts on the Bloch Hamiltonian as

$$\hat{\mathcal{T}}\hat{H}(\mathbf{k})\hat{\mathcal{T}}^{-1} = \hat{H}(-\mathbf{k}). \tag{A.14}$$

Let $|u_{n\mathbf{k}}\rangle$ be an eigenstate of the Bloch Hamiltonian at momentum $\mathbf{k}$

$$\hat{H}(\mathbf{k})|u_{n\mathbf{k}}\rangle = \varepsilon_n(\mathbf{k})|u_{n\mathbf{k}}\rangle. \tag{A.15}$$

By applying the TR operator on both sides and inserting $\hat{\mathcal{T}}^{-1}\hat{\mathcal{T}} = \mathbb{1}$ in the left-hand side, one obtains

$$\hat{\mathcal{T}}\hat{H}(\mathbf{k})\hat{\mathcal{T}}^{-1}\left(\hat{\mathcal{T}}|u_{n\mathbf{k}}\rangle\right) = \varepsilon_n(\mathbf{k})\left(\hat{\mathcal{T}}|u_{n\mathbf{k}}\rangle\right), \tag{A.16}$$

Using Eq. (A.14), this becomes

$$\hat{H}(-\mathbf{k})\left(\hat{\mathcal{T}}|u_{n\mathbf{k}}\rangle\right) = \varepsilon_n(\mathbf{k})\left(\hat{\mathcal{T}}|u_{n\mathbf{k}}\rangle\right). \tag{A.17}$$

This equation shows that the time-reversed state $\hat{\mathcal{T}}|u_{n\mathbf{k}}\rangle$ is an eigenstate of the Bloch Hamiltonian at momentum $-\mathbf{k}$, with the same energy as the original state at $\mathbf{k}$. We may therefore identify it with the time-reversed partner state

$$\hat{\mathcal{T}}|u_{n\mathbf{k}}\rangle = |u_{\bar{n},-\mathbf{k}}\rangle, \tag{A.18}$$

where $\bar{n}$ labels the band related to n by time reversal[16]. As a result, the energy spectrum satisfies

$$\varepsilon_n(\mathbf{k}) = \varepsilon_{\bar{n}}(-\mathbf{k}). \tag{A.19}$$

[16]The label $\bar{n}$ is introduced to emphasize that time reversal does not necessarily map a band onto itself. In spinful systems, for example, the time-reversal operator also flips the spinor part of the wavefunction. Thus, so a state with one spin character is mapped to its time-reversed partner with opposite spin character. This partner may be labeled by a different band index, if this index also includes the spin degree of freedom.

Thus time-reversal symmetry relates the spectrum at $\mathbf{k}$ to the spectrum at $-\mathbf{k}$. At generic points of the Brillouin zone, $\mathbf{k}$ and $-\mathbf{k}$ are distinct momenta. A special situation occurs when $\mathbf{k}$ and $-\mathbf{k}$ coincide, up to a reciprocal lattice vector $\mathbf{G}$. These momenta satisfy

$$\mathbf{\Gamma}_i = -\mathbf{\Gamma}_i + \mathbf{G} \tag{A.20}$$

and are called time-reversal invariant momenta, or TRIM. At these points, $\mathbf{\Gamma}_i$ and $-\mathbf{\Gamma}_i$ represent the same crystal momentum. Hence, Eq. (A.19) becomes a relation between states at the same point in the Brillouin zone

$$\varepsilon_n(\mathbf{\Gamma}_i) = \varepsilon_{\bar{n}}(\mathbf{\Gamma}_i). \tag{A.21}$$

For spin-1/2 particles, for which $\hat{\mathcal{T}}^2 = -\mathbb{1}$, the two states related by time reversal are orthogonal, as shown in Eq. (A.13). Therefore, at a TRIM each state has a distinct degenerate partner

$$|u_{\bar{n}\mathbf{\Gamma}_i}\rangle = \hat{\mathcal{T}}\,|u_{n\mathbf{\Gamma}_i}\rangle\,. \tag{A.22}$$

and the states $|u_{n\mathbf{\Gamma}_i}\rangle$ and $|u_{\bar{n}\mathbf{\Gamma}_i}\rangle$ form a Kramers pair.

In d spatial dimensions there are 2^d such momenta: two in one dimension, four in two dimensions, and eight in three dimensions.

Thus, while time-reversal symmetry through Eq. (A.19) only relates the spectrum at $\mathbf{k}$ and $-\mathbf{k}$ for a generic momentum, without necessarily producing a degeneracy at the same point in the Brillouin zone, it enforces an actual twofold degeneracy at the TRIM for systems with $\hat{\mathcal{T}}^2 = -\mathbb{1}$. In this case, each state has an orthogonal time-reversed partner with the same energy. As a consequence, in a TR-invariant insulator with $\hat{\mathcal{T}}^2 = -\mathbb{1}$, as in the case of spin-1/2 electrons, occupied states come in pairs related by time reversal, so that the occupied subspace contains an even number of bands.

A.3 Consequences for Berry curvature and Chern number

Time-reversal symmetry also constrains the geometrical properties of Bloch states. For a single isolated band, the Berry connection and Berry curvature are defined as

$$\mathbf{A}_n(\mathbf{k}) = i\,\langle u_{n\mathbf{k}}|\boldsymbol{\nabla}_{\mathbf{k}} u_{n\mathbf{k}}\rangle \tag{A.23}$$

and

$$\mathbf{\Omega}_n(\mathbf{k}) = \boldsymbol{\nabla}_{\mathbf{k}} \times \mathbf{A}_n(\mathbf{k}). \tag{A.24}$$

Under time reversal, a state in band n at momentum $\mathbf{k}$ is mapped to its time-reversed partner $\bar{n}$ at momentum $-\mathbf{k}$. As a consequence, the Berry curvature satisfies

$$\mathbf{\Omega}_n(\mathbf{k}) = -\mathbf{\Omega}_{\bar{n}}(-\mathbf{k}), \tag{A.25}$$

where the minus sign follows from the antiunitary nature of the time-reversal operator. For a TR-invariant set of occupied bands, the total Berry curvature therefore satisfies

$$\mathbf{\Omega}_{\mathrm{occ}}(\mathbf{k}) = -\mathbf{\Omega}_{\mathrm{occ}}(-\mathbf{k}). \tag{A.26}$$

As a consequence, its integral over the full Brillouin zone vanishes

$$\int_{\mathrm{BZ}} \mathbf{\Omega}_{\mathrm{occ}}(\mathbf{k}) \cdot d\mathbf{S} = 0 \tag{A.27}$$

and, in two dimensions, this implies that the total Chern number of a TR-invariant insulator is always trivial

$$C = \frac{1}{2\pi} \int_{\mathrm{BZ}} \Omega_{\mathrm{occ}}(\mathbf{k})\, d\mathbf{k} = 0. \tag{A.28}$$

Appendix B

Covariant derivative

In the evaluation of geometrical quantities, such as Berry phases, Berry curvatures and Chern numbers, one often encounters derivatives of the form

$$|\partial_{k_\alpha} u_n(\mathbf{k})\rangle\,. \tag{B.1}$$

These derivatives implicitly assume that the Bloch eigenstates $u_n(\mathbf{k})$ are differentiable functions of the crystal momentum. In numerical calculations, however, the eigenvectors are usually obtained independently at each $\mathbf{k}$ point by diagonalizing the Hamiltonian matrix $H(\mathbf{k})$. As a consequence, the states returned by the diagonalization routine may contain arbitrary $\mathbf{k}$-dependent phase factors. More generally, in the presence of a group of occupied bands, the occupied eigenstates may be mixed by an arbitrary unitary transformation at each $\mathbf{k}$. This gauge freedom can make ordinary finite differences ill defined unless a smooth gauge is fixed.

The *covariant derivative* provides a way to construct gauge-covariant finite differences between occupied states at nearby momenta. Its definition is naturally related to the idea of *parallel transport*, which we recall in the following.

The Berry connection associated with a set of states depending on a parameter $\boldsymbol{\xi}$ is defined, in the Abelian case, as

$$A_j^{(n)}(\boldsymbol{\xi}) = i\,\langle\psi_n(\boldsymbol{\xi})|\partial_{\xi_j}\psi_n(\boldsymbol{\xi})\rangle\,, \tag{B.2}$$

while, for a subspace spanned by several states, one introduces the non-Abelian Berry connection

$$A_{mn,j}(\boldsymbol{\xi}) = i\,\langle\psi_m(\boldsymbol{\xi})|\partial_{\xi_j}\psi_n(\boldsymbol{\xi})\rangle\,. \tag{B.3}$$

The Berry connection can be interpreted as a measure of how much the phases of the states change when moving in parameter space from point $\boldsymbol{\xi}$ to $\boldsymbol{\xi}+\delta\boldsymbol{\xi}$. Imposing the parallel-transport gauge means requiring that these phases remain unchanged under an infinitesimal displacement

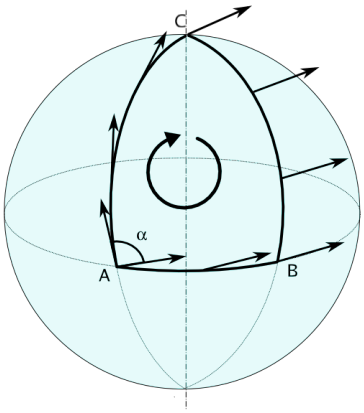


Figure B.1: Schematic representation of parallel transport on a curved surface. A vector transported along a closed path does not necessarily return with the same orientation, reflecting the curvature of the underlying space.

$\delta\boldsymbol{\xi}$. In the Abelian case, this amounts to imposing that

$$\langle\psi_n(\boldsymbol{\xi})|\psi_n(\boldsymbol{\xi}+\delta\boldsymbol{\xi})\rangle \quad \text{is real and positive} \quad \forall\boldsymbol{\xi} \tag{B.4}$$

or, equivalently

$$\langle\psi_n(\boldsymbol{\xi})|\partial_{\xi_j}\psi_n(\boldsymbol{\xi})\rangle = 0, \tag{B.5}$$

so that the Berry connection vanishes locally along the path. In the non-Abelian case, the analogous condition is that the overlap matrix

$$S_{mn} = \langle\psi_m(\boldsymbol{\xi})|\psi_n(\boldsymbol{\xi}+\delta\boldsymbol{\xi})\rangle \quad \text{is Hermitian and positive definite} \quad \forall\boldsymbol{\xi}. \tag{B.6}$$

It is important to stress that the Berry connection can be set to zero only locally along a path. If the path is closed, the states do not need to return to themselves, in general. The phase, or the unitary rotation in the non-Abelian case, accumulated after parallel transport around a closed loop is precisely the geometrical information encoded in the Berry phase, or in the Chern through the Berry curvature. This is analogous to the parallel transport of a vector on a curved surface, as shown in Figure B.1: when the vector is parallel transported along a closed path on a surface with nonzero curvature, it generally returns rotated with respect to its initial orientation. In this sense, we can think of the Berry phase as the phase "left over" after parallel transporting the states around the loop, while enforcing the Berry connection to vanish locally along the path.

We now specialize to Bloch eigenstates. Suppose that, from the diagonalization of the Bloch Hamiltonian, we obtain the occupied eigenstates at two nearby points of the Brillouin zone

$$\{|u_n(\mathbf{k})\rangle\}_{n=1}^{N_{\text{occ}}} \qquad \text{and} \qquad \{|u_n(\mathbf{k}+d\mathbf{k})\rangle\}_{n=1}^{N_{\text{occ}}}\,. \tag{B.7}$$

The overlap matrix between the two occupied subspaces is

$$S_{nm}(\mathbf{k}, \mathbf{k} + d\mathbf{k}) = \langle u_n(\mathbf{k}) | u_m(\mathbf{k} + d\mathbf{k}) \rangle \,. \tag{B.8}$$

This matrix, in general, is neither Hermitian nor positive, because of the arbitrary gauge choice made independently at the two momenta. Therefore, the states at $\mathbf{k} + d\mathbf{k}$ cannot be directly used to define a smooth finite difference.

A useful construction is to consider a unitary transformation of eigenstates at $\mathbf{k} + d\mathbf{k}$

$$|\tilde{u}_m(\mathbf{k} + d\mathbf{k}\rangle) = \sum_{l=1}^{N_{occ}} A_{lm} \, |u_l(\mathbf{k} + d\mathbf{k})\rangle \tag{B.9}$$

and to calculate the overlap

$$\begin{aligned} \tilde{S}_{nm}(\mathbf{k}, \mathbf{k} + d\mathbf{k}) \equiv \langle u_n(\mathbf{k}) | \tilde{u}_m(\mathbf{k} + d\mathbf{k}) \rangle &= \langle u_n(\mathbf{k}) | \left(\sum_{l=1}^{N_{occ}} A_{lm} \, |u_l(\mathbf{k} + d\mathbf{k})\rangle \right) \\ &= \sum_{l=1}^{N_{occ}} A_{lm} \, S_{nl}(\mathbf{k}, \mathbf{k} + d\mathbf{k}) \end{aligned} \,. \tag{B.10}$$

The new overlap matrix is therefore

$$\tilde{\mathbf{S}}(\mathbf{k}, \mathbf{k} + d\mathbf{k}) = \mathbf{A} \cdot \mathbf{S}(\mathbf{k}, \mathbf{k} + d\mathbf{k}) \tag{B.11}$$

and the easiest way to make it hermitian and positive is to construct it as the identity matrix, that is to take

$$\mathbf{A} = \mathbf{S}^{-1}(\mathbf{k}, \mathbf{k} + d\mathbf{k}). \tag{B.12}$$

The state obtained in the parallel-transport gauge is what we call the "dual" state of $|u_n(\mathbf{k})\rangle$ at $\mathbf{k} + d\mathbf{k}$

$$|\tilde{u}_n(\mathbf{k} + d\mathbf{k})\rangle = \sum_{l=1}^{N_{occ}} S^{-1}_{ln}(\mathbf{k}, \mathbf{k} + d\mathbf{k}) \, |u_l(\mathbf{k} + d\mathbf{k})\rangle \tag{B.13}$$

and can be used to define the finite-difference approximation of the covariant derivative centered in $\mathbf{k}$

$$|\tilde{\partial}_{k_\alpha} u_{n\mathbf{k}}\rangle \simeq \frac{|\tilde{u}_{n\mathbf{k}+d\mathbf{k}}\rangle - |u_{n\mathbf{k}}\rangle}{dk_\alpha} \tag{B.14}$$

which is manifestly gauge independent: it does not depend on the phases, or on the arbitrary unitary mixing within the occupied subspace, chosen by the diagonalization routine at $\mathbf{k} + d\mathbf{k}$. It may still transform with the same gauge choice as the state $|u_{n\mathbf{k}}\rangle$ at the reference point, but this dependence cancels in gauge-invariant quantities such as traces over the occupied subspace.

The dual states enjoy the property to be orthogonal to the originals states

$$\langle u_n(\mathbf{k})|\tilde{u}_m(\mathbf{k}+d\mathbf{k})\rangle = \delta_{nm} \tag{B.15}$$

from which follows

$$\langle u_n(\mathbf{k})|\tilde{\partial}_{k_\alpha} u_m(\mathbf{k})\rangle = 0, \tag{B.16}$$

that shows as the covariant derivative is orthogonal to the occupied states.

Finally, we stress that this construction requires the occupied subspace to be well defined at both $\mathbf{k}$ and $\mathbf{k}+d\mathbf{k}$. Therefore, the number of occupied states must remain constant, which is the case for an insulator with a finite gap separating occupied and unoccupied bands.

Appendix C

Fast-update algorithm

We illustrate the *fast-update algorithm* for efficiently computing the ratio of Jastrow-Slater wavefunction amplitudes, as defined in Eq. (5.70), between two configurations x and x'

$$\frac{\Psi_{JS}(x')}{\Psi_{JS}(x)}. \tag{C.1}$$

Such ratios are required both for constructing the Markov chains of configurations in the Metropolis algorithm and for evaluating local observables

$$\mathcal{A}_l(x) = \sum_{x'} \langle x| \hat{\mathcal{A}} |x'\rangle \frac{\Psi_{JS}(x')}{\Psi_{JS}(x)}. \tag{C.2}$$

In the following, we will refer to the specific case in which x and x' are consecutive configurations in the Markov chain. However, the algorithm applies also to the case in which x and x' are two configurations such that $\langle x| \hat{\mathcal{A}} |x'\rangle \neq 0$. Indeed, owing to the local nature of physical operators $\hat{\mathcal{A}}$, such configurations x' differ from x by only a few electron processes.

We start by choosing a specific representation for the configuration $|x\rangle$

$$|x\rangle = \hat{c}^\dagger_{R_1} \cdots \hat{c}^\dagger_{R_l} \cdots \hat{c}^\dagger_{R_{N_e}} |0\rangle , \tag{C.3}$$

where the collective index $R_l = (j_l, \eta_l, \sigma_l)$ gives the lattice position, orbital occupation, and spin configuration (along the z-axis) of the l-th electron, on a total number of N_e electrons, and $|0\rangle$ is the vacuum of the whole lattice. If we consider a Markov chain where each proposal corresponds to a move of a single electron (which can be a hopping to a different site, a change in the orbital sector, a flip in the spin[17], or a combination of these), that defines a new configuration

$$|x'\rangle = \hat{c}^\dagger_{R'_l} \hat{c}_{R_l} |x\rangle = \hat{c}^\dagger_{R_1} \cdots \hat{c}^\dagger_{R'_l} \cdots \hat{c}^\dagger_{R_{N_e}} |0\rangle . \tag{C.4}$$

[17] Note that this does not preserve $S_z = 0$, but we keep the discussion general.

In the following, we will try to keep the discussion as general as possible, and we will consider Monte Carlo steps that can involve more than one electron, as it is in the case of pair-hoppings or spin-exchanges, which lead from $|x\rangle$ to the configuration

$$|x'\rangle = \hat{c}^\dagger_{R'_{l_1}} \hat{c}_{R_{l_1}} \cdots \hat{c}^\dagger_{R'_{l_m}} \hat{c}_{R_{l_m}} |x\rangle \,, \tag{C.5}$$

where m is the number of electrons involved in the process.

C.1 Fast computation of the Slater determinant

We consider an auxiliary quadratic Hamiltonian that can be written as

$$\hat{H}_{aux} = \sum_{I,J}^{N_{states}} h_{I,J} \hat{c}^\dagger_I \hat{c}_J = \sum_{\alpha}^{N_{states}} \epsilon_\alpha \hat{\phi}^\dagger_\alpha \hat{\phi}_\alpha \tag{C.6}$$

where $N_{states} = n_b n_s N$ is the number of possible states that an electron can occupy if we consider n_b orbital degrees of freedom, n_s spin configurations, in a lattice with N sites. The $\hat{\phi}_\alpha$,$\hat{\phi}^\dagger_\alpha$ are the fermionic operators in which the Hamiltonian is diagonal, and define single-particle orbitals

$$\hat{\phi}^\dagger_\alpha = \sum_{I=1}^{N_{states}} U_{I,\alpha} \hat{c}^\dagger_I \qquad \text{and} \qquad \epsilon_\alpha = \sum_{I,J=1}^{N_{states}} U^*_{\alpha,I} h_{I,J} U_{J,\alpha} \tag{C.7}$$

where $\mathbf{U}$ is the unitary matrix diagonalizing the Hamiltonian.

Thus the non-interacting ground state $|\Phi_0\rangle$ can be constructed by the N_e lowest-energy orbitals as the Slater determinant

$$\langle x|\Phi_0\rangle = \langle x| \prod_{\alpha=1}^{N_e} \hat{\phi}^\dagger_\alpha |0\rangle = \langle 0| \hat{c}_{R_{N_e}} \cdots \hat{c}_{R_1} \left(\sum_I U_{I,1} \hat{c}^\dagger_I \right) \cdots \left(\sum_I U_{I,N_e} \hat{c}^\dagger_I \right) |0\rangle \tag{C.8}$$

$$= \langle x| \prod_{\alpha=1}^{N_e} \hat{\phi}^\dagger_\alpha |0\rangle = \langle 0| \hat{c}_{R_{N_e}} \cdots \hat{c}_{R_1} \left[\sum_p (-1)^p \prod_{\alpha=1}^{N_e} U_{p\{R_j\},\alpha} \right] \hat{c}^\dagger_{R_1} \cdots \hat{c}^\dagger_{R_{N_e}} |0\rangle \tag{C.9}$$

where the sum over p considers all possible permutations of the electronic states $\{R_j\}$ in $|x\rangle$. Then, we finally get the Slater wavefunction

$$\Phi_0(x) = \langle x|\Phi_0\rangle = \det \tilde{\mathbf{U}} \tag{C.10}$$

where we denoted by $\tilde{\mathbf{U}}$ the $N_e \times N_e$ matrix containing the elements $\tilde{U}_{j,\alpha} := U_{R_j,\alpha}$ which are obtained taking the N_e lowest energy-ordered columns and only the rows corresponding to the

occupied electronic states of the matrix $\mathbf{U}$

$$\tilde{\mathbf{U}} = \begin{pmatrix} U_{R_1,1} & \dots & U_{R_1,N_e} \\ \vdots & \ddots & \vdots \\ U_{R_l,1} & \dots & U_{R_l,N_e} \\ \vdots & \ddots & \vdots \\ U_{R_{N_e},1} & \dots & U_{R_{N_e},N_e} \end{pmatrix}. \tag{C.11}$$

Notice, in particular, that the order of the rows in $\tilde{\mathbf{U}}$ is determined by the one of the creation operators in Eq. (C.3).

Then, when calculating the ratio between the Slater determinants in two consequent configurations of the Markov chain that differ by the hoppings of m electrons with indices $\{l_r\}$, for $r = 1, \dots, m$, we have

$$\frac{\langle x'|\Phi_0\rangle}{\langle x|\Phi_0\rangle} = \frac{\langle x|\hat{c}_{R_{l_m}}\hat{c}^\dagger_{R'_{l_m}} \cdots \hat{c}_{R_{l_1}}\hat{c}^\dagger_{R'_{l_1}}|\Phi_0\rangle}{\langle x|\Phi_0\rangle} = \frac{\det \tilde{\mathbf{U}}'}{\det \tilde{\mathbf{U}}} \tag{C.12}$$

where the matrix $\tilde{\mathbf{U}}'$ differs from $\tilde{\mathbf{U}}$ only in the m rows corresponding to the electrons with the indices l_r, whose elements change from $U_{R_{l_r},\alpha}$ to $U_{R'_{l_r},\alpha}$. By denoting with K_r the new collective index of the l_r-th electron (i.e., $K_r := R'_{l_r}$), the updated matrix elements are given by

$$\tilde{U}'_{j,\alpha} = \tilde{U}_{j,\alpha} + \sum_{r=1}^{m} \delta_{j,l_r}(U_{K_r,\alpha} - \tilde{U}_{l_r,\alpha}) = \tilde{U}_{j,\alpha} + \sum_{r=1}^{m} \delta_{j,l_r}\, \nu_\alpha^{K_r,l_r} \tag{C.13}$$

where we have defined $\nu_\alpha^{K_r,l_r} = U_{K_r,\alpha} - \tilde{U}_{l_r,\alpha}$. Moreover, by rewriting

$$\tilde{U}'_{j,\alpha} = \sum_\beta \tilde{U}_{j,\beta}\big(\delta_{\beta,\alpha} + \sum_{r=1}^{m} \tilde{U}^{-1}_{\beta,l_r}\, \nu_\alpha^{K_r,l_r}\big) = \sum_\beta \tilde{U}_{j,\beta} Q_{\beta,\alpha} \tag{C.14}$$

we have defined the matrix $\mathbf{Q}$ whose elements are

$$Q_{\beta,\alpha} = \delta_{\beta,\alpha} + \sum_{r=1}^{m} \tilde{U}^{-1}_{\beta,l_r}\, \nu_\alpha^{K_r,l_r} = \delta_{\beta,\alpha} + \sum_{r=1}^{m} \mathcal{B}^r_\beta\, \mathcal{A}^r_\alpha, \tag{C.15}$$

where $\mathcal{B}^r_\beta = \tilde{U}^{-1}_{\beta,l_r}$ and $\mathcal{A}^r_\alpha = \nu_\alpha^{K_r,l_r}$. Therefore, from Eq. (C.14) we have $\tilde{\mathbf{U}}' = \tilde{\mathbf{U}}\mathbf{Q}$, which implies

$$\frac{\det \tilde{\mathbf{U}}'}{\det \tilde{\mathbf{U}}} = \det \mathbf{Q}. \tag{C.16}$$

The determinant of $\mathbf{Q}$ can be computed by solving the eigenvalue problem $\mathbf{Q}\mathbf{v} = \lambda\mathbf{v}$,

$$\sum_{\alpha} Q_{\beta,\alpha} v_{\alpha} = v_{\beta} + \sum_{r=1}^{m} \mathcal{B}_{\beta}^{r} \sum_{\alpha=1}^{N_e} \mathcal{A}_{\alpha}^{r}\, v_{\alpha} = \lambda\, v_{\beta} \tag{C.17}$$

which implies that all the vectors $\mathbf{v}$ that are orthogonal to the subspace defined by the vectors $\boldsymbol{\mathcal{A}}^r$ are eigenvectors with $\lambda = 1$; the number of such vectors is at least $N_e - m$, provided that the vectors $\boldsymbol{\mathcal{A}}^r$ are linearly independent for $r = 1, \ldots, m$. Moreover, the vector with components $v_{\alpha} = \sum_{r=1}^{m} x_r\, \mathcal{B}_{\alpha}^{r}$ is an eigenvector provided that the coefficients x_r satisfy

$$\sum_{s=1}^{m} \Big(\delta_{r,s} + \sum_{\alpha=1}^{N_e} \mathcal{A}_{\alpha}^{r}\, \mathcal{B}_{\alpha}^{s} \Big) x_s = \lambda\, x_r. \tag{C.18}$$

Therefore, there are m non-trivial eigenvalues of $\mathbf{Q}$ that are the ones of the $m \times m$ matrix $\mathbf{C}$ with elements

$$C_{r,s} = \delta_{r,s} + \sum_{\alpha=1}^{N_e} \mathcal{A}_{\alpha}^{r}\, \mathcal{B}_{\alpha}^{s}. \tag{C.19}$$

From the previous definitions, we see that

$$\sum_{\alpha} \mathcal{A}_{\alpha}^{r}\, \mathcal{B}_{\alpha}^{s} = \sum_{\alpha} \nu_{\alpha}^{K_r,l_r}\, \tilde{U}_{\alpha,l_s}^{-1} = \sum_{\alpha} (U_{K_r,\alpha} - \tilde{U}_{l_r,\alpha})\, \tilde{U}_{\alpha,l_s}^{-1} = \sum_{\alpha} U_{K_r,\alpha}\, \tilde{U}_{\alpha,l_s}^{-1} - \delta_{r,s}, \tag{C.20}$$

which implies that the final expression of the ratio of the two determinants is given by

$$\frac{\det \tilde{\mathbf{U}}'}{\det \tilde{\mathbf{U}}} = \det \mathbf{C} = \det \Big(\sum_{\alpha} U_{K_r,\alpha}\, \tilde{U}_{\alpha,l_s}^{-1} \Big) = \det\big(W_{K_r,l_s}\big). \tag{C.21}$$

This allows us to finally introduce the $N_{states} \times N_e$ matrix $\mathbf{W}$, whose elements are given by

$$W_{I,j} = \sum_{\alpha} U_{I,\alpha} \tilde{U}_{\alpha,j}^{-1}, \tag{C.22}$$

which can be stored at the beginning of the calculation. Then, the ratio of the determinants at each Monte Carlo move can be evaluated by extracting the $m \times m$ sub-matrices of $\mathbf{W}$ obtained by considering only the elements W_{K_r,l_s} for $r, s = 1, \ldots, m$ and evaluating the determinant of these much smaller matrices.

In addition to evaluating the ratio, once the new configuration $|x'\rangle$ is accepted along the Markov chain, the matrix $\tilde{\mathbf{U}}$ must be updated. In particular, we have that $\big(\tilde{\mathbf{U}}'\big)^{-1} = \mathbf{Q}^{-1}\tilde{\mathbf{U}}^{-1}$, the inverse of the matrix $\mathbf{Q}$ being given by

$$Q_{\alpha,\beta}^{-1} = \delta_{\alpha,\beta} - \sum_{r,s=1}^{m} \mathcal{B}_{\alpha}^{r}\, C_{r,s}^{-1}\, \mathcal{A}_{\beta}^{s}. \tag{C.23}$$

Indeed, we can easily verify that $\sum_\alpha Q_{\beta,\alpha}\, Q^{-1}_{\alpha,\gamma} = \delta_{\beta,\gamma}$:

$$\sum_\alpha \left(\delta_{\beta,\alpha} + \sum_{t=1}^{m} \mathcal{B}^t_\beta\, \mathcal{A}^t_\alpha\right)\left(\delta_{\alpha,\gamma} - \sum_{r,s=1}^{m} \mathcal{B}^r_\alpha\, C^{-1}_{r,s}\, \mathcal{A}^s_\gamma\right) \tag{C.24}$$

$$= \sum_\alpha \left(\delta_{\beta,\alpha}\delta_{\alpha,\gamma} + \delta_{\alpha,\gamma}\sum_{t=1}^{m} \mathcal{B}^t_\beta\, \mathcal{A}^t_\alpha - \delta_{\beta,\alpha}\sum_{r,s=1}^{m} \mathcal{B}^r_\alpha\, C^{-1}_{r,s}\, \mathcal{A}^s_\gamma - \sum_{t,r,s=1}^{m} \mathcal{B}^t_\beta\, \mathcal{A}^t_\alpha \mathcal{B}^r_\alpha\, C^{-1}_{r,s}\, \mathcal{A}^s_\gamma\right) \tag{C.25}$$

$$= \delta_{\beta,\gamma} + \sum_{t=1}^{m} \mathcal{B}^t_\beta\, \mathcal{A}^t_\gamma - \sum_{r,s=1}^{m} \mathcal{B}^r_\beta\, C^{-1}_{r,s}\, \mathcal{A}^s_\gamma - \sum_{t,r,s=1}^{m} \mathcal{B}^t_\beta\, C^{-1}_{r,s}\, \mathcal{A}^s_\gamma \sum_\alpha \mathcal{A}^t_\alpha \mathcal{B}^r_\alpha. \tag{C.26}$$

The result is straightforward if, from Eq. (C.19), we substitute $\sum_\alpha \mathcal{A}^t_\alpha \mathcal{B}^r_\alpha = C_{t,r} - \delta_{t,r}$.

Then, the updated matrix elements of $\left(\tilde{\mathbf{U}}'\right)^{-1}$ are given by

$$\left(\tilde{\mathbf{U}}'\right)^{-1}_{\alpha,j} = \sum_\beta Q^{-1}_{\alpha,\beta}\, \tilde{U}^{-1}_{\beta,j} = \tilde{U}^{-1}_{\alpha,j} - \sum_{r,s=1}^{m} \tilde{U}^{-1}_{\alpha,l_r}\, C^{-1}_{r,s}\left(\sum_\beta U_{K_s,\beta}\, \tilde{U}^{-1}_{\beta,j} - \delta_{l_s,j}\right). \tag{C.27}$$

Finally, the updated $\mathbf{W}'$ matrix is obtained by multiplying both sides of the previous equation by $U_{i,\alpha}$ and summing over α

$$W'_{I,j} = W_{I,j} + \sum_{r=1}^{m} W_{I,l_r}\, b^{(r)}_j \tag{C.28}$$

where

$$b^{(r)}_j = -\sum_{s=1}^{m} C^{-1}_{r,s}\left(W_{K_s,j} - \delta_{l_s,j}\right). \tag{C.29}$$

So, instead of computing the Slater determinant at each Monte Carlo step, which would cost $O(N^3_{states}) \sim O(N^3)$ operations, the fast-update algorithm provides for storing the $\mathbf{W}$ matrix at the beginning of the calculation and using it for calculating the ratio between Slater determinants, through Eq. (C.21) which is inexpensive in the common case in which the number m of electrons involved in the hopping process is small. If the new configuration is accepted in the Markov chain, it is enough to update the $\mathbf{W}$ matrix through Eq. (C.28) which costs $O(N_{states}\, N_e) \sim O(N^2)$.

C.2 Fast computation of the Jastrow factor

Let us now consider the contributions arising from the Jastrow factors

$$\hat{\mathcal{J}}_d = \exp\left[-\frac{1}{2}\sum_{i,j}\sum_{\alpha,\beta} v^{\alpha,\beta}_{i,j}\, \hat{n}_{i,\alpha}\hat{n}_{j,\beta}\right], \tag{C.30}$$

$$\hat{\mathcal{J}}_s = \exp\left[-\frac{1}{2}\sum_{i,j}\sum_{\alpha,\beta} u^{\alpha,\beta}_{i,j}\, \hat{S}^z_{i,\alpha}\hat{S}^z_{j,\beta}\right]. \tag{C.31}$$

A straightforward calculation of the amplitude of the generic Jastrow factor $\hat{\mathcal{J}}$ on the configuration $|x\rangle$, namely $\mathcal{J}(x)$, requires $O(N^2)$ operations whenever the Jastrow operator is diagonal in the basis $\{|x\rangle\}$, as is the case for charge and spin Jastrow factors above when the configurations are given by Eq. (C.3).

The same computational cost is required when computing the ratio $\mathcal{J}(x')/\mathcal{J}(x)$ at each Monte Carlo step. However, when two configurations differ by only a few fermionic hoppings, it is possible to apply a fast computation of the ratio, reducing the cost to $O(N)$ operations.

Indeed, let us consider, for simplicity, a single hopping $\hat{c}^\dagger_{R'_l}\hat{c}_{R_l}$ as the one in Eq. (C.4). This process affects both the electronic charge $n_{i,\alpha}$ and the spin configuration $S^z_{i,\alpha}$ at the generic site-orbital (i,α). Dropping the electron index l and making the indices explicit, i.e., $R_l = R = (j,\eta,\sigma)$ and $R'_l = R' = (j',\eta',\sigma')$, the electronic charge and the spin configuration are modified as

$$n'_{i,\alpha} = n_{i,\alpha} + \delta_{i,j'}\delta_{\alpha,\eta'} - \delta_{i,j}\delta_{\alpha,\eta}, \tag{C.32}$$

$$S^{z'}_{i,\alpha} = S^z_{i,\alpha} + \sigma'\,\delta_{i,j'}\delta_{\alpha,\eta'} - \sigma\,\delta_{i,j}\delta_{\alpha,\eta}. \tag{C.33}$$

From these relations, the ratio between the Jastrow factors evaluated on $|x'\rangle$ and $|x\rangle$ is[18]

$$\begin{cases} \dfrac{\mathcal{J}_d(x')}{\mathcal{J}_d(x)} = \exp\Big[-T_d\,[\eta',j'] + T_d\,[\eta,j] + u^{\eta,\eta'}_{j,j'} - u^{\eta,\eta}_{j,j}\Big] \\ \dfrac{\mathcal{J}_s(x')}{\mathcal{J}_s(x)} = \exp\Big[-\sigma'\,T_s\,[\eta',j'] + \sigma\,T_s\,[\eta,j] + \sigma\,\sigma'\,v^{\eta,\eta'}_{j,j'} - v^{\eta,\eta}_{j,j}\Big] \end{cases}$$

where $\mathbf{T}_d$ and $\mathbf{T}_d$ are $n_b \times N$ matrices whose elements are

$$T_d\,[\nu,m] = \sum_{i,\alpha} u^{\alpha,\nu}_{i,m} n_{i,\alpha} \qquad \text{and} \qquad T_s\,[\nu,m] = \sum_{i,\alpha} v^{\alpha,\nu}_{i,m} S^z_{i,\alpha}. \tag{C.34}$$

The evaluation of the ratios can be done in $O(1)$ operations once the $\mathbf{T}_d$ and $\mathbf{T}_s$ matrices are stored at the beginning of the calculation. Then, if the new configuration is accepted, the matrices have to be updated as

$$\begin{cases} T'_d\,[\nu,m] = T_d\,[\nu,m] + u^{\nu,\eta'}_{m,j'} - u^{\nu,\eta}_{m,j} \\ T'_s\,[\nu,m] = T_s\,[\nu,m] + \sigma'\,v^{\nu,\eta'}_{m,j'} - \sigma\,v^{\nu,\eta}_{m,j} \end{cases}$$

which require $O(N_{sites})$ operations.

[18] Note that the following results hold under the assumption that the intra-orbital on-site terms are the same for every orbital, i.e., $v^{\alpha,\alpha}_{i,i} = v^{\beta,\beta}_{i,i}$.

In the following, we extend the Jastrow ratio calculations and the **T**-matrices updates to two particular multi-electron hopping processes that are

$$\begin{cases} |x'\rangle = \hat{c}^{\dagger}_{j,\eta,\downarrow}\hat{c}_{j',\eta',\downarrow}\hat{c}^{\dagger}_{j',\eta',\uparrow}\hat{c}_{j,\eta,\uparrow}\,|x\rangle & : \text{ spin-exchange} \\ |x'\rangle = \hat{c}^{\dagger}_{j',\eta',\downarrow}\hat{c}_{j,\eta,\downarrow}\hat{c}^{\dagger}_{j',\eta',\uparrow}\hat{c}_{j,\eta,\uparrow}\,|x\rangle & : \text{ pair-hopping} \end{cases},$$

both involving two electrons.

The corresponding Jastrow ratios are

$$\text{spin-exchange} : \begin{cases} \dfrac{\mathcal{J}_d(x')}{\mathcal{J}_d(x)} = 1 \\ \dfrac{\mathcal{J}_s(x')}{\mathcal{J}_s(x)} = \exp\Big[-2\,T_s\,[\eta',j'] + 2\,T_s\,[\eta,j] + 4\,v^{\eta,\eta'}_{j,j'} - 4\,v^{\eta,\eta}_{j,j}\Big] \end{cases},$$

$$\text{pair-hopping} : \begin{cases} \dfrac{\mathcal{J}_d(x')}{\mathcal{J}_d(x)} = \exp\Big[-2\,T_d\,[\eta',j'] + 2\,T_d\,[\eta,j] + 4\,u^{\eta,\eta'}_{j,j'} - 4\,u^{\eta,\eta}_{j,j}\Big] \\ \dfrac{\mathcal{J}_s(x')}{\mathcal{J}_s(x)} = 1 \end{cases}.$$

The updates of the **T** matrices are

$$\text{spin-exchange} : \begin{cases} T'_d\,[\nu,m] = T_d\,[\nu,m] \\ T'_s\,[\nu,m] = T_s\,[\nu,m] + 2\,v^{\nu,\eta'}_{m,j'} - 2\,v^{\nu,\eta}_{m,j} \end{cases},$$

$$\text{pair-hopping} : \begin{cases} T'_d\,[\nu,m] = T_d\,[\nu,m] + 2\,u^{\nu,\eta'}_{m,j'} - 2\,u^{\nu,\eta}_{m,j} \\ T'_s\,[\nu,m] = T_s\,[\nu,m] \end{cases}.$$

Bibliography

[1]L. D. Landau, "On the theory of phase transitions", Zh. Eksp. Teor. Fiz. **7**, edited by D. ter Haar, 19–32 (1937).

[2]V. L. Ginzburg and L. D. Landau, "On the Theory of superconductivity", Zh. Eksp. Teor. Fiz. **20**, edited by D. ter Haar, 1064–1082 (1950).

[3]F. D. M. Haldane, "Model for a Quantum Hall Effect without Landau Levels: Condensed-Matter Realization of the 'Parity Anomaly'", Phys. Rev. Lett. **61**, 2015–2018 (1988).

[4]C. L. Kane and E. J. Mele, "Z_2 Topological Order and the Quantum Spin Hall Effect", Phys. Rev. Lett. **95**, 146802 (2005).

[5]C. L. Kane and E. J. Mele, "Quantum Spin Hall Effect in Graphene", Phys. Rev. Lett. **95**, 226801 (2005).

[6]B. A. Bernevig, T. L. Hughes, and S.-C. Zhang, "Quantum Spin Hall Effect and Topological Phase Transition in HgTe Quantum Wells", Science **314**, 1757–1761 (2006).

[7]D. Ceresoli and R. Resta, "Orbital magnetization and Chern number in a supercell framework: Single **k**-point formula", Phys. Rev. B **76**, 012405 (2007).

[8]R. Favata and A. Marrazzo, "Single-point spin Chern number in a supercell framework", Electronic Structure **5**, 014005 (2023).

[9]R. Bianco and R. Resta, "Mapping topological order in coordinate space", Phys. Rev. B **84**, 241106 (2011).

[10]N. Baù and A. Marrazzo, "Theory of local $\mathbb{Z}_2$ topological markers for finite and periodic two-dimensional systems", Phys. Rev. B **110**, 054203 (2024).

[11]N. Baù and A. Marrazzo, "Local Chern marker for periodic systems", Phys. Rev. B **109**, 014206 (2024).

[12]R. Favata, N. Baù, and A. Marrazzo, "Fluctuations and correlations of local topological order parameters in disordered two-dimensional topological insulators", Phys. Rev. Lett. **135**, 026603 (2025).

[13]A. Marrazzo, M. Gibertini, D. Campi, N. Mounet, and N. Marzari, "Prediction of a Large-Gap and Switchable Kane-Mele Quantum Spin Hall Insulator", Phys. Rev. Lett. **120**, 117701 (2018).

[14]R. Favata, D. Piccioni, A. Parola, and F. Becca, "Interaction-induced phases in the half-filled bernevig-hughes-zhang model in one dimension", Phys. Rev. B **111**, 155105 (2025).

[15]D. Vanderbilt, *Berry Phases in Electronic Structure Theory: Electric Polarization, Orbital Magnetization and Topological Insulators* (Cambridge University Press, 2018).

[16]N. Marzari and D. Vanderbilt, "Maximally localized generalized Wannier functions for composite energy bands", Phys. Rev. B **56**, 12847–12865 (1997).

[17]M. V. Berry, "Quantal phase factors accompanying adiabatic changes", Proceedings of the Royal Society of London. A. Mathematical and Physical Sciences **392**, 45–57 (1984).

[18]B. Bernevig and T. Hughes, *Topological Insulators and Topological Superconductors* (Princeton University Press, 2013).

[19]R. D. King-Smith and D. Vanderbilt, "Theory of polarization of crystalline solids", Phys. Rev. B **47**, 1651–1654 (1993).

[20]R. Resta, "Macroscopic polarization in crystalline dielectrics: the geometric phase approach", Rev. Mod. Phys. **66**, 899–915 (1994).

[21]J. Zak, "Berry's phase for energy bands in solids", Phys. Rev. Lett. **62**, 2747–2750 (1989).

[22]L. Li, C. Yang, and S. Chen, "Winding numbers of phase transition points for one-dimensional topological systems", Europhysics Letters **112**, 10004 (2015).

[23]L. Fu and C. L. Kane, "Time reversal polarization and a Z_2 adiabatic spin pump", Phys. Rev. B **74**, 195312 (2006).

[24]L. Fu and C. L. Kane, "Topological insulators with inversion symmetry", Phys. Rev. B **76**, 045302 (2007).

[25]K. v. Klitzing, G. Dorda, and M. Pepper, "New Method for High-Accuracy Determination of the Fine-Structure Constant Based on Quantized Hall Resistance", Phys. Rev. Lett. **45**, 494–497 (1980).

[26]D. J. Thouless, M. Kohmoto, M. P. Nightingale, and M. den Nijs, "Quantized Hall Conductance in a Two-Dimensional Periodic Potential", Phys. Rev. Lett. **49**, 405–408 (1982).

[27]M. Fruchart and D. Carpentier, "An introduction to topological insulators", Comptes Rendus Physique **14**, 779–815 (2013).

[28]J. C. Y. Teo, L. Fu, and C. L. Kane, "Surface states and topological invariants in three-dimensional topological insulators: Application to $Bi_{1-x}Sb_x$", Phys. Rev. B **78**, 045426 (2008).

[29]D. N. Sheng, Z. Y. Weng, L. Sheng, and F. D. M. Haldane, "Quantum Spin-Hall Effect and Topologically Invariant Chern Numbers", Phys. Rev. Lett. **97**, 036808 (2006).

[30]A. A. Soluyanov and D. Vanderbilt, "Smooth gauge for topological insulators", Phys. Rev. B **85**, 115415 (2012).

[31]E. Prodan, "Robustness of the spin-Chern number", Phys. Rev. B **80**, 125327 (2009).

[32]Y. Yang, Z. Xu, L. Sheng, B. Wang, D. Y. Xing, and D. N. Sheng, "Time-Reversal-Symmetry-Broken Quantum Spin Hall Effect", Phys. Rev. Lett. **107**, 066602 (2011).

[33]C.-C. Liu, W. Feng, and Y. Yao, "Quantum Spin Hall Effect in Silicene and Two-Dimensional Germanium", Phys. Rev. Lett. **107**, 076802 (2011).

[34]Y. Xu, B. Yan, H.-J. Zhang, J. Wang, G. Xu, P. Tang, W. Duan, and S.-C. Zhang, "Large-Gap Quantum Spin Hall Insulators in Tin Films", Phys. Rev. Lett. **111**, 136804 (2013).

[35]B. A. Bernevig and S.-C. Zhang, "Quantum Spin Hall Effect", Phys. Rev. Lett. **96**, 106802 (2006).

[36]M. König, S. Wiedmann, C. Brüne, A. Roth, H. Buhmann, L. W. Molenkamp, X.-L. Qi, and S.-C. Zhang, "Quantum Spin Hall Insulator State in HgTe Quantum Wells", Science **318**, 766–770 (2007).

[37]A. P. Schnyder, S. Ryu, A. Furusaki, and A. W. W. Ludwig, "Classification of topological insulators and superconductors in three spatial dimensions", Phys. Rev. B **78**, 195125 (2008).

[38]A. Kitaev, V. Lebedev, and M. Feigel'man, "Periodic table for topological insulators and superconductors", in Aip conference proceedings (2009), pp. 22–30.

[39]C.-K. Chiu, J. C. Y. Teo, A. P. Schnyder, and S. Ryu, "Classification of topological quantum matter with symmetries", Rev. Mod. Phys. **88**, 035005 (2016).

[40]A. Altland and M. R. Zirnbauer, "Nonstandard symmetry classes in mesoscopic normal-superconducting hybrid structures", Phys. Rev. B **55**, 1142–1161 (1997).

[41]L. Fu, "Topological Crystalline Insulators", Phys. Rev. Lett. **106**, 106802 (2011).

[42]I. C. Fulga, B. van Heck, J. M. Edge, and A. R. Akhmerov, "Statistical topological insulators", Phys. Rev. B **89**, 155424 (2014).

[43]G. Ortiz and R. M. Martin, "Macroscopic polarization as a geometric quantum phase: Many-body formulation", Phys. Rev. B **49**, 14202–14210 (1994).

[44]R. Resta, "Quantum-Mechanical Position Operator in Extended Systems", Phys. Rev. Lett. **80**, 1800–1803 (1998).

[45]Q. Niu and D. J. Thouless, "Quantised adiabatic charge transport in the presence of substrate disorder and many-body interaction", Journal of Physics A: Mathematical and General **17**, 2453 (1984).

[46]Q. Niu, D. J. Thouless, and Y.-S. Wu, "Quantized Hall conductance as a topological invariant", Phys. Rev. B **31**, 3372–3377 (1985).

[47]R. Resta and S. Sorella, "Electron Localization in the Insulating State", Phys. Rev. Lett. **82**, 370–373 (1999).

[48]I. Gilardoni, F. Becca, A. Marrazzo, and A. Parola, "Real-space many-body marker for correlated $\mathbb{Z}_2$ topological insulators", Phys. Rev. B **106**, L161106 (2022).

[49]L. Fidkowski and A. Kitaev, "Effects of interactions on the topological classification of free fermion systems", Phys. Rev. B **81**, 134509 (2010).

[50]F. D. M. Haldane, "Nonlinear Field Theory of Large-Spin Heisenberg Antiferromagnets: Semiclassically Quantized Solitons of the One-Dimensional Easy-Axis Néel State", Phys. Rev. Lett. **50**, 1153–1156 (1983).

[51]I. Affleck, T. Kennedy, E. H. Lieb, and H. Tasaki, "Rigorous results on valence-bond ground states in antiferromagnets", Phys. Rev. Lett. **59**, 799–802 (1987).

[52]T. Kennedy, "Exact diagonalisations of open spin-1 chains", Journal of Physics: Condensed Matter **2**, 5737 (1990).

[53]F. Pollmann, A. M. Turner, E. Berg, and M. Oshikawa, "Entanglement spectrum of a topological phase in one dimension", Phys. Rev. B **81**, 064439 (2010).

[54]A. M. Turner, F. Pollmann, and E. Berg, "Topological phases of one-dimensional fermions: An entanglement point of view", Phys. Rev. B **83**, 075102 (2011).

[55]A. Montorsi, F. Dolcini, R. C. Iotti, and F. Rossi, "Symmetry-protected topological phases of one-dimensional interacting fermions with spin-charge separation", Phys. Rev. B **95**, 245108 (2017).

[56]J. Li, R.-L. Chu, J. K. Jain, and S.-Q. Shen, "Topological Anderson Insulator", Phys. Rev. Lett. **102**, 136806 (2009).

[57]C. W. Groth, M. Wimmer, A. R. Akhmerov, J. Tworzydło, and C. W. J. Beenakker, "Theory of the Topological Anderson Insulator", Phys. Rev. Lett. **103**, 196805 (2009).

[58]Y. Xing, L. Zhang, and J. Wang, "Topological Anderson insulator phenomena", Phys. Rev. B **84**, 035110 (2011).

[59]Y. E. Kraus, Y. Lahini, Z. Ringel, M. Verbin, and O. Zilberberg, "Topological States and Adiabatic Pumping in Quasicrystals", Phys. Rev. Lett. **109**, 106402 (2012).

[60]H. Huang and F. Liu, "Quantum Spin Hall Effect and Spin Bott Index in a Quasicrystal Lattice", Phys. Rev. Lett. **121**, 126401 (2018).

[61]J.-N. Fuchs, R. Mosseri, and J. Vidal, "Landau levels in quasicrystals", Phys. Rev. B **98**, 165427 (2018).

[62]T. A. Loring, "Bulk spectrum and K-theory for infinite-area topological quasicrystals", J. Math. Phys. **60**, 081903 (2019).

[63]R. Chen, D.-H. Xu, and B. Zhou, "Topological Anderson insulator phase in a quasicrystal lattice", Phys. Rev. B **100**, 115311 (2019).

[64]H. Roche Carrasco, J. Schirmann, A. Mordret, and A. G. Grushin, "Family of Aperiodic Tilings with Tunable Quantum Geometric Tensor", Phys. Rev. Lett. **135**, 236603 (2025).

[65]A. Agarwala and V. B. Shenoy, "Topological Insulators in Amorphous Systems", Phys. Rev. Lett. **118**, 236402 (2017).

[66]N. P. Mitchell, L. M. Nash, D. Hexner, A. M. Turner, and W. T. M. Irvine, "Amorphous topological insulators constructed from random point sets", Nature Physics **14**, 380–385 (2018).

[67]M. Costa, G. R. Schleder, M. Buongiorno Nardelli, C. Lewenkopf, and A. Fazzio, "Toward Realistic Amorphous Topological Insulators", Nano Letters **19**, 8941–8946 (2019).

[68]Q. Marsal, D. Varjas, and A. G. Grushin, "Topological Weaire–Thorpe models of amorphous matter", Proceedings of the National Academy of Sciences **117**, 30260–30265 (2020).

[69]P. Corbae, J. D. Hannukainen, Q. Marsal, D. Muñoz-Segovia, and A. G. Grushin, "Amorphous topological matter: Theory and experiment", Europhysics Letters **142**, 16001 (2023).

[70]P. Corbae, S. Ciocys, D. Varjas, E. Kennedy, S. Zeltmann, M. Molina-Ruiz, S. M. Griffin, C. Jozwiak, Z. Chen, L.-W. Wang, A. M. Minor, M. Scott, A. G. Grushin, A. Lanzara, and F. Hellman, "Observation of spin-momentum locked surface states in amorphous Bi_2Se_3", Nature Materials **22**, 200–206 (2023).

[71]I. C. Fulga, F. Hassler, A. R. Akhmerov, and C. W. J. Beenakker, "Scattering formula for the topological quantum number of a disordered multimode wire", Phys. Rev. B **83**, 155429 (2011).

[72]I. C. Fulga, F. Hassler, and A. R. Akhmerov, "Scattering theory of topological insulators and superconductors", Phys. Rev. B **85**, 165409 (2012).

[73]C. Tauber, "Effective vacua for Floquet topological phases: A numerical perspective on the switch-function formalism", Phys. Rev. B **97**, 195312 (2018).

[74]P. Elbau and G. M. Graf, "Equality of Bulk and Edge Hall Conductance Revisited", Communications in Mathematical Physics **229**, 415–432 (2002).

[75]L. Jezequel, C. Tauber, and P. Delplace, "Estimating bulk and edge topological indices in finite open chiral chains", Journal of Mathematical Physics **63**, 10.1063/5.0096720 (2022).

[76]H. Li and F. D. M. Haldane, "Entanglement Spectrum as a Generalization of Entanglement Entropy: Identification of Topological Order in Non-Abelian Fractional Quantum Hall Effect States", Phys. Rev. Lett. **101**, 010504 (2008).

[77]E. Prodan, T. L. Hughes, and B. A. Bernevig, "Entanglement Spectrum of a Disordered Topological Chern Insulator", Phys. Rev. Lett. **105**, 115501 (2010).

[78]M. B. Hastings and T. A. Loring, "Almost commuting matrices, localized Wannier functions, and the quantum Hall effect", Journal of Mathematical Physics **51**, 10.1063/1.3274817 (2010).

[79]M. B. Hastings and T. A. Loring, "Topological insulators and C^* algebras: Theory and numerical practice", Annals of Physics **326**, 1699–1759 (2011).

[80]T. A. Loring and M. B. Hastings, "Disordered topological insulators via C*-algebras", Europhysics Letters **92**, 67004 (2011).

[81]T. A. Loring, "K-theory and pseudospectra for topological insulators", Annals of Physics **356**, 383–416 (2015).

[82]T. A. Loring and H. Schulz-Baldes, "The Spectral Localizer for Even Index Pairings", New York Journal of Mathematics **23**, 1271–1301 (2017).

[83]D. Muñoz-Segovia, P. Corbae, D. Varjas, F. Hellman, S. M. Griffin, and A. G. Grushin, "Structural spillage: An efficient method to identify noncrystalline topological materials", Phys. Rev. Res. **5**, L042011 (2023).

[84]A. Baldereschi, "Mean-Value Point in the Brillouin Zone", Phys. Rev. B **7**, 5212–5215 (1973).

[85]I. Souza, J. Íñiguez, and D. Vanderbilt, "Dynamics of Berry-phase polarization in time-dependent electric fields", Phys. Rev. B **69**, 085106 (2004).

[86]N. Sai, K. M. Rabe, and D. Vanderbilt, "Theory of structural response to macroscopic electric fields in ferroelectric systems", Phys. Rev. B **66**, 104108 (2002).

[87]T. Thonhauser, "Theory of orbital magnetization in solids", International Journal of Modern Physics B **25**, 1429–1458 (2011).

[88]W. Kohn, "Density Functional and Density Matrix Method Scaling Linearly with the Number of Atoms", Phys. Rev. Lett. **76**, 3168–3171 (1996).

[89]O. Pozo, C. Repellin, and A. G. Grushin, "Quantization in Chiral Higher Order Topological Insulators: Circular Dichroism and Local Chern Marker", Phys. Rev. Lett. **123**, 247401 (2019).

[90] A. A. Aligia and G. Ortiz, "Quantum Mechanical Position Operator and Localization in Extended Systems", Phys. Rev. Lett. **82**, 2560–2563 (1999).

[91] E. V. Lopes, F. C. de Lima, C. Lewenkopf, and A. Fazzio, "Engineering Quantum Phases in Two Dimensions via Vacancy-Induced Electronic Reconstruction", arXiv preprint arXiv:2603.17122 (2026).

[92] B. D. Assunção, G. J. Ferreira, and C. H. Lewenkopf, "Phase transitions and scale invariance in topological Anderson insulators", Phys. Rev. B **109**, L201102 (2024).

[93] M. D. Caio, G. Möller, N. R. Cooper, and M. J. Bhaseen, "Topological marker currents in Chern insulators", Nature Physics **15**, 257–261 (2019).

[94] The StraWBerryPy code package is available at `https://github.com/strawberrypy-developers/strawberrypy.git`.

[95] A. Marrazzo, S. Beck, E. R. Margine, N. Marzari, A. A. Mostofi, J. Qiao, I. Souza, S. S. Tsirkin, J. R. Yates, and G. Pizzi, "Wannier-function software ecosystem for materials simulations", Rev. Mod. Phys. **96**, 045008 (2024).

[96] The TBmodels code package is available at `https://tbmodels.greschd.ch/en/latest/index.html`.

[97] D. Gresch, Q. S. Wu, G. W. Winkler, R. Häuselmann, M. Troyer, and A. A. Soluyanov, "Automated construction of symmetrized Wannier-like tight-binding models from ab initio calculations", Phys. Rev. Mater. **2**, 103805 (2018).

[98] S. Coh and D. Vanderbilt, *Python tight binding (pythtb)*, 2022.

[99] M. E. Fisher, "Correlation Functions and the Critical Region of Simple Fluids", Journal of Mathematical Physics **5**, 944–962 (1964).

[100] M. Tuckerman, *Statistical mechanics: theory and molecular simulation*, Oxford Graduate Texts (OUP Oxford, 2023).

[101] J. Song, H. Liu, H. Jiang, Q.-f. Sun, and X. C. Xie, "Dependence of topological Anderson insulator on the type of disorder", Phys. Rev. B **85**, 195125 (2012).

[102] E. Prodan, "Non-commutative tools for topological insulators", New Journal of Physics **12**, 065003 (2010).

[103] C. B. C. P. Orth T. Sekera and T. L. Schmidt, "The topological Anderson insulator phase in the Kane-Mele model", Sci. Rep. **2**, `10.1038/srep24007` (2016).

[104] P. Bampoulis, C. Castenmiller, D. J. Klaassen, J. van Mil, Y. Liu, C.-C. Liu, Y. Yao, M. Ezawa, A. N. Rudenko, and H. J. W. Zandvliet, "Quantum Spin Hall States and Topological Phase Transition in Germanene", Phys. Rev. Lett. **130**, 196401 (2023).

[105]D. J. Klaassen, I. Boutis, C. Castenmiller, and P. Bampoulis, "Tunability of topological edge states in germanene at room temperature", J. Mater. Chem. C **12**, 15975–15980 (2024).

[106]M. Ezawa, "A topological insulator and helical zero mode in silicene under an inhomogeneous electric field", New Journal of Physics **14**, 033003 (2012).

[107]P. Hohenberg and W. Kohn, "Inhomogeneous Electron Gas", Phys. Rev. **136**, B864–B871 (1964).

[108]W. Kohn and L. J. Sham, "Self-Consistent Equations Including Exchange and Correlation Effects", Phys. Rev. **140**, A1133–A1138 (1965).

[109]L. Hedin, "New Method for Calculating the One-Particle Green's Function with Application to the Electron-Gas Problem", Phys. Rev. **139**, A796–A823 (1965).

[110]M. S. Hybertsen and S. G. Louie, "Electron correlation in semiconductors and insulators: Band gaps and quasiparticle energies", Phys. Rev. B **34**, 5390–5413 (1986).

[111]J. P. Perdew, K. Burke, and M. Ernzerhof, "Generalized Gradient Approximation Made Simple", Phys. Rev. Lett. **77**, 3865–3868 (1996).

[112]P. Giannozzi, S. Baroni, N. Bonini, M. Calandra, R. Car, C. Cavazzoni, D. Ceresoli, G. L. Chiarotti, M. Cococcioni, I. Dabo, A. Dal Corso, S. de Gironcoli, S. Fabris, G. Fratesi, R. Gebauer, U. Gerstmann, C. Gougoussis, A. Kokalj, M. Lazzeri, L. Martin-Samos, N. Marzari, F. Mauri, R. Mazzarello, S. Paolini, A. Pasquarello, L. Paulatto, C. Sbraccia, S. Scandolo, G. Sclauzero, A. P. Seitsonen, A. Smogunov, P. Umari, and R. M. Wentzcovitch, "QUANTUM ESPRESSO: a modular and open-source software project for quantum simulations of materials", Journal of Physics: Condensed Matter **21**, 395502 (2009).

[113]P. Giannozzi, O. Andreussi, T. Brumme, O. Bunau, M. Buongiorno Nardelli, M. Calandra, R. Car, C. Cavazzoni, D. Ceresoli, M. Cococcioni, N. Colonna, I. Carnimeo, A. Dal Corso, S. de Gironcoli, P. Delugas, R. A. DiStasio, A. Ferretti, A. Floris, G. Fratesi, G. Fugallo, R. Gebauer, U. Gerstmann, F. Giustino, T. Gorni, J. Jia, M. Kawamura, H.-Y. Ko, A. Kokalj, E. Küçükbenli, M. Lazzeri, M. Marsili, N. Marzari, F. Mauri, N. L. Nguyen, H.-V. Nguyen, A. Otero-de-la-Roza, L. Paulatto, S. Poncé, D. Rocca, R. Sabatini, B. Santra, M. Schlipf, A. P. Seitsonen, A. Smogunov, I. Timrov, T. Thonhauser, P. Umari, N. Vast, X. Wu, and S. Baroni, "Advanced capabilities for materials modelling with Quantum ESPRESSO", Journal of Physics: Condensed Matter **29**, 465901 (2017).

[114]P. Giannozzi, O. Baseggio, P. Bonfà, D. Brunato, R. Car, I. Carnimeo, C. Cavazzoni, S. de Gironcoli, P. Delugas, F. Ferrari Ruffino, A. Ferretti, N. Marzari, I. Timrov, A. Urru, and S. Baroni, "Quantum ESPRESSO toward the exascale", The Journal of Chemical Physics **152**, 10.1063/5.0005082 (2020).

[115] D. R. Hamann, M. Schlüter, and C. Chiang, "Norm-Conserving Pseudopotentials", Phys. Rev. Lett. **43**, 1494–1497 (1979).

[116] "Maximally localized Wannier functions: Theory and applications, author = Marzari, Nicola and Mostofi, Arash A. and Yates, Jonathan R. and Souza, Ivo and Vanderbilt, David", Rev. Mod. Phys. **84**, 1419–1475 (2012).

[117] I. Souza, N. Marzari, and D. Vanderbilt, "Maximally localized Wannier functions for entangled energy bands", Phys. Rev. B **65**, 035109 (2001).

[118] G. Pizzi, V. Vitale, R. Arita, S. Blügel, F. Freimuth, G. Géranton, M. Gibertini, D. Gresch, C. Johnson, T. Koretsune, J. Ibañez-Azpiroz, H. Lee, J.-M. Lihm, D. Marchand, A. Marrazzo, Y. Mokrousov, J. I. Mustafa, Y. Nohara, Y. Nomura, L. Paulatto, S. Poncé, T. Ponweiser, J. Qiao, F. Thöle, S. S. Tsirkin, M. Wierzbowska, N. Marzari, D. Vanderbilt, I. Souza, A. A. Mostofi, and J. R. Yates, "Wannier90 as a community code: new features and applications", Journal of Physics: Condensed Matter **32**, 165902 (2020).

[119] V. Popescu and A. Zunger, "Effective Band Structure of Random Alloys", Phys. Rev. Lett. **104**, 236403 (2010).

[120] V. Popescu and A. Zunger, "Extracting E versus $\vec{k}$ effective band structure from supercell calculations on alloys and impurities", Phys. Rev. B **85**, 085201 (2012).

[121] M. Zacharias and F. Giustino, "Theory of the special displacement method for electronic structure calculations at finite temperature", Phys. Rev. Res. **2**, 013357 (2020).

[122] Q. Wu, S. Zhang, H.-F. Song, M. Troyer, and A. A. Soluyanov, "WannierTools: An open-source software package for novel topological materials", Computer Physics Communications **224**, 405–416 (2018).

[123] A. R. Cabral, H. F. Galbiatti, R. Kwitko-Ribeiro, and B. Lehmann, "Platinum enrichment at low temperatures and related microstructures, with examples of hongshiite (PtCu) and empirical Pt_2HgSe_3 from Itabira, Minas Gerais, Brazil", Terra Nova **20**, 32–37 (2008).

[124] A. Vymazalova, F. Laufek, M. Drábek, A. Cabral, J. Haloda, T. Sidorinova, B. Lehmann, H. Galbiatti, and J. Drahokoupil, "Jacutingaite, Pt_2HgSe_3, A new platinum-group mineral species from the Cauê iron-ore deposit, Itabira District, Minas Gerais, Brazil", The Canadian Mineralogist **50**, 431–440 (2012).

[125] A. Marrazzo, N. Marzari, and M. Gibertini, "Emergent dual topology in the three-dimensional Kane-Mele Pt_2HgSe_3", Phys. Rev. Res. **2**, 012063(R) (2020).

[126] D. R. Hamann, "Optimized norm-conserving Vanderbilt pseudopotentials", Phys. Rev. B **88**, 085117 (2013).

[127]M. van Setten, M. Giantomassi, E. Bousquet, M. Verstraete, D. Hamann, X. Gonze, and G.-M. Rignanese, "The PseudoDojo: Training and grading a 85 element optimized norm-conserving pseudopotential table", Computer Physics Communications **226**, 39–54 (2018).

[128]W.-Y. Shan, J. Lu, H.-Z. Lu, and S.-Q. Shen, "Vacancy-induced bound states in topological insulators", Phys. Rev. B **84**, 035307 (2011).

[129]R.-J. Slager, L. Rademaker, J. Zaanen, and L. Balents, "Impurity-bound states and Green's function zeros as local signatures of topology", Phys. Rev. B **92**, 085126 (2015).

[130]S.-S. Diop, L. Fritz, M. Vojta, and S. Rachel, "Impurity bound states as detectors of topological band structures revisited", Phys. Rev. B **101**, 245132 (2020).

[131]N. F. Mott and R. Peierls, "Discussion of the paper by de Boer and Verwey", Proceedings of the Physical Society **49**, 72 (1937).

[132]Y. Cao, V. Fatemi, S. Fang, K. Watanabe, T. Taniguchi, E. Kaxiras, and P. Jarillo-Herrero, "Unconventional superconductivity in magic-angle graphene superlattices", Nature **556**, 43–50 (2018).

[133]J. Kanamori, "Electron Correlation and Ferromagnetism of Transition Metals", Progress of Theoretical Physics **30**, 275–289 (1963).

[134]A. Georges, L. d. Medici, and J. Mravlje, "Strong Correlations from Hund's Coupling", Annual Review of Condensed Matter Physics **4**, 137–178 (2013).

[135]J. Hubbard, "Electron Correlations in Narrow Energy Bands", Proc. R. Soc. London, Ser. A **276**, 238–257 (1963).

[136]M. C. Gutzwiller, "Effect of Correlation on the Ferromagnetism of Transition Metals", Phys. Rev. Lett. **10**, 159–162 (1963).

[137]Y. Nagaoka, "Ferromagnetism in a Narrow, Almost Half-Filled s Band", Phys. Rev. **147**, 392–405 (1966).

[138]H. A. Bethe, "Zur Theorie der Metalle", Zeitschrift für Physik **71**, 205–226 (1931).

[139]E. H. Lieb and F. Y. Wu, "Absence of mott transition in an exact solution of the short-range, one-band model in one dimension", Phys. Rev. Lett. **21**, 192–192 (1968).

[140]M. Qin, H. Shi, and S. Zhang, "Benchmark study of the two-dimensional Hubbard model with auxiliary-field quantum Monte Carlo method", Phys. Rev. B **94**, 085103 (2016).

[141]H. Xu, C.-M. Chung, M. Qin, U. Schollwöck, S. R. White, and S. Zhang, "Coexistence of superconductivity with partially filled stripes in the Hubbard model", Science **384**, eadh7691 (2024).

[142]W. F. Brinkman and T. M. Rice, "Application of Gutzwiller's Variational Method to the Metal-Insulator Transition", Phys. Rev. B **2**, 4302–4304 (1970).

[143]W. Metzner and D. Vollhardt, "Ground-state properties of correlated fermions: exact analytic results for the gutzwiller wave function", Phys. Rev. Lett. **59**, 121–124 (1987).

[144]H. Yokoyama and H. Shiba, "Variational Monte-Carlo Studies of Hubbard Model. I", Journal of the Physical Society of Japan **56**, 1490–1506 (1987).

[145]H. Yokoyama and H. Shiba, "Variational Monte-Carlo Studies of Hubbard Model. II", Journal of the Physical Society of Japan **56**, 3582–3592 (1987).

[146]H. Yokoyama and H. Shiba, "Variational Monte-Carlo Studies of Hubbard Model. III. Intersite Correlation Effects", Journal of the Physical Society of Japan **59**, 3669–3686 (1990).

[147]R. Jastrow, "Many-Body Problem with Strong Forces", Phys. Rev. **98**, 1479–1484 (1955).

[148]W. L. McMillan, "Ground State of Liquid He^4", Phys. Rev. **138**, A442–A451 (1965).

[149]L. Reatto and G. V. Chester, "Phonons and the properties of a bose system", Phys. Rev. **155**, 88–100 (1967).

[150]M. Capello, F. Becca, M. Fabrizio, S. Sorella, and E. Tosatti, "Variational Description of Mott Insulators", Phys. Rev. Lett. **94**, 026406 (2005).

[151]M. Capello, F. Becca, S. Yunoki, M. Fabrizio, and S. Sorella, "From Luttinger liquid to Mott insulator: The correct low-energy description of the one-dimensional Hubbard model by an unbiased variational approach", Phys. Rev. B **72**, 085121 (2005).

[152]M. Capello, F. Becca, S. Yunoki, and S. Sorella, "Unconventional metal-insulator transition in two dimensions", Phys. Rev. B **73**, 245116 (2006).

[153]E. Manousakis, "The spin-$\frac{1}{2}$ Heisenberg antiferromagnet on a square lattice and its application to the cuprous oxides", Rev. Mod. Phys. **63**, 1–62 (1991).

[154]D. Piccioni, C. Apostoli, F. Becca, G. Mazzola, A. Parola, S. Sorella, and G. E. Santoro, "Jastrow wave function for the spin-1 Heisenberg chain: The string order revealed by the mapping to the classical Coulomb gas", Phys. Rev. B **108**, 104417 (2023).

[155]R. P. Feynman, "Atomic Theory of the Two-Fluid Model of Liquid Helium", Phys. Rev. **94**, 262–277 (1954).

[156]R. P. Feynman and M. Cohen, "Energy Spectrum of the Excitations in Liquid Helium", Phys. Rev. **102**, 1189–1204 (1956).

[157]L. F. Tocchio, F. Becca, and C. Gros, "Backflow correlations in the Hubbard model: An efficient tool for the study of the metal-insulator transition and the large-U limit", Phys. Rev. B **83**, 195138 (2011).

[158]S. Barbarino, G. Sangiovanni, and J. C. Budich, "First-order topological quantum phase transition in a strongly correlated ladder", Phys. Rev. B **99**, 075158 (2019).

[159]V. Gurarie, "Single-particle Green's functions and interacting topological insulators", Phys. Rev. B **83**, 085426 (2011).

[160]A. Blason and M. Fabrizio, "Unified role of Green's function poles and zeros in correlated topological insulators", Physical Review B **108**, 10.1103/physrevb.108.125115 (2023).

[161]Z. Wang and S.-C. Zhang, "Simplified Topological Invariants for Interacting Insulators", Phys. Rev. X **2**, 031008 (2012).

[162]A. Amaricci, L. Privitera, F. Petocchi, M. Capone, G. Sangiovanni, and B. Trauzettel, "Edge state reconstruction from strong correlations in quantum spin Hall insulators", Phys. Rev. B **95**, 205120 (2017).

[163]R. Resta, *Geometry and Topology in Electronic Structure Theory*, http://www-dft.ts.infn.it/~resta/gtse/draft.pdf, Unpublished notes, 2022.

[164]J. Bardeen, L. N. Cooper, and J. R. Schrieffer, "Theory of Superconductivity", Phys. Rev. **108**, 1175–1204 (1957).

[165]A. J. Leggett, "Superfluidity", Rev. Mod. Phys. **71**, S318–S323 (1999).

[166]R. B. Laughlin, "Anomalous Quantum Hall Effect: An Incompressible Quantum Fluid with Fractionally Charged Excitations", Phys. Rev. Lett. **50**, 1395–1398 (1983).

[167]S. R. White, "Density matrix formulation for quantum renormalization groups", Phys. Rev. Lett. **69**, 2863–2866 (1992).

[168]T. Giamarchi, *Quantum Physics in One Dimension* (Oxford University Press, 2003).

[169]K. G. Wilson, "The renormalization group and critical phenomena", Rev. Mod. Phys. **55**, 583–600 (1983).

[170]P. Corboz, R. Orús, B. Bauer, and G. Vidal, "Simulation of strongly correlated fermions in two spatial dimensions with fermionic projected entangled-pair states", Phys. Rev. B **81**, 165104 (2010).

[171]Z.-X. Li and H. Yao, "Sign-Problem-Free Fermionic Quantum Monte Carlo: Developments and Applications", Annual Review of Condensed Matter Physics **10**, 337–356 (2019).

[172]A. Georges, G. Kotliar, W. Krauth, and M. J. Rozenberg, "Dynamical mean-field theory of strongly correlated fermion systems and the limit of infinite dimensions", Rev. Mod. Phys. **68**, 13–125 (1996).

[173]F. Becca and S. Sorella, *Quantum Monte Carlo Approaches for Correlated Systems* (Cambridge University Press, 2017).

[174]N. Metropolis, A. W. Rosenbluth, M. N. Rosenbluth, A. H. Teller, and E. Teller, "Equation of State Calculations by Fast Computing Machines", The Journal of Chemical Physics **21**, 1087–1092 (1953).

[175]W. K. Hastings, "Monte Carlo Sampling Methods Using Markov Chains and Their Applications", Biometrika **57**, 97–109 (1970).

[176]S. Sorella, "Green Function Monte Carlo with Stochastic Reconfiguration", Phys. Rev. Lett. **80**, 4558–4561 (1998).

[177]S. Sorella, "Wave function optimization in the variational Monte Carlo method", Phys. Rev. B **71**, 241103 (2005).

[178]F. Haldane, "'Luttinger liquid theory' of one-dimensional quantum fluids. I. Properties of the Luttinger model and their extension to the general 1D interacting spinless Fermi gas", Journal of Physics C: Solid State Physics **14**, 2585 (1981).

[179]A. Luther and V. J. Emery, "Backward Scattering in the One-Dimensional Electron Gas", Phys. Rev. Lett. **33**, 589–592 (1974).

[180]N. F. Mott, "Metal-Insulator Transition", Rev. Mod. Phys. **40**, 677–683 (1968).

[181]X. Lu, P. Stepanov, W. Yang, M. Xie, M. A. Aamir, I. Das, C. Urgell, K. Watanabe, T. Taniguchi, G. Zhang, A. Bachtold, A. H. MacDonald, and D. K. Efetov, "Superconductors, orbital magnets and correlated states in magic-angle bilayer graphene", Nature **574**, 653–657 (2019).

[182]S. Rachel and K. Le Hur, "Topological insulators and Mott physics from the Hubbard interaction", Phys. Rev. B **82**, 075106 (2010).

[183]M. Hohenadler, T. C. Lang, and F. F. Assaad, "Correlation Effects in Quantum Spin-Hall Insulators: A Quantum Monte Carlo Study", Phys. Rev. Lett. **106**, 100403 (2011).

[184]S.-L. Yu, X. C. Xie, and J.-X. Li, "Mott Physics and Topological Phase Transition in Correlated Dirac Fermions", Phys. Rev. Lett. **107**, 010401 (2011).

[185]Y. Yamaji and M. Imada, "Mott physics on helical edges of two-dimensional topological insulators", Phys. Rev. B **83**, 205122 (2011).

[186]M. Hohenadler, Z. Y. Meng, T. C. Lang, S. Wessel, A. Muramatsu, and F. F. Assaad, "Quantum phase transitions in the Kane-Mele-Hubbard model", Phys. Rev. B **85**, 115132 (2012).

[187]J. C. Budich, R. Thomale, G. Li, M. Laubach, and S.-C. Zhang, "Fluctuation-induced topological quantum phase transitions in quantum spin-Hall and anomalous-Hall insulators", Phys. Rev. B **86**, 201407 (2012).

[188]M. Hohenadler, F. Parisen Toldin, I. F. Herbut, and F. F. Assaad, "Phase diagram of the Kane-Mele-Coulomb model", Phys. Rev. B **90**, 085146 (2014).

[189]Y. Tada, R. Peters, M. Oshikawa, A. Koga, N. Kawakami, and S. Fujimoto, "Correlation effects in two-dimensional topological insulators", Phys. Rev. B **85**, 165138 (2012).

[190]T. Yoshida, R. Peters, S. Fujimoto, and N. Kawakami, "Topological antiferromagnetic phase in a correlated Bernevig-Hughes-Zhang model", Phys. Rev. B **87**, 085134 (2013).

[191]J. C. Budich, B. Trauzettel, and G. Sangiovanni, "Fluctuation-driven topological Hund insulators", Phys. Rev. B **87**, 235104 (2013).

[192]A. Amaricci, J. C. Budich, M. Capone, B. Trauzettel, and G. Sangiovanni, "First-Order Character and Observable Signatures of Topological Quantum Phase Transitions", Phys. Rev. Lett. **114**, 185701 (2015).

[193]J. Imriška, L. Wang, and M. Troyer, "First-order topological phase transition of the Haldane-Hubbard model", Phys. Rev. B **94**, 035109 (2016).

[194]S. R. Manmana, A. M. Essin, R. M. Noack, and V. Gurarie, "Topological invariants and interacting one-dimensional fermionic systems", Phys. Rev. B **86**, 205119 (2012).

[195]L. Barbiero, L. Santos, and N. Goldman, "Quenched dynamics and spin-charge separation in an interacting topological lattice", Phys. Rev. B **97**, 201115 (2018).

[196]H. Guo and S.-Q. Shen, "Topological phase in a one-dimensional interacting fermion system", Phys. Rev. B **84**, 195107 (2011).

[197]S. R. White, "Equivalence of the antiferromagnetic Heisenberg ladder to a single S=1 chain", Phys. Rev. B **53**, 52–55 (1996).

[198]M. den Nijs and K. Rommelse, "Preroughening transitions in crystal surfaces and valence-bond phases in quantum spin chains", Phys. Rev. B **40**, 4709–4734 (1989).

[199]M. Fishman, S. R. White, and E. M. Stoudenmire, "The ITensor Software Library for Tensor Network Calculations", SciPost Phys. Codebases, 4 (2022).

[200]S. R. White and D. A. Huse, "Numerical renormalization-group study of low-lying eigenstates of the antiferromagnetic S=1 Heisenberg chain", Phys. Rev. B **48**, 3844–3852 (1993).

[201]F. Anfuso and A. Rosch, "String order and adiabatic continuity of Haldane chains and band insulators", Phys. Rev. B **75**, 144420 (2007).

[202]A. Montorsi and M. Roncaglia, "Nonlocal Order Parameters for the 1D Hubbard Model", Phys. Rev. Lett. **109**, 236404 (2012).

[203]L. Barbiero, A. Montorsi, and M. Roncaglia, "How hidden orders generate gaps in one-dimensional fermionic systems", Phys. Rev. B **88**, 035109 (2013).

[204] A. Blason and M. Fabrizio, "Exciton topology and condensation in a model quantum spin Hall insulator", Phys. Rev. B **102**, 035146 (2020).

[205] A. Amaricci, G. Mazza, M. Capone, and M. Fabrizio, "Exciton condensation in strongly correlated quantum spin Hall insulators", Phys. Rev. B **107**, 115117 (2023).

[206] I. Pasqua, A. Blason, and M. Fabrizio, "Exciton condensation driven by bound states of Green's function zeros", Phys. Rev. B **110**, 125144 (2024).

[207] S. Miyakoshi and Y. Ohta, "Antiferromagnetic topological insulator state in the correlated Bernevig-Hughes-Zhang model", Phys. Rev. B **87**, 195133 (2013).

[208] A. Amaricci, A. Valli, G. Sangiovanni, B. Trauzettel, and M. Capone, "Coexistence of metallic edge states and antiferromagnetic ordering in correlated topological insulators", Phys. Rev. B **98**, 045133 (2018).

[209] M. Calandra Buonaura and S. Sorella, "Numerical study of the two-dimensional Heisenberg model using a Green function Monte Carlo technique with a fixed number of walkers", Phys. Rev. B **57**, 11446–11456 (1998).

[210] V. Khaustov, J. Köster, M. W. Ochapski, A. Zakharov, D. Convertino, Z. M. Gebeyehu, L. Martini, N. Mishra, G. Marini, M. Calandra, U. Kaiser, S. Forti, and C. Coletti, "Reversible semimetal-semiconductor phase transition in CVD-grown monolayer $MoTe_2$", 2D Materials, 10.1088/2053-1583/adbcc0 (2025).

[211] L. Rademaker and M. Gibertini, "Gate-tunable imbalanced Kane-Mele model in encapsulated bilayer jacutingaite", Phys. Rev. Mater. **5**, 044201 (2021).

[212] János K. Asbóth, László Oroszlány, and András Pályi, *A Short Course on Topological Insulators* (Springer International Publishing, 2016).